WARWICK
THE UNIVERSITY OF WARWICK

A Thesis Submitted for the Degree of PhD at the University of Warwick

Permanent WRAP URL:
http://wrap.warwick.ac.uk/102613/

Copyright and reuse:
This thesis is made available online and is protected by original copyright.
Please scroll down to view the document itself.
Please refer to the repository record for this item for information to help you to cite it.
Our policy information is available from the repository home page.

For more information, please contact the WRAP Team at: wrap@warwick.ac.uk

warwick.ac.uk/lib-publications

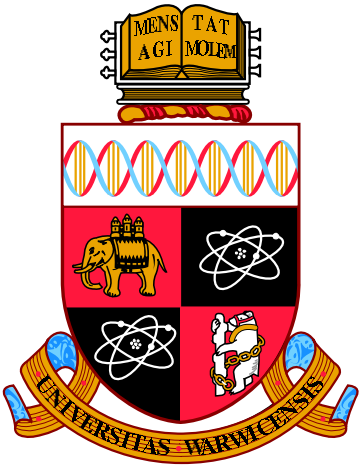

The Evolution of Cataclysmic Variables

by

Anna Francesca Pala

Thesis

Submitted to the University of Warwick for the degree of

Doctor of Philosophy

Department of Physics

March 2018

THE UNIVERSITY OF
WARWICK

Contents

List of Tables **v**

List of Figures **vii**

Acknowledgments **xi**

Declarations **xii**

Abstract **xiv**

Abbreviations **xv**

Chapter 1 Introduction **1**

1.1 Basics of stellar evolution 2

1.1.1 Evolution of low and intermediate mass stars 5

1.2 White dwarfs 7

1.2.1 Mass distribution 9

1.2.2 Atmospheres 10

1.3 Binary stars 13

1.3.1 Mass transfer in binaries 14

1.3.2 Common envelope 17

1.4 Cataclysmic Variables 18

1.4.1 CV formation and evolution 18

1.4.2 AML mechanisms 22

1.5 Observational properties of CVs 25

1.5.1 CV spectral appereance 25

1.5.2 Accretion discs 27

1.5.3 Disc outbursts 29

1.5.4 Nova eruptions 32

1.5.5 CV classification 33

1.6 Testing the models of CV evolution . . . 33
1.6.1 Angular momentum loss rates . . . 34
1.6.2 Masses . . . 36
1.6.3 Period distribution, space density and period bouncers . . . 37
1.7 Thesis outline . . . 38

Chapter 2 Observations and Techniques 39
2.1 Astronomical detectors . . . 39
2.1.1 Charge–Coupled Devices . . . 39
2.1.2 Photomultipliers . . . 41
2.2 Spectroscopic observations . . . 42
2.2.1 Cosmic Origin Spectrograph on the *Hubble Space Telescope* . 43
2.2.2 Space Telescope Imaging Spectrograph on the *Hubble Space Telescope* . . . 44
2.2.3 X–shooter at the Very Large Telescope . . . 46
2.2.4 The ESO Faint Object Spectrograph and Camera 2 . . . 51
2.3 Photometric observations . . . 52
2.3.1 *Kepler* . . . 52
2.3.2 TMO61, OC61 and PROMPT observations . . . 53
2.3.3 JAST/T80Cam . . . 54
2.3.4 Small and Moderate Aperture Research Telescope System . . 54
2.4 Methods . . . 55
2.4.1 Light curve extraction from TIME–TAG observations . . . 55
2.4.2 Aperture photometry . . . 57
2.4.3 Fitting routines . . . 58
2.4.4 System parameters . . . 59
2.5 Summary . . . 63

Chapter 3 Effective Temperatures and Masses of CV White Dwarfs 64
3.1 Introduction . . . 64
3.2 Observations . . . 66
3.2.1 COS observations . . . 66
3.2.2 STIS observations . . . 71
3.2.3 X–shooter observations . . . 72
3.3 Data analysis . . . 75
3.3.1 Optical data . . . 75
3.3.2 Ultraviolet data . . . 77
3.4 Discussion . . . 87
3.4.1 $\log g$ correction of published $T_{\rm eff}$ values . . . 87
3.4.2 Notes on individual objects . . . 90

3.4.3 Systems with previous $T_{\rm eff}$ measurements . . . 95
3.4.4 Eclipsing systems . . . 99
3.4.5 Effective temperature of CV white dwarfs as a probe of their evolution . . . 101
3.4.6 CV white dwarf masses . . . 105
3.5 Conclusions . . . 107

Chapter 4 Evidence for spiral density waves in the accretion disc of SDSS J123813.73–033933.0 111
4.1 Introduction . . . 111
4.2 Observations . . . 112
4.2.1 Photometry . . . 112
4.2.2 Spectroscopy . . . 113
4.3 Results . . . 114
4.3.1 Superoutburst and superhumps . . . 114
4.3.2 System parameters and optical spectral fitting . . . 115
4.3.3 Light curve analysis . . . 122
4.3.4 Ultraviolet spectroscopy and light curve . . . 127
4.3.5 Energetics of the brightenings . . . 132
4.4 Discussion . . . 134
4.4.1 SDSS1238 as a period bouncer . . . 134
4.4.2 The origin of the optical and ultraviolet variability in SDSS1238 135
4.5 Conclusions . . . 141

Chapter 5 The SU UMa QZ Lib: a period bouncer 144
5.1 Introduction . . . 144
5.2 Observation and data reduction . . . 145
5.2.1 Spectroscopic observations . . . 145
5.2.2 Photometric observations . . . 146
5.3 The lightcurve . . . 147
5.4 Time resolved spectrosopy . . . 150
5.5 Doppler Tomography . . . 151
5.6 The spectra . . . 152
5.6.1 The model . . . 152
5.6.2 The spectra after outburst . . . 154
5.6.3 The quiescent spectra . . . 155
5.7 Discussion . . . 158
5.8 Conclusions . . . 162

Chapter 6 CHiCaS: The Compact binary HIgh CAdence Survey 164
6.1 Introduction 164
6.2 The search for period bouncers 165
6.3 The Compact binary HIgh CAdence Survey 166
6.3.1 Scientific objectives 167
6.3.2 Observations 168
6.3.3 Preliminary results 170
6.4 Summary and future work 174

Chapter 7 Concluding summary and future work 177
7.1 Summary 177
7.2 Future work 180

List of Tables

2.1 Effective wavelengths and passbands for the filters in the Johnson system and the SDSS filters. . . . 52
2.2 Properties of the JAST CCD camera. . . . 54
2.3 Effective wavelengths passbands for the JAST/T80Cam filters. . . . 55

3.1 Log of the *HST*/COS observations. . . . 67
3.2 Log of the *HST*/STIS observations. . . . 71
3.3 Log of the X–shooter observations. . . . 73
3.4 CV white dwarf gravitational redshifts, masses, radii and surface gravities from X–shooter phase–resolved observations. . . . 76
3.5 Results for 1RXS J023238.8–371812 for the two different fitting methods for the disc emission lines. . . . 80
3.6 $T_{\rm eff}$ for 1RXS J023238.8–371812 allowing different $\log g$. . . . 82
3.7 Characteristics of the 45 CV white dwarfs observed with COS and STIS. . . . 89
3.8 Results for BD Pav, QZ Ser and V485 Cen derived from the COS and the STIS data. . . . 94
3.9 Optimal set of parameters for the two homogeneous slabs of veiling gas. . . . 100
3.10 Simulated accuracy on the *Gaia* parallaxes estimated with PyGaia and the corresponding accuracy on the mass determination. . . . 107

4.1 Summary of the ground–based CCD observations for the monitoring of the superoutburst of SDSS1238. . . . 113
4.2 Best-fit parameters and their range of variations for the model used to fit the SED of SDSS1238. . . . 119
4.3 Stellar and binary parameters for SDSS1238. . . . 121
4.4 Effective temperature variation of the white dwarf in SDSS1238. . . . 130

5.1 Summary of the observations of QZ Lib. . . . 146

5.2 Range of variations for the free parameters in the slab model. 153
5.3 Cooling sequence for the white dwarf in QZ Lib after its 2004 super–outburst. 154
5.4 The evolution of FWHM, equivalent width, and line flux for the main Balmer and He I lines lines in the spectra of QZ Lib. 158
5.5 Best fit parameters for the isothermal and isobaric hydrogen slab in QZ Lib. 158
5.6 System parameters for QZ Lib. 160

6.1 Summary of the observations of CHiCaS0650. 170
6.2 White dwarf candidates from CHiCaS0650. 171

List of Figures

1.1 HR diagram based on Hipparcos data of 20 546 nearby stars. 3
1.2 The pp chain. 4
1.3 The CNO cycle. 5
1.4 The triple–alpha process. 7
1.5 The evolution of low and intermediate mass stars in the HR diagram. 8
1.6 Initial–final mass relationship from open clusters. 9
1.7 Surface gravity and mass distribution of a spectroscopic sample of DA white dwarfs from the Palomar Green Survey. 10
1.8 Chemical structure of a typical DB and DA white dwarf. 11
1.9 Sample white dwarf spectra from the Sloan Digital Sky Survey. . . . 12
1.10 Cross–section of the Roche equipotential surfaces in the orbital plane for a binary system with $q = M_2/M_1 = 0.25$. 13
1.11 Mass transfer in binaries. 15
1.12 Cataclysmic variable formation. 19
1.13 The orbital period distribution of 1429 semi–detached binaries containing a white dwarf and a Roche–lobe filling low–mass secondary. . 20
1.14 Cataclysmic variable evolution. 21
1.15 Schematic of the magnetic braking mechanism. 23
1.16 X–shooter spectrum of the dwarf nova IR Com as a sample spectrum of a quiescent CV. 25
1.17 Double peaked emission line formation in an accretion disc. 26
1.18 Schematic of the Hawley–Balbus instability in an accretion disc. . . . 28
1.19 Schematic of dwarf nova outbursts. 29
1.20 O–C diagram for the superhumps observed during the 2010 superoutburst of SW UMa. 31
1.21 Effective temperatures of a sample of 43 CV white dwarfs. 35

2.1 Readout process in a CCD camera. 40
2.2 Schematic of a photomultiplier. 42

2.3 Schematic of a spectrograph. 43
2.4 Schematic of the COS detectors. 45
2.5 X–shooter spectral format. 46
2.6 Sample sections of X–shooter calibration frames for the VIS arm. . . 49
2.7 X–shooter VIS and NIR spectrum of the CV SDSS J123813.73–033932.9 before and after the correction with `molecfit`. 50
2.8 Example of a CORRTAG frame. 56
2.9 Section of a g band image from JAST/T80Cam. 57
2.10 Doppler shift of the lines in the CV IR Com. 61
2.11 Schematics of the donor and the white dwarf reflex motion. 62

3.1 Orbital period sampling of the *HST* observing programs. 65
3.2 *HST*/STIS and *HST*/COS white dwarf dominated far–ultraviolet spectra. 68
3.3 Sample light curves of quiescent CVs. 69
3.4 Sample light curves of CVs in outburst or in an intermediate state. . 69
3.5 *HST*/COS spectra of the nine CVs dominated by emission from the accretion flow. 70
3.6 X–shooter spectra for four CVs for which the radial velocity curve could not be reconstructed. 74
3.7 X–shooter spectra for three CVs for which the radial velocity curve could be reconstructed. 75
3.8 Radial velocity curves from X–shooter phase–resolved observations. . 76
3.9 *HST*/COS spectrum of 1RXS J023238.8–371812. 78
3.10 *HST*/COS spectrum of 1RXS J023238.8–371812 along with the best–fit model for the two different fitting methods. 81
3.11 The correlation between the effective temperature systematic uncertainties and the white dwarf mass. 83
3.12 Correlation between white dwarf effective temperature and reddening. 86
3.13 Ultraviolet spectra of cool, warm and hot CV white dwarfs in our sample along with the best–fit model. 88
3.14 Light curves for seven targets which experienced an outburst within two months before the *HST* observations. 91
3.15 Lightcurves for CC Scl and SDSS J164248.52+134751.4. 93
3.16 textitHST/COS spectra of CC Scl and SDSS J164248.52+134751.4 along with the best–fit models. 93
3.17 Comparison between the *HST*/COS and the *HST*/STIS spectra of BD Pav, QZ Ser and V485 Cen. 94
3.18 Lightcurves for BD Pav. 95
3.19 Lightcurve for CU Vel. 95

3.20 Comparison between the *HST*/COS and the *IUE* spectra of CU Vel. 96
3.21 *HST*/COS spectrum of SDSS J040714.78–064425.1. 99
3.22 *HST*/COS spectrum of SDSS J100658.41+233724.4 along with the best model with and without absorption from the veiling gas. 100
3.23 *HST*/STIS spectrum of DV UMa along with the best model with and without absorption from the veiling gas. 100
3.24 Effective temperature as function of the orbital period. 103
3.25 *Gaia* parallax accuracy as a function of the distance and the G_p *Gaia* magnitude. 108
3.26 Mass accuracy from the uncertainties on the *Gaia* parallaxes as a function of the distance and the G_p *Gaia* magnitude. 108

4.1 Superoutburst light curve of SDSS1238. 114
4.2 Trailed spectra for the Mg II line and the K I lines detected in the X–shooter spectra. 116
4.3 VLT/X–shooter average spectrum of SDSS1238. 117
4.4 SED for SDS1238. 118
4.5 White dwarf Mg II absorption line at 4 481 along with the theoretical line profile computed for different strenghts of the magnetic field. . . 120
4.6 *K2* for SDSS1238. 122
4.7 Amplitude spectrum of the *K2* light curve. 123
4.8 Statistic of the brightenings. 125
4.9 *K2* light curve folded with respect to the 40.26 min ephemeris of the double-humps alog with the best fir model. 126
4.10 Statistics and $O-C$ diagram of the double humps. 126
4.11 *HST*/COS average spectrum of SDSS1238. 127
4.12 *HST*/COS light curve of SDSS1238. 128
4.13 *HST*/COS spectra of SDSS1238 extracted at the minimum and at the maximum brightness level. 129
4.14 Best–fit results for the 19 *HST* sub–spectra for the two–component fit and the three–component fit. 131
4.15 *HST* light curve in comparison with *K2* data of a sample brightening and with the *K2* light curve folded with respect to the 40.26 min ephemeris of the double-humps. 132
4.16 Comparison between the *HST* synthetic K_p magnitudes and the *K2* light curve folded with respect to the 40.26 min ephemeris of the double-humps. 133
4.17 Luminosity of SDSS1238 calculated from the average brightening light curve. 133
4.18 Secondary parameters in comparison with the theoretical predictions. 134

4.19 Doppler maps of SDSS1238 computed from the Balmer and the Calcium H & K emission lines detected in the X–shooter data. 138
4.20 Schematic drawing of the phase shifts of the double humps during the brightenings. 139

5.1 Finding chart of QZ Lib. 147
5.2 SMARTS and EFOSC2 light curves for QZ Lib. 148
5.3 AAVSO ligthcurve for QZ Lib from 2004 up to 2016. 149
5.4 AAVSO ligthcurve for QZ Lib in the period 17 April 2013 – 5 May 2013. 149
5.5 Radial velocity curve for the white dwarf in QZ Lib. 150
5.6 Doppler maps for QZ Lib from phase–resolved X–shooter observations. 152
5.7 EFOSC2 spectra of QZ Lib obtained one, two and six months after its 2004 superoutburst. 155
5.8 EFOSC2 spectrum of QZ Lib taken on 2004–08–27 along with the best–fit model. 156
5.9 Averaged X–shooter spectrum of QZ Lib. 157
5.10 X–shooter average spectrum of QZ Lib along with the best–fit model. 159
5.11 X–shooter spectrum of QZ Lib in comparison with the expected emission of a M6.5–dwarf companion. 161
5.12 QZ Lib mass ratio and the upper limit on the effective temperature of its donor star in comparison with the revised CV evolutionary track from Knigge et al. (2011). 162

6.1 The *gSDSS*–band image of CHiCaSJ0650. 169
6.2 Colour–colour diagrams for CHiCaS0650. 172
6.3 Colour–magnitude diagram for CHiCaS0650. 173
6.4 Lightcurves of the two CV candidates and sample lightcurves for two white dwarf candidates from CHiCaS0650. 174
6.5 Sample lightcurves for six stars from CHiCaS0650. 175

Acknowledgments

First of all, I would like to thank Boris Gänsicke for his invaluable guidance throughout my PhD. During these four years, he has been a constant source of inspiration and motivation, teaching me what being a researcher means. I am deeply grateful for his patience and his continuous support, especially during the most difficult moments.

Special thanks go to Roberto Raddi, Linda Schmidtobreick, Alessandro Ederoclite, Louise Wang, Elmé Breedt and Javier Abril. Thanks for the great time spent together, the constructive discussions and, above all, for your encouragement and friendship.

For my funding, I would like to thank the European Research Council. I would also like to express my gratitude to the European Southern Observatory for having made possible my stays in Santiago.

Finally, a special mention goes to the great moments with Álvaro, Anto, Edo (la Reina) and Edu: the funniest and most unproductive times of my PhD, and probably those where I have eaten more chocolate than ever. Siempre nos quedarán los Chupa Chups de Pamplona!

Infine, il ringraziamento più grande va a papà, Laura, e Antonino, senza i quali non avrei mai raggiunto questo traguardo.

Declarations

I hereby declare that this thesis has not been submitted in any previous application for a higher degree. This thesis is submitted to the University of Warwick in support of my application for the degree of Doctor of Philosophy.
This thesis represents my own work, except where references to other works are given. I am the PI of the X–shooter and CHiCaS observing programs and I have personally carried out the X–shooter observations.
Chapters 1 and 2 provide information gathered from the literature while the following Chapters are based on refereed publications that I have submitted and prepared during my period of study:

- Chapter 3 is based on:

    1. Pala, A. F., Gänsicke B. T., Townsley D., Boyd D., Cook M. J., De Martino D., Godon P., Haislip J. B., Henden A. A., Hubeny I., Ivarsen K. M., Kafka S., Knigge C., LaCluyze A. P., Long K. S., Marsh T. R., Monard B., Moore J. P., Myers G., Nelson P., Nogami D., Oksanen A., Pickard R., Poyner G., Reichart D. E., Rodriguez Perez D., Schreiber M. R., Shears J., Sion E. M., Stubbings R., Szkody, P. and Zorotovic, M., "Effective temperatures of cataclysmic-variable white dwarfs as a probe of their evolution", MNRAS, 466:2855–2878 (2017).
    2. Pala, A. F. and Gänsicke B. T., "Dynamical Masses of Accreting White Dwarfs", ASPC, 509, 91(2017).

- Chapter 4 is based on: Pala A. F., Gänsicke B. T., Marsh T. R., Breedt E., Hermes J. J., Landstreet J. D., Schreiber M. R., Townsley D., Wang L., Aungwerojwit A., Hambsch F.–J., Monard B., Myers G., Nelson P., Pickard

R., Poyner G. and Stubbings R., "Evidence for spiral density waves in the accretion disc of SDSS J123813.73–033933.0", in preparation for submission to MNRAS.

- Chapter 5 is based on: Pala A. F., Schmidtobreick L., Tappert C., Gänsicke B. T and Mehner A., "The cataclysmic variable QZ Lib: a period bouncer", submitted to MNRAS.

- Chapter 6 is based on an ongoing observing program aimed to identify, for the first time, the predicted population of period bouncers.

The work presented was carried out by the author except in the cases outlined below:

- Chapter 3: the simulated accuracy on the Gaia parallaxes estimated with PyGaia was performed by N. P. Gentile Fusillo. All subsequent analyses were performed by the author herself.

- Chapter 4: the reduction of the raw *K2* data was performed by Elmé Breedt. The analysis of the superoutburst and *K2* lightcurves with MIDAS/TSA was performed by B. T. Gänsicke. The Doppler maps were computed by L. Wang. The magnetic atmospheric models were computed by J. D. Landstreet. The observations of the superouburst were obtained with help of a team of amateur observers. All subsequent analyses were performed by the author herself.

- Chapter 5: the reduction and the Fourier analysis of the EFOSC2 and SMARTS data was performed by L. Schmidtobreick, who also computed the Doppler maps. All subsequent analyses were performed by the author herself.

- Chapter 6: the probability to be a white dwarf for the objects in CHiCaS0650 were computed by N. P. Gentile Fusillo.

Abstract

Cataclysmic variables (CVs) are short–period ($\simeq$ 80 min to $\simeq$ day) binaries in which a white dwarf accretes from a low–mass companion. Since both stellar components are structurally simple and there is a sufficiently large number of relatively bright CVs known, it is possible to carry out detailed observational population studies. Therefore CVs are one of the best–suited classes to test, constrain, and further develop our understanding of the evolution of all interacting compact binaries, such as black hole binaries, X-ray transients, milli–second pulsars and, more importantly, Type Ia Supernova (SN Ia), our yardsticks for measuring distances on cosmological distance scales.

In this thesis, I present the study of a large sample of CV white dwarfs. Their effective temperatures are determined from the analysis of their ultraviolet *Hubble Space Telescope* (*HST*) spectra and provide a test for the current models of CV evolution. Our results highlight the presence of a number of discrepancies between current population models and observations, particularly the lack of period bounce systems, i.e. highly evolved CVs with brown dwarf companions, which are predicted to make up for $\simeq 40 - 70\,\%$ of the present day Galactic CV population.

The combination of the *HST* data with optical phase–resolved X–shooter observations is a powerful tool to identify period bouncers. We study the spectral energy distribution of QZ Lib, in which we identify the coolest white dwarf at the longest orbital period below the period gap and we spectroscopically confirm the presence of a brown dwarf donor. These characteristics make QZ Lib the strongest period bouncer candidate identified so far.

Although successful, this method requires the use of expensive space–based and large ground–based facilities, indicating the need for a more efficient observing strategy. We present here CHiCaS, the Compact binary HIgh CAdence Survey which represents the first systematic attempt to identify, via the detection of their eclipses, the elusive population of period bouncers. By the end of next year, this program will deliver one minute cadence lightcurves for $\simeq 2.5$ million objects as faint as $g \simeq 21.5$, along with full colour information. CHiCaS will also provide a complete and unbiased view into the short term variability of thousands of binaries, eclipsing systems, pulsating stars and CVs in the period gap.

In our *HST* sample, we identify another remarkable CV: SDSS J123813.73–033932.9. Its lightcurve shows sudden increases in brightness, up to $\simeq 0.45$ mag, occurring quasi–periodically every 8–12 hours (the "brightenings") and a nearly sinusoidal variation at half the orbital period (the "double–humps"). The *HST* observations show that these phenomena arise from the heating and cooling of a fraction of the white dwarf, which we conclude being caused by a modulation in the accretion rate owing to spiral density waves and thermal instabilities in the accretion disc.

Finally, constraining the white dwarf masses to a few per cent is important in order to investigate their potential as SN Ia progenitors. It has been shown that CV white dwarfs are, on average, more massive than their detached progenitors, thus suggesting that they can grown in mass. In this work, the study of the reflex motion of the two stellar components in four CVs allows to accurately measure their masses. However, this method can be applied only to those systems in which the two stellar components are not outshone by the light of the accretion flow. Next year, the ESA *Gaia* satellite will provide accurate parallaxes for all the targets from our *HST* sample and, from the knowledge of their distances, we will accurately measure their masses, thus carrying out a stringent test for the mass growth hypothesis of CV white dwarfs.

Abbreviations

2MASS ..... Two Micron All–Sky Survey
A/D ..... Analog–to–digital
AAVSO ..... American association of variable star observers
ADC ..... Atmospheric dispersion corrector
AGB ..... Asymptotic giant branch
AML ..... Angular momentum loss
APASS ..... AAVSO Photometric All–Sky Survey
ASAS–SN ..... All–Sky Automated Survey for Supernovae
BOA ..... Bright object aperture
CAML ..... Consequential angular momentum loss
CBA ..... Center for Backyard Astrophysics
CCD ..... Charge–coupled device
CE ..... Common envelope
CEFCA ..... Centro de Estudios de Física del Cosmos de Aragón
CHiCaS ..... Compact binary high cadence survey
COS ..... Cosmic Origin Spectrograph
CTIO ..... Cerro Tololo Inter–American Observatory
CV ..... Cataclysmic Variable
DD ..... Double–degenerate
DPAC ..... Data Processing and Analysis Consortium
DR2 ..... Data Release 2
DSS ..... Digitized Sky Survey
EFOSC2 ..... ESO Faint Object Spectrograph and Camera 2
ESA ..... European Space Agency
EPIC ..... Ecliptic Plane Input Catalogue
ESO ..... European Southern Observatory

eCAML ..... Empirical consequential angular momentum loss

FITS ..... Flexible Image Transport System

FoV ..... Field of view

FUV ..... Far ultraviolet

FWHM ..... Full width half maximum

GWR ..... Gravitational wave radiation

HR ..... Hertzsprung–Russell

HST ..... Hubble Space Telescope

IDL ..... Interactive Data Language

IFMR ..... Initial–final mass relationship

INT ..... Isaac Newton Telescope

IPAC ..... Infrared Processing and Analysis Center

JAST ..... Javalambre Auxiliary Survey Telescope

LIGO ..... Laser Interferometer Gravitational–Wave Observatory

MAMA ..... Multi–anode multichannel array

MB ..... Magnetic braking

MCMC ..... Markov–chain Monte Carlo

MWDD ..... Montreal White Dwarf Database

NASA ..... National Aeronautics and Space Administration

NED ..... NASA/IPAC Extragalactic Database

NIR ..... Near–infrared

NUV ..... Near–ultraviolet

OAJ ..... Observatorio Astrofísico de Javalambre

OC61 ..... Optical Craftsman 0.61m Telescope

Pan–STARRS Panoramic Survey Telescope and Rapid Response System

PCEB ..... Post common envelope binary

PSA ..... Principal science aperture

pp ..... proton–proton

PROMPT ..... Panchromatic Robotic Optical Monitoring and Polarimetry Telescopes

RATS ..... RApid Temporal Survey

RGB ..... Red giant branch

RMS ..... Root mean square

SD ..... Single–degenerate

SDSS ..... Sloan Digital Sky Survey

SED ..... Spectral energy distribution

SMARTS ..... Small and Moderate Aperture Research Telescope System
SNR ..... Signal–to–noise ratio
SNe Ia ..... Supernovae Ia
STIS ..... Space Telescope Imaging Spectrograph
STScI ..... Space Telescope Science Institute
TMO61 ..... Tortugas Mountain Observatory 0.61m Telescope
UNC ..... University of North Carolina
USNO ..... United States Naval Observatory
UVB ..... Ultraviolet–blue
VIS ..... Visible
VLT ..... Very Large Telescope
VSNET ..... Variable Star Network
VST ..... VLT Survey Telescope
WFC ..... Wide Field Camera

A nonna Elena
e nonna Pasqualina

Chapter 1

Introduction

The majority of the Solar–type stars in our Galaxy are found in binary systems ($\simeq 58\%$, Fuhrmann et al. 2017); this fraction increases up to $\simeq 80\%$ for more massive stars (O–B spectral types, Raghavan et al. 2010). Given their abundance, binaries play a crucial role by influencing the star formation and the chemical evolution of the Galaxy (e.g. Malkov and Zinnecker 2001; De Donder and Vanbeveren 2004; Eldridge et al. 2008; Sana et al. 2012). In fact, they give rise to some of the most exotic objects (e.g. Eta Carinae Damineli 1996, blue stragglers Leonard 1989, barium stars Han et al. 1995 and many others) and some of the most powerful events in the Universe, such as Supernovae Ia (SNe Ia), the fundamental yardstick to measure distances on cosmological scale (Branch and Tammann, 1992) that led to the discovery of an accelerating expansion of the Universe (Riess et al., 1998; Perlmutter et al., 1999).

Among all the many classes of binaries that can be found in the Milky Way, of particular interest are the so–called cataclysmic variables, which are composed of a white dwarf accreting mass from a Roche–lobe filling low–mass companion star. These systems are relatively numerous, nearby and fairly bright and therefore they allow a direct measurement of fundamental physical parameters (such as masses, temperatures, abundances and rotation rates) that are difficult or impossible to determine in other types of accreting binaries, such as X–ray binaries, which are usually too faint for accurate radial velocity or spectral fitting studies. For this reason, cataclysmic variables are one of the best–suited classes to test, constrain, and further develop our understanding of the evolution of compact, interacting binaries.

However, the improved observing facilities and the advent of large spectroscopic and time–domain surveys have highlighted major discrepancies between the standard model of cataclysmic variable evolution and the observations, with impor-

tant implications for many astrophysical fields. In fact, cataclysmic variables are composed by objects whose underlying physics should be well understood, therefore a failure in the theory describing such simple systems undermines our faith in understanding of more complex binaries, such as X–ray transients, milli–second pulsars and, more importantly, SNe Ia. Given the relevance of SNe Ia as a tool to probe the fundamental physical properties of the Universe, it is crucial to thoroughly investigate the disagreements between the observations and the theory describing cataclysmic variables, which is the ultimate goal of this work.

This first Chapter provides the theoretical background necessary to understand cataclysmic variables and their evolution and sets the scene for the study presented in the following Chapters.

1.1 Basics of stellar evolution

Stars are formed in large molecular clouds which start collapsing under their own gravity. Following the contraction, the cloud splits up giving rise to several fragments, each one of them potentially evolving into a star. In the first phases of the contraction, the potential energy of the infalling gas is converted into thermal energy that can freely escape the condensation nucleus since the gas density is low. Therefore a fragment can collapse only if its mass is high enough that its own gravity can overwhelm the thermal pressure of the gas (Jeans, 1902). With the contraction proceeding, the density in the inner region increases and the gas becomes optically thick and the energy released during the continuous collapse cannot escape into the surrounding space. Consequently the temperature of the cloud starts increasing: a protostar is born. However, not all protostars evolve into stars: if their mass is below the hydrogen burning limit ($M \simeq 0.08 - 0.087\,\mathrm{M}_{\odot}$, depending on the chemical composition, Baraffe et al. 1997; Chabrier and Baraffe 1997), the protostar core will never reach the temperature and density necessary to ignite hydrogen fusion. Such objects are known as brown dwarfs. In the first phases of their life, these sub–stellar objects burn lithium and deuterium, which are quickly converted into helium. Once this source of energy is exhausted, brown dwarfs only shine owing to their thermal cooling and the gravitational energy released by their contraction, and will never become stars. On the other hand, protostars whose mass is above the hydrogen burning limit eventually start to fuse hydrogen into helium in their cores. The energy released by the nuclear reactions halts the gravitational collapse and the star evolves onto the main sequence, defined as the phase in which nuclear fusion of hydrogen in the core is the only source of energy in the star.

Main sequence stars occupy a branch that diagonally crosses the Hertzsprung–Russell (HR) diagram, where the luminosity of a star is plotted versus its effective

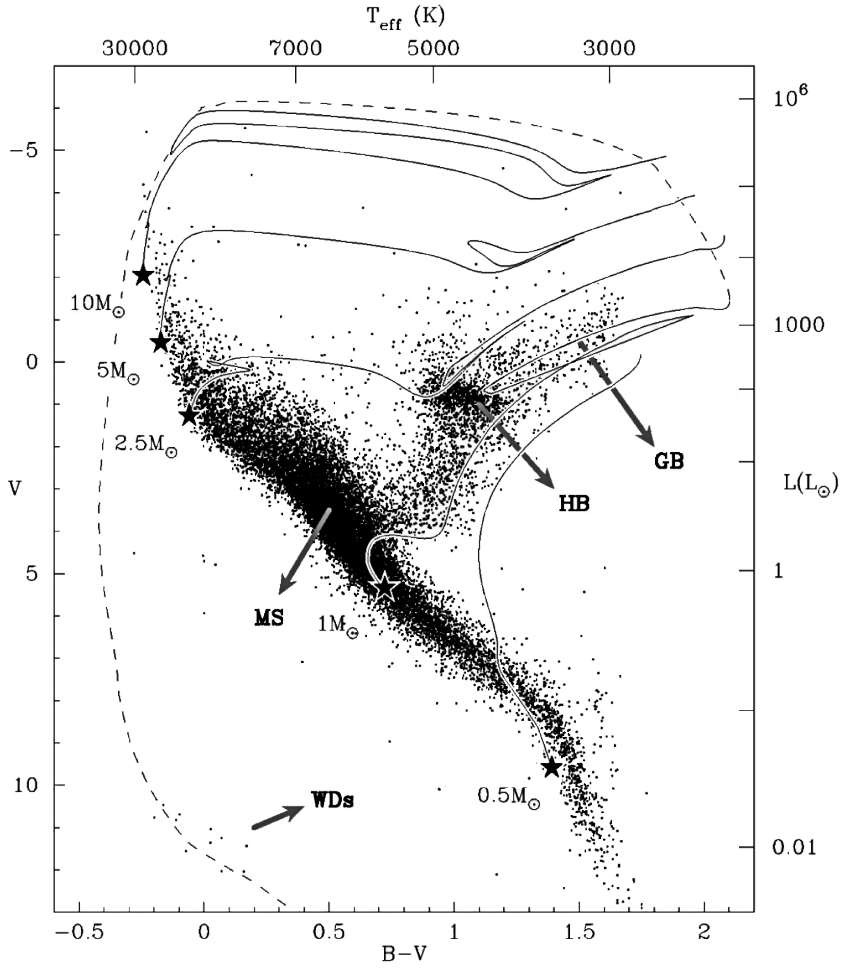

Figure 1.1: HR diagram based on Hipparcos data of 20 546 nearby stars, highlighting the position of the different evolutionary phases described in Section 1.1.1. The grey lines represent evolutionary tracks for stars of different masses, starting from the main sequence and following their evolution up to the giant branch (solid line), until they become white dwarfs (dashed lines). Courtesy of Marc van der Sluys.

temperature (Figure 1.1). The HR diagram is a fundamental tool to investigate the properties of stars and their evolution given the fact that, during their life, stars move across it and occupy different locations.

The evolution and the final stages of the life of a star are mainly defined by one parameter: its mass. The mass (M) determines the time required for a star to exhaust its hydrogen reservoir at its current luminosity (L), called the *nuclear time–scale*:

$$t_{\rm nuc} = \frac{0.007 M c^2}{L} \tag{1.1}$$

where c is the speed of light. The hydrogen burning rate strongly depends on the core temperature which, in turn, increases with the stellar mass. However, following

$$
\begin{aligned}
&(1)\ {}^{1}_{1}\mathrm{H} + {}^{1}_{1}\mathrm{H} \rightarrow {}^{2}_{1}\mathrm{H} + e^{+} + \nu_e \\
&(2)\ {}^{2}_{1}\mathrm{H} + {}^{1}_{1}\mathrm{H} \rightarrow {}^{3}_{2}\mathrm{He} + \gamma \\
&(3)\ {}^{3}_{2}\mathrm{He} + {}^{3}_{2}\mathrm{He} \rightarrow {}^{4}_{2}\mathrm{He} + {}^{1}_{1}\mathrm{H} + {}^{1}_{1}\mathrm{H}
\end{aligned}
$$

Figure 1.2: The pp chain starts with two protons forming a deuteron and emitting one positron and one neutrino (1). The deuteron then unites with another proton to form the helium isotope ${}^{3}_{2}\mathrm{He}$ by emitting a photon (2). Two ${}^{3}_{2}\mathrm{He}$ nuclei then fuse to form a ${}^{4}_{2}\mathrm{He}$ nucleus, releasing two protons (3). In order to form one ${}^{4}_{2}\mathrm{He}$ nucleus, reactions (1) and (2) must occur twice. The net balance is that four protons are converted into one nucleus of helium. It is worth noting that, in order for the pp chain to produce helium, a beta–decay of one proton into a neutron is required in the small amount of time that the two protons are close together in reaction (1). The pp chain described here is the most common reaction to form a nucleus of helium in stars with $M \lesssim 1.5\,\mathrm{M}_{\odot}$, although a small fraction of ${}^{4}_{2}\mathrm{He}$ is obtained from slightly different reactions.

the changing in the physical condition of the core during the stellar evolution (see Section 1.1.1), only a fraction of the total hydrogen content is actually fused into helium. Thus the amount of time that a star spends in the main sequence phase (t_{MS}) is shorter than t_{nuc} and it is related to the stellar mass by the relationship:

$$t_{\mathrm{MS}} \propto M^{-2 \div 3} \tag{1.2}$$

More massive stars have higher core temperatures and thus burn hydrogen more efficiently, spending less time on the main sequence compared to lower mass stars. For example, while our Sun will spend $\simeq 10\,\mathrm{Gyr}$ on the main sequence phase, a $15\,\mathrm{M}_{\odot}$ star will last only $\simeq 10\,\mathrm{Myr}$.

Since the core temperature (T_{c}) is intimately related to the stellar mass, the latter also determines which nuclear reactions take place in the core. Low–mass stars ($M \lesssim 1.5\,\mathrm{M}_{\odot}$, $T_{\mathrm{c}} \simeq 10^{6}\,\mathrm{K}$) burn hydrogen trough the proton–proton chain (pp chain, Figure 1.2), while higher mass stars ($M \gtrsim 1.5\,\mathrm{M}_{\odot}$, $T_{\mathrm{c}} \simeq 10^{7}\,\mathrm{K}$) burn hydrogen through the CNO cycle (Figure 1.3).

Stars of different masses follows different evolutionary paths and, at the and of their life, leave behind different remnants. The objects studied in this thesis are the so–called white dwarfs, i.e. the final state of the life of low and intermediate mass stars ($0.8\,\mathrm{M}_{\odot} \lesssim M \lesssim 10 - 12\,\mathrm{M}_{\odot}$, Siess 2007). Therefore, the following discussion is restricted to the evolution of stars in this mass range, since the evolution of more massive objects is beyond the scope of this work.

(1) ${}^{12}_{6}\mathrm{C} + {}^{1}_{1}\mathrm{H} \rightarrow {}^{13}_{7}\mathrm{N} + \gamma$

(2) ${}^{13}_{7}\mathrm{N} \rightarrow {}^{13}_{6}\mathrm{C} + e^{+} + \nu_e$

(3) ${}^{13}_{6}\mathrm{C} + {}^{1}_{1}\mathrm{H} \rightarrow {}^{14}_{7}\mathrm{N} + \gamma$

(4) ${}^{14}_{7}\mathrm{N} + {}^{1}_{1}\mathrm{H} \rightarrow {}^{15}_{8}\mathrm{O} + \gamma$

(5) ${}^{15}_{8}\mathrm{O} \rightarrow {}^{15}_{7}\mathrm{N} + e^{+} + \nu_e$

(6) ${}^{15}_{7}\mathrm{N} + {}^{1}_{1}\mathrm{H} \rightarrow {}^{12}_{6}\mathrm{C} + {}^{4}_{2}\mathrm{He}$

Figure 1.3: In the CNO cycle, four protons are fused to form a ${}^{4}_{2}\mathrm{He}$ nucleus by using carbon, oxygen and nitrogen as catalysts. The reaction rate of the CNO cycle is set by the slowest reaction, i.e. the proton capture by a nucleus of nitrogen (4). This rate strongly dependeds on the temperature, therefore CNO cycle only becomes dominant for stars more massive than $M \gtrsim 1.5\,\mathrm{M}_{\odot}$.

1.1.1 Evolution of low and intermediate mass stars*

Once the hydrogen in the core is exhausted, the source of energy that prevented the star during its main sequence life to gravitationally collapse is now switched off. Consequently the star, which now has a core of helium, begins to contract. The time necessary for a star to contract under its own gravity if the nuclear energy sources were turned off is called *thermal time–scale*:

$$t_{\mathrm{th}} = \frac{GM^2/R}{2L} \tag{1.3}$$

where G and R are the gravitational constant and the radius of the star, respectively. The following increase of temperature and density in the stellar interior leads to the ignition of hydrogen burning in a shell surrounding the core. However, the helium core continues to contract as it cools and its mass is increased by the helium produced by the burning of hydrogen in the shell above.

Owing to the stronger and stronger gravitational field felt by the shell, its pressure (and hence temperature) increases, thus increasing the rate at which the hydrogen is fused into helium. The energy that is produced by these nuclear reactions cannot all be carried away by the surrounding envelope, since the efficiency at which the energy is radiated away is limited by the photon diffusion rate. Consequently, the outer layers expands, the stellar radius increases and its effective temperature diminishes. The star becomes redder and moves horizontally to the right in the HR diagram, entering the subgiant phase.

With the increase of density and pressure in the core, the helium atoms become more and more packed and, in stars with $M \lesssim 2.3\,\mathrm{M}_{\odot}$, the core becomes

*This Section is based upon Shu (1982) and Karttunen et al. (2007).

degenerate, i.e. the gravitational pull is not counterbalanced by the thermal pressure but by the pressure of degenerate electrons. In fact, in these extreme conditions, electrons are forced to get close together. However, they cannot violate Pauli's exclusion principle and therefore cannot occupy exactly the same quantum mechanical state. This, combined with Heisenberg's uncertainty principle, which states that if a particle is confined in a small region of space its momentum becomes indeterminate, implies that electrons compressed to high density generate a pressure. This pressure is independent of the temperature of the gas, i.e. from the thermal motion of the electrons, and sustains the core against the gravitational collapse. In more massive stars, the core does not become degenerate since the temperature is higher and the density is lower.

The presence of such compact core results in a fast increase in the hydrogen burning rate in the above shell and the outer layers start expanding rapidly. The star moves vertically in the HR diagram along the red giant branch (RGB). In stars with initial masses of $0.1\,\mathrm{M}_\odot \lesssim M \lesssim 0.7\,\mathrm{M}_\odot$, the core never reaches the temperature required for the helium burning. Once the shell burning is exhausted, these stars are expected to leave behind a degenerate helium core with $M \lesssim 0.4\,\mathrm{M}_\odot$, i.e. a helium white dwarf. However, such low mass stars evolve on time–scales much longer than the age of our Galaxy and so far none of them have left the main sequence.

In more massive stars, the temperature in the core keeps increasing until it reaches $\simeq 10^8\,\mathrm{K}$. At this temperature, the fusion of helium into carbon and oxygen is ignited through the triple–alpha process (Figure 1.4).

In stars with a degenerate core, pressure and temperature are no longer correlated, therefore following an increase in temperature, the core does not expand as a normal gas would. The trigger of the helium fusion hence occurs as a nuclear runaway, called helium flash, during which the temperature increases and the resulting expansion of the core removes the degeneracy.

In stars with main sequence masses of $M \gtrsim 2.3\,\mathrm{M}_\odot$, the higher temperature in the core prevents the electron from becoming degenerate and the ignition of helium occurs in a quiet way.

With the expansion of the core, the hydrogen burning shell moves outwards to lower pressure regions and the rate at which hydrogen burns is reduced. The star finds a new thermal equilibrium and its envelope contracts. During this phase, the star becomes hotter while keeping a constant radius, therefore moves along the horizontal branch (HB) while burning helium in its core and hydrogen in a surrounding shell.

When all helium in the core has been burnt into carbon and oxygen, the core starts contracting again determining the ignition of helium in a shell outside the core, while hydrogen keeps burning in an outer shell. Following similar mechanisms

$$
\begin{aligned}
&(1)\ {}^{4}_{2}\mathrm{He} + {}^{4}_{2}\mathrm{He} \rightarrow {}^{8}_{4}\mathrm{Be} + \gamma \\
&(2)\ {}^{8}_{4}\mathrm{Be} + {}^{4}_{2}\mathrm{He} \rightarrow {}^{12}_{6}\mathrm{C} + \gamma \\
&(3)\ {}^{12}_{6}\mathrm{C} + {}^{4}_{2}\mathrm{He} \rightarrow {}^{16}_{8}\mathrm{O} + \gamma
\end{aligned}
$$

Figure 1.4: At temperatures higher than $\simeq 10^8\,\mathrm{K}$, helium is efficiently fused into carbon trough the triple–alpha process (1 and 2). Since the beryllium decays in $2.6\times10^{-16}\,\mathrm{s}$ back into helium, in order for the production of carbon to be successful, the collision of the three helium nuclei must be almost simultaneous. Additionally, some carbon nuclei fuse with helium to form oxygen (3).

as along the giant branch, the envelope expands and the core contracts, meanwhile the star ascends the asymptotic giant branch (AGB).

In the final stages of evolution of low and intermediate mass stars ($0.8\,\mathrm{M}_\odot \lesssim M \lesssim 8\,\mathrm{M}_\odot$), the core never becomes hot enough to ignite the carbon burning. Instead, the increasing central pressure causes the electrons in the nucleus to become degenerate while the outer layers expand and are gradually lost: the star enters the planetary nebula phase during which it ejects the envelope and leaves behind a carbon–oxygen core that is shrinking and warming up, thus crossing the HR diagram from right to left. Eventually, the core finds its own equilibrium and starts cooling down, becoming a white dwarf (Figure 1.5).

Finally, if the main sequence mass is in the range $8\,\mathrm{M}_\odot \lesssim M \lesssim 10-12\,\mathrm{M}_\odot$, then also carbon is ignited and the star ends its life as an oxygen–neon white dwarf.

1.2 White dwarfs

White dwarfs are the remnants of low and intermediate mass stars ($M \lesssim 10-12\,\mathrm{M}_\odot$, Siess 2007), which represent over $\simeq 95\%$ of the stars in the Milky Way (Althaus et al., 2010), making white dwarfs the most common remnant in our Galaxy. No fusion reactions take place in the interior of white dwarfs. However, they are still hot owing to phases of burning and contraction, and therefore gravitational energy release, that the progenitor has experienced in the final stages of its life. Consequently white dwarfs shine because this internal energy is radiated away in the surrounding space.

White dwarfs are extremely compact objects, comparable in size to the Earth and with masses up to $M \simeq 1.44\,\mathrm{M}_\odot$. This limiting mass is known as "Chandrasekhar's limit" (Chandrasekhar, 1931) and it is set by the degenerate condition of the electrons in their cores. The degeneracy pressure depends on the electron density and, as degenerate matter can be packed more tightly than ordinary matter, more massive white dwarfs are actually smaller than less massive ones. Moreover, in

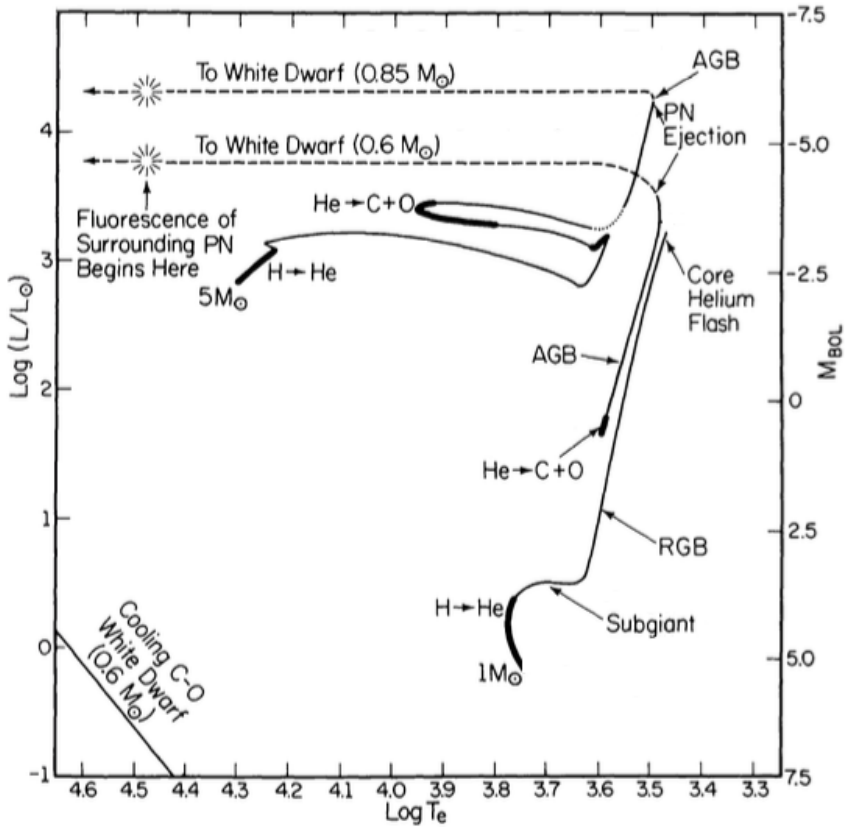

Figure 1.5: The evolution of low and intermediate mass stars in the HR diagram. Figure adapted from Iben (1991)

more massive white dwarfs the gravitational pressure forces electrons to be confined in smaller and smaller space regions thus making them relativistic. Interestingly, a relativistic degenerate gas exerts less pressure than a non–relativistic one and there is not an equilibrium configuration in which the degenerate pressure can counterbalance the gravitational collapse for $M \gtrsim 1.44\,\mathrm{M}_{\odot}$, which is the before mentioned Chandrasekhar's limit.

Above the Chandrasekhar's limit, the increase of central density and temperature leads to the thermonuclear ignition of carbon in a degenerated environment, giving rise to a SN Ia explosion. Two different formation channels are usually considered for these events. The first is the so called double–degenerate scenario in which two white dwarfs merge, exceeding the Chandrasekhar limit and causing the explosion (Webbink, 1984; Iben and Tutukov, 1984). The second is the single–degenerate scenario in which a white dwarf accretes from a non–degenerate companion star (Whelan and Iben, 1973; Nomoto, 1982). However, the mechanisms that lead to these explosions are still not completely understood and further theoretical and observational efforts are required to fully unveil the nature of the SNe Ia progenitors.

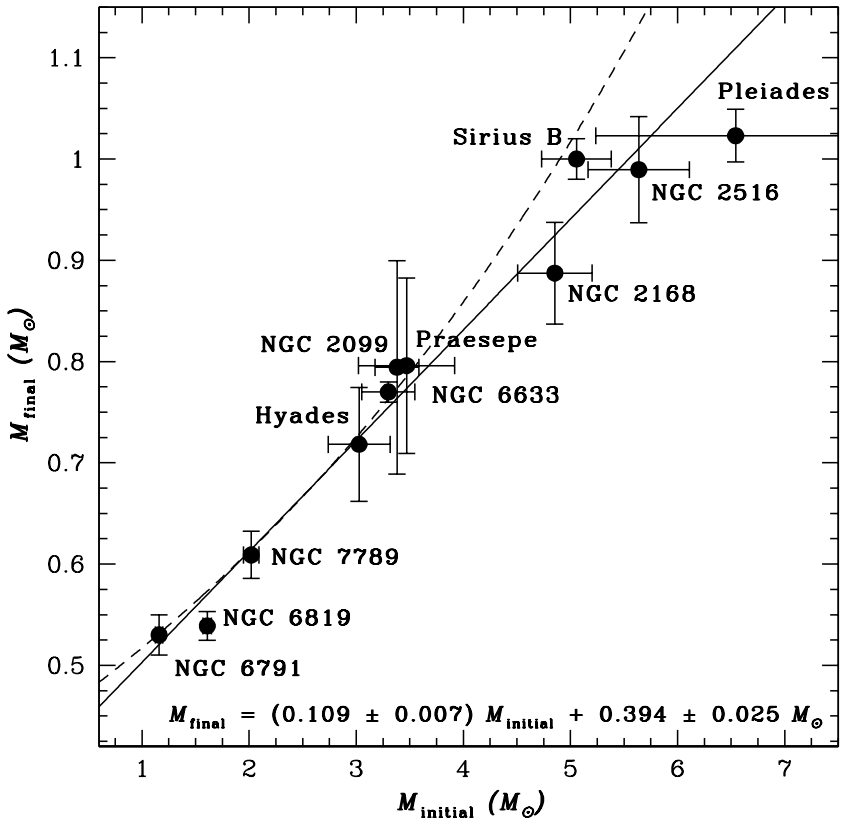

Figure 1.6: Initial–final mass relationship from open clusters. Figure from Kalirai et al. (2008).

1.2.1 Mass distribution

The initial–final mass relationship (IFMR, Figure 1.6) links the mass of a present day white dwarf with that of its main sequence progenitor. Since the mass distribution of the Galactic white dwarf population peaks at $M \simeq 0.6\,\mathrm{M}_\odot$ (Koester et al. 1979; Liebert et al. 2005; Kepler et al. 2007, Figure 1.7) the most common white dwarfs have carbon–oxygen cores and descend from progenitors in the mass range $0.8\,\mathrm{M}_\odot \lesssim M \lesssim 2\,\mathrm{M}_\odot$.

About 10% of the white dwarfs in the present day Galactic population have helium cores (Figure 1.7). However, as explained in Section 1.1.1, they cannot have formed via single star evolution. Instead, the currently observed helium white dwarfs have formed in binary systems: after leaving the main sequence and becoming a giant, the envelope of the white dwarf progenitor is stripped owing to the interaction with a companion star. Consequently, the helium core is exposed, leaving a helium white dwarf in a close binary system (Sarna et al., 1999).

It has been suggested that also a fraction of the massive oxygen–neon white dwarfs, located at the high–mass tail of the distribution, form in binary systems, as a consequence of the merge of two carbon–oxygen white dwarfs in close binaries

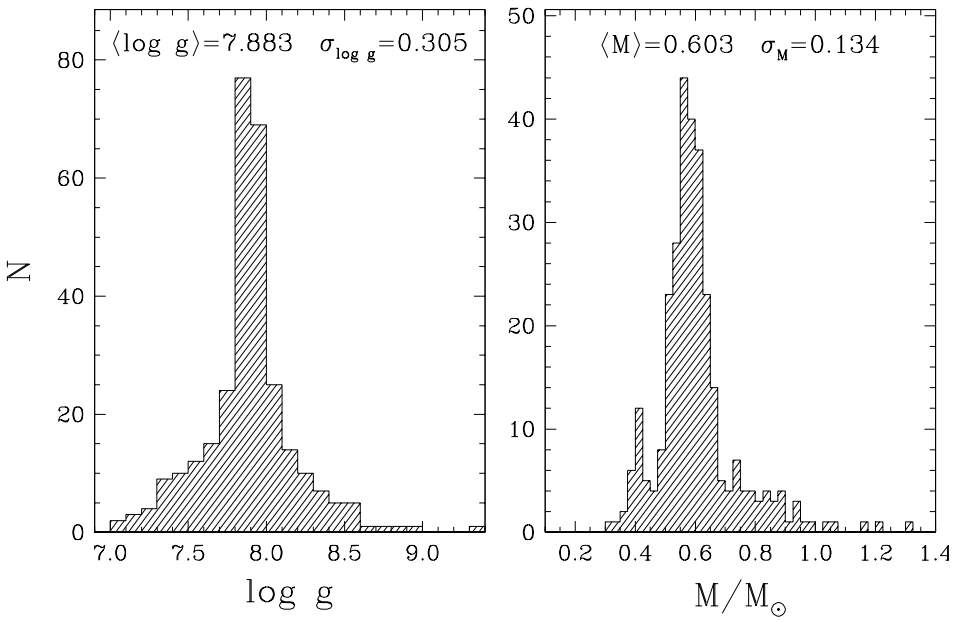

Figure 1.7: Surface gravity and mass distribution of a spectroscopic sample from the Palomar Green Survey, composed of 298 DA white dwarfs with effective temperatures $T_{\rm eff} \gtrsim 13\,000$ K. Figure from Liebert et al. (2005).

(Guerrero et al., 2004; Lorén-Aguilar et al., 2009).

1.2.2 Atmospheres

A typical $0.6\,M_\odot$ white dwarf is composed of a degenerate carbon–oxygen core that contains $\simeq 99\%$ of the mass of the star. This core is surrounded by a layer of helium ($\simeq 0.01\,M_\odot$) on top of which lies a thin atmosphere of hydrogen ($\simeq 10^{-4}\,M_\odot$, Figure 1.8, Althaus et al. 2010).

Since the gravitational settling of the elements occurs on time–scales that are much shorter than the white dwarf cooling age (Paquette et al., 1986; Koester, 2009), the vast majority of the Galactic white dwarfs ($\simeq 80\%$) have hydrogen atmosphere (DA white dwarfs, Kleinman et al. 2013; Giammichele et al. 2012). Their spectra are characterised by Lyman (in the ultraviolet) and Balmer (in the optical) hydrogen absorption features (top spectrum in Figure 1.9) that are heavily broadened by the strong gravitational field: a typical carbon–oxygen white dwarf with $M = 0.6\,M_\odot$ has a surface gravity $\log(g) = 8$, where g is expressed in cgs units of cm/s^2 (for comparison the surface gravity of the Earth is $\log(g) \simeq 3$ and that of the Sun is $\log(g) \simeq 4.5$).

The remaining fraction of white dwarfs have atmospheres that are dominated either by helium (DB white dwarfs), or contain carbon (DQ white dwarfs), or are featureless (DC white dwarfs), or even shows traces of heavy elements (DZ white dwarfs, Figure 1.9). In the past, it has been suggested that DB white dwarfs

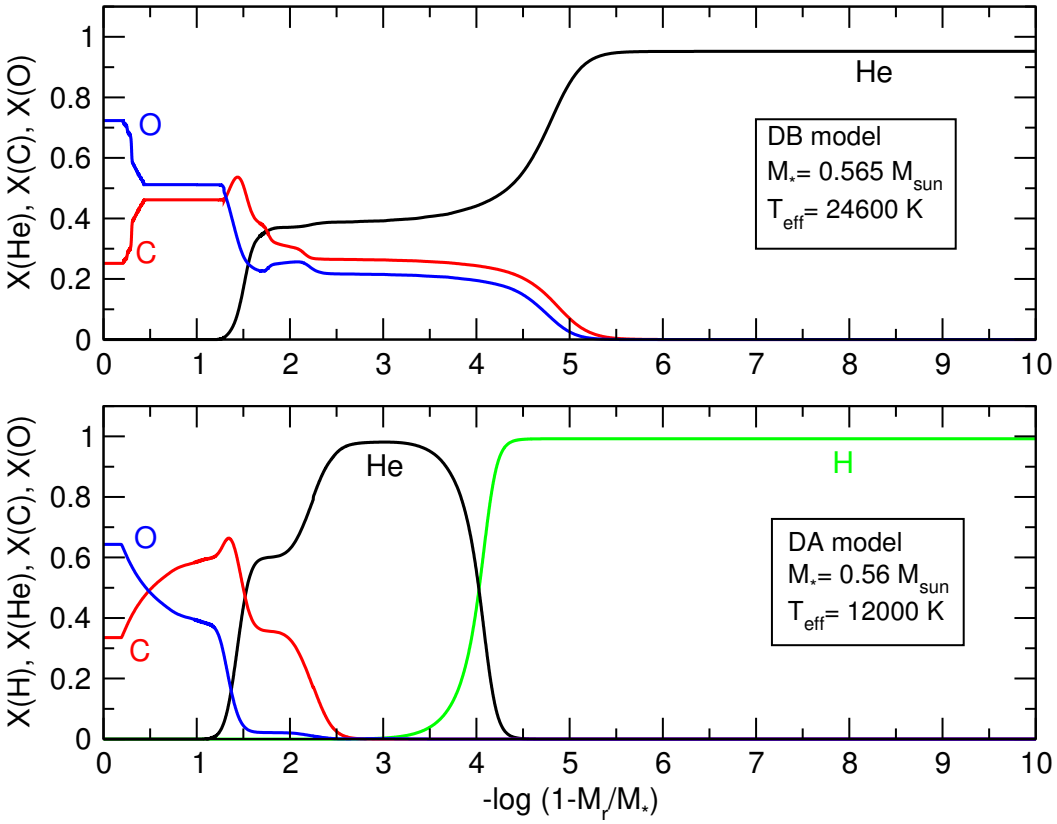

Figure 1.8: Chemical structure of a typical DB (top) and DA (bottom) white dwarf. The factional abundances (X) of hydrogen (H), helium (He), carbon (C) and oxygen (O) are reported as a function of the logarithm of the fractional mass at a given radius (M_r). The photons arising from the white dwarf photosphere that are directly detectable come from regions at which the optical depth is comparable to unity, located at $-\log(1 - M_r/M_*) \gtrsim 15$, thus the directly observable atmosphere of a white dwarf is outside the right edge of this figure. Figure adapted from Althaus et al. (2010).

descend from DAs in which convection has dredged up part of the underlying helium (Fontaine and Wesemael, 1987). More recent theories suggest that a small fraction of white dwarfs can be born as DBs, emerging from the planetary nebula phase with virtually no hydrogen in their envelopes (Bergeron et al., 2011). DC white dwarfs are continuum dominated and do not show absorption features in their spectra because, owing to their effective temperatures ($T_{\rm eff} \lesssim 6\,000\,{\rm K}$ for DAs and $T_{\rm eff} \lesssim 11\,000\,{\rm K}$ for DBs), the electrons of the elements in the photosphere are mainly found in the ground level and thus there are no electrons available to generate absorption lines at visible wavelengths. DQ white dwarfs are thought to form when convection in the helium layer pollutes the atmosphere with carbon dredged up from the core (Pelletier et al., 1986; Koester and Knist, 2006; Dufour et al., 2007). Finally, the pollution of the atmosphere of DZ white dwarfs suggests on going accretion from a companion

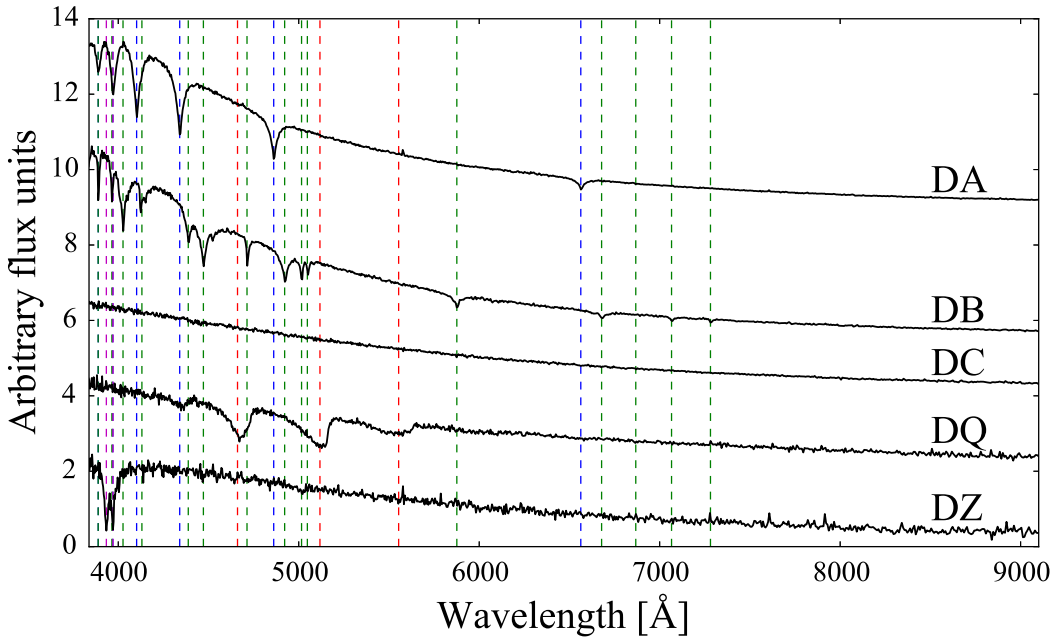

Figure 1.9: Sample white dwarf spectra from the Sloan Digital Sky Survey (SDSS, York et al. 2000). The spectrum of the DA white dwarf only shows hydrogen absorption features (blue lines); helium absorption lines and C_2 molecular bands are visible in the spectra of the DB and DQ white dwarfs (green and red lines respectively), while calcium (magenta lines) can be detected in the spectrum of the DZ white dwarfs. No absorption features are present in the spectra of DC white dwarfs.

star (as it is the case of white dwarfs in cataclysmic variables, see Section 1.4) or recent accretion of tidally disrupted planetesimals (Koester and Wolff, 2000; Jura, 2003; Farihi et al., 2010; Gänsicke et al., 2012; Raddi et al., 2015; Vanderburg et al., 2015; Gentile Fusillo et al., 2017).

Observations provide direct access to the white dwarf atmosphere and since its spectral appearance is determined by $T_{\rm eff}$ and $\log(g)$, ideally, a spectral fit with synthetic atmosphere models to the white dwarf spectrum would provide both its effective temperature and surface gravity. For this reason several theoretical models reproducing the emergent flux from a white dwarf photosphere have been developed (Hubeny, 1988; Bergeron et al., 1991; Hubeny and Lanz, 1995; Koester, 2010; Tremblay et al., 2013) which find application in many scientific works investigating the physical properties of the observed Galactic white dwarf sample (Bergeron et al., 1991; Gianninas et al., 2011; Giammichele et al., 2012).

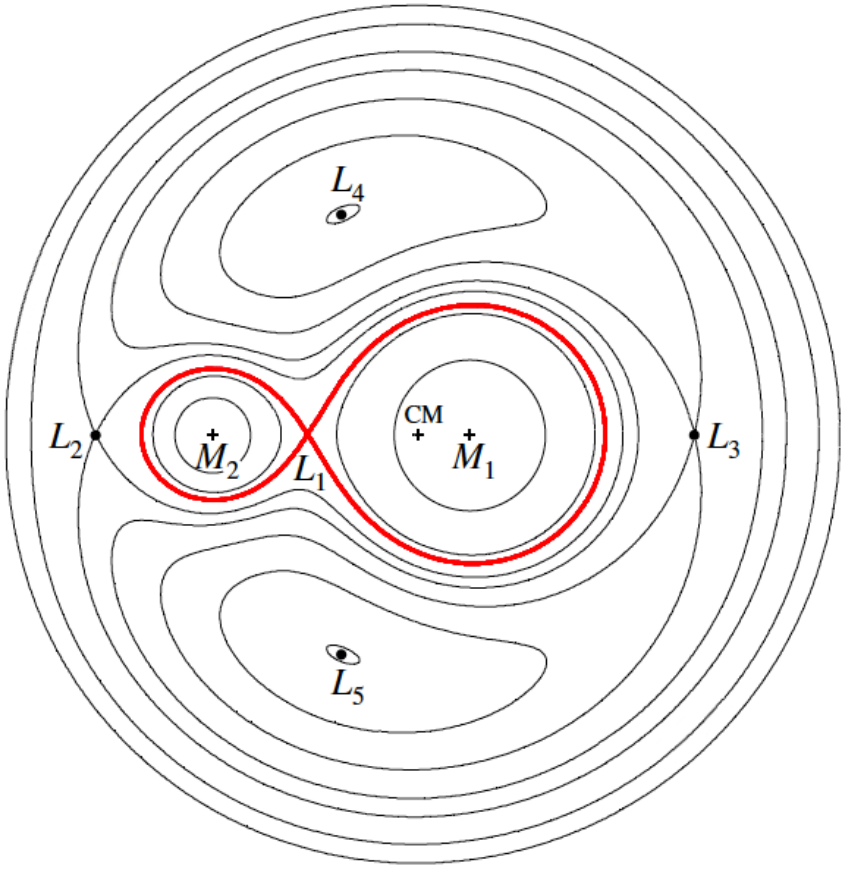

Figure 1.10: Cross–section of the Roche equipotential surfaces in the orbital plane for a binary system with $q = M_2/M_1 = 0.25$. CM illustrates the location of the centre of mass of the system. The Roche lobes are highlighted in red. The Roche potential has five equilibrium points in which the gravity and centrifugal force cancel each other: this are the Lagrangian points ($L_1 - L_5$). The Roche lobes touch in the inner Lagragian point L_1. Figure adapted from Frank et al. (2002)

1.3 Binary stars

In the previous Section, the evolution of isolated stars and their final products have been described. However, as discussed above, the majority of the Solar–type stars in our Galaxy, and up to $\simeq 80\%$ of massive stars, are born in binary systems. Evolution of such objects can differ from that of isolated stars because, if the system is tight enough, the two stars will interact at some point in their lives thus influencing their mutual evolution (Kopal, 1978).

The two stellar components of a binary systems are in a rotating frame of reference and the presence of a centrifugal force modifies the gravitational potential. The effective potential originating from the combination of the centrifugal and gravitational potentials is called *Roche potential*. The equipotential surfaces of the Roche potential are spherical close to each stellar surface (where the gravitational

potential of one of the stars is dominant) while, moving away from the two stellar objects (where the centrifugal potential is stronger), they become ellipsoidal (Figure 1.10). The inner equipotential surfaces enclosing both stars are called *Roche lobes*.

The two lobes touch in one point in between the two stars, the first (or inner) Lagrangian point L_1. Here, the gravitational pulls from the two stars cancel each other thus a particle passing trough L_1 will move from a region where it is gravitationally bound to one star to a region where it is gravitationally bound to the other. As described in Section 1.1.1, a star, once exhausted the nuclear fuel in its core, will leave the main sequence and start expanding. If this star is part of a close binary, then it will get in touch with its Roche lobe. Alternatively, a star can fill its Roche lobe if, because of angular momentum losses (see Section 1.4.2), the orbital separation decreases thus reducing the Roche lobe size.

The shape of the equipotential surfaces of the Roche potential is completely determined by the system mass ratio, $q = M_2/M_1$, where M_2 is the mass of the Roche–lobe filling star (the secondary) and M_1 is the mass of its companion (the primary), while the orbital separation a determine their size. Particularly, the size of the Roche lobes is defined by the equation (Eggleton, 1983):

$$R_{\rm L} = \frac{a\, 0.49\, x^{2/3}}{0.6x^{2/3} + \ln(1 + x^{1/3})} \tag{1.4}$$

where $x = q$ returns the size of the secondary's Roche lobe, while $x = 1/q$ returns the size of the primary's Roche lobe. Whether the components of a binary system will interact or not depends only on these two parameters, q and a, and, regardless of the mechanism that brings the secondary in touch with its Roche lobe, it will start mass transfer onto the other stellar component.

1.3.1 Mass transfer in binaries

A star is in hydrostatic equilibrium, i.e. the thermal pressure that drives the expansion of the gas is counterbalanced by the gravitational force that holds the star together. However, when a star gets in touch with its Roche lobe, its photosphere around L_1 does not feel the gravitational pull anymore and it is free to expand into the surrounding vacuum, entering the Roche lobe of its companion. Here, the effective gravity pulls the matter toward the detached primary, giving rise to a mass transfer stream (Figure 1.11).

Because of the transfer of mass and the redistribution of angular momentum in the system, the mass ratio, the orbital separation and thus the orbital period change. The way in which these changes occur determines whether the accretion process is stable or not and a self–sustained mass transfer will be established only

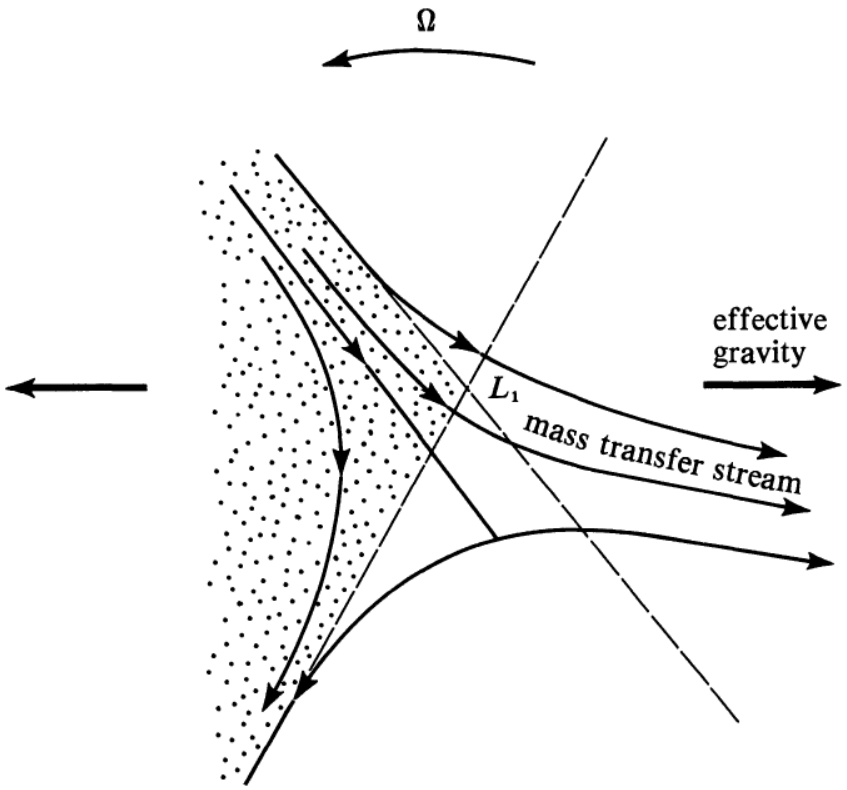

Figure 1.11: The binary system rotates with angular speed Ω and the matter inside the Roche lobes feels an effective gravity (black arrows). When one of two stellar components gets in touch with its Roche lobe, its photosphere near L_1 is not in hydrostatic equilibrium anymore because the gravitational pull vanishes in L_1. Since the internal pressure of the gas is not counterbalanced by gravity anymore, it expands freely into the Roche lobe of the companion, giving rise to a mass–transfer stream. Figure from Shu (1982).

when the effect of such variations forces the mass–losing star to stay constantly in touch with its Roche lobe (Frank et al., 2002).

The starting point to derive how these quantities vary is the orbital angular momentum J:

$$J = M_1 M_2 \left(\frac{Ga}{M}\right)^{1/2} \tag{1.5}$$

where $M = M_1 + M_2$ is the total mass of the system. The logarithmically differentiation of this equation provides the relationship governing the evolution of a mass–transferring system:

$$\frac{\dot{a}}{a} = \frac{2\dot{J}}{J} - \frac{2\dot{M}_1}{M_1} - \frac{2\dot{M}_2}{M_2} + \frac{\dot{M}}{M} \tag{1.6}$$

where the dots represent the derivatives with respect to the time.

It is usually assumed that all the mass lost by one star is accreted by the other thus no mass is lost by the system ($\dot{M} = 0$), and Equation 1.6 can be written as (King, 1988):

$$\frac{\dot{a}}{a} = \frac{2\dot{J}}{J} - \frac{2\dot{M}_2}{M_2}(1 - q) \tag{1.7}$$

Under the assumption of *conservative mass transfer*, i.e. also the total angular momentum of the system is conserved ($\dot{J} = 0$), since $\dot{M}_2 < 0$ by definition, it becomes clear from Equation 1.7 that the system expands ($\dot{a} > 0$) if mass is transferred from the less massive to the more massive while the binary shrinks ($\dot{a} < 0$) in the opposite case. In fact angular momentum must be conserved so moving matter closer to the centre of mass implies a wider orbit for the secondary (first case). On the contrary, when matter is moved further away from the centre of mass,the orbital separation has to be reduced (second case).

The consequent variation of the Roche lobe radius is given by the relationship:

$$\frac{\dot{R}_L}{R_L} = \frac{2\dot{J}}{J} - \frac{2\dot{M}_2}{M_2}\left(\frac{5}{6} - q\right) \tag{1.8}$$

and therefore two different cases can be identified accordingly to the value of q with respect to 5/6 (Ritter, 1976):

- $q > 5/6$, under the assumption of conservative mass–transfer, the Roche lobe size is reduced thus keeping the secondary in touch with it. In this case, the mass transfer process proceeds in an violent and possibly catastrophic way and it stops when enough matter has been accreted on the companion so that $q \lesssim 5/6$.
- $q \lesssim 5/6$, in this case the size of the Roche lobe increases under conservative mass transfer. The secondary loses contact with the Roche lobe and accretion is halted. However, if the secondary expands owing to nuclear evolution (i.e. leaves the main sequence becoming a giant) or if the system shrinks by losing angular momentum, then the mass transfer can proceed in a stable way.

Finally, the stability of the mass transfer process is also related to the response of the secondary to the mass loss. If the time–scale at which the secondary loses mass (Knigge et al., 2011):

$$t_{\dot{M}_2} = \frac{M_2}{\dot{M}_2} \tag{1.9}$$

is much longer than its thermal time scale defined in Section 1.1.1, then the secondary has enough time to adjust its radius to the new mass configuration and

accretion is stable (Section 1.5.2). On the contrary, when the mass loss occurs faster than the thermal time–scale, the star has not the time to find a new equilibrium configuration and it is driven out of thermal equilibrium and expands. In this situation a runaway mechanism starts and mass transfer becomes unstable, leading to a common envelope phase (Section 1.3.2).

1.3.2 Common envelope

Unstable mass transfer in binaries leads to the formation of a common envelope (CE). In this configuration, the core of the donor and its companion orbit each other inside a common envelope that, if it is not co–rotating with the system, it can exert a drag force onto the two stellar components. In this case, the two stars transfer their orbital energy to the envelope and, as a consequence of the energy loss, they spiral in and get closer while the envelope gains energy and is expelled. The duration of the common envelope phase is thought to be very short, lasting $\lesssim 10^3$ yr.

The physics behind this phase is not well modelled yet and it is usually parametrised with the so–called "α prescription". In this approach, the efficiency at which the two stars transfer their energy to the envelope, i.e. the fraction of orbital energy that is used to expel the envelope, is defined by the parameter (Paczynski, 1976; Tutukov and Yungelson, 1979; Webbink, 1984):

$$\alpha = \frac{\Delta E_{\rm bind}}{\Delta E_{\rm orb}} \tag{1.10}$$

where $\Delta E_{\rm bind}$ is the binding energy of the envelope and $\Delta E_{\rm orb}$ is the change in the orbital energy. These two quantity are defined as follow:

$$\Delta E_{\rm bind} = -\frac{G M_{\rm D} M_{\rm e}}{\lambda R_{\rm L,A}} \tag{1.11}$$

where $M_{\rm D}$ and $M_{\rm e}$ are the initial mass of the donor and of the envelope, respectively, $R_{\rm L,A}$ is the Roche lobe radius of the accretor and λ is a parameter ($\simeq 1$) that accounts for the envelope density distribution, while

$$\Delta E_{\rm orb} = -\frac{G}{2}\left[\frac{M_{\rm c} M_{\rm A}}{a_{\rm f}} - \frac{M_{\rm D} M_{\rm A}}{a_{\rm i}}\right] \tag{1.12}$$

where $M_{\rm c}$ is the mass of the core of the donor, $M_{\rm A}$ is the mass of the accretor and $a_{\rm i}$ and $a_{\rm f}$ are the initial and final orbital separations, respectively. Using the definition of binding and orbital energy, Equation 1.10 can be rewritten as:

$$\frac{G M_{\rm D} M_{\rm e}}{\lambda R_{\rm L,A}} = \alpha \frac{G}{2}\left[\frac{M_{\rm c} M_{\rm A}}{a_{\rm f}} - \frac{M_{\rm D} M_{\rm A}}{a_{\rm i}}\right] \tag{1.13}$$

This is the "standard α–formalism", in which is commonly assumed that the donor mass does not change during the common envelope phase. From the study of a large sample of post common–envelope binaries (PCEBs), Zorotovic et al. (2010) have studied the energy balance problem described by Equation 1.13 and have shown that the current population of PCEB can be reproduced assuming $\alpha \simeq 0.2 - 0.3$.

1.4 Cataclysmic Variables

Cataclysmic variables (CVs) are close interacting binaries in which a white dwarf (the primary) accretes mass from a Roche–lobe filling companion star (the secondary or donor), which is on or near the main sequence, via stable mass transfer (Warner, 1995). In the absence of a strong magnetic field ($B \lesssim 10\,\mathrm{MG}$), the flow of material lost by the secondary gives rise to an accretion disc around the white dwarf.

1.4.1 CV formation and evolution

The progenitors of CVs are wide binary systems in which the more massive star, which leaves the main sequence first, fill its Roche lobe during the first giant branch or asymptotic giant branch phase. The system then enters a phase of unstable mass transfer from the more massive primary to the less massive secondary and the system evolves into a CE configuration, with the primary's envelope engulfing both stars. After the envelope is expelled, a close short orbital period detached PCEB is left behind. This PCEB is composed by the core of the giant primary, which evolves into a white dwarf, and a low–mass secondary star. Owing to subsequent angular momentum losses (AMLs) via magnetic braking (MB, which arises from a stellar wind associated with the magnetic activity of the secondary, Section 1.4.2) and gravitational wave radiation (GWR, Section 1.4.2), the PCEB evolves into a semi–detached configuration, becoming a CV (Figure 1.12).

CVs are systems characterized by a separation on the order of few solar radii and orbital periods $80\,\mathrm{min} \lesssim P_{\mathrm{orb}} \lesssim 2\,\mathrm{d}$. This configuration causes the secondary to overflow its Roche–lobe and to lose mass through the inner Lagrangian point, which then forms an accretion disc around the white dwarf (Section 1.5.2).

The long–period cutoff is dictated by the requirement for stable mass transfer: $q = M_{\mathrm{sec}}/M_{\mathrm{WD}} \lesssim 1$ (see Section 1.3.1, M_{WD} and M_{sec} denote the white dwarf and secondary masses). Since M_{WD} must be lower than the Chandrasekhar limit (Section 1.2.1), also the mass of the secondary is constrained below this limit, determining a maximum orbital period of $\lesssim 14\,\mathrm{h}$. Few CVs, such as GK Per ($P_{\mathrm{orb}} = 47.92\,\mathrm{h}$), have longer orbital periods than this limit. In these cases, the secondary is evolving into a giant and, having a lower density than a main sequence star of the same mass, it can fill its Roche lobe size at longer orbital periods.

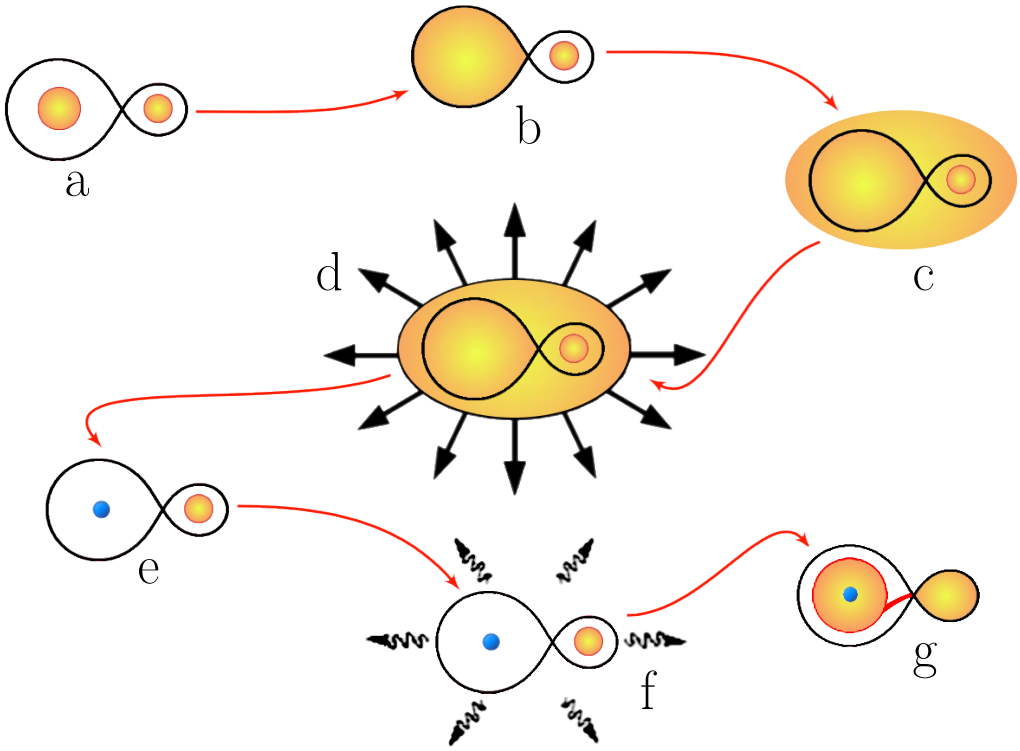

Figure 1.12: Formation of a CV: the progenitors of CVs are binary systems consisting of two main sequence stars, with $M_1 > M_2$ **(a)**. The more massive star evolves first, filling its Roche lobe **(b)** and starts mass transfer onto the less massive companion. Because of $q > 1$, mass transfer is dynamically unstable and leads to the formation of a CE **(c)**. The two stars transfer orbital energy to the envelope which is rapidly expelled **(d)**. A PCEB composed of a white dwarf and low–mass secondary is left behind **(e)**. The system loses angular momentum through magnetic braking and gravitational wave radiation **(f)**. Consequently the orbital separation and the Roche lobe size decreases, bringing the secondary in touch with its Roche lobe. This starts mass transfer onto the white dwarf **(g)**: a CV is formed.

In the standard model of CV evolution, the stability of the accretion process on long time scales (of the order of 10^7 Gyr, Kolb and Stehle 1996) requires a mechanism of AML which continuously shrinks the system and keeps the secondary in touch with its Roche lobe. In the frequently referenced framework of disrupted magnetic braking scenario, at least two different AML mechanisms drive CV evolution (Rappaport et al. 1983, Paczynski and Sienkiewicz 1983, Spruit and Ritter 1983).

For orbital periods $P_{\rm orb} \gtrsim 3\,{\rm h}$, the angular momentum is predominantly removed by MB, with typical mass transfer rates of $\dot{M} \sim 10^{-9} - 10^{-8}\,{\rm M}_\odot\,{\rm yr}^{-1}$ (Spruit and Ritter, 1983). For $P_{\rm orb} \lesssim 3\,{\rm h}$, the dominant AML mechanism is GWR,

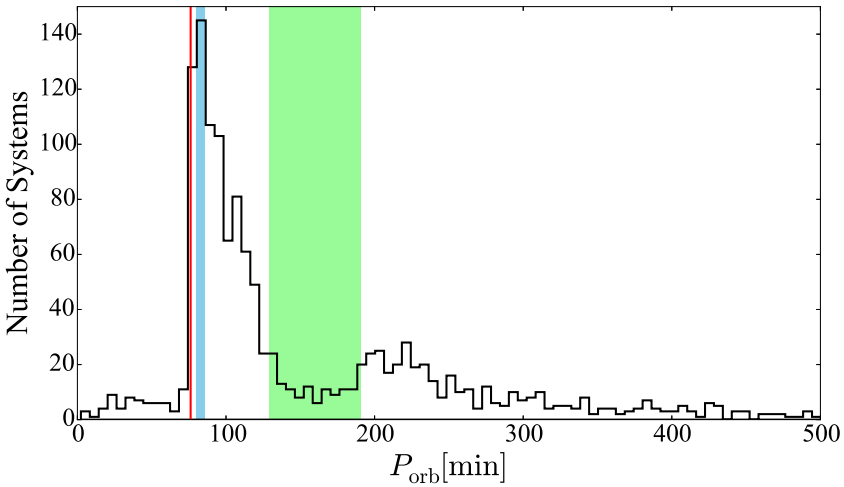

Figure 1.13: The orbital period distribution of 1429 semi–detached binaries containing a white dwarf and a Roche–lobe filling low–mass secondary (Ritter and Kolb 2003, 7th Edition, Release 7.24, December 2015). The systems located at short orbital periods ($P_{\rm orb} \lesssim 75$ min) are the AM CVn stars and CVs hosting an evolved donor. The green band highlights the period gap ($2.15\,{\rm h} \lesssim P_{\rm orb} \lesssim 3.18\,{\rm h}$, Knigge 2006), the blue box indicates the period spike ($80\,{\rm min} \lesssim P_{\rm orb} \lesssim 86\,{\rm min}$, Gänsicke et al. 2009) and the red line shows the period minimum position ($P_{\rm min} = 76.2\,{\rm min}$, Knigge 2006),

with typical $\dot{M} \sim 5 \times 10^{-11}\,{\rm M}_{\odot}\,{\rm yr}^{-1}$ (Patterson, 1984).

Another fundamental ingredient for CV evolution is the internal structure of the secondary and its response to mass loss (Knigge, 2006; Knigge et al., 2011). In fact, in CVs the time scale on which the secondary loses mass is comparable to its thermal time scale. The star is stripped of its external layer but the rate at which the hydrogen is burnt in its core requires a certain time ($\tau_{\rm adj}$) to adjust accordingly to its lower mass, which is a fraction of the thermal time scale of the secondary ($\tau_{\rm adj} \simeq 0.05\,\tau_{\rm th}$, Knigge et al. 2011). Consequently, the donor is driven slightly out of thermal equilibrium and is hotter and bloated compared to an isolated main sequence star of the same mass. This deviation from thermal equilibrium is thought to be the cause of the major features observed in the orbital period distribution (Figure 1.13): the "period gap" and the "period minimum".

The period gap is the dearth of known CVs in the period range $2\,{\rm h} \lesssim P_{\rm orb} \lesssim 3\,{\rm h}$. At $P_{\rm orb} \simeq 3\,{\rm h}$ the donor star becomes fully convective and MB via a stellar wind is thought to be greatly reduced (see Section 1.4.2 for more details). Consequently, the mass transfer rate diminishes and the secondary returns to thermal equilibrium, shrinking and losing contact with its Roche lobe. The system then evolves as a detached binary through the period gap. Following the diminution of MB (Rappaport et al., 1983), the system evolves through GWR only, which slowly reduces the orbital separation and brings the secondary again in touch with its Roche lobe at

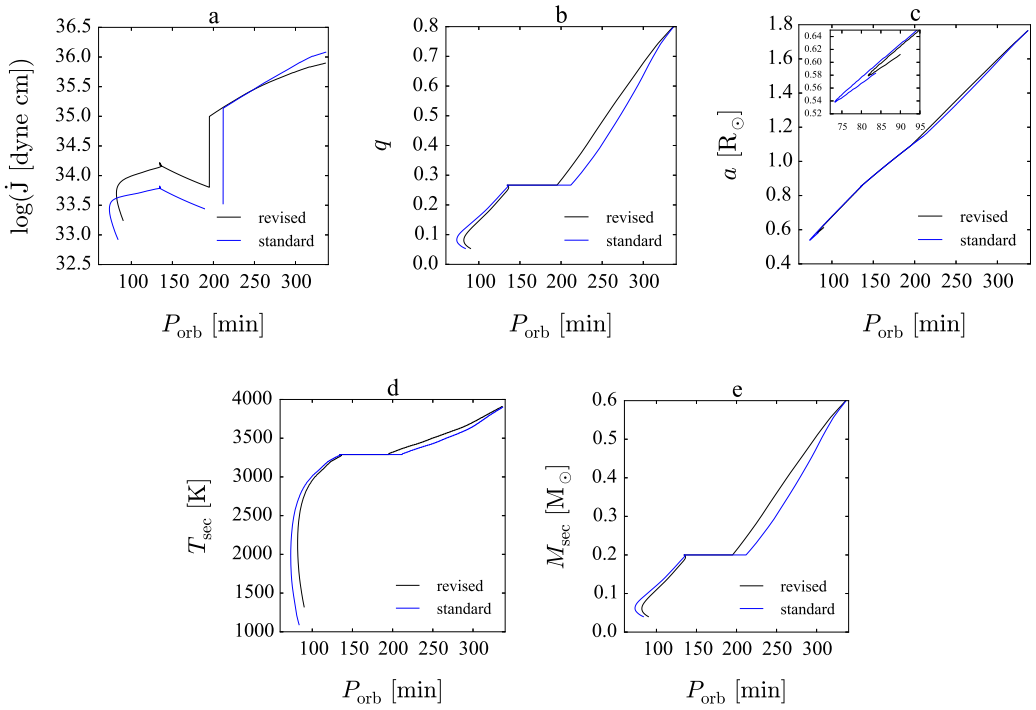

Figure 1.14: The standard model of CV evolution (blue line) from Knigge et al. (2011), calculated assuming $M_{\rm WD} = 0.75\,{\rm M}_{\odot}$. Different stages of CV evolution are driven by different AML mechanisms, whose efficiencies vary with the orbital period. Since MB is more efficient than GWR, systems above the period gap are characterised by higher angular momentum loss rates than systems below the gap (a). As mass is transferred from the secondary to the white dwarf, the mass ratio decreases (b), becoming $q < 0.1$ for period bouncer systems. Also the orbital separation shrinks until the secondary becomes a brown dwarf (c) and the system expands evolving back towards longer $P_{\rm orb}$. The secondary's effective temperature (d) and mass (e) decrease during the evolution of the system, eventually becoming those characteristic of a brown dwarf, after the system evolves through the period minimum. The inclusion of residual magnetic braking below the period gap (black line) shifts the period minimum toward longer $P_{\rm orb}$ (see Section 1.6).

$P_{\rm orb} \simeq 2\,{\rm h}$.

Below the period gap, CVs continue evolving towards shorter orbital periods, until they reach the period minimum at $\simeq 70-75\,{\rm min}$ (Knigge et al., 2011; Goliasch and Nelson, 2015; Kalomeni et al., 2016). Since the time that a CV spends at a given orbital period (and thus its detection probability at that $P_{\rm orb}$) is inversely proportional to the rate at which $P_{\rm orb}$ varies and CVs pass through the period minimum twice while they bounce back, an accumulation of systems is expected to be observed at the period minimum (the so–called "period minimum spike", Kolb and Baraffe 1999). At the period minimum, the time–scale at which the secondary loses mass is much shorter compared to its thermal time–scale, therefore the secondary is

driven out of thermal equilibrium and stops shrinking in response to the mass loss. Differently from the situation before the period minimum, now the mass transfer is not driven by AMLs that, by shrinking the system, keep the secondary in touch with its Roche lobe but by the fact that the donor expands in response to the mass loss and keeps contact with the expanding Roche lobe (as described in Section 1.3.1, in the case in which mass is transferred from the less massive to the more massive star, the net effect is the increase of the Roche lobe size and the orbital separation). It is worth noticing that the system is still losing angular momentum through GWR. Therefore, passing the period minimum, CVs evolve towards longer orbital periods and are called "period bouncers". Period bouncers are characterised by mass ratios $q = M_{\rm sec}/M_{\rm WD} \leq 0.1$ and donors with masses below the hydrogen burning limit and effective temperatures $T \lesssim 1\,700\,{\rm K}$ (Figure 1.14).

1.4.2 AML mechanisms

The standard model of CV evolution described above includes two mechanisms of AML: MB and GWR. However, additional AML mechanisms have been proposed over the last years in order to explain the discrepancies between theory and observation (see Section 1.6). Here, a brief overview of the AMLs playing a crucial role in the evolution of CVs is presented.

Magnetic braking

Magnetic braking arises from a slightly magnetised stellar wind (Huang, 1966; Mestel, 1968; Verbunt and Zwaan, 1981) which, owing to its electric charge, is forced to follow the line of the stellar magnetic field. At the stellar poles, these lines are open and thus the wind is expelled in the outer space. Since the magnetic field lines co–rotate with the star, the particles composing the wind carry with them some angular momentum, slowing down the stellar rotation (Schatzman, 1962; Kraft, 1967).

However, in compact binaries, the secondary is tidally locked and therefore its rotation rate equals the orbital period. The net effect is that orbital angular momentum is carried away from the system and the orbital period and separation are consequently reduced, resulting in the spin up of the secondary as it orbits on tighter (and hence of shorter orbital period) orbits (Figure 1.15).

The origin of the stellar magnetic field, fundamental to feed the MB mechanisms, is quite uncertain and it is though to arise from a dynamo effect in the tachocline, i.e. the region between the radiative core and the convective envelope of a star (Parker, 1955; MacGregor and Charbonneau, 1997; Charbonneau and MacGregor, 1997). The efficiency of MB is strongly related to the intensity and configuration of the magnetic field (Schreiber et al., 2010). MB requires long open field lines, like those in Figure 1.15, but at $M_2 \simeq 0.2 - 0.3\,{\rm M}_\odot$ (Knigge et al., 2011)

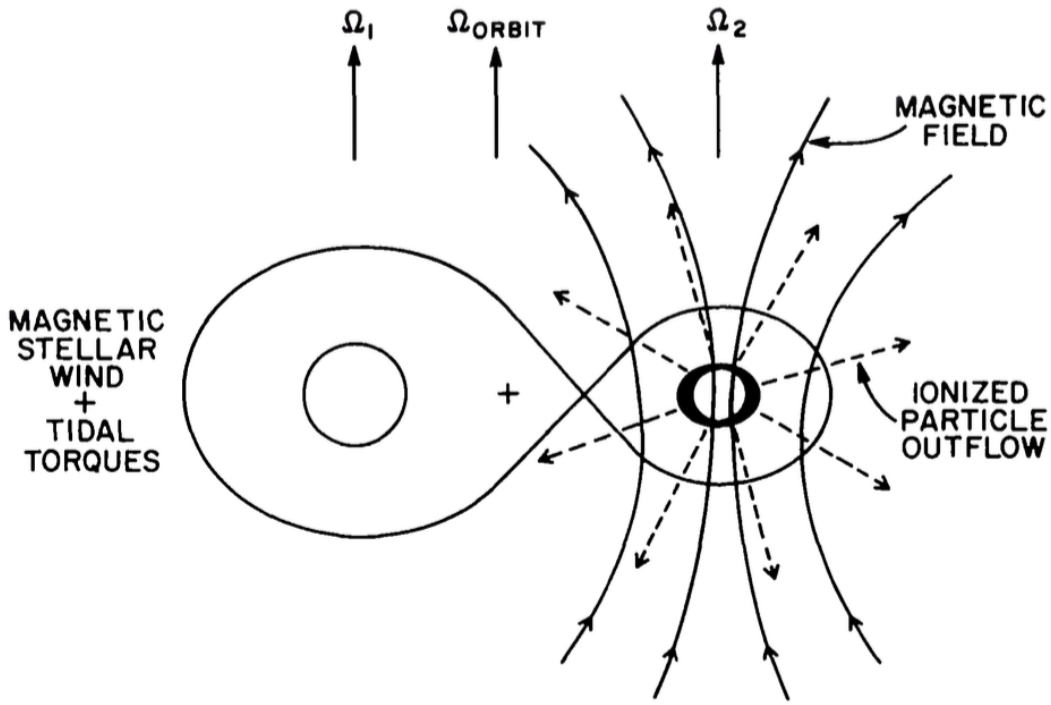

Figure 1.15: Schematic of the magnetic braking mechanism. The ionised particles from the secondary stellar field are forced to follow the magnetic field line and are driven far away from the system. They carry with them angular momentum which is finally removed from the system since the secondary is tidally locked with the orbital period through tidal interaction. Figure from Iben (1991).

the secondary becomes fully convective. The intensity of the magnetic field results then greatly reduced and its topology changes, causing the field lines to close at the stellar surface. This, in turn, impedes the escape of the stellar wind and reduces the angular momentum removal.

This transition to a fully convective star and the resulting change in the magnetic field topology of the secondary is thought to be the origin of the period gap observed in the CV period distribution (the disrupted magnetic braking scenario, Section 1.4.1). However there is some observational evidence that lower mass stars should also be able to sustain large magnetic field (Giampapa and Liebert, 1986; Linsky et al., 1995; Hodgkin et al., 1995; Delfosse et al., 1998), thus suggesting the presence of a "residual" MB at short orbital periods (Patterson, 1998; Knigge et al., 2011).

Magnetic braking is still poorly modelled since the physics behind it is not completely understood yet and the rate at which the system loses angular momentum trough MB cannot be accurately calculated from the theory. This rate can be estimated observationally from the accretion luminosity and taking into account the other AML mechanisms described in the following Sections.

Gravitational wave radiation

Binary systems emit gravitational waves which carry away energy and determine a spiralling inwards of the two stars. These ripples in the space–time have been predicted in 1916 by Einstein in its General Relativity Theory and their existence has been recently confirmed by the Laser Interferometer Gravitational–Wave Observatory (LIGO) and Virgo experiments with the detection of black hole (Abbott et al., 2016a,b, 2017; The LIGO Scientific Collaboration et al., 2017) and neutron star mergers (The LIGO Scientific Collaboration and The Virgo Collaboration, 2017).

The rate at which GWR removes angular momentum from the system can be accurately calculated from the theory of General Relativity (Paczyński, 1967; Webbink, 1976):

$$\dot{J}_{\rm GWR} = \frac{-32}{5}\frac{G^{7/2}}{c^5}\frac{M_1 M_2 M^{1/2}}{a^{7/2}} \tag{1.14}$$

where M_1, M_2 and $M = M_1 + M_2$ are the masses of the two components of the binary and the total mass of the system, respectively. GWR acts continuously in every binary system and it is responsible, for example, for the shrinkage of the orbit in compact binaries, such as double white dwarfs, double neutron stars and neutron star plus black hole binaries. Since $\dot{J}_{\rm GWR}$ is inversely proportional to the orbital separation, its efficiency increases as the system gets tighter.

GWR is less efficient than MB and, in CVs, it only becomes dominant below the period gap, when the orbital separation is smaller and MB has been greatly reduced by the transition of the secondary into a fully convective star.

Additional AML mechanisms

The idea of consequential AML (CAMLs), i.e. a mechanism of AML generated by the mass transfer process itself, partially driving CV evolution has been introduced long time ago (Webbink, 1985; King and Kolb, 1995). Different scenarios to explain its origin have been proposed. For example, Livio and Pringle (1994) suggested AML by a magnetic disc wind while Schenker et al. (1998) analysed the case of friction between the secondary star and the white dwarf ejecta after a nova explosion. However these mechanisms always failed to reproduce the observed CV orbital period distribution. Recently, Schreiber et al. (2016) presented an alternative model in which an empirical CAML (eCAML) is derived in order to reproduce the CV orbital period and mass distributions along with their space density. Schreiber et al. (2016) argue that the best physical explanation for this eCAML would be the friction between the secondary and the white dwarf ejecta during nova explosions, with a different recipe to the one used by Schenker et al. (1998). However, more detailed models and observations of nova eruptions are required to confirm this hypothesis.

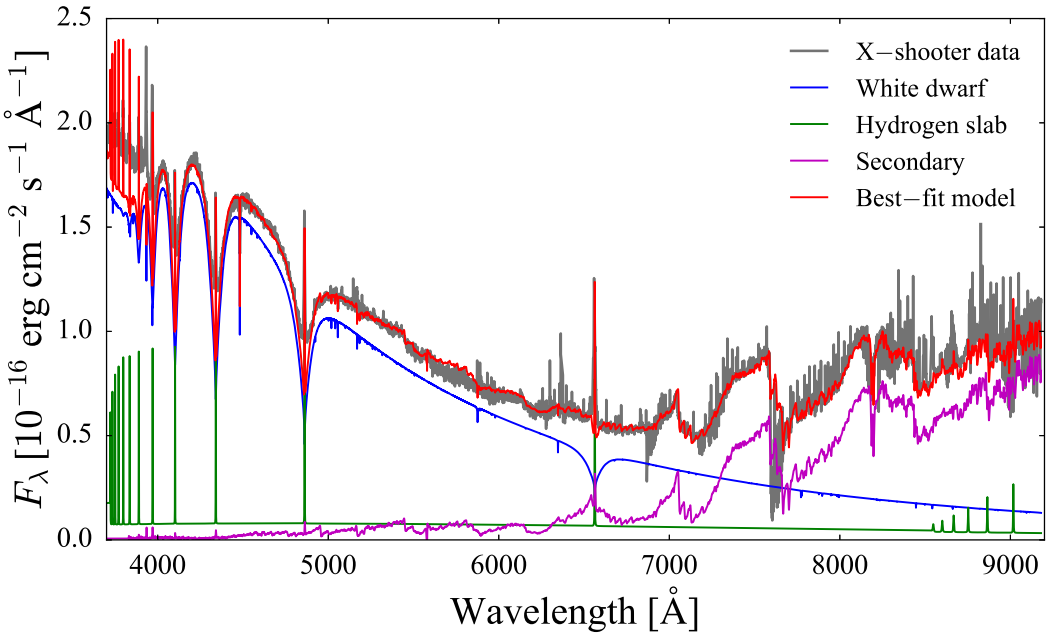

Figure 1.16: X–shooter spectrum of the dwarf nova IR Com as a sample spectrum of a quiescent CV. The observed spectrum (grey) is well modelled with the sum (red) of three components: a white dwarf (blue), an isothermal and isobaric hydrogen slab model approximating the disc emission (green) and a M6 secondary (magenta).

Similarly, Nelemans et al. (2016) investigated the possibility that asymmetric mass ejection during nova explosions could make the orbit slightly eccentric. The eccentricity would enhance the mass transfer rate leading to an unstable mass transfer process in the system and this would bring in agreement the theoretical predicted and observed CV white dwarf mass distribution and space density. However, also in this study, the poor theoretical and observational knowledge of the nova phenomenon does not allow to draw definitive conclusion on the origin of the CAML mechanism and on its real effects on CV evolution.

1.5 Observational properties of CVs

1.5.1 CV spectral appereance

CV white dwarfs are relatively hot objects ($T_{\rm eff} \gtrsim 10\,000$ K, Sion 1999) since they are heated by the energy released by the infalling material (Sion, 1995; Townsley and Bildsten, 2003). Their spectral energy distribution (SED) peaks in the ultraviolet and their atmospheres are polluted by the accreting material. Their spectra are characterised by pressure broadened hydrogen absorption lines and sharp metal absorption features (blue line in Figure 1.16).

The secondary stars are cool low mass objects and their emission peaks at

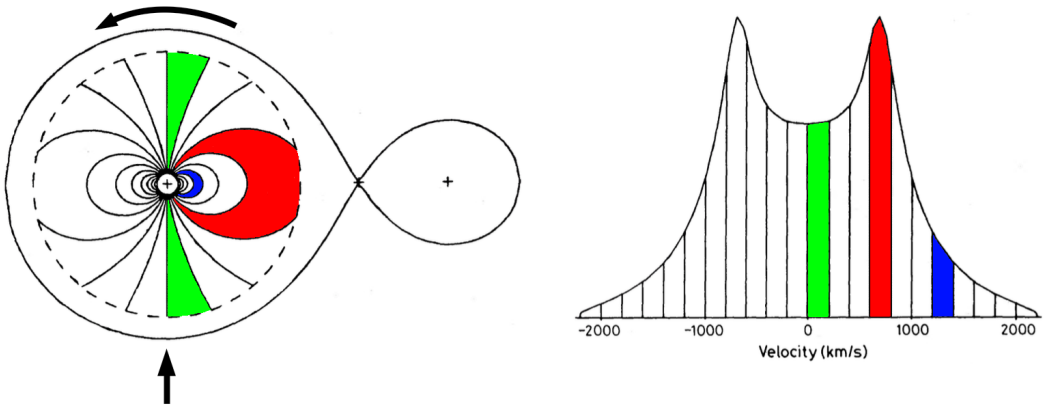

Figure 1.17: Double peaked emission line formation in an accretion disc. The line of sight of the observer is indicated by the vertial arrow. On the left, an edge–on view of the accretion disc for a system with $q = 0.15$ is shown, with the solid line representing the Roche lobes. The colours highlight the regions of constant Keplerian velocity that form a dipole pattern at the disc surface. On the right, the emission line profile is illustrated as observed when the disc is viewed side–on. The colours highlight the velocity bins originating in the corresponding area of the disc in the left diagram. Figure adapted from Horne and Marsh (1986)

infrared wavelengths (magenta line in Figure 1.16), where it dominates the overall system emission. Typically, donor stars in CVs have $M_2 \lesssim 0.7\,\mathrm{M}_\odot$ and $\log(g) \simeq 5$ (Knigge et al., 2011). They are colder than the white dwarf companion ($T_{\mathrm{eff}} \lesssim 3\,000\,\mathrm{K}$) so their spectra are characterized by several molecular absorption bands, such as TiO, H_2O and sometimes CO. When the secondary is not outshone by the disc emission, absorption from Na I (11 381/11 403 Å) and K I (11 690/11 769 Å and 12 432/12 522 Å) can also be identified.

Accretion disc in CVs are thin discs of gaseous material and their temperature distribution varies from $T \simeq 3\,000\,\mathrm{K}$ at the cool outer edge up to $T \simeq 30\,000\,\mathrm{K}$ in the central regions, owing to the release of gravitational energy of the gas approaching the white dwarf. The disc emission peaks at the visible wavelengths (green line in Figure 1.16) and their spectra are composed by a thermal continuum plus several emission lines, originating from the bright spot and from an optically thin upper layer of the disc (see Warner 1995 for a detailed review). In fact, in CV spectra, the disc signature can be recognised in strong emission lines from low ionization states in the optical (such as H I, He I, He II, Fe II, Ca II and O I) and highly ionized species in the ultraviolet (Lyα, He II, C II, C IV, N II, N V and O III). The emission lines originates from the decay to lower energy levels of electrons that have been excited by collision with other atoms or by photo–ionisation.

Owing to the high rotational velocity ($\simeq 1\,000\,\mathrm{kms}^{-1}$), the emission lines are broadened from a few to tens of Å and are characterised by a double peak profile, arising as a consequence of the symmetry and the Keplerian radial velocity profile

of the disc (Figure 1.17). The line wings originate from the innermost regions (blue in Figure 1.17), which have higher velocities than the outer ones but are smaller and contribute with less flux; the core originates from the regions along the line of sight, which have a large area but zero radial velocity (green in Figure 1.17), and finally, the large regions with intermediate radial velocities are the location where the double peaks form (red in Figure 1.17).

1.5.2 Accretion discs

The mass transferred via Roche lobe overflow cannot accrete directly onto the white dwarf since it has an excess of angular momentum. Instead, it follows a ballistic trajectory determined by the Roche potential with an initial elliptic orbit around the primary (Lubow and Shu, 1975). The presence of the secondary determines the slow precession of this orbit thus the stream will intercepts itself at some point. While the gas dissipates energy via internal shocks, it has no possibility to get rid of angular momentum and therefore it settles at a distance called circularisation radius, i.e. on the orbit having the lowest energy for the given angular momentum, forming an annulus around the white dwarf (Flannery, 1975). In this annulus, several dissipative processes take place, such as collisions, shocks and viscous dissipation, that transform the orbital energy into internal gas energy.

While the gas loses its internal energy, the internal torques allow the redistribution of angular momentum: the stream slowly spirals inwards while the outer parts gain angular momentum, thus spreading outwards, giving rise to a configuration known as *accretion disc*. The stream from the secondary hits the disc transferring its kinetic energy to the accreting material, causing it to be heated and to radiate away this surplus of energy. This encounter region is called bright spot (see Warner 1995 and reference therein).

The internal energy of the disc is radiated away with a luminosity:

$$L_{\rm disc} = \frac{GM_1\dot{M}}{2R_1} \tag{1.15}$$

Defining the accretion luminosity:

$$L_{\rm acc} = \frac{GM_1\dot{M}}{R_1} \tag{1.16}$$

as the luminosity emitted if all the kinetic energy of the accreting material is released at the primary surface, the disc luminosity results:

$$L_{\rm disc} = \frac{1}{2}L_{\rm acc} \tag{1.17}$$

therefore half of the gravitational energy is released while the gas stream spirals

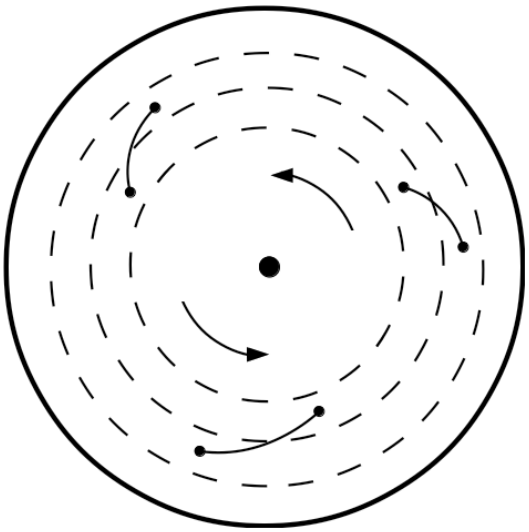

Figure 1.18: Schematic edge–on view of an accretion disc illustrating the Hawley–Balbus instability. Magnetic field lines connect blobs at different radii and are stretched by the differential rotation in the disc. The magnetic field results amplified creating turbulences that move blobs of material between different annuli and exchanges angular momentum through the disc. Figure adapted from Hellier (2001).

towards the primary, while the other half is available to be released close to the primary surface (Frank et al., 2002).

Accretion discs can be described as a series on concentric annuli, each one rotating with Keplerian velocity:

$$\Omega_{\rm K}(r) = \left(\frac{GM_1}{r^3}\right)^{1/2} \tag{1.18}$$

where r is the distance of each annulus from the primary. Equation 1.18 implies differential rotation inside the disc. During the rotation, each annulus slides past adjacent annuli but viscosity opposes to this motion creating friction. Consequently, outer annuli are sped up while inner annuli are slowed down and the viscosity allows angular momentum to flow through the disc. The viscosity acting in accretion discs originates from magnetic instabilities, also known as Hawley–Balbus instability (Hawley and Balbus, 1998). In fact, the gas in the accretion disc is ionised and therefore slightly magnetised and the magnetic field lines connect blobs of gas sitting at different radii. However, inner blobs move faster than the outers, thus they try to drag the outers while the outers pull them backward. Owing to their magnetic connection, the outer blobs are forced to move faster, thus they gain angular momentum and move outwards. On the contrary, inner blobs are slowed down, hence they lose angular momentum and move inwards (Figure 1.18). The field line are consequently even more stretched, translating into a stronger magnetic field that

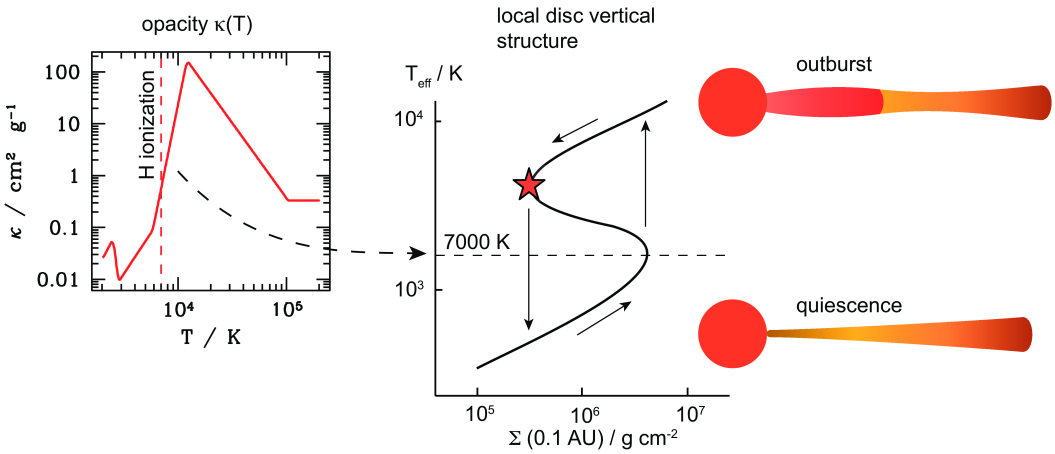

Figure 1.19: Schematic of dwarf nova outbursts. On the left, the dependency of the opacity is plotted as a function of the temperature. Once the hydrogen is fully ionised, the opacity stops growing with the temperature. On the right, the relationship between the disc surface density Σ and the temperature is shown. The arrows show the cycle followed by the disc during the outburst. Figure adapted from Armitage (2011).

efficiently moves blobs of gas at different radii and exchanges angular momentum through the disc.

1.5.3 Disc outbursts

CVs are characterised by periods of quiescence, in which the accretion onto the white dwarf is greatly reduced, interrupted by bright *outbursts*. These phenomena are thermal instabilities in the disc which cause a variation in the mass transfer rate through it (Osaki, 1974; Hameury et al., 1998; Meyer and Meyer-Hofmeister, 1984).

The origin of disc outbursts can be found in the strong dependency between the gas opacity (i.e. the capacity of its atoms to interact with photons) and its temperature. CVs in quiescence have cold discs which are mainly composed of neutral hydrogen. The low ionisation level determines also a weak coupling between the disc gas and the magnetic field, therefore the mechanism feeding the Hawley–Balbus instability (see Section 1.5.2) is strongly reduced resulting in a low viscosity. When the disc is heated up to $\simeq 7\,000\,\mathrm{K}$, hydrogen begins to be ionised. Compared to a neutral gas, a partially ionised gas has a higher opacity (left panel of Figure 1.19), and the opacity strongly depends on the temperature. With a higher opacity and more charged particles, the viscosity in the disc increases owing to the Hawley–Balbus instability. The increased viscosity traps the heat, rapidly resulting in the complete ionisation of the hydrogen (right panel of Figure 1.19). Once the hydrogen is fully ionised, the opacity is no longer sensitive to the variation in temperature and the disc settles in an equilibrium configuration with a much higher

temperature compared to the quiescent state. Given the high density and viscosity, the rate at which angular momentum is transferred trough the disc becomes faster than the rate at which matter is stripped from the secondary. Consequently the disc is drained of material, which is quickly accreted onto the white dwarf. The outburst ends when the density of the outer regions drops below a critical value (highlighted with a star in Figure 1.19), settling into a lower temperature and viscosity, where hydrogen is no longer ionised. This cooling wave spreads inward and then the disc returns to the viscosity and luminosity typical of its quiescent state.

During an outburst, CVs typically brighten by 2–5 magnitudes, occasionally up to 9 magnitudes (Warner 1995; Maza and Gonzalez 1983; Templeton 2007). This increase in luminosity occurs rapidly, on the time–scale of about a day, first at optical wavelengths and hours to a day later in the ultraviolet (Hassall et al. 1983; Schreiber et al. 2003, 2004). The outburst recurrence time ranges from weeks to decades and these events are unpredictable.

Typically, outbursts last a few days. However, in some CVs, outbursts lasting about two weeks to a month have been observed. These are slightly brighter than normal outbursts and are called *superoutbursts*. Moreover, lightcurves of low mass–ratio CVs during superoutbursts are characterised by periodic humps in brightness, typically of $0.2 - 0.3$ mag, called *superhumps*. The origin of these phenomena is a coupling between the thermal instability, which trigger the outburst, and the tidal interaction of the disc outer edge with the secondary (Osaki, 1996). During a superoutburst, the thermal instability determines an increase in the mass transfer rate and angular momentum transfer through the disc, resulting in its expansion up to a critical radius, above which the disc is tidally unstable for asymmetric perturbations (Osaki, 1989). As found by Whitehurst (1988), below a critical mass ratio value ($q < 0.25$), the outer edge of the disc is subject to tidal torques from the secondary thus the orbits deviate from a circular shape. This makes the disc elliptical and asymmetric with respect to the line connecting the centres of the two star. Thus the disc has a bulge pointing towards the secondary and located slightly ahead of it, since the disc outer edge orbits faster than the secondary. The orbits of the particles at the disc outer edge intercept each other and dissipate energy, thus making the disc brighter as the bulge pass close to the secondary, giving rise to the excess of light observed during the superhumps. Moreover, the tidal interaction between the bulge and the secondary makes the disc precessing with a superhump period ($P_{\rm SH}$) typically a few percent longer than the orbital one.

Since the appearance of superhumps is intimately connected to the system mass ratio, different studies have attempted to develop a method to determine q from $P_{\rm SH}$ using the period excess:

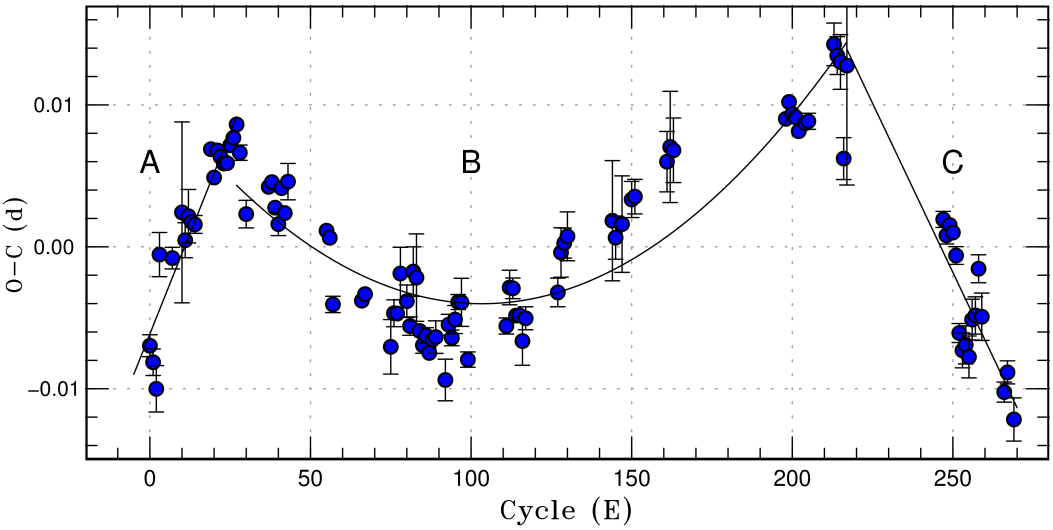

Figure 1.20: O–C diagram for the superhumps observed during the 2010 superoutburst of SW UMa, showing the three stages of superhump evolution. Figure adapted from Kato and Osaki (2013).

$$\epsilon = \frac{P_{\rm SH}}{P_{\rm orb}} - 1 \tag{1.19}$$

In order to estimate the mass ratio from the superhump period, an empirical calibration between ϵ and q is required (see for example Patterson et al. 2005b). From the study of a large sample of CVs in superoutburst, Kato et al. (2009) have identified three stages during the evolution of superhumps (Figure 1.20): (i) initially superhumps have the longest $P_{\rm SH}$ observed during the whole duration of the superoutburst (stage A); (ii) during a second phase, $P_{\rm SH}$ first drops slightly but then starts growing again (stage B); (iii) in the final phase $P_{\rm SH}$ results practically constant (stage C). Since $P_{\rm SH}$ varies during the superoutburst, the stage at which to apply the $\epsilon - q$ relationship is crucial to accurately determine q. Traditionally, $P_{\rm SH}$ determined during stage B is used to estimate q (Patterson et al., 2005b; Kato et al., 2009; Patterson, 2011).

However, Kato and Osaki (2013) have shown that using stage B superhumps systematically underestimate q for low mass ratio systems ($q \lesssim 0.09$), and argued that this is because the disc precession rate is not only determined by the secondary tidal torque but also by the pressure within the disc. The latter starts to become important at the transition from stage A to stage B superhumps, when an eccentric wave diffuses from the location of the tidal instability (i.e. the 3:1 resonance radius) into the inner region of the disc (Osaki and Kato, 2013). Therefore stage B superhumps are affected by the effect of the disc pressure which is difficult to quantify. Kato and Osaki (2013) proposed an alternative method to measure q from dynamical models of stage A superhumps, which occur before the precession is slowed by

the disc pressure (Pearson, 2006), finding:

$$q(\epsilon^*) = -0.0016 + 2.60(\epsilon^*) + 3.33(\epsilon^*)^2 + 79.0(\epsilon^*)^3; \tag{1.20}$$

where ϵ^* is the precession rate and is related to the period excess by the equation:

$$\epsilon^* = \frac{\epsilon}{1+\epsilon} = 1 - \frac{P_{\rm orb}}{P_{\rm SH}} \tag{1.21}$$

Equation 1.20 allow to measure the system mass ratio with a maximum uncertainty of 0.0004 in q, in the range $0.025 \leq q \leq 0.394$. The results of Kato and Osaki's method are in good agreement with independent q measurements from eclipse light curves and provide an accurate mass ratio determination. However, since stage A superhumps are observed only one or two days after the superoutburst beginning, it is crucial to obtain photometric observations in this time span in order to avoid underestimating q.

1.5.4 Nova eruptions

As their name suggests, CVs are not stable objects but often undergo dramatic events: some CVs have been observed to experience sudden increases in their brightness with amplitudes of $8 - 15$ magnitudes. These phenomena are called *classical nova explosions* and are thermonuclear explosions at the white dwarf surface. The material accreted on the white dwarf surface is compressed by the strong gravitational field in such a way that it is in an electron degenerate state. The continuous mass accretion leads to an increase of the temperature and pressure until the conditions for pp burning (Figure 1.2) are reached. With the onset of nuclear burning, the temperature rises but the accreted layer of material is degenerate and it does not expand accordingly. Therefore a runaway effect starts since the efficiency of nuclear reactions increases with rising temperature (the pp efficiency is proportional to $\sim T^4$), which in turn increases the rate at which hydrogen fuses. When the temperature exceeds $\simeq 2 \times 10^7$ K, nuclear reactions start to involve also carbon nuclei through the CNO cycle (Figure 1.3). This process is much more efficient ($\propto T^{18}$) and so the runaway speeds up with a very strong temperature dependence. The great energy input at the base of the accreted layer drives the layer into convective motion, which dredge up carbon from the core of the white dwarf to the surface, thus increasing the rate of the CNO burning. The runaway lasts until the temperature is high enough to allow the gas pressure to exceed the degeneracy pressure. Once the degeneracy is removed the accreted layer expands outwards at $\simeq 3000\,{\rm km\,s^{-1}}$, ejecting (part of) the accreted envelope.

1.5.5 CV classification

According to the morphology of their light curves, CVs can be classified in the following classes:

- *Recurrent novae*: these are CVs that are found to repeat their nova eruptions on time scales of years to decades.
- *Dwarf novae*: in these systems, periods of quiescence are interrupted by disc outbursts, whose recurrence time varies from days to decades, typically lasting from $\simeq 2 - 20$ days, correlated with the interval between outbursts. Subclasses of dwarf novae are: WZ Sge stars, in which only superoutbursts have been observsed; SU UMa stars, undergoing both normal disc outbursts and superoutbursts and U Gem, CVs experiencing only normal disc outbursts.
- *Nova-like variables*: this class of CVs is characterised by high mean accretion rates which keep the disc usually in a stable hot state, equivalent to a dwarf nova in permanent outburst. In this high state, the disc dominates the spectral appearance even in the far ultraviolet. However, occasionally the accretion rate drops (low state) and unveils the white dwarf (e.g. Gänsicke et al. 1999; Knigge et al. 2000; Hoard et al. 2004; Rodríguez-Gil et al. 2015).
- *Magnetic CVs*: in these systems the magnetic field of the primaries can disrupt the accretion disc. The accretion stream is conveyed onto the magnetic poles of the white dwarf by the field lines, releasing strong X–ray emission.

1.6 Testing the models of CV evolution

The disrupted magnetic braking scenario described in Section 1.4.1 is the most widely used model of CV evolution. It has been developed specifically to explain the existence of the period gap and the period minimum and, for a long time, remained practically untested.

CVs are typically identified based on their accretion luminosity, thus favouring the discovery of long–period systems, that are characterised by mass accretion rates of about one order of magnitude higher than those of short–period CVs. CVs are also identified thanks to their disc outbursts and this identification method disfavours the discovery of low mass transfer rate systems, which are expected to rarely, maybe never, experience outbursts. For many years, the detection of CVs has been therefore biased towards high luminosity and high mass accretion rate systems. A turning point in the history of CV discovery has been the advent of the Sloan Digital Sky Survey (SDSS, York et al. 2000). In the last decade, SDSS has led to the spectroscopic detection of several hundred CVs (Szkody et al., 2002a, 2003, 2004, 2005,

2006, 2007, 2009, 2011), most of which were selected as quasar candidates based on their unusual *ugriz* colours. As such, the SDSS CVs represent the first large and homogeneous sample reaching faint apparent magnitudes ($g \simeq 20$), without making use of the outburst properties of the systems.

From the study of the SDSS CV sample, two important theoretical predictions have been confirmed:

- the SDSS CV sample includes many eclipsing systems. From the study of the eclipse lightcurve of these CVs, Littlefair et al. (2006) have identified the first brown dwarf in a CV, confirming that secondary stars can survive the stellar to sub–stellar transition in accreting systems.

- The period minimum spike was predicted to exist but never detected in the period distribution of the known CVs. This is because CVs at the period minimum are characterised by low mass accretion rates and rarely outburst and are therefore intrinsically faint. Thanks to SDSS, many faint accreting white dwarfs have been discovered and, investigating the period distribution of the SDSS CV sample, Gänsicke et al. (2009) identified for the first time the period minimum spike at $P_{\rm orb} \simeq 80 - 86\,{\rm min}$.

Although in the last years many improvements in the observational technologies have led to important discoveries in the CV field and confirmed some theoretical predictions, it is also true that major discrepancies between the theory and the observations have emerged. In the following Sections, some of the most striking disagreements are described in detail since they provide the starting point of this study.

1.6.1 Angular momentum loss rates

The evolution of CVs is driven by AMLs which continuously shrink the system, keep the secondary in touch with its Roche lobe and set the mass accretion rate onto the white dwarf. Since different period ranges are characterised by different mass transfer rates (Figure 1.14 a), $P_{\rm orb}$ (one of the most easily measured system parameter in CVs) provides a first rough estimate of the accretion rate and the evolutionary stage of the system. A more precise measurement of the mean accretion rate can be derived from the white dwarf effective temperature ($T_{\rm eff}$): its value is set by compressional heating of the accreted material (Sion, 1995), providing a constraint on the secular mean of the mass accretion rate ($\langle \dot{M} \rangle$), averaged over the thermal time–scale of the white dwarf envelope (10^3 – 10^5 yr), and is one of the best available tests for the present models of CV evolution (Townsley and Bildsten, 2003).

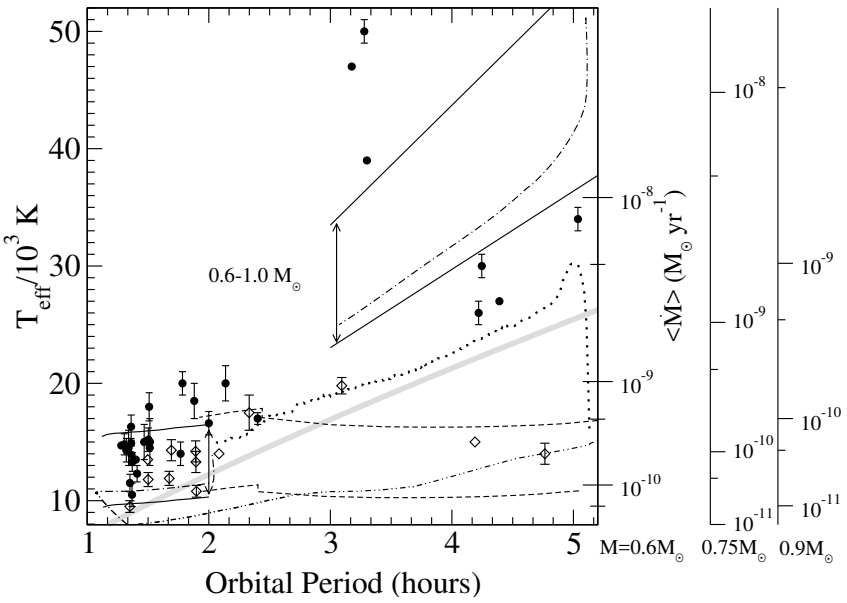

Figure 1.21: Effective temperatures of a sample of 43 CV white dwarfs (solid circles: non–magnetic systems, open diamonds: magnetic CVs). The unknown mass of the white dwarf dominates the uncertainties in the temperature determination (see Section 3.3.2). The empirical relationship from Patterson (1984) is shown in tick grey, along with some theoretical models: disrupted magnetic scenario (Howell et al. 2001; between solid lines, dot–dashed line), Andronov et al. (2003; dot–dot–dash line), Ivanova and Taam (2004; dotted line) and evolution under GWR only (between dashed lines). Figure from Townsley and Gänsicke (2009).

Townsley and Gänsicke (2009) carried out a first test of the present models of CV evolution by reviewing the available CV white dwarf effective temperatures (Figure 1.21) and their main findings can be summarised as follows:

- CVs below the period gap have typically $T_{\rm eff} \simeq 15\,000\,{\rm K}$ and are hotter than expected if their evolution was driven only by GWR;
- above the period gap, CVs are characterised by higher mass transfer rates than those below, in agreement with the disrupted magnetic braking scenario, although their $\langle \dot{M} \rangle$ result lower than theoretically predicted;
- the presence of the hot VY Scl stars at the upper edge of the period gap is not accounted for by the theory.

Given the small size of the CV sample available to Townsley and Gänsicke (2009), their results might be subject to some observational biases and the study of a larger sample is required in order to obtain better statistics and improve our understanding of CV evolution.

1.6.2 Masses

The evolution and the final fate of CV white dwarfs are, as for all types of accreting white dwarfs, of key interest in the framework of SNe Ia progenitors. Although early work showed the average mass of CV white dwarfs to lie in the range $\langle M_{\rm WD}\rangle \simeq 0.8 - 1.2\,{\rm M}_{\odot}$ (Warner, 1973; Ritter, 1987), higher than that of isolated white dwarfs $\langle M_{\rm WD}\rangle \simeq 0.6\,{\rm M}_{\odot}$ (Koester et al., 1979; Liebert et al., 2005; Kepler et al., 2007), historically CVs have not been considered as a major component of the SNe Ia progenitor population. This is because most models for classical novae (see Section 1.5.4) predict that not only most (if not all) of the accreted matter (Prialnik and Kovetz, 1995) but also some of the underlying core material (Epelstain et al., 2007) would be ejected during the eruption (as supported by the observed abundances of nova ejecta, Gehrz et al. 1998), preventing mass growth. Nevertheless, Zorotovic et al. (2011) showed that CV white dwarf masses are genuinely higher than both those of their detached progenitors and those of single white dwarfs, suggesting that CV white dwarfs may grow in mass.

The average mass of CV white dwarfs cannot be explained invoking a different parent populations for the present day CVs and isolated white dwarfs. In fact, the IFMR shown in Figure 1.6 implies progenitors of spectral type from mid to late B ($2\,{\rm M}_{\odot} \lesssim M \lesssim 6\,{\rm M}_{\odot}$) in the case of CVs ($\langle M_{\rm WD}\rangle = 0.83 \pm 0.23\,{\rm M}_{\odot}$), and from late A to late G ($0.7\,{\rm M}_{\odot} \lesssim M \lesssim 2\,{\rm M}_{\odot}$) for single white dwarfs ($\langle M_{\rm WD}\rangle = 0.603 \pm 0.134\,{\rm M}_{\odot}$). However, the distribution of these parent populations are in disagreement with the results of the current population synthesis models for the Galaxy, thus this hypothesis has to be ruled out. Finally, as Zorotovic et al. (2011) have shown, observational biases have also been ruled out, leaving the the debate on whether mass growth can occur or not still wide open.

Wijnen et al. (2015) investigated the effect on CV evolution of white dwarf mass growth either during nova cycles or through thermal time–scale mass transfer during the pre–CV phase, finding that this cannot explain the discrepancy between the mean masses of isolated and CV white dwarfs. Alternative explanations for the mass difference between isolated and CV white dwarfs are consequential angular momentum losses and asymmetric mass ejection during nova explosions described in Section 1.4.2. These could lead to dynamically unstable mass transfer in CVs hosting low–mass white dwarfs, which would not survive as semi–detached binaries but would merge into single objects (Schreiber et al., 2016; Nelemans et al., 2016). On the other hand, recent work on CV evolution support the mass growth idea (Goliasch and Nelson, 2015) and it has been shown (Hillman et al., 2016) that a quasi–steady helium burning after several nova cycles can lead a CV white dwarf to reach the Chandrasekhar limit. At present, none of these hypotheses have definitive arguments that could settle the debate on the possibility of mass growth

in CVs. Equally, stronger observational constraints on the properties of accreting white dwarfs are required. In particular, only $\simeq$ 50 CVs, out of over 1400 systems with measured orbital periods (Ritter and Kolb, 2003), have accurate mass determinations (largely based on the light curve analysis of eclipsing systems). It is therefore essential to increase the number of systems with an accurate mass measurement and diversify the method employed to measure those masses, in order to improve our understanding of the long–term evolution of CVs and investigate their potential role as SNe Ia progenitors.

1.6.3 Period distribution, space density and period bouncers

Other major discrepancies between theory and observations suggest that our understanding of CV evolution is actually incomplete:

1. the observed period minimum ($80 - 86$ min, Gänsicke et al. 2009) is about 10 minutes longer than the theoretically predicted ($\simeq 70 - 75$ min, Knigge et al. 2011; Goliasch and Nelson 2015; Kalomeni et al. 2016);

2. binary population synthesis models (de Kool, 1992; Kolb, 1993) predict a CV space density about 1–2 order of magnitude higher than observed (Patterson, 1998; Pretorius and Knigge, 2012);

3. between $\simeq 40\%$ (Goliasch and Nelson, 2015) and $\simeq 70\%$ (Kolb, 1993; Knigge et al., 2011) of the present Galactic CV population is expected to have evolved past the period minimum but, despite more than 40 years of extensive research on CVs and more than 1400 systems known (Ritter and Kolb, 2003), only a handful of period bouncer *candidates* have been identified so far (e.g. Patterson et al. 2005a; Unda-Sanzana et al. 2008; Littlefair et al. 2006; Patterson 2011; Kato et al. 2015, 2016; McAllister et al. 2017; Neustroev et al. 2017, and many others)

Interestingly, many discrepancies could be solved if additional AML mechanisms are taken into account in the model of CV evolution (Knigge et al., 2011). In fact, if angular momentum is removed more efficiently from the system, the secondary mass is eroded faster and the period minimum is reached at longer $P_{\rm orb}$. Moreover, the CAML described in Section 1.4.2 could also solve the space density disagreements: the CAML due to nova explosions (either in the Schreiber et al. 2016 or Nelemans et al. 2016 prescription) determines unstable mass transfer in systems containing low–mass white dwarfs. As a consequence, the two stellar components would merge and the system would disappear as CV. In this way, a smaller number of CVs is formed, lowering the theoretical space density.

Finally, the lack of period bouncers in the observed CV population could be explained by limitations in the detection methods followed so far. In fact, owing to their low mass transfer rates, period bouncers are expected to rarely, maybe never, experience outbursts, disabling the traditional identification method. Moreover, they are expected to be intrinsically faint ($V \simeq 20.5$ mag) and would be also of difficult detection in the SDSS footprint.

Given the fact that the physical mechanisms causing the additional AML at short periods are still not clear, finding the elusive population of the period bouncers becomes fundamental in order to carry out a critical test of the present models of CV evolution.

1.7 Thesis outline

In this Chapter, the theory of CV formation and evolution has been presented. Many predictions of the current models describing CV evolution are not confirmed by the observations and major discrepancies between theory and observations are currently present. These have major implications in many astrophysical fields and can potentially undermine our current understanding of more fundamental phenomena, such as SNe Ia which are important to probe the structure of the Universe on cosmological scales.

In this thesis, the results of a large observational effort aimed to investigate and solve these disagreements are presented. Observations have been carried out using the most advanced ground and space–based facilities, such as the Very Large Telescope (VLT) and the *Hubble Space Telescope* (*HST*). The observations, the data reduction and analysis techniques used in this work are described in Chapter 2. Chapter 3 presents the results of a large *HST* survey that doubled the size of the sample of CV white dwarfs for which an accurate temperature measurement is currently available. Two objects in this sample, SDSS J123813.73–033933.0 and QZ Lib, are studied in detail in Chapter 4 and Chapter 5, given the peculiarity observed in their lightcurves and spectra. One of the most striking result of the *HST* survey is the missed identification of the period bouncer CVs. Chapter 6 presents a new observing program aimed to unambiguously identify, for the first time, the missing population of period bouncers. Finally, the thesis conclusions and the plan for future work are presented in Chapter 7.

Chapter 2

Observations and Techniques

In this Chapter, the instruments and the methodology used throughout this work are presented. The first part introduces the astronomical detectors and their properties and a second Section presents the observations carried out to obtain the data analysed in this thesis. These are both spectroscopic and photometric and have been obtained using ground and space–based facilities. Finally, in the last Section, the data analysis techniques, which range from lightcurve extraction to statistical tools for spectral fitting, are described.

2.1 Astronomical detectors

2.1.1 Charge–Coupled Devices

In solid materials, electrons are organised in two bands, one of low energy (the valence band) and one of high energy (the conducting band) levels. The energy gap between these two bands defines the conductive properties of the material itself: in insulators the energy gap is large and electrons occupy the valence band and cannot access the conducting one. In contrast, in a conductor, the two bands may overlap and the electrons are free to move between them. In semiconductors, the size of the energy gap between the two bands is intermediate between that of conductors and insulators and an electron can move from the valence to the conduction band if sufficient energy is provided. This can be either in the form of thermal energy or of an incoming photon through the photoelectric effect.

The most commonly used detectors in astronomical observations are the charge–coupled devices (CCDs). These are wafers of semiconducting material electrically partitioned in small squares called pixels, each one of them acting as a potential well for the electric potential. When an incoming photon hits an electron in the CCD wafer, it provides the energy required for the electron to jump in the

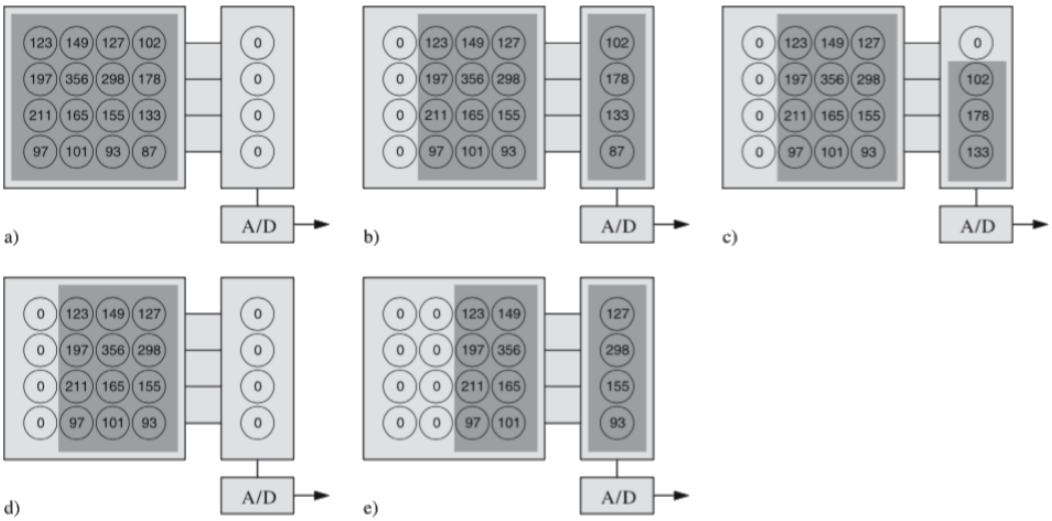

Figure 2.1: Readout process in a CCD camera. During the exposure, photons from the astronomical source free the electrons which are then trapped in the corresponding pixel (small circle) by the electric potential (**a**). The numbers in each pixel represent the number of electrons accumulated during the integration time. Once the exposure is finished, a voltage difference is applied in order to shift each column to the right (**b**). The column at the right edge of the CCD moves into the readout buffer. By applying another voltage difference, the charge in the readout buffer is shifted vertically, one pixel at the time, into the A/D converter (**c**), which converts the number of electrons into a digital signal that is sent to a computer. After the readout buffer has been read (**d**), each CCD column is again shifted one by one to the right (**e**). Another column is moved in the readout buffer and the process is repeated until all the columns have been read. Image from Karttunen et al. (2007).

conduction band. However, the electric potential well keeps the electron trapped in the pixel, where more electrons are freed and accumulated by the incoming flux of photons from the astronomical source. At the end of the exposure, the charge accumulated in each pixel is transferred to some amplifiers at the edge of the wafer and then read out.

CCDs are read by applying a series of cycling voltage differences in order to shift the charge pixel by pixel until it reaches the readout buffer. This process is called "charge coupling" and CCDs derive their name from it. From the readout buffer, each pixel is then transferred to an analog–to–digital (A/D) converter where the electrons are converted into digital numbers and the signal is sent to a computer (Figure 2.1).

The charge coupling process introduces a noise in the signal. This, together with the additional noise introduced by the A/D conversion, is called *readout noise*. The readout noise is related to the speed at which the detector is read: slow reading, i.e. slow transfer charge time in the column shifting process, reduces the noise while

faster reading increases it. However, the shifting charge process is overall fast and the readout time actually is limited by the A/D conversion, which typically requires $\simeq 20 - 100$ seconds. The CCD readout time is a limiting factor when observing rapidly variable targets, such as CVs, for which exposure times of the order of few tens of seconds might be required in order to catch the intrinsic system variability. Binning over adjacent pixels, that are then read together as one bigger pixel, allows to reduce the dead time of the CCD readout along with the readout noise and increases the time resolution achievable.

Before the advent of CCDs, the most commonly used detectors were photographic plates. These are films, usually composed of silver bromide, that form a negative image of the observed source when exposed to its light. Despite providing great advantages compared to the bare human eyes, such as allowing the detection of millions of faint objects and to permanently store the information, photographic plates present two major disadvantages. First, their efficiency, i.e. the number of photons detected over the overall incident flux, is extremely low ($\simeq 4\,\%$). Second, their response is non–linear, that is the density of the image observed on the plate does not increase linearly with the flux of incoming photons.

On the contrary, CCD cameras have nearly linear response, that is the number of electrons measured in the A/D is directly proportional to the number of incident photons, making their calibration quite straightforward. Furthermore their efficiency is high, of the order of $\simeq 80 - 90\%$. Thanks to these properties and becoming widely available, CCD cameras represents a turning point for modern observational astronomy.

2.1.2 Photomultipliers

CCD sensitivity usually peaks in the optical and extends in the near–infrared, so they are optimal for observations in the wavelength range $\lambda \simeq 3\,000 - 10\,000\,\text{Å}$. As described in the previous Chapter, the SED of CV white dwarfs peaks in the ultraviolet and, at these wavelength, the CCD sensitivity quickly decreases. Other types of detectors, such as photomultipliers, have higher sensitivity than CCDs in this wavelength range.

The basic elements of photomultipliers are photocathodes that, similarly to a CCD, work with the photoelectric effect. Photocathodes are made up of a negative (the cathode) and a positive (the anode) electrode. When a photon hits the cathode, the electron that is freed moves to the anode, giving rise to an electric current. This current provides a measurement of the incident photon flux. Photocathodes have a linear response with respect to the amount of incoming light and their efficiency peaks in the ultraviolet, with typical values of $\simeq 20 - 30\,\%$.

The electric current measured by a photocathode can be amplified by millions

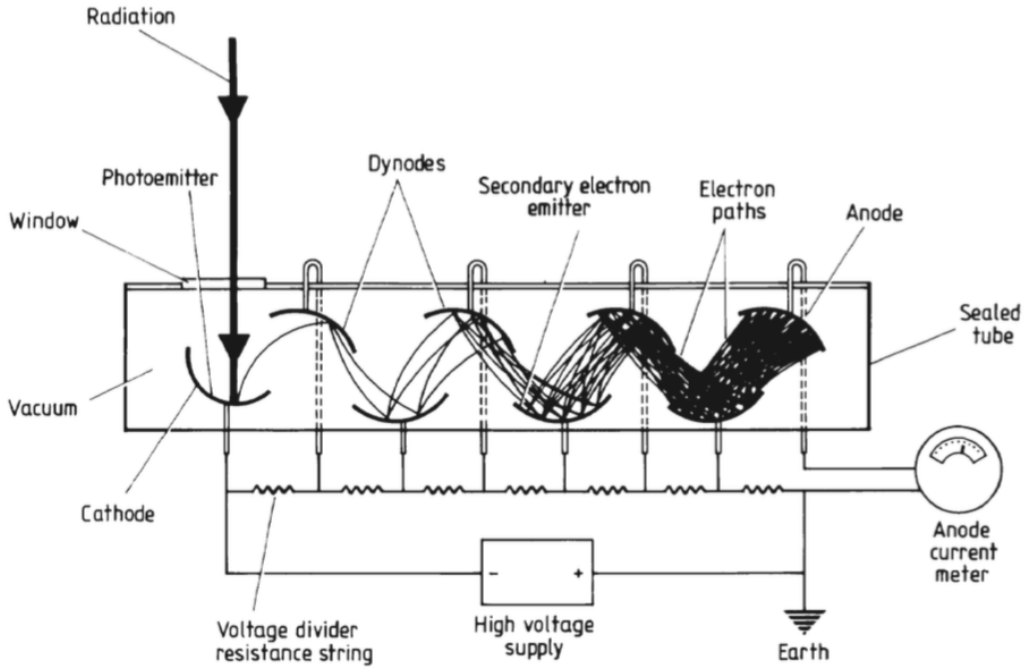

Figure 2.2: Schematic of a photomultiplier. Image from Kitchin (2013).

of times using photomultipliers. In these devices, the electron freed in the cathode is accelerated by an electric field and hits another electrode called dynode, where it frees more electrons. These hit another dynode and so on, giving rise to a chain reaction and amplifying the current generated by the incoming photon (Figure 2.2). Voltages of $\simeq 1\,500\,\mathrm{V}$ are typically used and the incoming photon can generate a pulse of about 10^8 electrons. By measuring the the amplitude of this pulse, a measure of the energy of the incoming photon from the astronomical source is obtained.

2.2 Spectroscopic observations

Spectroscopy is the study of the incoming flux of an astronomical source as a function of the wavelength and spectrographs are the instruments that spread the flux into its constituent colours. These instruments are located at focal plane of the telescope where the object of interest is selected using a slit or an aperture. The light is then collimated onto a disperser element (either a prism, a grating or a grism) which, by diffracting or reflecting the incoming light, separates it as a function of the wavelength. Then the dispersed light is focused on the detector, where the spectrum is recorded and read out (Figure 2.3).

Spectrographs in which the light is dispersed in two orthogonal directions using two dispersing elements are called échelle spectrographs. These instruments

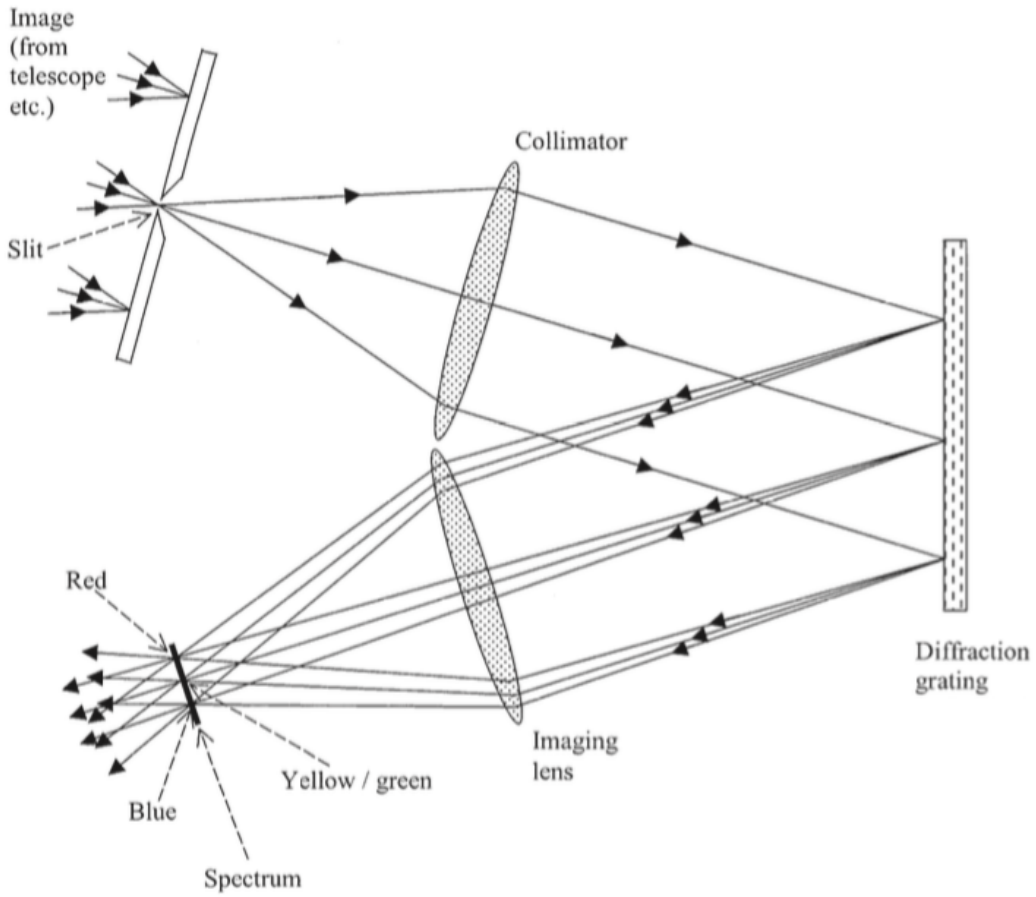

Figure 2.3: Schematic of a spectrograph: the light from the source enters through the slit and is collimated onto a dispersive element (a diffraction grating in this example), which spreads the light into its wavelength components. These are then focused onto the detector, where they are recorded. Image from Kitchin (2013).

work at high dispersion order and allow to achieve spectral resolutions of the order of $R = \lambda/\delta\lambda \simeq 10^4 - 10^5$.

This Section provides a description of the spectrographs used to collect the spectra analysed in this work, together with an overview of the data reduction techniques.

2.2.1 Cosmic Origin Spectrograph on the *Hubble Space Telescope*

The Cosmic Origin Spectrograph (COS, Green et al. 2012) is a slit–less spectrograph installed onboard the *Hubble Space Telescope* (*HST*) since May 2009. COS has two independent observing channels, the far–ultraviolet (FUV), covering the wavelength range $900 - 2\,150$ Å, and the near–ultraviolet (NUV), covering $1\,650 - 3\,200$ Å. The detectors of both channels are photon–counting photomultiplier devices (see Section 2.1.2) but they use different technologies in order to maximise the efficiency in

their corresponding wavelength range (Figure 2.4). The FUV detector is a photon–counting micro–channel plate while the NUV is a multi–anode multichannel array (MAMA).

The NUV and FUV detectors generate an electric current which is proportional to the incoming photon flux. However, the micro–channel plates can only work properly inside a safety range since an extremely high count rate can drastically reduce the quantum efficiency of the detector. In order to preserve the detectors from permanent damages, or even the total loss, the COS spectrograph is equipped with two entrance apertures of 2.5 arcsec in diameter. For most observations, the Principal Science Aperture (PSA) is used while bright objects exceeding the detector safety thresholds must be observed through the Bright Object Aperture (BOA), where a neutral density filter attenuates the incoming flux.

Moreover, before their approval, every COS observing program is checked to ensure that it meets the safety requirement. During the exposure, the global count rate is continuously monitored and the instrument is shut off if a violation is detected. Particular attention is paid to observing programs targeting variable objects. In this case the investigators must provide external monitoring the weeks before the *HST* observations are scheduled in order to demonstrate the safety of the observations.

The spectrograph is equipped with different gratings that allow both low ($R \simeq 3\,000$) and high resolution ($R \simeq 20\,000$) spectroscopic observations. The instrument offers two observing modes: in the TIME–TAG mode the position on the detector, the arrival time and the pulse height (only for the FUV channel) of each incoming photon are recorded, allowing the construction of the light curve of the observed object at a time resolution of 32 ms. In the ACCUM mode only the position on the detector is recorded.

The reduction of the COS data is performed through the automated pipeline CALCOS developed the Space Telescope Science Institute (STScI). Both the raw data and the final products can be retrieved from the *HST* archive[1].

2.2.2 Space Telescope Imaging Spectrograph on the *Hubble Space Telescope*

The Space Telescope Imaging Spectrograph (STIS, Woodgate et al. 1998) is a general purpose spectrograph installed onboard *HST* since February 1997. The instruments provides both spectroscopy and broadband imaging. Thanks to four bands, the spectral range from 1 000 Å up to 10 000 Å is covered and different instrument setups allow to perform low ($R \simeq 26$, using prisms) to high ($R \simeq 200\,000$, using échelle gratings) resolution spectroscopy.

[1] https://archive.stsci.edu/hst/search.php

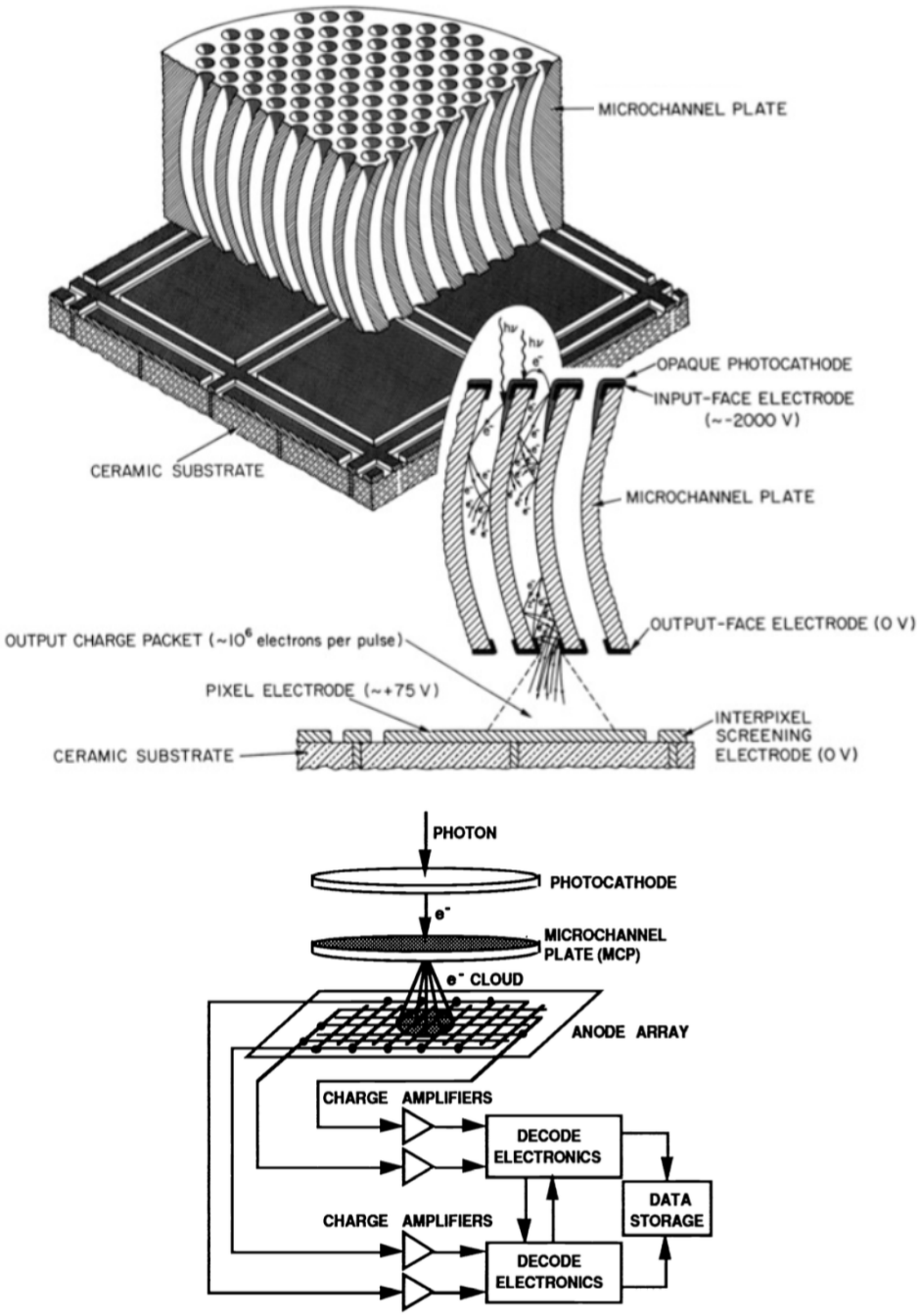

Figure 2.4: Schematic of the COS detectors. *Top*: photon–counting micro–channel plate. The incoming photon frees an electron from the photocathode. This is an opaque CsI electrode which has maximum sensitivity in the wavelength range $\lambda \simeq 1\,150-1\,750$ Å. Moreover, in order to maximise the sensitivity, the FUV detector is windowless. The electron is accelerated by a high voltage and, hitting the micro–channel walls, generate an avalanche of electrons. The pulse of current then reaches the anode where it is measured. Figure adapted from Timothy and Bybee (1977). *Bottom*: in contrast to the FUV detector, the NUV MAMA detector has a semi–transparent cesium telluride photocathode. It is also equipped with a magnesium fluoride window and it is sensitive in the range $\lambda \simeq 1\,150-3\,200$ Å. Once the electron hits the photocatode, the following avalanche of electrons reach an anode array and then it is read. Figure from Kasle and Morgan (1991).

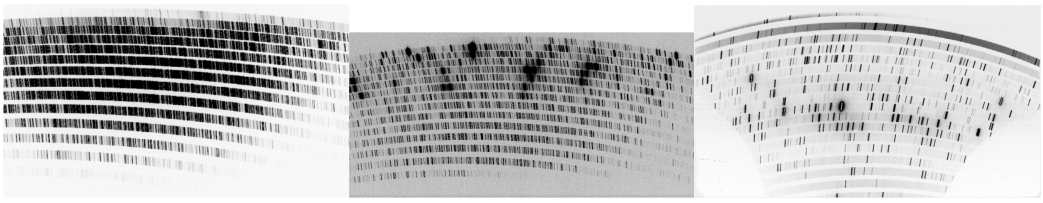

Figure 2.5: X–shooter spectral format for the UVB (left), VIS (middle) and NIR (right) arms from ThAr calibration frames. Image from Vernet et al. (2011).

STIS can perform both slit and aperture spectroscopy and allows the TIME–TAG and ACCUM observing modes.

The optical (VIS) and near–infrared (NIR) bands are equipped with two CCDs while the two ultraviolet bands (FUV and NUV) have two MAMA detectors. The NUV is a twin of the NUV COS detector. Similarly to COS, also the STIS ultraviolet detectors are subject to damages due to excessive illumination, and a bright object policy protection is followed as in the case of the COS observations.

The reduction of the STIS data is automatically performed at STScI with the pipeline CALSTIS and all STIS data (both the raw and the pipeline final products) can be retrieved from the *HST* archive.

2.2.3 X–shooter at the Very Large Telescope

X–shooter is an échelle medium resolution spectrograph ($R \simeq 5\,000 - 10\,000$) available at the Very Large Telescope (VLT) in Cerro Paranal (Chile, Vernet et al. 2011) since 2009. The instrument has been designed to cover in one exposure the wavelength range from $\simeq 3\,000$ Å up to $\simeq 25\,000$ Å. In order to do so, the instrument is equipped with three arms: blue (UVB, $\lambda \simeq 3\,000 - 5\,595$ Å), visual (VIS, $\lambda \simeq 5\,595 - 10\,240$ Å) and near–infrared (NIR, $\lambda \simeq 10\,240 - 24\,800$ Å). In each of these, the optics, the coatings, the dispersive elements and the detectors have been optimised to maximise the sensitivity in the corresponding wavelength range.

The UVB and VIS detectors are $2\,048 \times 4\,102$ 15 μm pixel CCDs. The NIR detector is a 2k × 2k 18 μm pixel CCD. The instrument offers different slits that allow different spectral resolutions. Moreover, broadband imaging is also possible with the Johnson and SDSS filters.

Thanks to two dichroics that separate first the UVB and VIS light and then the VIS and NIR light, each arm works independently from the others, with its own shutter and slit mask. The UVB and VIS arms are also equipped with two atmospheric dispersion correctors (ADCs). Unfortunately, due to mechanical problems, both ADCs were disabled on August 1st 2012. The observations reported in this work have all been obtained without the ADCs. To obviate this problem, the

observations have been carried out at the parallactic angle in order to minimise the effect of the atmospheric dispersion. Two new fully functioning ADCs have been installed on X–shooter since May 2017.

Thanks to its wide wavelength coverage X–shooter is the ideal instrument to observe CVs since, in one exposure, the white dwarf (dominating the UVB), the accretion disc (dominating the VIS) and the companion star (dominating the NIR) can be simultaneously observed, thus obtaining the whole spectral energy distribution of the system in one shot. Moreover, the large aperture of the VLT (8.2 m) allows to obtain signal–to–noise ratios (SNR) of the order of $\simeq 10$ for faint targets ($V \simeq 18$ mag) with short exposure times ($\simeq 5$ min), making X–shooter the perfect instrument to perform high time resolution spectroscopic observations of CVs.

X–shooter data reduction

The European Southern Observatory (ESO), the intergovernmental science and technology organisation that manages the VLT observatory, provides a pipeline to reduce the X–shooter data, which can be run through the workflow management tool Reflex (Freudling et al., 2013). The Reflex environment allows to organise the data and graphically visualise each reduction step. It also allows to repeat and customise selected steps in order to optimise the data reduction.

The X–shooter data reduction pipeline includes several steps, the most important of which are described in the following.

- *Master bias.* The readout noise introduces small fluctuation in the signal, due to the charge coupling process and the A/D conversion. Pixels with low counts could therefore be assigned negative numbers which would then require an additional bit to store the sign information. A bias level is added to every pixel in order to avoid negative counts. The bias level is estimated by taking a series of zero time exposures and averaging them. This *master bias* provides the signal due to the electronics. Alternatively, the bias level can be measured from the overscan regions, i.e. additional columns in the CCD that are not exposed to the source light, and are read out after the exposure is complete, also providing an estimate of the readout noise. These allow more accurate bias estimates since its level could vary during the night. The X–shooter pipeline estimates the bias level from the overscan regions since they provide usually more accurate results.

- *Master flat.* The CCD response is not uniform over all the detector but small pixel–to–pixel variations are present and need to be removed before any scientific data analysis. This is performed by constructing a *master flat* from

averaging several flat frames obtained from the exposure of an uniform source of light, usually a Tungsten lamp. However, these frames would also contain the spectral energy distribution of the lamp. In order to remove it, the flat frames are first averaged together and then collapsed along the spatial direction, thus obtaining a 1D spectrum of the lamp. This is then fitted with a polynomial function and finally the 2D flat frame is divided by the best–fit model, removing the spectral shape of the lamp and creating the *master flat* frame.

- *Master dark.* Electrons in the CCD follow a Maxwellian velocity distribution, therefore some of them will have the energy necessary to move from the valence to the conduction band. These electrons introduce additional noise in the signal which is called dark current. The dark current can be reduced by cooling the detector and thus reducing the number of electrons sitting in the tail of the Maxwellian distribution. All the X–shooter detectors are cooled with liquid nitrogen to temperatures of 153 K, 135 K and 105 K for the UVB, VIS and NIR respectively. Although cooling reduces the dark–current, its effect cannot be completely removed and the related noise needs to be estimated and corrected for. The level of the dark current for the UVB and VIS detectors is proportional to the exposure time, so dark frames are obtained with the shutter closed and exposure time that can be consequently scaled to match the science exposure time. For the NIR detector, the dark current is not linear with time, therefore dark frames have the same exposure time as the science frames. A *master dark* is then obtained averaging the dark frames together. Since the dark–current is basically negligible for the UVB and VIS detector ($< 0.2e^-$/pix/h and $< 1.1e^-$/pix/h respectively), the *master dark* is only created for the NIR detector.

- *Spectral format evaluation.* In this step, an initial guess for the wavelength calibration and the échelle order position on the CCD is computed using a physical model of the instrument and the environmental conditions at the moment of the science exposure (such as atmospheric temperature and pressure). The initial input for this computation is an image of an arc lamp obtained through one pinhole (left panel of Figure 2.6). A flat field obtained through one pinhole is then used to compute the centre of each order position (middle panel of Figure 2.6).

- *Wavelength calibration.* Échelle spectra are complex since the use of two dispersing elements creates strongly curved orders and determines a change in the slit height and width projection along the orders. Accurate wavelength calibration requires also accurate spatial scale calibration. The instrumental

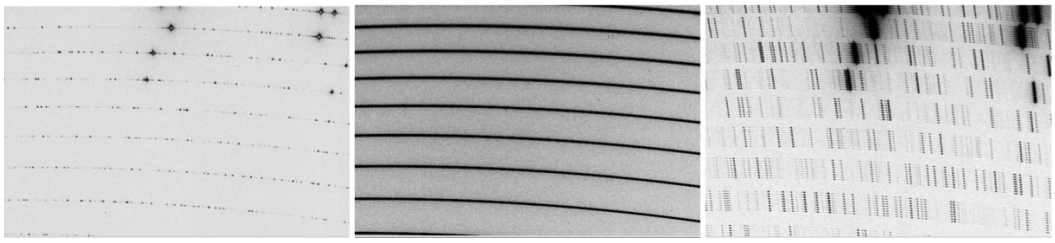

Figure 2.6: Sample sections (1 365 pix × 925 pix) of X–shooter calibration frames for the VIS arm. A single pinhole arc and a continuum frame used for the spectral format evaluation are shown in the left and middle panel respectively. On the right, a nine–pinhole arc frame used to create the 2D distortion map of the order is shown. Image from Vernet et al. (2011).

model defines the wavelength solution, i.e. the position X and Y of each pixel is a function of wavelength, order number and slit position in the form of Chebyshev polynomials. The initial guesses for this model are defined in the previous step. An image of an arc lamp is obtained through a mask of nine equidistant pinholes and is used to create a 2D distortion map of the orders (right panel of Figure 2.6). The instrumental model is fitted to the set of detected arc–lines in this 2D image, obtaining simultaneously the wavelength and spatial scale solutions, achieving an accuracy of better than $\simeq 2\,\mathrm{km/s}$ over the whole wavelength range.

- *Instrument response.* Determination of the instrument response requires the observation of a standard star, which is a star with a well modelled spectral energy distribution. Flux standards are often observed through a wide slit to minimise slit losses. The instrument response is computed by dividing a model of the standard star (in units of $\mathrm{erg\,cm^{-2}\,s^{-1}\,\AA^{-1}}$) by the observed spectrum of the standard star corrected for the exposure time, the atmospheric extinction and the detector gain.

- *Flux calibration.* The science spectrum is flux calibrated by firstly dividing the observed spectrum by the exposure time and the detector gain, and then multiplying this ratio by the instrument response. The calibrated spectrum is in units of $\mathrm{erg\,cm^{-2}\,s^{-1}\,\AA^{-1}}$.

- *Telluric line removal.* As a consequence of the interaction of the astronomical source light with the Earth's atmosphere, many absorption lines (mainly from OH and H_2O) are easily detectable in the X–shooter spectra. These lines are particularly strong in the NIR, where the water vapour in the atmosphere completely absorbs the stellar flux. Since the region affected by the telluric contamination contains stellar features (such as the Na doublet at $\simeq 8\,200\,\mathrm{\AA}$, or the K doublet at $\simeq 12\,450\,\mathrm{\AA}$), it is important to accurately remove this

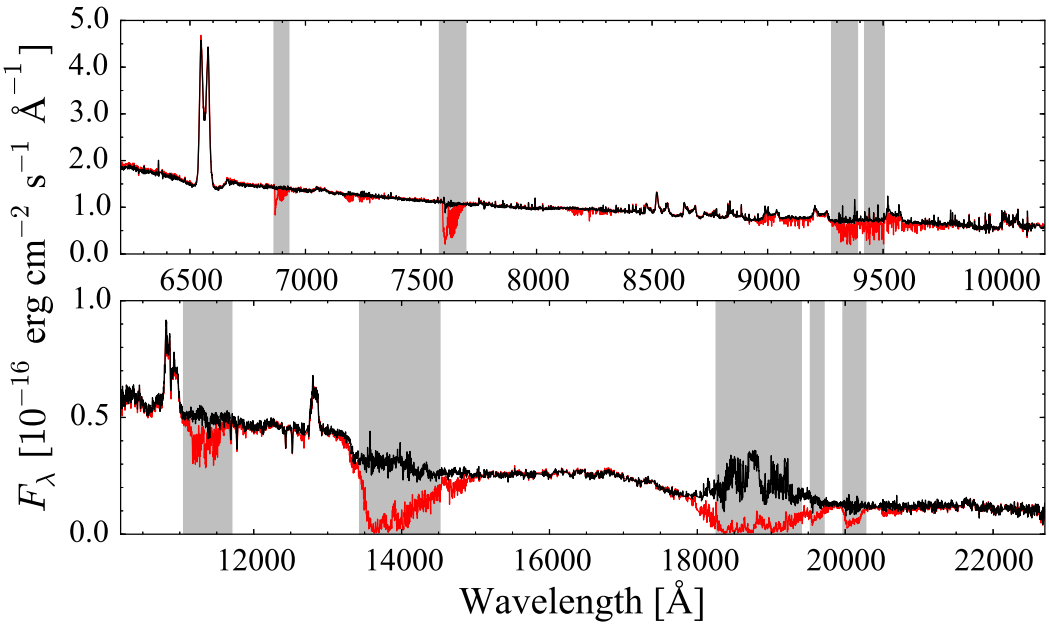

Figure 2.7: X–shooter VIS and NIR spectrum of the CV SDSS J123813.73–033932.9 showing the contamination from the telluric lines, highlighted with the grey bands, before (red) and after the correction with `molecfit` (black). The emission features at $\simeq$ 14 000 Å and $\simeq$ 19 000 Å are residuals from the correction of saturared telluric bands.

contamination from the science spectrum. The traditional approach to this problem is to observe a telluric standard, i.e. an early type star that is almost featureless (except for the hydrogen lines) and close on the sky to the science target. The telluric standard observation should be carried out close in time to the science observations to rule out temporal variation in the atmosphere. The continuum of the standard spectrum can be normalised with a spline fit or using a model spectrum. The obtained spectrum then contains only the telluric feature and, after a rescaling, can be used to remove the telluric line in the target spectrum. However, this method requires (i) to obtain high SNR spectra of the telluric standard to avoid adding noise to the science spectra, and (ii) the use of precious and costly telescope time that could be otherwise dedicated to other science observations. An alternative approach to this problem is offered by `molecfit` (Smette et al., 2015; Kausch et al., 2015), a tool developed at Institute for Astro– and Particle Physics at the University of Innsbruck in collaboration with ESO. This tool uses synthetic modelling of the Earth's atmospheric transmission to compute the most appropriate atmospheric profile at the time of the observation. `Molecfit` uses the atmospheric temperature, pressure and humidity as input parameters for a radiative transfer model, which also includes a comprehensive database of

parameters for the molecular species present in the Earth's atmosphere. After computing the best–fit model reproducing the observed telluric features, `molecfit` corrects the science spectrum for it (Figure 2.7). Thanks to this theoretical approach to the telluric absorption problem, `molecfit` allows to dedicate more telescope time to science observations. The telluric correction of all X–shooter data presented here has been performed with `molecfit`.

Wavelength shifts between arms

During the development of `molecfit`, the Austrian team reported the detection of a shift of one pixel in the predicted and observed wavelength position of the telluric lines. This shift was also detected in the sky lines and was later confirmed to partially arise from a misalignment between the target position in the acquisition image and the slit position. Although this misalignment has been fixed in October 2014, the data acquired since then still shows a residual shift[2]. This results in a systematic error in the wavelength calibration which can be corrected by using theoretical templates of sky emission lines to calculate the shift of each spectrum with respect of the expected position.

2.2.4 The ESO Faint Object Spectrograph and Camera 2

The ESO Faint Object Spectrograph and Camera 2 (EFOSC2) is a versatile instrument for photometric and low resolution spectroscopic observations, located at the ESO La Silla Observatory (Chile). The instrument offers different observing modes, including multi–object spectroscopy, polarimetry and coronography. In this work, EFOSC2 has been used to acquire long–slit spectroscopy and photometric observations.

EFOSC2 is equipped with a CCD Camera of $2\,048 \times 2\,048$ pixels, each one of size $15 \times 15\,\mu$m, and pixel scale $0.12''$/pixel. Spectroscopy was performed using the $1''$ slit along with the low (grism # 6, $R \simeq 500$) and the medium resolution (grism # 10, $R \simeq 1\,300$) grisms, which cover the wavelength range $\lambda \simeq 3\,860 - 8\,070$ Å and $\lambda \simeq 6\,280 - 8\,200$ Å, respectively. Grism # 6 suffers from second order contamination which reduces the actual useful wavelength range to $\lambda \simeq 3\,860 - 6\,280$ Å.

Photometric observations were acquired using the V–band filter. The observations and data reduction described in Chapter 5 have been carried out by Dr. Linda Schmidtobreick.

[2] A report on the wavelength shift can be found at https://www.eso.org/sci/facilities/paranal/instruments/xshooter/doc/XS_wlc_shift_150615.pdf

Table 2.1: Effective wavelengths and passbands for the filters in the Johnson system and the SDSS filters.

Johnson system			SDSS		
Filter	Effective wavelength (Å)	Band width (Å)	Filter	Effective wavelength (Å)	Band width (Å)
U	3663	650	u	3594.9	558.4
B	4361	890	g	4640.6	1158.4
V	5448	840	r	6122.3	1111.2
R	6407	1580	i	7439.5	1044.6
I	7980	1540	z	8897.1	1124.6

2.3 Photometric observations

Photometry is the measurement of the incoming flux from an astronomical source, which is given in magnitudes. The magnitude scale provides the relative flux of an astronomical object with respect to a reference star. Defining m_0 and F_0 as the magnitude and the flux of this reference star, the magnitude m of all the other objects of flux F is defined as:

$$m - m_0 = -2.5 \log_{10} \frac{F}{F_0} \tag{2.1}$$

Flux measurements, and therefore magnitudes, are usually obtained using filters, i.e. optical elements that transmit light in a certain wavelength range. In order to obtain an absolute flux measurement, the definition of a zero point, i.e. of a reference source, is necessary. Commonly used is the Vega system, where the reference object is the star Vega, which is assumed to have zero magnitude in all filters. In this magnitude system, one of the most commonly used filters are the Johnson filters (Table 2.1).

The SDSS filter system is also widely used, whose filters are characterised by wider wavelength passbands, covering the entire optical wavelength range (Table 2.1). In contrast to the Johnson system, the zero point of the SDSS filter is defined in the AB magnitude system, where a zero magnitude source is defined as having constant flux $F_\nu = 3631\,\mathrm{Jy}$ in all filters.

This Section provides a description of the photometric observations carried out in this work.

2.3.1 *Kepler*

The *Kepler* satellite is a 0.95 m aperture telescope with a $105\,\mathrm{deg}^2$ FoV in a Earth–trailing heliocentric orbit. *Kepler* was launched in March 2009 with the aim to

continuously observe single stars in the Cygnus–Lyra region in order to detect Earth analogues in the habitable zone (Borucki et al., 2010). In 2013 the failure of one reaction wheel determined the end of the *Kepler* mission. A solution to the problem was later found using the Solar radiation pressure to balance the spacecraft and the second *Kepler* mission, *K2*, began in March 2014. In this second mission, the pointing of the telescope is adjusted every $\simeq$ 80 days to find a new balance position and to prevent the Solar light entering the telescope, thus allowing about 4.5 different pointings (called campaigns) per year.

The *Kepler* detector is an array of 42 CCDs, each one of $2\,200 \times 1\,024$ pixels. The pixel size is $27 \times 27\,\mu$m and the pixel scale is $3.98''$/pixel. The instrument sensitivity is maximised in the wavelength range $\lambda \simeq 4\,184 - 9\,050$ Å. Two observing modes are offered: a short (1 min) and a long (30 min) cadence setting. *Kepler* observing capability is limited by the onboard storage therefore the data from only $\simeq 150\,000$ targets in the FoV that are brighter than $R \simeq 16$ mag are stored on the spacecraft and transmitted to the Earth once per month.

The data reduction of the *Kepler* data analysed in Chapter 4 has been carried out by Dr. Elmé Breedt.

2.3.2 TMO61, OC61 and PROMPT observations

The Tortugas Mountain Observatory 0.61m Telescope (TMO61) located in New Mexico, the Optical Craftsman 0.61m Telescope (OC61) located in New Zealand and the Panchromatic Robotic Optical Monitoring and Polarimetry Telescopes (PROMPT) located in Chile are small telescopes that provided the photometric observations reported in Chapter 3 and Chapter 4.

The TMO61 and the OC61 are AAVSONet Telescopes, i.e. a network of remote, robotically controlled, and automatically queued telescopes managed by the American Association of Variable Star Observers (AAVSO). Both these telescope have a diameter of 61 cm, equipped with two CCD cameras of size $3\,348 \times 2\,574$ and $3\,056 \times 3\,056$, and pixel sizes $5.4\,\mu\text{m} \times 5.4\,\mu$m and $12\,\mu\text{m} \times 12\,\mu$m, respectively. The observations were carried by Arne Henden, whose also took care of the data reduction.

The PROMPT–Chile telescopes consist of six 40 cm diameter robotic telescopes, built by the University of North Carolina (UNC) and managed by Skynet, a prioritized queue scheduling system developed at UNC. The detail of the CCD cameras can be found in the Skynet website[3]. After the observations, the user can retrieve the data already reduced from the database.

[3] https://skynet.unc.edu/

Table 2.2: Properties of the JAST CCD camera.

FoV	$1.4° \times 1.4°$
CCD format	$9\,216\,\text{pix} \times 9\,232\,\text{pix}$
Pixel size	$10\,\mu\text{m} \times 10\,\mu\text{m}$
Pixel scale	$0.55''$/pixel
Number or read modes	16
Redout time (# 5)	12 s
Readout noise (# 5)	$3.4\,e^-$ (RMS)
Minimum exposure time	0.1 s
Dark current	$0.00008\,e^-$/pixel/s
CCD operating temperature	$-100°$ C

2.3.3 JAST/T80Cam

The Javalambre Auxiliary Survey Telescope (JAST) is a 80 cm telescope located at the newly born Observatorio Astrofísico de Javalambre (Teruel, Spain, Cenarro et al. 2010), managed and constructed by the Centro de Estudios de Física del Cosmos de Aragón (CEFCA). JAST has a large FoV of 1.4 ° in diameter and its equipped with T80Cam, a large–format 9.2 k × 9.2 k pixel CCD camera that, at the time of its purchase (2011), was the largest CCD detector employed in astronomy.

The T80Cam CCD camera (Table 2.2) has pixels of 10 μm size and it is read simultaneously from 16 ports which allow different readout times, the shortest of which is 3 s, with typical readout noise of $\simeq 4\,e^-$ (RMS). The observations carried out in this work used the readout mode # 5, i.e. with 12 s readout time and $\simeq 3.4\,e^-$ (RMS) readout noise. Thanks to this characteristic and its large FoV, T80Cam is the ideal instrument to perform high–time resolution photometry on large areas of the sky. Moreover, T80Cam is equipped with a set of 12 filters (Table 2.3), some of them overlapping with the SDSS filters.

2.3.4 Small and Moderate Aperture Research Telescope System

The Small and Moderate Aperture Research Telescope System (SMARTS) are four telescopes of 1.5 m, 1.3 m, 1.0 m and 0.9 m aperture, located at Cerro Tololo Inter–American Observatory (CTIO, Chile).

The SMARTS observations reported in this work (Chapter 5) have been obtained using the 1.0 m telescope, which is equipped with a 4 064 × 4 064 pixel CCD camera. The camera FoV is $20' \times 20'$ with a pixel scale of $0.289''$/pixel.

The observations were acquired using the V band filter and both the observations and data reduction described in Chapter 5 have been carried out by Dr. Linda Schmidtobreick.

Table 2.3: Effective wavelengths passbands for the JAST/T80Cam filters.

Filter	Effective wavelength (Å)	Band width (Å)
uJAVA	3485	508
*J*0378	3785	168
*J*0395	3950	100
*J*0410	4100	200
*J*0430	4300	200
gSDSS	4803	1409
*J*0515	5150	200
rSDSS	6254	1388
*J*0660	6600	145
iSDSS	7668	1535
*J*0861	8610	400
zSDSS	9114	1409

2.4 Methods

2.4.1 Light curve extraction from TIME–TAG observations

The TIME–TAG observing mode offered by the *HST* UV spectrographs allows to record the time of arrival, the position on the detector and the pulse height of each detected event every 32 ms. It is therefore possible to reconstruct lightcurves from these time–resolved ultraviolet observations.

After the observations, the instrument pipelines generate a FITS[4] file, named CORRTAG, containing the time of arrival, the pulse height and the coordinates (physical and wavelength calibrated) on the detector of each photon. The coordinates are corrected for the Doppler shift due to the orbital spacecraft motion.

In Figure 2.8, an example of a CORRTAG frame is shown where each dot corresponds to a detected photon. The stellar spectrum is highlighted in red and corresponds to the band extending from the left (bluer wavelengths) to the right (redder wavelengths) in the middle of the detector. The bright spots visible on the stellar spectrum and highlighted in cyan correspond to the emission from the geo–coronal Lyα ($1\,206\,\text{Å} < \lambda < 1\,225\,\text{Å}$) and O I ($1\,297\,\text{Å} < \lambda < 1\,311\,\text{Å}$) lines. On the bottom, the geo–coronal Lyα is also visible through the BOA aperture (magenta), while the green band corresponds to the spectrum of the wavelength calibration lamp used by the CALCOS pipeline to calibrate the science spectrum.

The lightcurve extracted from CORRTAG files and used in this work have been

[4]Flexible Image Transport System (FITS) is a standardised digital format where data are stored as images of tables. An ASCII reader contains the information about the data summarised with keywords.

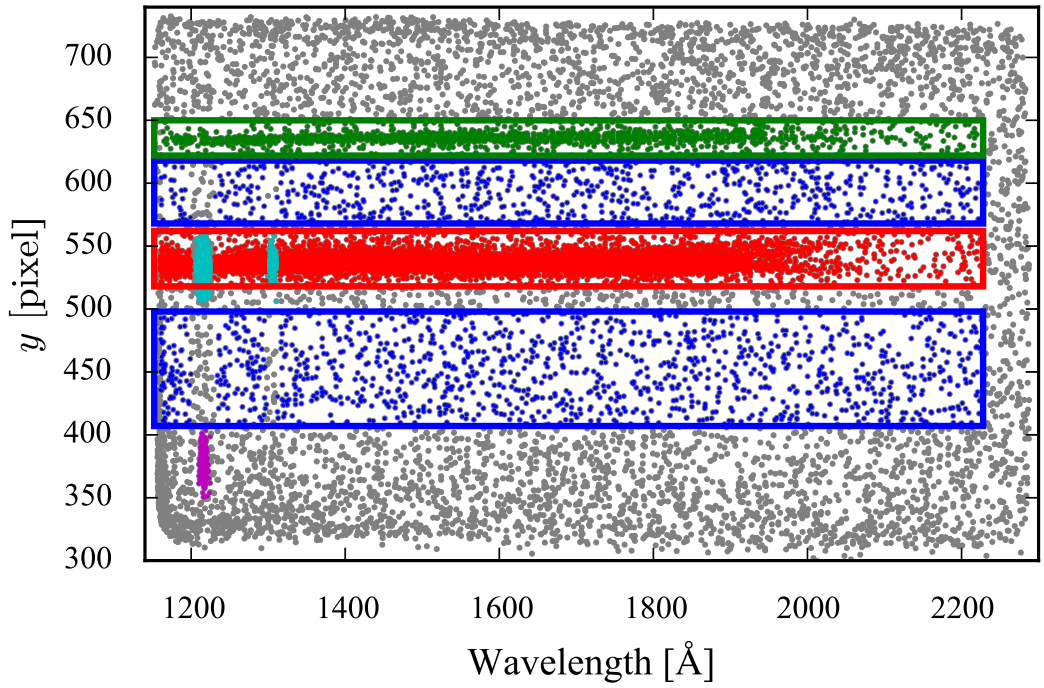

Figure 2.8: Example of a CORRTAG frame. The rectangles highlight the region on the detector from which the counts of the star (red) and the background (blue) are extracted. Shown in green is the position of the spectrum from the wavelength calibration lamp while the geocoronal emission lines from Lyα (1 216 Å) and O I (1 300 Å) are highlighted in cyan. These regions are excluded from the lightcurve extraction procedure. The detector is also receiving flux from the BOA, which is falling into a void region of the sky and therefore is only illuminated by the Lyα geocoronal emission line (magenta).

obtained following the subsequent procedure. First, three rectangular regions on the detector are identified: a central one enclosing the object spectrum and other two, one above and one below the spectrum, to measure the background. The geo–coronal emission lines from Lyα (1 206 Å $< \lambda <$ 1 225 Å) and O I (1 297 Å $< \lambda <$ 1 311 Å) and any emission from the accretion disc, not representative of the intrinsic variability of the underlying white dwarf, are masked. The data are binned into five second bins and the number of events in each rectangle is counted. This number is normalised by the bin size and the area of the rectangle. The number of counts of each bin corresponding to the stellar spectrum is then corrected for the number of counts from the background. Finally, this difference is multiplied by the area of the region enclosing the object spectrum. This returns the lightcurve of the target in counts per second.

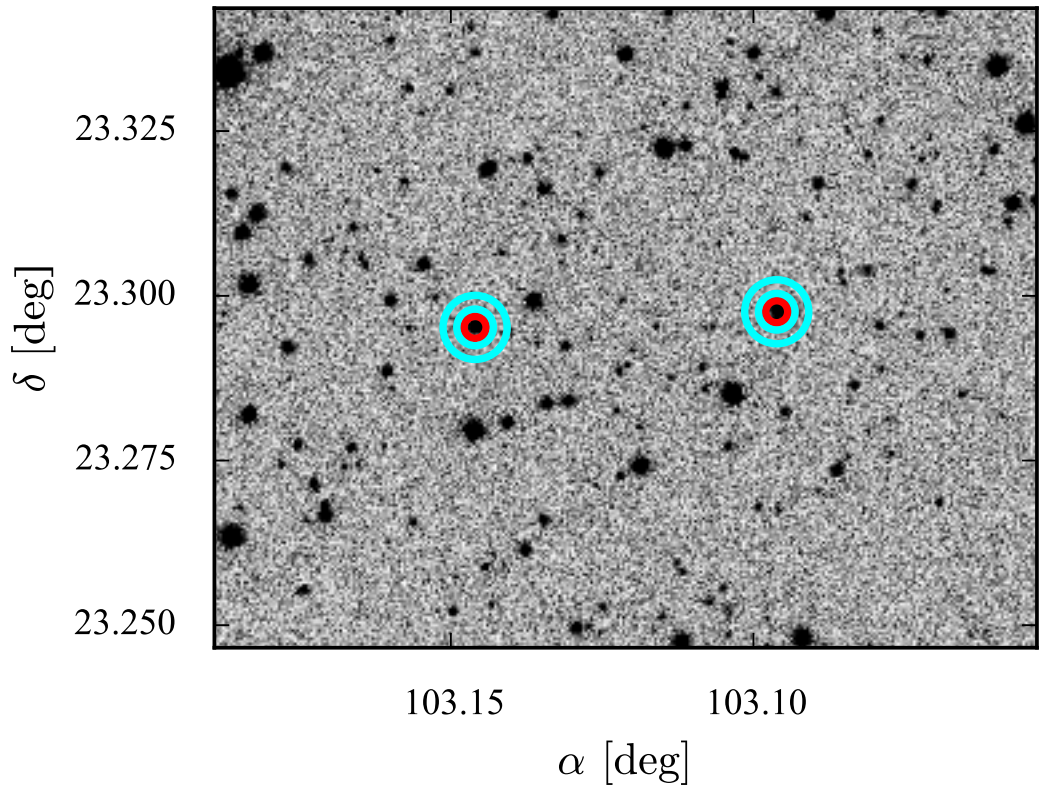

Figure 2.9: Section of a g band image from JAST/T80Cam. The science apertures (red) are shown for the target (left) and the reference star (right). The sky apertures are shown in cyan.

2.4.2 Aperture photometry

Aperture photometry is the standard way to extract the flux information from CCD photometric observations. This technique consists in selecting a small region on the detector enclosing the object of interest. A second region, usually a circular annulus centred on the target, identifies the pixels from which the background level is estimated. The total flux of the source is then obtained from the sum of the pixels in the star aperture after the median value of the background pixels has been subtracted (Figure 2.9).

The instrumental magnitude needs to be calibrated towards one of the standard magnitude systems in order to be used for a scientific analysis. To convert the instrumental magnitude into a physical magnitude, the same procedure described above is repeated for a reference star. This is a non–variable object of known magnitude and similar brightness to the target of interest. In order to minimise systematic effects, the same aperture sizes is used for both stars for the flux extraction. Once the instrumental magnitude of the reference star has been extracted, this is compared to the tabulated valued. The difference between the two returns the offset

that has to be applied to the target instrument magnitude to convert it into the chosen standard magnitude system. The calibration can be improved by including as many reference stars as possible. The offset is then determined from the median of the differences between the instrumental and tabulated magnitudes.

The choice of the size of the region enclosing the target is crucial: a big aperture will include more background pixels and will introduce bigger uncertainties related to the background subtraction. On the other hand, a small aperture will result in flux losses of the object of interest. A balance between these two extremes needs to be found and the optimal aperture size can be estimated trough an interactive procedure.

In this approach, a first extraction of the flux is performed with an aperture whose size is chosen by eye to meet the above requirements. From this first run, a source similar to the target (not necessarily a reference star) is chosen. This test object is used to study the variation of the SNR as a function of the aperture size. This test is not performed on the target because its intrinsic variability (e.g. eclipses) could affect the results. The flux extraction procedure is repeated on the test object several times with increasing aperture sizes. At the end, the optimal aperture size is found from the value that maximises the SNR.

Several packages are currently available and allow to perform this measurement automatically. In this thesis, aperture photometry has been performed using SExtractor (Bertin and Arnouts, 1996). This program requires as input the parameters characterising the CCD (such as gain, pixel scale and saturation level) and, after running a source detection algorithm, performs aperture photometry on each source present on the astronomical image. As output, SExtractor returns, for each one of them, the instrumental flux and magnitude.

2.4.3 Fitting routines

The fit of observed CV spectra with synthetic atmosphere models allows to determine important system parameters, such as distances, effective temperatures and stellar rotation rates. In statistic, this problem is called regression analysis and consists in determining a set of parameters of a function that best reproduces the data. Different methods and algorithms are available to perform this kind of analysis, in particular, in this thesis, the least squares minimisation and the Markov–Chain–Monte–Carlo (MCMC) methods have been used.

Least squares minimisation

Least squares minimisation has been performed using the Levenberg–Marquardt method implemented in the scipy.optimize.leastsq Python function. The Levenberg–Marquardt algorithm allows to find the minimum of a function, in this case the sum

of the squared weighted residuals between an observed CV spectrum and a synthetic spectral model. The algorithm is a combination of the steepest descent method and the Gauss–Newton method. In the steepest descent method, the minimum of a function is found by taking steeps in the direction of its negative gradient while the Gauss–Newton method performs the search for the minimum by locally linearising the function.

Levenberg–Marquardt algorithm uses the steepest descent to search for the minimum when the parameters are far from the optimal values and, once close to the minimum, it switches to Gauss–Newton method, which uses a linear search and thus has a fast convergence when close to the optimal solution.

Markov–Chain–Monte–Carlo (MCMC) method

Levenberg–Marquardt is based on matrix inversion and therefore, when the problem involves a large number of parameters, it can be slow and require large amounts of memory to store the matrices. Another limitation is that when the initial guess is close to a local minimum, the algorithm can get stuck in this position without finding a best–fit solution.

An alternative fitting procedure is the MCMC method. In this method, the parameter space is explored with random steps. The procedure requires an initial guess as starting point. In most cases, a good initialisation is using the best fit parameters from a previous least square minimisation run. Starting from the initial guess, the algorithm makes a random jump in the parameter space. The new position corresponds to a new set of parameters, which are either accepted or rejected according to their probability. This is computed as combination of a chi–square function and a prior probability obtained from external constraints to the problem. After an initial phase of burn–in, the newly drawn parameters result independent from the initial guess.

The MCMC method does not return a set of best–fit parameters but their posterior distribution, which can be used to estimate their mean values and standards deviations, thus providing also robust uncertainty estimates. The Python package EMCEE by Foreman-Mackey et al. (2013) has been used to implement the MCMC method in this work.

2.4.4 System parameters

Measuring white dwarf masses

Precise measurements of white dwarf masses allow to test the present models of CV evolution (see Section 1.6.2). There are different methods to measure masses of CV white dwarfs. When the accretion disc partially, or completely, outshines the white

dwarf at optical wavelengths, the mass of the white dwarf can be inferred from ultraviolet spectroscopy. If the distance d to the system is know, then the scaling factor S between the best–fit model H and the ultraviolet spectrum f :

$$S = \frac{f}{H} = \frac{R_{\rm WD}^2}{d^2} \tag{2.2}$$

returns the white dwarf radius $R_{\rm WD}$; by assuming a mass–radius relationship (Hamada and Salpeter, 1961) it is then possible to measure the mass of the white dwarf.

Another possibility is to study the reflex motion of the two stars around the common centre of mass. During their orbital motion, the white dwarf and the secondary get alternatively close to the observer. As a consequence of the Doppler effect, this motion can be observed in the stellar spectra as a periodical redshift and blueshift of the lines (Figure 2.10).

The shift of the observed wavelength $\lambda_{\rm obs}$ with respect to the rest wavelength λ_0, provides a measurement of the velocity of the star along the line of sight, the so–called radial velocity:

$$V = c\left(\frac{\lambda_{\rm obs} - \lambda_0}{\lambda_0}\right) \tag{2.3}$$

where c is the speed of light. This shift can be directly measured from the stellar spectra by fitting the absorption features with a combination of a polynomial accounting for the continuum and a Gaussian, which returns both the central wavelength $\lambda_{\rm obs}$ and the line broadening.

From phase–resolved spectroscopic observations, the radial velocity curve of the system can be reconstructed. In a circular orbit, the radial velocity varies in a sinusoidal way during one orbital cycle:

$$V = \gamma + K\sin[2\pi(\phi - \phi_0)] \tag{2.4}$$

where γ is the systemic velocity, K is the velocity amplitude, ϕ is the orbital phase and ϕ_0 is the zero point of the ephemeris. Spectroscopic observation in which absorption lines from both the primary and the secondary are detectable allow to measure the radial velocity amplitudes of both stars, K_1 and K_2, and the systemic velocity γ. In CVs, the Mg II line at 4 481 Å is usually used for the white dwarf, while the Na I line at 8 200 Å or the K I lines near 1.2 μm are used for the secondary.

Figure 2.11 shows a sketch of the radial velocities of the two stars in a CV. The purple and blue curves represent this variation for, respectively, the donor and the more massive white dwarf. These sinusoids are not centred on zero but are shifted by the velocity of the system with respect to the observer (the systemic velocity γ). The emission from the white dwarf is in addition gravitationally redshifted. Therefore the difference between the γ velocities of the two stellar compo-

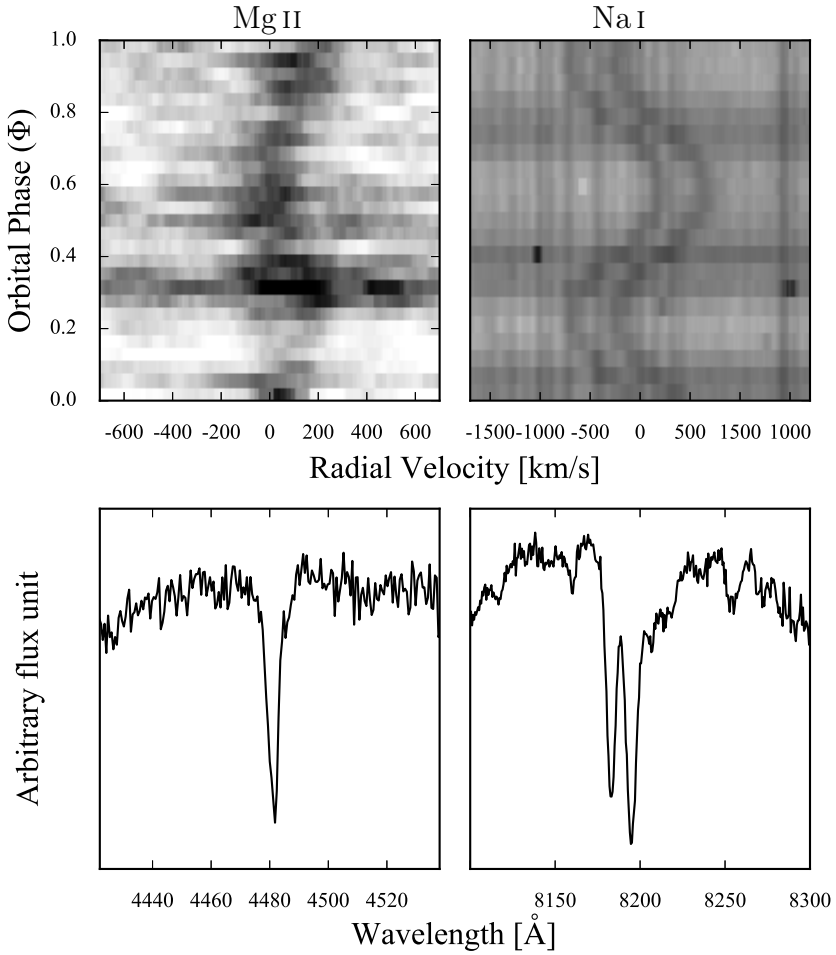

Figure 2.10: X–shooter trailed spectra for the CV IR Com (top) showing the alternating redshift and blueshift of the absorption lines of the primary (Mg II line at 4 481 Å, left) and the seconday (Na I doublet at 8 200 Å, right) as the two stars orbit around the common centre of mass. The line profiles in the rest reference frame are shown in the bottom panels.

nents (black arrow) returns the white dwarf gravitational redshift, $v_{\rm grav}$(WD), which is a direct measurement of its surface gravity and is defined as follow (Greenstein and Trimble, 1967):

$$v_{\rm grav}({\rm WD}) = \gamma_{\rm WD} - \gamma_{\rm donor} - v_{\rm grav}({\rm donor}) = 0.635\,\frac{M_{\rm WD}}{M_\odot}\,\frac{R_\odot}{R_{\rm WD}}\,{\rm km\,s^{-1}} \qquad (2.5)$$

and, assuming a mass–radius relationship, it provides a direct measurement of the white dwarf mass. At the surface of both the white dwarf and the secondary, a contribution from the gravitational field of the companion is present. Since the secondary is a low mass object (typically $M_{\rm donor} \lesssim 0.7\,{\rm M}_\odot$), its effect on the white

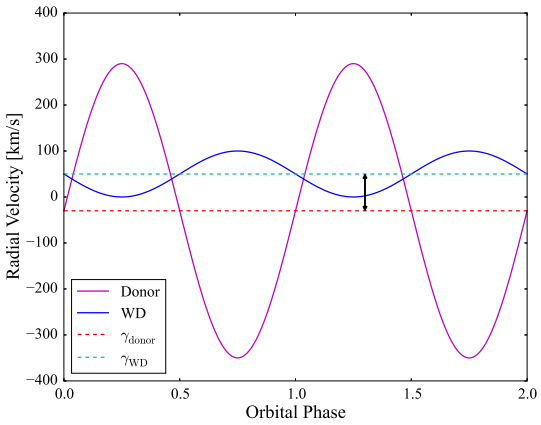

Figure 2.11: Sketch of the donor (purple) and white dwarf (blue) radial velocity variations, as the two stars orbit around the common centre of mass. The two curves are shifted from zero according to the velocity of the system with respect to the observer. In the case of the white dwarf, this shift includes in addition the gravitational redshift. The difference between $\gamma_{\rm donor}$ and $\gamma_{\rm WD}$ returns the gravitational redshift of the white dwarf (black arrow), and is a direct measurement of its surface gravity.

dwarf gravitational redshift results $v_{\rm grav}({\rm donor}) \lesssim 1\,{\rm km s^{-1}}$, and is of the same order of the contribution of the gravitational field of a typical CV white dwarf ($M_{\rm WD} \simeq 0.8\,{\rm M_\odot}$) at the secondary surface. Both these effects are negligible compared to the typical uncertainties ($\sim 5-10\,{\rm km s^{-1}}$) on $v_{\rm grav}({\rm WD})$ and can be ignored.

Additional system parameters

If the secondary is tidally locked, the equatorial radial velocity:

$$v_2 \sin i = \frac{2\pi R_2}{P_{\rm orb}} \sin i \tag{2.6}$$

can be determined from the rotational broadening of the absorption lines in its spectrum. In CVs, the secondary is filling its Roche–lobe therefore its radius R_2 equals the Roche–radius, which is a function of only q and a (Equation 1.4). Combining Equation 2.6 with the *mass functions*:

$$\frac{(M_{\rm donor} \sin i)^3}{(M_{\rm WD}+M_{\rm donor})^2} = \frac{P_{\rm orb}K_1^3}{2\pi G} \qquad \frac{(M_{\rm WD} \sin i)^3}{(M_{\rm WD}+M_{\rm donor})^2} = \frac{P_{\rm orb}K_2^3}{2\pi G} \tag{2.7}$$

also the system inclination i can be determined.

Finally, from the knowledge of both K_1 and K_2, the mass ratio can be determined with the following relation which directly descends from Equation 2.7:

$$\frac{K_1}{K_2} = \frac{M_{\rm donor}}{M_{\rm WD}} = q \tag{2.8}$$

2.5 Summary

This Chapter provided an overview of the astronomical detectors and instruments used to carry out the observations presented in this work. The last part of the Chapter was dedicated to outline the data analysis techniques used through this thesis. The following Chapters present an application of these techniques which allow to accurately determine the physical parameters of several CVs, thus carrying out a crucial test of the present model of CV evolution.

Chapter 3

Effective Temperatures and Masses of CV White Dwarfs

3.1 Introduction

The currently available observations confirm a number of predictions of binary evolution theory, such as the different mechanisms of angular momentum loss driving CV evolution at long and short orbital periods (Townsley and Gänsicke, 2009). However, there are a number of discrepancies between current population models and observations that undermine our confidence in the models of compact binary evolution and formation.

While there are now over 1 400 CVs with an orbital period determination (Ritter and Kolb, 2003), comparatively little is known about their accreting white dwarfs: reliable[1] $T_{\rm eff}$ measurements are available for only 43 CV white dwarfs (Townsley and Gänsicke, 2009), only $\simeq$ 50 have an accurate mass determination (Zorotovic et al., 2011) and only 11 have both. To improve our knowledge of CV evolution, it is essential to increase the number of objects with an accurate $T_{\rm eff}$ and mass measurement.

The SED of CV white dwarfs peaks in the ultraviolet and, at these wavelengths, the contamination from the accretion flow and the secondary star is often small or negligible compared to their contribution at optical wavelengths (Section 1.5.1). Therefore space–based ultraviolet observations are necessary for a white dwarf $T_{\rm eff}$ determination (Szkody et al. 2002c; Gänsicke et al. 2006; Sion et al. 2008 and many others). For this purpose, we carried out a large *Hubble Space Telescope*

[1] A temperature measurement is defined reliable when the white dwarf can be unambiguously detected either in the ultraviolet spectrum (from a broad Lyα absorption profile and, possibly, sharp absorption metal lines) or if its ingress and egress can be seen in eclipse light curves.

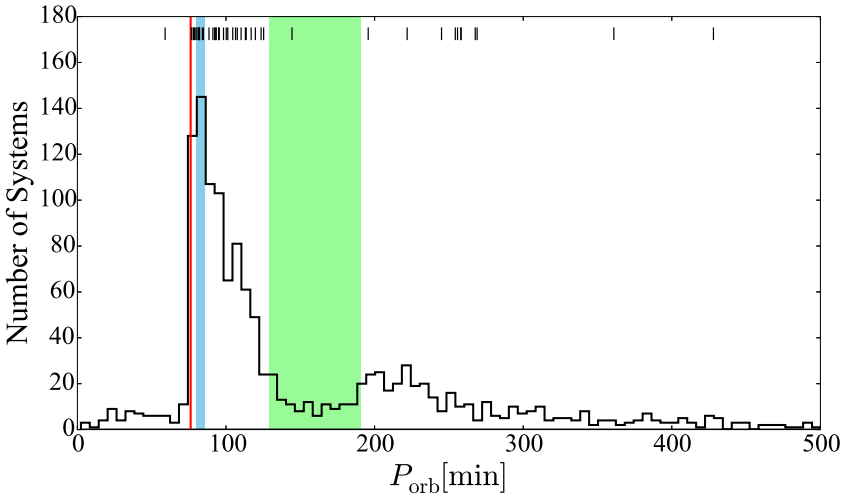

Figure 3.1: The orbital period distribution from Figure 1.13 is repeated here to highlight the orbital period sampling of the *HST* observing programs, with the vertical lines along the top marking the orbital periods of the objects included in the survey.

(*HST*) program in which we obtained high–resolution ultraviolet spectroscopic observations of 40 CVs with COS (Section 2.2.1) and this sample was complemented with eight systems (three of which are in common with the COS sample) observed during two programs carried out with STIS (Section 2.2.2).

The targets were selected to sample the entire orbital period range of the galactic CV population (Figure 3.1). Moreover, in order to ensure that the white dwarf would dominate the emission in the ultraviolet, the targets were selected among CVs in which the white dwarf and/or the secondary are discernable at optical wavelengths (implying a relative low contamination from the accretion flow) and that are bright enough to be observed within a reasonable number of spacecraft orbits (2–5). Four objects with previous $T_{\rm eff}$ measurements were included for comparison with our results (CU Vel, DV UMa, GW Lib and SDSS J103533.02+055158). In particular, we selected two eclipsing systems (DV UMa and SDSS J103533.02+055158) to compare our spectroscopic analysis with results obtained from modelling the eclipse light curve (e.g. Feline et al. 2004; Littlefair et al. 2006, 2008), which is the most commonly used method for determining white dwarf $T_{\rm eff}$ from ground based observations.

The ultraviolet spectroscopic observations for these 45 CVs are presented in this Chapter. For 36 of them, the white dwarf is recognisable through its broad Lyα absorption profile and we measure the white dwarf $T_{\rm eff}$ by fitting the *HST* data assuming $\log g = 8.35$, which corresponds to the average mass for CV white dwarfs ($\simeq 0.8\,{\rm M}_{\odot}$). Our results nearly double the number of CV white dwarfs with an accurate temperature measurement, providing a direct measurement of $\langle \dot{M} \rangle$ and testing the present day CV population evolution models.

Finally, the mass retention efficiency is a key question in both the theoretical and observational study of accreting white dwarfs in interacting binaries, with important implications for their potential as progenitors for SNe Ia (see Section 1.6.2). In order to increase the number of systems with an accurate mass measurement and diversify the method employed to measure those masses, we have obtained phase–resolved observations of 23 CV white dwarfs in the *HST* sample that are visible from the southern hemisphere with the X–shooter spectrograph located at the VLT. From radial velocity measurements of the white dwarf and its companion star, we can dynamically measure the white dwarf mass with an accuracy $\simeq 5$ per cent ($\simeq 0.05\,M_{\odot}$), carrying out a strong statistical test of the mass erosion versus mass growth hypotheses. Here, we report on the first results of this observing program, presenting the masses for four CVs in our sample. Furthermore, next year, the ESA (European Space Agency) *Gaia* mission will provide accurate parallaxes in the second data release DR2 for all the targets in the *HST* sample. From the knowledge of the temperature and the distance, the white dwarf mass can then be estimated assuming a mass–radius relationship and we here present a simulation on the accuracy of the white dwarf masses that these observations will allow to achieve.

3.2 Observations

3.2.1 COS observations

The COS data were collected in 122 *HST* orbits from October 2012 to March 2014 (program ID 12870, Table 3.1). Each CV was observed using the PSA for two to five consecutive spacecraft orbits. The data from all the orbits were summed to produce an average ultraviolet spectrum for each object. We used the G140L grating, which has a nominal resolution of $R \simeq 3\,000$, at the central wavelength of 1 105 Å and the FUV channel, covering the wavelength range $1\,105 - 2\,253$ Å. The detector sensitivity quickly decreases in the red portion of the spectrum, reducing the useful range to $\simeq 1\,150 - 1\,730$ Å.

The COS FUV detector consists of a photon–counting micro–channel plate which converts the incoming photons into electronic pulses. An excessive photon flux could result in permanent damages, and even the loss, of the detector (see Section 2.2.1). This is very important in the framework of CV observations since during dwarf nova outbursts (Section 1.5.3) CVs can easily reach, and exceed, the COS detector safety threshold. To avoid damage to the detectors an intensive monitoring of each target was required before the observations. This monitoring program was carried out by the global amateur community and some additional small telescopes (AAVSO, PROMPT and many others), and only their outstanding support has made this *HST* survey possible.

Table 3.1: Log of the *HST*/COS observations. The systems are ordered by orbital period. The V–band magnitudes listed here are the quiescent values reported from the literature and do not represent the brightness during the COS observations (see Figures 3.3 and 3.4).

System	$P_{\rm orb}$ (min)	Type	V (mag)	$E(B-V)$ (mag)	Observation date (DD/MM/YY)	Number of orbits	Total exposure time (s)	State
V485 Cen*	59.03	SU UMa	17.7	0.071^a	16/03/13	4	9907	*q*
GW Lib*	76.78	WZ Sge	16.5	0.03^b	30/05/13	3	7417	*q*
SDSS J143544.02+233638.7*	78.00	WZ Sge?	18.2	0.029^a	09/03/13	3	7123	*q*
OT J213806.6+261957*	78.10	WZ Sge	16.1	0.063^a	25/07/13	2	4760	*q*
SDSS J013701.06–091234.8*	79.71	SU UMa	18.7	0.024^c	13/09/13	4	10505	*q*
SDSS J123813.73–033932.9*	80.52	WZ Sge	17.8	0.006^c	01/03/13	3	7183	*q*
PU CMa	81.63	SU UMa	16.2	0.09^a	22/03/13	2	4757	*eq*
V1108 Her*	81.87	WZ Sge	17.7	0.025^c	06/06/13	3	7327	*q*
ASAS J002511+1217.2*	82.00	WZ Sge	17.5	0.025^c	15/11/12	3	7183	*q*
SDSS J103533.02+055158.4*	82.22	WZ Sge?	18.8	0.009^c	08/03/13	5	12282	*q*
CC Scl*	84.10	DN/IP	17.0	0.013^a	29/06/13	2	4668	*q*
SDSS J075507.70+143547.6*	84.76	WZ Sge?	18.2	0.028^a	14/12/12	3	7183	*q*
1RXS J105010.8–140431*	88.56	WZ Sge	17.0	0.018^c	10/05/13	3	7363	*q*
MR UMa	91.17	SU UMa	16.7	0.02^a	04/04/13	2	4401	*q*
QZ Lib*	92.36	WZ Sge	17.5	0.054^c	26/04/13	3	7512	*q*
SDSS J153817.35+512338.0	93.11	CV	18.6	0.012^a	16/05/13	2	4704	*q*
1RXS J023238.8–371812*	95.04	WZ Sge	18.8	0.027^a	01/11/12	5	12556	*q*
SDSS J093249.57+472523.0	95.48	DN?	17.9	0.014^a	11/01/13	2	4326	*eq*
BB Ari*	101.20	SU UMa	17.9	0.105^a	27/09/13	2	4817	*q*
DT Oct	104.54	SU UMa	16.5	0.145^a	20/05/13	2	4875	*eq*
IY UMa	106.43	SU UMa	18.4	0.012^c	30/03/13	2	4195	*q*
SDSS J100515.38+191107.9*	107.60	SU UMa	18.2	0.025^a	31/01/13	3	7093	*q*
RZ Leo*	110.17	WZ Sge	19.2	0.029^c	11/04/13	4	10505	*q*
CU Vel*	113.04	SU UMa	17.0	$< 0.02^d$	18/01/13	2	4634	*q*
AX For*	113.04	SU UMa	18.5	0.027^c	11/07/13	3	7483	*q*
SDSS J164248.52+134751.4*	113.60	DN	18.6	0.063^a	12/10/12	3	7240	*eq*
QZ Ser	119.75	SU UMa	17.9	0.038^c	21/06/13	4	10505	*q*
IR Com*	125.34	DN	18.0	0.016^c	08/02/13	3	6866	*q*
SDSS J001153.08–064739.2*	144.40	U Gem	17.8	0.029^a	09/11/12	5	12601	*q*
OR And	195.70	VY Scl	18.2	0.158^a	10/07/13	3	7361	*hs*
BB Dor	221.90	VY Scl	18.0	0.03^a	13/02/13	3	7272	*is*
SDSS J040714.78–064425.1*	245.04	U Gem	17.8	0.08^a	24/01/13	2	4315	*q*
CW Mon	254.30	U Gem	16.8	0.044^c	30/11/12	2	4774	*eq*
V405 Peg	255.81	CV	18.2	0.064^c	07/12/12	3	7303	*eq*
HS 2214+2845	258.02	U Gem	16.8	0.078^a	18/06/13	2	4680	*q*
BD Pav*	258.19	U Gem	15.4	0.0^b	14/06/13	3	7375	*q?*
SDSS J100658.41+233724.4	267.71	U Gem	18.3	0.018^c	20/03/14	5	12494	*q*
HM Leo	268.99	U Gem	17.5	0.021^c	22/02/13	4	9979	*eq*
SDSS J154453.60+255348.8	361.84	U Gem?	16.9	0.032^c	22/04/13	–	–	*?*
HS 0218+3229	428.02	U Gem	15.5	0.05^c	22/12/12	3	7159	*q*
HS 1055+0939	541.88	U Gem	15.5	0.025^a	15/04/13	2	4688	*eq*

Notes. The $E(B-V)$ data have been retrieved from: (*a*) the NASA/IPAC Extragalactic Database (NED); (*b*) GW Lib: Bullock et al. (2011), BD Pav: Sion et al. (2008); (*c*) the three–dimensional map of interstellar dust reddening based on Pan–STARRS 1 and 2MASS (Two Micron All–Sky Survey) photometry (Green et al., 2015); (*d*) this work. The NED data are the galactic colour excess and represent an upper limit for the actual reddening while the Pan–STARRS data are the actual reddening for the systems with a known distance. The last column reports the state of the system during the *HST* observations: *eq*, early quiescence, i.e. observed close to an outburst; *q*, quiescence; *hs*, high state; *is*, intermediate state. For the systems highlighted with a star, phase–resolved X–shooter observations have also been obtained (Section 3.2.3.)

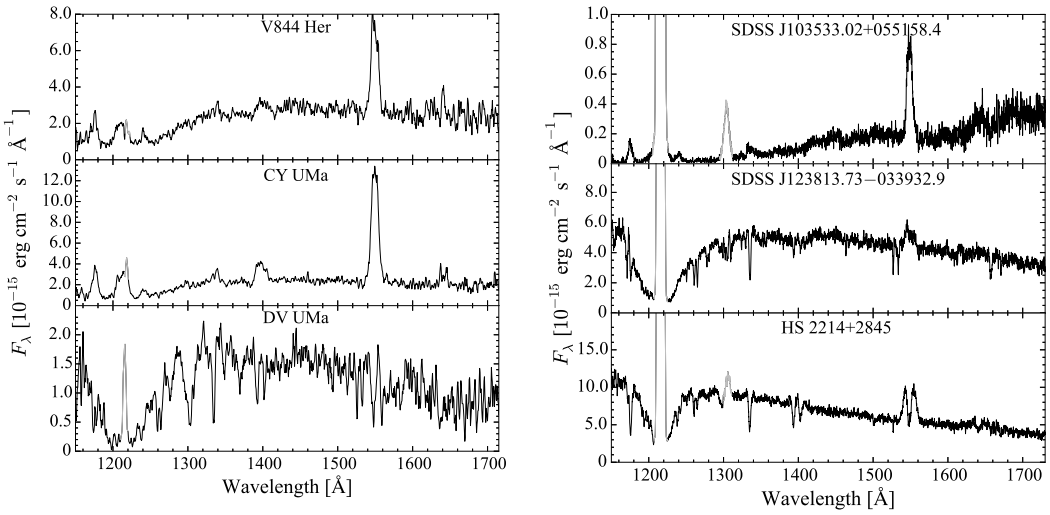

Figure 3.2: *HST*/STIS spectra (left) and *HST*/COS spectra (right) for six objects in which the white dwarf dominates the far–ultraviolet. The geocoronal emission lines of Lyα (1 216 Å) and O I (1302 Å) are plotted in grey.

Among our 41 COS targets, only SDSS J154453.60+255348.8 could not be observed since it showed strong variations in its optical brightness in the days before the *HST* observation.

After an outburst, the white dwarf does not cool immediately to its quiescent temperature since it has been heated by the increased infall of material. The time required to cool back to the quiescent temperature has been modelled and is related to the outburst amplitude and duration (Sion, 1995; Townsley and Bildsten, 2004; Piro et al., 2005). It has been observed that the cooling can take from days or weeks up to several years (Long et al. 1995; Gänsicke and Beuermann 1996; Slevinsky et al. 1999; Piro et al. 2005, see Szkody et al. 2016 for an extreme case). Therefore the effective temperature measured in a system in which an outburst has recently occurred provides only an upper limit for its quiescent effective temperature and, consequently, for $\langle \dot{M} \rangle$.

The right panels of Figure 3.2 show three sample COS ultraviolet spectra of quiescent CVs in which the white dwarf dominates the emission, as seen from the broad Lyα absorption centred on 1 216 Å. The shape of the Lyα line changes with $T_{\rm eff}$, becoming more defined and narrower in the hotter white dwarfs, while the continuum slope of the spectrum becomes steeper.

While the majority of the CVs in our sample have been observed in quiescence (Figure 3.3), obvious signatures of the white dwarf were missing in the spectra of nine systems: seven of them experienced an outburst shortly before the *HST* observation while the remaining two systems (OR And and BB Dor) are VY Scl stars (Figure 3.4) and were caught in the high state and intermediate state respectively,

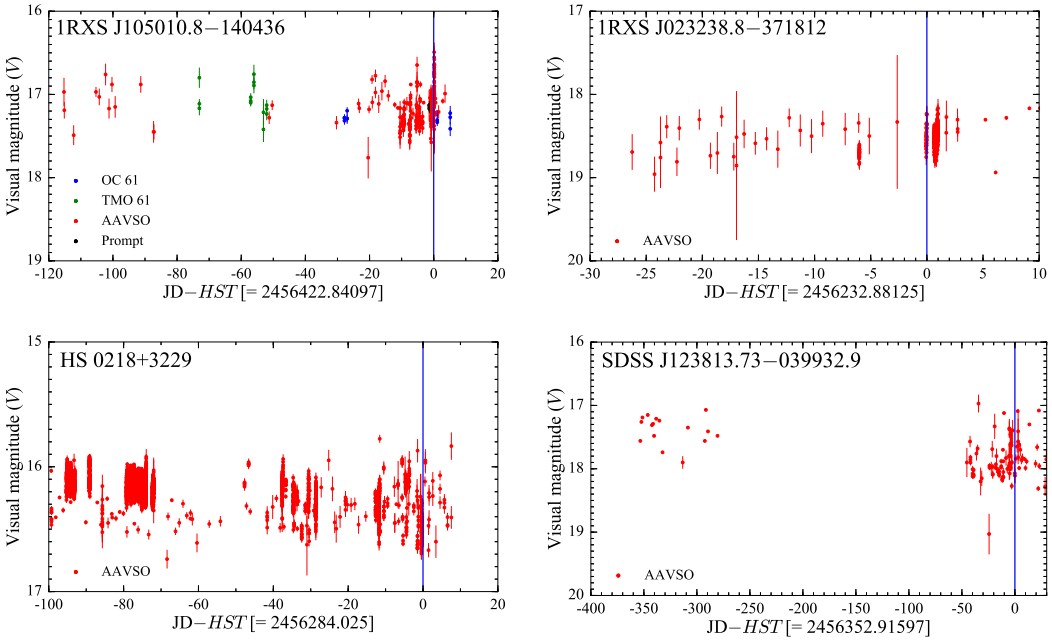

Figure 3.3: Sample light curves for four targets in our sample which have been observed in quiescence. The blue line represents the date of the *HST* observation, which has been subtracted from the Julian date on the x–axis. Note the different time range on the x–axes.

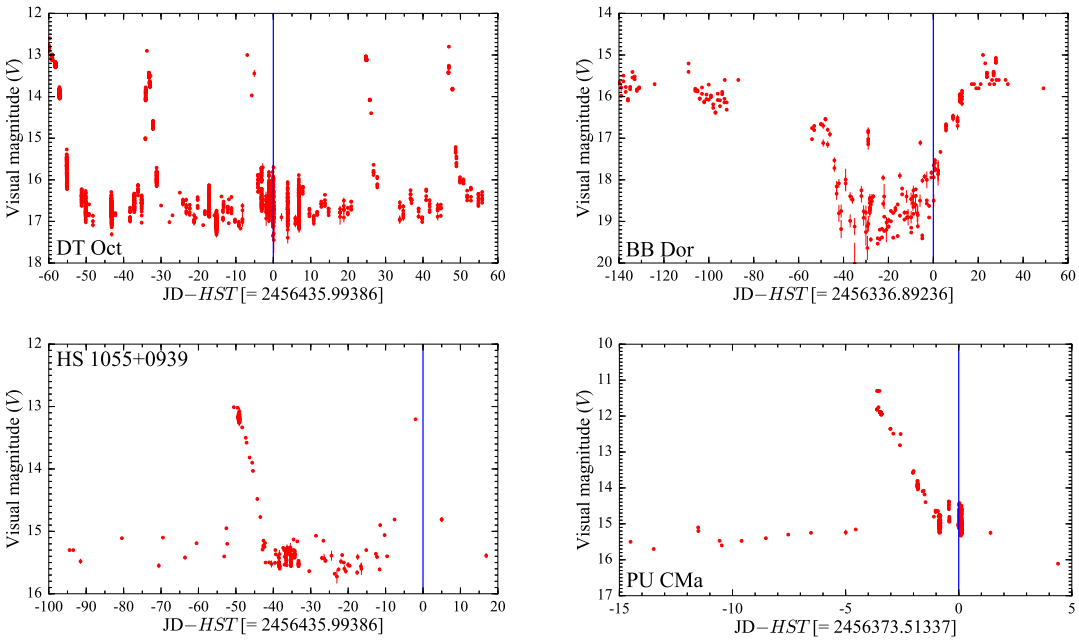

Figure 3.4: Sample light curves for four targets in our sample which have been observed close to an outburst or in an intermediate state. The blue line represents the date of the *HST* observation, which has been subtracted from the Julian date on the x–axis. Note the different time range on the x–axes. The data have been retrieved from the AAVSO database.

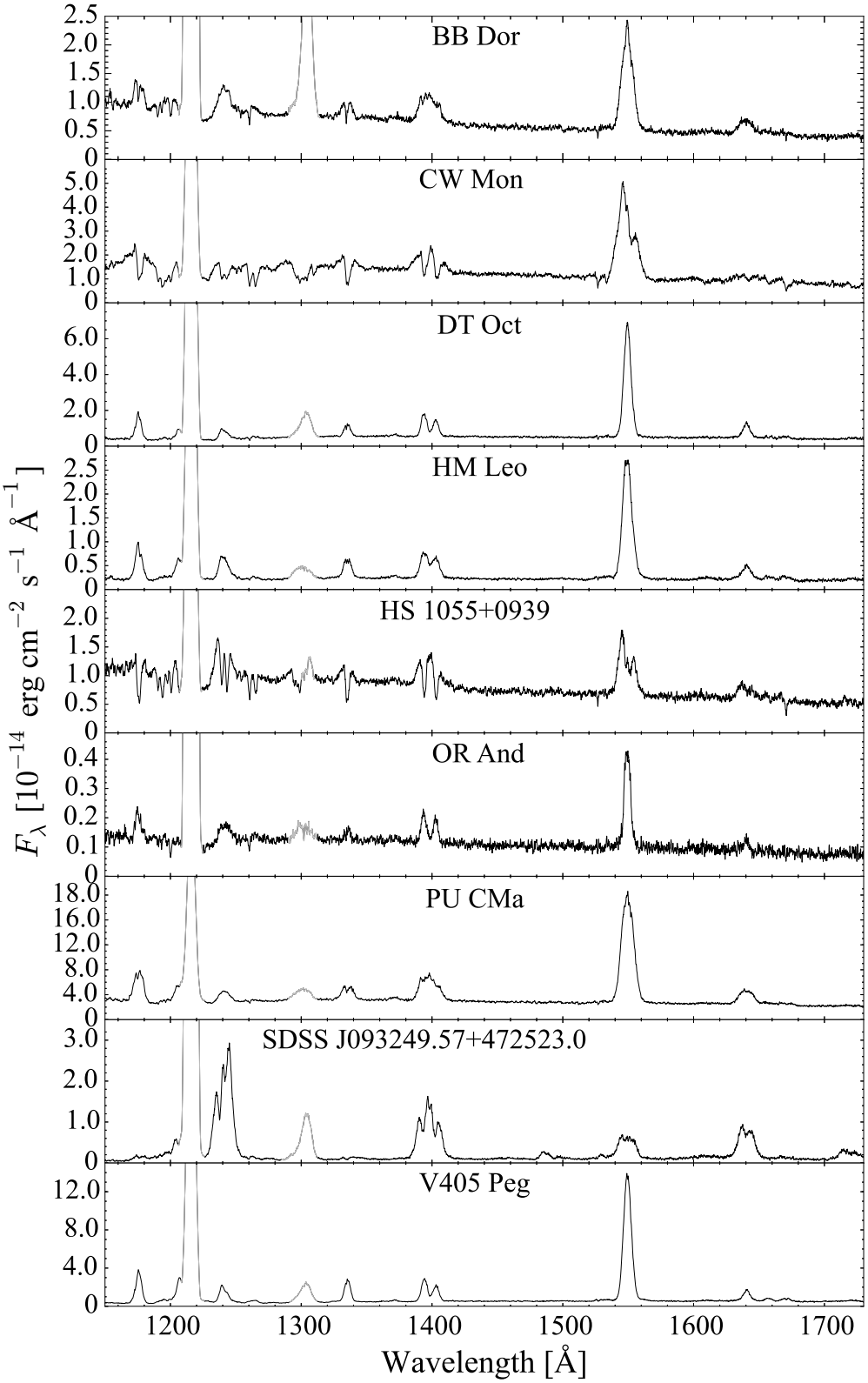

Figure 3.5: *HST*/COS spectra of the nine CVs dominated by emission from the accretion flow, outshining the white dwarf. Strong emission lines of C III (1 175 Å), N IV (1 242 Å), C II (1 335 Å), Si IV (1 400 Å), C IV (1 550 Å) and He IV (1 640 Å) are clearly visible. The wavelength ranges affected by the geocoronal emission lines of Lyα (1 216 Å) and O I (1 302 Å) are plotted in grey.

Table 3.2: Log of the *HST*/STIS observations. The systems are ordered by orbital period. The fourth column reports the instrumental magnitudes measured from the acquisition images, which were obtained through the $F28 \times 50LP$ filter.

System	$P_{\rm orb}$ (min)	Type	$F28 \times 50LP$ (mag)	$E(B-V)$ (mag)	Observation date (DD/MM/YY)	Number of orbits	Total exposure time (s)	State
V485 Cen	59.03	SU UMa	17.9	0.071^a	15/04/04	1	900	*q*
V844 Her	78.69	SU UMa	17.4	0.013^c	23/02/03	1	900	*q*
UV Per	93.44	SU UMa	17.9	0.0^b	11/12/02	1	900	*q*
RZ Sge	98.32	SU UMa	18.0	0.302^a	13/06/03	1	900	*q*
CY UMa	100.18	SU UMa	17.3	0.012^a	27/12/02	1	830	*q*
QZ Ser	119.75	SU UMa	16.9	0.038^c	07/10/03	1	900	*q*
DV UMa	123.62	SU UMa	18.6	0.014^c	08/02/04	1	900	*q*
BD Pav	258.19	U Gem	14.6	0.0^b	09/02/03	1	600	*q*

Notes. The $E(B-V)$ data have been retrieved from: (*a*) the NASA/IPAC Extragalactic Database (NED); (*b*) UV Per: Szkody (1985), BD Pav: Sion et al. (2008); (*c*) the three–dimensional map of interstellar dust reddening based on Pan–STARRS 1 and 2MASS photometry (Green et al., 2015). The NED data are the galactic colour excess and represent an upper limit for the actual reddening while the Pan–STARRS data are the actual reddening for the systems with a known distance. The last column reports the state of the system during the *HST* observations: *q*, quiescence.

preventing a detection of the white dwarf. For the purpose of completeness, the spectra of these nine objects are shown in Figure 3.5, but a detailed analysis of these systems is outside the scope of this work and is presented elsewhere (e.g. Godon et al. 2016). In Section 3.3, we analyse the 31 systems in which the white dwarf signature is easily recognisable from a broad Lyα absorption profile.

3.2.2 STIS observations

The STIS data were collected as part of two snapshot programs (programs ID 9357 and 9724) in Cycle 11 and 12 (Table 3.2). Snapshot programs are designed to fill short gaps in the weekly *HST* observing schedule, therefore each CV was observed with exposure times of only 600 to 900 seconds, through the 52" $\times$ 0.2" aperture. We used the G140L grating at the central wavelength 1 425 Å and the FUV–MAMA detector to obtain spectra covering the wavelength range 1 150−1 700 Å at a nominal resolution of $R \simeq 1\,000$.

Similar to the COS–FUV detector, the MAMA detector is also subject to damage by excessive illumination but, contrary to the COS program, the snapshot programs did not have a long term schedule which could allow detailed monitoring before the STIS observations. We analysed the STIS acquisition images to determine the source brightness immediately before the spectrum acquisition. These images were acquired with the $F28 \times 50LP$ filter (central wavelength of 7 228.5 Å and full width at half–maximum of 2 721.6 Å). We determined the corresponding magnitude following the method described in Araujo-Betancor et al. (2005a). By comparison

with published magnitudes and the system brightness in SDSS and AAVSO Photometric All–Sky Survey APASS, we verified that all the targets were observed in quiescence.

These snapshot programs produced ultraviolet spectra of 69 CVs (e.g. Gänsicke et al. 2003; Araujo-Betancor et al. 2005b; Rodríguez-Gil et al. 2004). Here we analyse the remaining eight objects in which the white dwarf dominates the ultraviolet emission. We show three sample STIS spectra of quiescent CVs in the left panel of Figure 3.2 where the broad Lyα absorption centred on 1216 Å reveals the white dwarf photosphere.

Three of the eight systems observed by STIS (BD Pav, QZ Ser and V485 Cen) are in common with the COS sample and we present a detailed comparison of the two datasets in Section 3.4.2.

Adding the five additional CVs observed with STIS to the 31 from the COS survey results in our total sample of 36 CVs in which the white dwarf dominates the overall spectral emission.

3.2.3 X–shooter observations

From the *HST* sample, we selected those CVs in which the white dwarf (i) was the dominant source of emission in the ultraviolet and (ii) for which a dynamical study has never been carried out before. In this subset, we identified the systems visible from the Southern hemisphere (23 CVs highlighted with a star in Table 3.2.1) and we obtained phase–resolved X–shooter observations for all of them. The observations covered a whole orbit period of each system, except in the case of AX For (October 25, 2013), BD Pav, QZ Lib and SDSS J001153.08–064739.2, whose observations were interrupted owing to technical problems and covered only half of the orbital period. The exposure times were selected to optimise the SNR and, at the same time, to minimise the orbital smearing. For each arm, we used a slit width matching the seeing during the observations. Since the ADCs of X–shooter were broken at the time of the observations, the slit angle was reset to the parallactic angle position after one hour of exposures.

The data were reduced using the Reflex pipeline (Freudling et al., 2013). To account for the well documented wavelength shift between the three arms (Section 2.2.3) we used theoretical templates of sky emission lines to calculate the shift of each spectrum with respect of the expected position. We then applied this shift when we corrected the data for the barycentric radial velocity. Finally, a telluric correction was performed using `molecfit` (Smette et al., 2015; Kausch et al., 2015).

Table 3.3: Log of the X–shooter observations and summary of the metal lines detected in the spectra of the 23 CVs observed with X–shooter.

		UVB		VIS		NIR		Metal lines detected	
System	Observation date (DD/MM/YY)	Exposure time N×T(s)	Slit width (″)	Exposure time N×T(s)	Slit width (″)	Exposure time N×T(s)	Slit width (″)	White dwarf	Secondary
V485 Cen	04/03/14	29 × 270	1.0	22 × 362	0.9	29 × 300	0.9	–	–
GW Lib	03/06/14	14 × 353	1.0	16 × 300	0.9	18 × 300	0.9	Mg II	–
SDSS J143544.02+233638.7	11/05/15	10 × 694	1.0	10 × 730	0.9	10 × 760	0.9	–	–
OT J213806.6+261957	20/10/14	16 × 304	1.0	14 × 335	0.9	16 × 337	0.9	–	K I
	28/09/16	28 × 186	1.0	26 × 190	0.9	30 × 200	0.9	–	K I
SDSS J013701.06–091234.8	19/10/10	20 × 200	1.0	20 × 215	0.9	20 × 110	0.9	–	Na I
SDSS J123813.73–033932.9	12/05/15	12 × 480	1.0	10 × 587	0.9	12 × 520	0.9	Mg II	K I
V1108 Her	12/05/15	12 × 480	1.0	10 × 587	0.9	12 × 520	0.9	Mg II	K I
ASAS J002511+1217.2	14/11/10	40 × 200	1.0	40 × 215	0.9	40 × 110	0.9	–	–
SDSS J103533.02+055158.4	11/05/15	8 × 880	1.0	8 × 913	0.9	8 × 950	0.9	–	–
CC Scl	20/10/14	16 × 300	1.0	16 × 335	0.9	16 × 361	0.9	–	K I
SDSS J075507.70+143547.6	26/02/15	9 × 730	1.0	9 × 694	0.9	9 × 760	0.9	Mg II	–
1RXS J105010.8–140431	11/05/15	19 × 300	1.0	15 × 364	0.9	15 × 420	0.9	Mg II	–
QZ Lib	12/05/15	9 × 410	1.0	7 × 465	0.9	7 × 510	0.9	–	–
1RXS J023238.8–371812	25/10/13	11 × 606	1.0	19 × 294	0.9	31 × 200	0.9	–	–
BB Ari	20/10/14	9 × 659	1.0	9 × 690	0.9	9 × 730	0.9	–	–
SDSS J100515.38+191107.9	26/02/15	9 × 750	1.0	9 × 709	0.9	9 × 780	0.9	–	K I
RZ Leo	23/03/11	20 × 300	1.0	20 × 315	0.9	20 × 110	0.9	–	Na I
CU Vel	25/10/13	10 × 606	1.0	17 × 294	0.9	29 × 200	0.9	–	K I
AX For	25/10/13	7 × 606	1.0	13 × 294	0.9	22 × 200	0.9	Mg II	K I
	24/09/15	12 × 610	1.3	12 × 592	1.2	12 × 642	1.2	Mg II	K I
SDSS J164248.52+134751.4	12/05/15	10 × 696	1.0	10 × 730	0.9	10 × 770	0.9	–	–
IR Com	05/03/14	29 × 270	1.0	21 × 412	0.9	31 × 300	0.9	Mg II	Na I, K I
SDSS J001153.08–064739.2	20/10/14	4 × 618	1.0	4 × 650	0.9	4 × 700	0.9	–	Na I, K I
BD Pav	03/06/14	14 × 354	1.0	16 × 300	0.9	18 × 300	0.9	–	Na I, K I

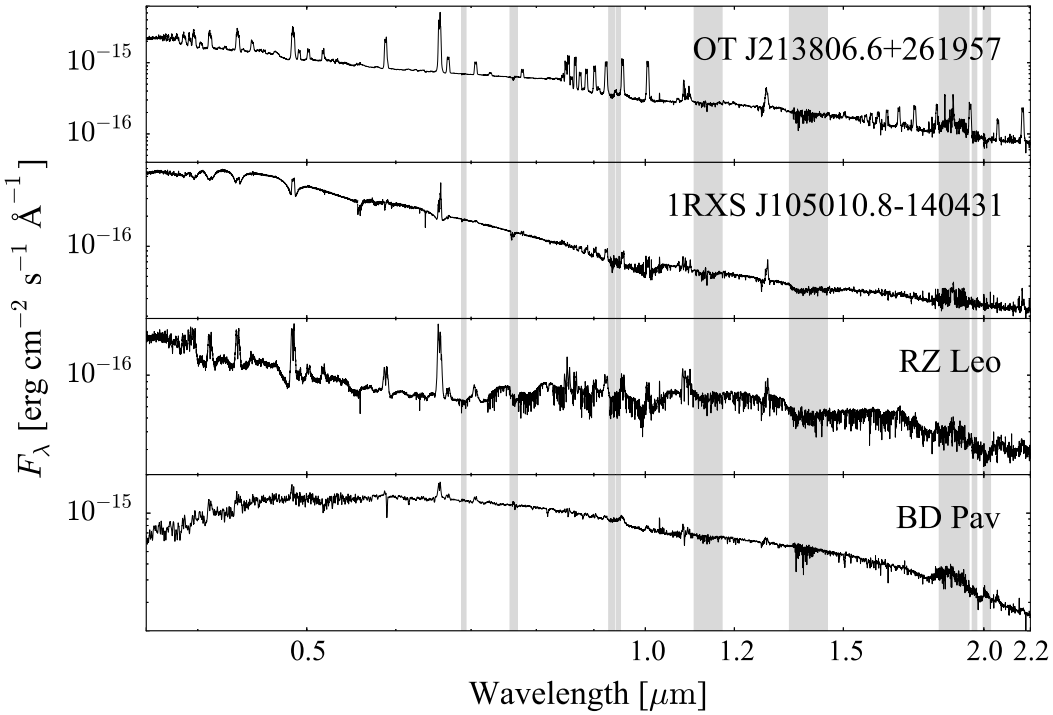

Figure 3.6: X–shooter spectra for four CVs in our sample for which the radial velocity curve could not be reconstructed. In OT J213806.6+261957, the emission is dominated by the disc. In 1RXS J105010.8–140431 the white dwarf is dominant in the blue part of the spectrum, where the Balmer lines are clearly visible. However, no metal lines arising in either the white dwarf or secondary photosphere are detected. In the spectrum of RZ Leo, the secondary dominates the emission in the near–infrared, however no signature of the white dwarf is detected in the blue portion of the spectrum; Finally, the spectrum of BD Pav is completely dominated by the secondary. The grey bands highlight the regions affected by the residuals of the telluric correction.

In eight of the 23 CVs observed with X–shooter, we could not identify any metal absorption feature from either the white dwarf or the secondary. In three of them we could only detect the Mg II arising from the white dwarf photosphere but we could not identify any lines from the secondary. In the spectra of eight CVs, the emission is either dominated by the secondary or the disc while the white dwarf signature is absent. Sample X–shooter spectra of the different cases are shown in Figure 3.6. Finally, we could identify both the white dwarf and secondary signature in only four of them (Figure 3.7): SDSS J123813.73–033932.9 (SDSS1238), V1108 Her, AX For and IR Com. A log of the spectroscopic observations is provided in Table 3.3 and the radial velocity analysis is presented in the next Section.

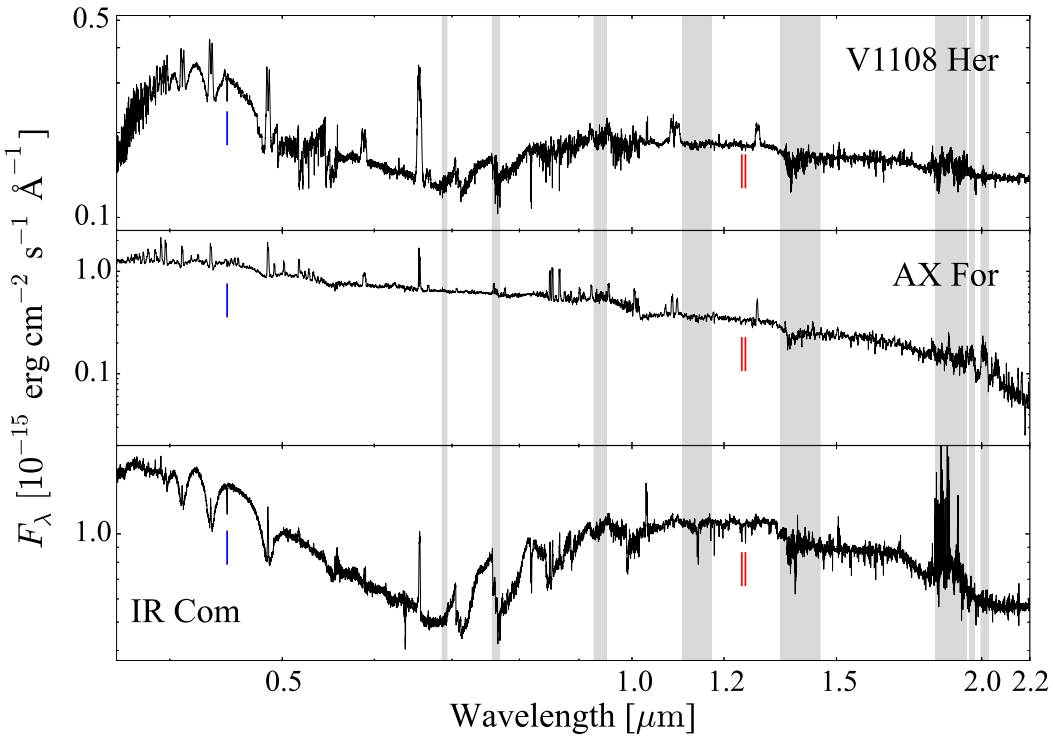

Figure 3.7: X–shooter spectra for three CVs in our sample for which the radial velocity curve could be reconstructed. The spectrum of V1108 Her is contamined by the emission of a background star, visible in the absorptions bands at $\simeq 5\,000$ Å. SDSS J123813.73–033932.9 is the object of study of Chapter 4 and its spectral energy distribution is shown, in more detail, in Figure 4.3. The blue and red lines point out the position of the Mg II (4 481 Å) and K I absorption lines (12 432/12 522 Å) respectively, while the grey bands highlight the regions affected by the residuals of the telluric correction.

3.3 Data analysis

3.3.1 Optical data

We identified the Mg II absorption line at 4 481 Å in the X–shooter spectra, which originates in the white dwarf photosphere, and several absorption features arising from the secondary photosphere, such as Na I (8 183/8 194 Å and 11 381/11 403 Å), K I (11 690/11 769 Å and 12 432/12 522 Å). Among these, the K I (12 432/12 522 Å) lines are the strongest and the only visible in the spectra of all systems, while the Na I doublet is only visible in the spectra of IR Com. These lines, together with the Mg II absorption feature, were used to track the reflex motion of the two stellar components.

Owing to the relatively low SNR ratio of our data ($\simeq 10 - 20$ in the UVB and $\simeq 5$ in the NIR) and to the presence of strong residuals from the sky lines subtraction in the NIR, we decided to simultaneously fit all the spectra of each object to achieve more robust radial velocity measurements (as done, for example,

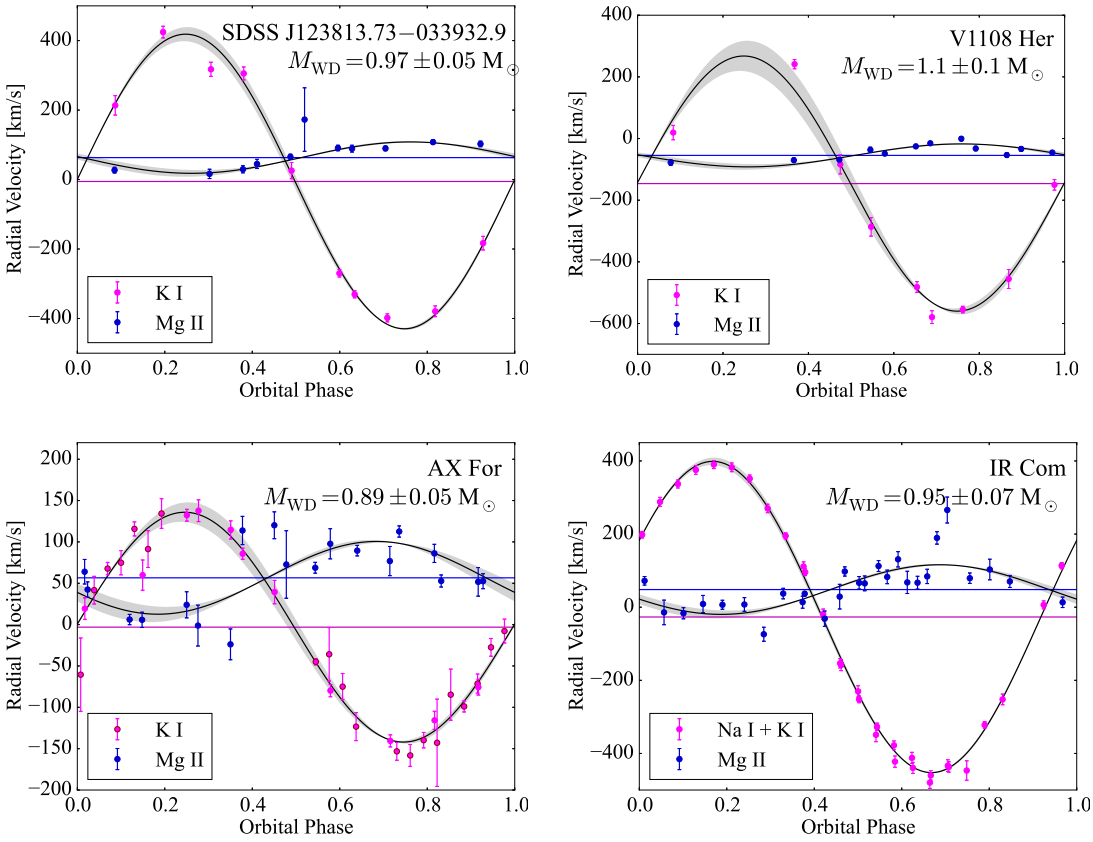

Figure 3.8: Radial velocity curves of four CVs in our sample from X–shooter phase–resolved observations. The radial velocities of the donor (magenta) were measured from the K I 12 432.24/12 522.11 Å absorption doublet, while the white dwarf radial velocities (blue) were measured from the Mg II 4 481.25 Å absorption line. The radial velocities of the secondary in IR Com were measured from the Na I 11 381/11 403 Å and K I 12 432.24/12 522.11 Å absorption doublets. By fitting the data with two sinusoids (black), we reconstructed the reflex motion of both the white dwarf and the donor star and determined the gravitational redshift of these CV white dwarfs.

Table 3.4: CV white dwarf gravitational redshifts, masses, radii and surface gravities from X–shooter phase–resolved observations.

System	v_{grav}(WD) (kms^{-1})	log(g)	M_{WD} (M$_\odot$)	R_{WD} (R$_\odot$)	q = $\frac{K_{WD}}{K_{sec}}$	M_{sec} (M$_\odot$)
SDSS J123813.73–033932.9	74 ± 10	8.56(6)	0.97(5)	0.0085(6)	0.08(1)	0.08(1)
V1108 Her	91 ± 20	8.71(13)	1.1(1)	0.007(1)	0.09(1)	0.09(2)
AX For	60 ± 6	8.43(6)	0.89(5)	0.0094(6)	0.32(4)	0.28(4)
IR Com	70 ± 11	8.53(7)	0.95(7)	0.0087(7)	0.16(1)	0.16(2)

Notes. For SDSS1238, the white dwarf mass has been evaluated using additional constraints on the mass ratio from the superhumps analysis (see Chapter 4 for more details).

by Parsons et al. 2012).

We first fitted the K I absorption lines using a combination of a constant and a double Gaussian of fixed separation. We allowed the position of the Gaussians

to change accordingly to Equation 2.4. In the case of IR Com, we fitted the K I and Na I doublets simultaneously, using a model composed by a constant and two double Gaussians of fixed separation. We fitted the Mg II absorption lines using a combination of a constant and a single Gaussian. The two fitting procedures returned the gamma velocities of the white dwarf and the secondary ($\gamma_{\rm WD}$ and $\gamma_{\rm sec}$, Figure 3.8), which carry information on the white dwarf surface gravity, since their difference is a measurement of the white dwarf gravitational redshift (Section 2.4.4). By assuming the mass–radius relationship from Hamada and Salpeter (1961) and using Equation 2.5, we measured the masses of the four CV white dwarfs (Table 3.4).

The accuracy we achieved on the masses is directly related to the quality of the data. The signal–to–noise ratio is crucial to precisely measure radial velocities: this appears clear, for example, in the case of AX For, whose observations were affected by clouds, causing large scatter of some points. Also, it is fundamental to well sample the orbital period. This can be seen by comparing the results for IR Com and V1108 Her: in the first case, the data are almost evenly distributed along the orbital period and allow to obtain accuracy of the order ~ 7 per cent. In the second case, the presence of a close background star which contaminated some of our observations, forced us to reject some spectra, resulting in poor orbital sampling and larger uncertainties.

3.3.2 Ultraviolet data

Ultraviolet spectra are particularly suitable for the study of CV white dwarfs because, at these wavelengths, the spectral energy distribution is often dominated by the white dwarf while the donor star does not contribute at all. However, some contamination from the disc, the bright spot (the region where the ballistic stream from the companion intersects the disc) or the boundary layer (the interface between the accretion disc and the white dwarf) can dilute the emission from the white dwarf photosphere. As described in Section 1.2.2, the overall shape of a white dwarf spectrum is determined by its effective temperature therefore the white dwarf effective temperature can be accurately measured by fitting the *HST* data with synthetic white dwarf atmosphere models.

In Figure 3.9, we show the COS data of 1RXS J023238.8–371812 as an example of a typical CV spectrum from our sample. The broad Lyα absorption at $\simeq 1\,216$ Å, the quasi–molecular absorption bands of H_2^+ at $\simeq 1400$ Å and several sharp absorption lines (e.g. C I 1 460/1 490 Å, Si II 1 526/1 533 Å, C I 1 657 Å) reveal the white dwarf photosphere. The white dwarf dominates the ultraviolet emission but the non–zero flux detected in the core of the Lyα suggests the presence of a secondary continuum component whose origin is still not clear. It has been argued that this second component could arise from the bright spot, from a hot boundary

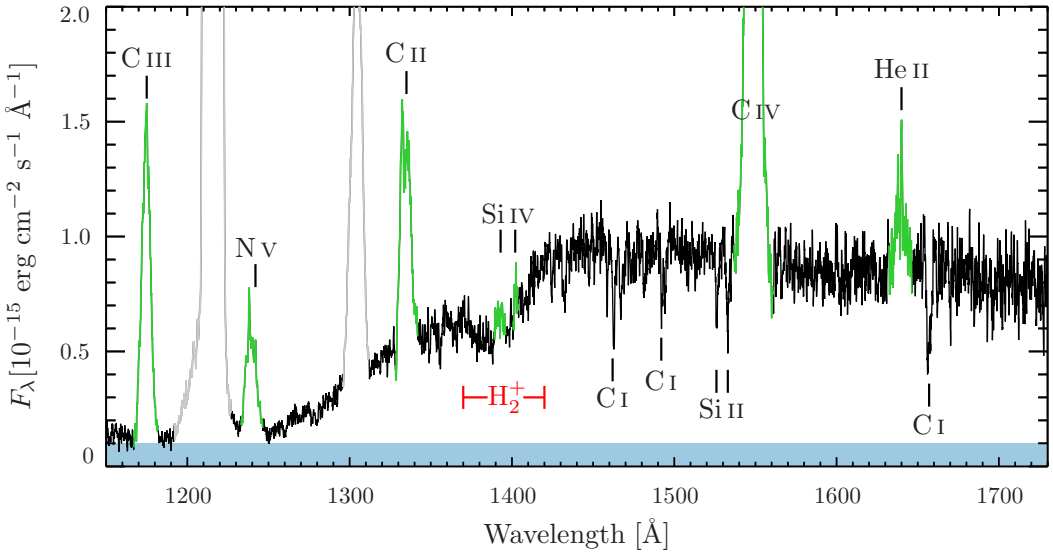

Figure 3.9: *HST*/COS spectrum of 1RXS J023238.8–371812. Plotted in green are the emission lines of C III (1 175 Å), N V (1 242 Å), C II (1 335 Å), Si IV (1 400 Å), C IV (1 550 Å) and He II (1 640 Å). The red band underlines the position of the H_2^+ quasi–molecular absorption bands. The blue band highlights the presence of a second, flat continuum component which, in this case, contributes $\simeq$ 10 per cent of the observed flux. The geocoronal emission lines of Lyα (1 216 Å) and O I (1 302 Å) are plotted in grey.

layer, or from the disc (Long et al., 1993; Godon et al., 2004a; Gänsicke et al., 2005). In addition we detect emission lines, which are broadened by the Keplerian velocity distribution of the disc. A model to fit the data has to account for these three contributions (white dwarf, second component and emission lines) detected in a CV spectrum.

We used TLUSTY and SYNSPEC (Hubeny, 1988; Hubeny and Lanz, 1995) to compute a grid of synthetic spectra of white dwarf atmospheres, covering $T_{\rm eff}$ = 10 000 − 70 000 K in steps of 100 K, and metal abundances Z of 0.01, 0.10, 0.20, 0.50 and 1.00 times their solar values[2].

Ideally, a spectral fit to the ultraviolet data would provide both $T_{\rm eff}$ and $\log g$ (Section 1.2.2). However these two quantities correlate: an increase in the temperature translates into a larger fraction of ionised hydrogen and narrower Lyman and Balmer lines; this effect can be counterbalanced by a higher gravity which increases pressure broadening. It is not possible to break this degeneracy from the sole analysis of the *HST* data since they only provide the Lyα absorption profile which, in the case of cool CV white dwarfs, is limited to only the red wing of the line. Therefore we needed to make an assumption on the surface gravity. Most previously

[2]Using a single metallicity is sufficient to account for the presence of the metal lines in the fit, which are relatively weak. Possible deviations of single element abundances from the overall scaling with respect to the solar values do not affect the results of the χ^2 minimisation routine. In fact, varying the abundances of individual elements has no effect on the measured $T_{\rm eff}$.

published work analysing CV white dwarf ultraviolet spectra assumed $\log g = 8.00$, corresponding to $0.6\,M_{\odot}$, the average mass of isolated white dwarfs (Koester et al., 1979; Liebert et al., 2005; Kepler et al., 2007) unless an independent white dwarf mass determination was available. However, Zorotovic et al. (2011) demonstrated that the average mass of white dwarfs in CVs is actually higher than that of isolated white dwarfs, $\simeq 0.8\,M_{\odot}$ ($\log g \simeq 8.35$). Since the canonical assumption $\log g = 8.00$ does not reflect the observed average mass of CV white dwarfs, we generated our grid of models assuming $\log g = 8.35$. Finally, for the four systems in our sample for which we dynamically measured the masses from the X–shooter data, we generated a grid of models assuming the surface gravities reported in Table 3.4.

The COS ultraviolet spectra are contaminated by geocoronal emission of Lyα (1 216 Å) and O I (1 302 Å) and we masked these wavelength regions for our spectral analysis. Furthermore, we noticed the presence of an additional continuum component in all our systems, which contributes $\simeq 10-30$ per cent of the observed flux. In order to account for this, we included in the fit a blackbody, a power law or a constant flux[3] (in F_{λ}), which can reproduce different slopes in the second component and are representative of different physical processes (thermalised emission in the case of the blackbody, optically thin emission in the case of the power law). Using a χ^2 minimisation routine, we fitted the grid of model spectra to the *HST* data and measured the effective temperatures of the 36 CV white dwarfs.

To investigate the influence of the disc emission lines on our fitting procedure, we carried out our spectral analysis using two different methods: (i) we masked all the emission lines (*Mask*); (ii) we included the emission lines as Gaussian profiles, allowing three free parameters: amplitude, wavelength and width (*Gaussian fit*).

We illustrate the differences between the two methods using 1RXS J023238.8–371812. Figure 3.10 shows the COS spectrum along with the best–fit models obtained masking the emission lines (left panels) and including the lines in the fit (right panels), for all three different second components (from top to bottom: blackbody, power law and constant). The temperatures measured with the two methods typically only differ by $\simeq 3$ K (see Table 3.5), demonstrating that including or masking the disc lines has no influence on the fit result (see also Szkody et al. 2010). Therefore, to use as much of the data as possible, we decided to include the lines in the fit (*Gaussian fit*).

The uncertainties of the individual fits listed in Table 3.5 are purely statistical, as derived from the fitting procedure. They are unrealistically small and do not reflect the real uncertainties, which are instead dominated by several systematic

[3]The constant is a special case of a power law and accounts for the easiest case with no slope, as it requires only one free parameter (a scaling factor), while power law and blackbody require two (respectively, a temperature and an exponent, plus a scaling factor). For this reason, we included the constant flux as an additional mode for the second component.

Table 3.5: Results for 1RXS J023238.8–371812 for the two different fitting methods for the disc emission lines, in which the emission lines are either masked (*Mask*) or included as Gaussian profiles (*Gaussian fit*). The surface gravity was fixed to $\log g = 8.35$. The last two rows (average) report the mean and the standard deviations for each method.

Emission lines	Second component	$T_{\rm eff}$ (K)	dof	χ^2
Mask	blackbody	$13\,543 \pm 36$	1856	1794
Mask	power law	$13\,574 \pm 36$	1856	1808
Mask	constant	$13\,462 \pm 28$	1857	1861
Gaussian fit	blackbody	$13\,540 \pm 34$	2191	2170
Gaussian fit	power law	$13\,573 \pm 34$	2191	2186
Gaussian fit	constant	$13\,466 \pm 26$	2192	2245
Mask	average	$13\,526 \pm 57$		
Gaussian fit	average	$13\,526 \pm 55$		

effects, analysed in the following sections.

The unknown nature of the second component

The first systematic uncertainty in our fitting procedure arises from the unknown nature of the additional emission component. The blackbody, the power law or the constant are not constrained outside the ultraviolet wavelength range, and only serve to account for different slopes in the detected additional continuum component. They thus represent a very simplified model of the additional continuum contribution and it is likely that none of them provides a realistic physical description of this emission component.

From a statistical point of view, and owing to the limited wavelength coverage of our data, we cannot discriminate among the three of them, and they all result in fits of similar quality and in very similar temperatures for the white dwarf (see Table 3.5). These differences in $T_{\rm eff}$ reflect a systematic effect related to presence of this additional flux. For this reason, we decided to adopt as final $T_{\rm eff}$ measurement the mean of the results obtained with the three different additional components. To evaluate the magnitude of the related systematic uncertainty, we calculated both the standard deviation of the $T_{\rm eff}$ values obtained with the three different additional components and the sum in quadrature of the statistical errors of the individual fits. We assumed as final and more realistic estimate for the systematic uncertainty the larger of these two. Additional systematic effects are analysed in the following sections.

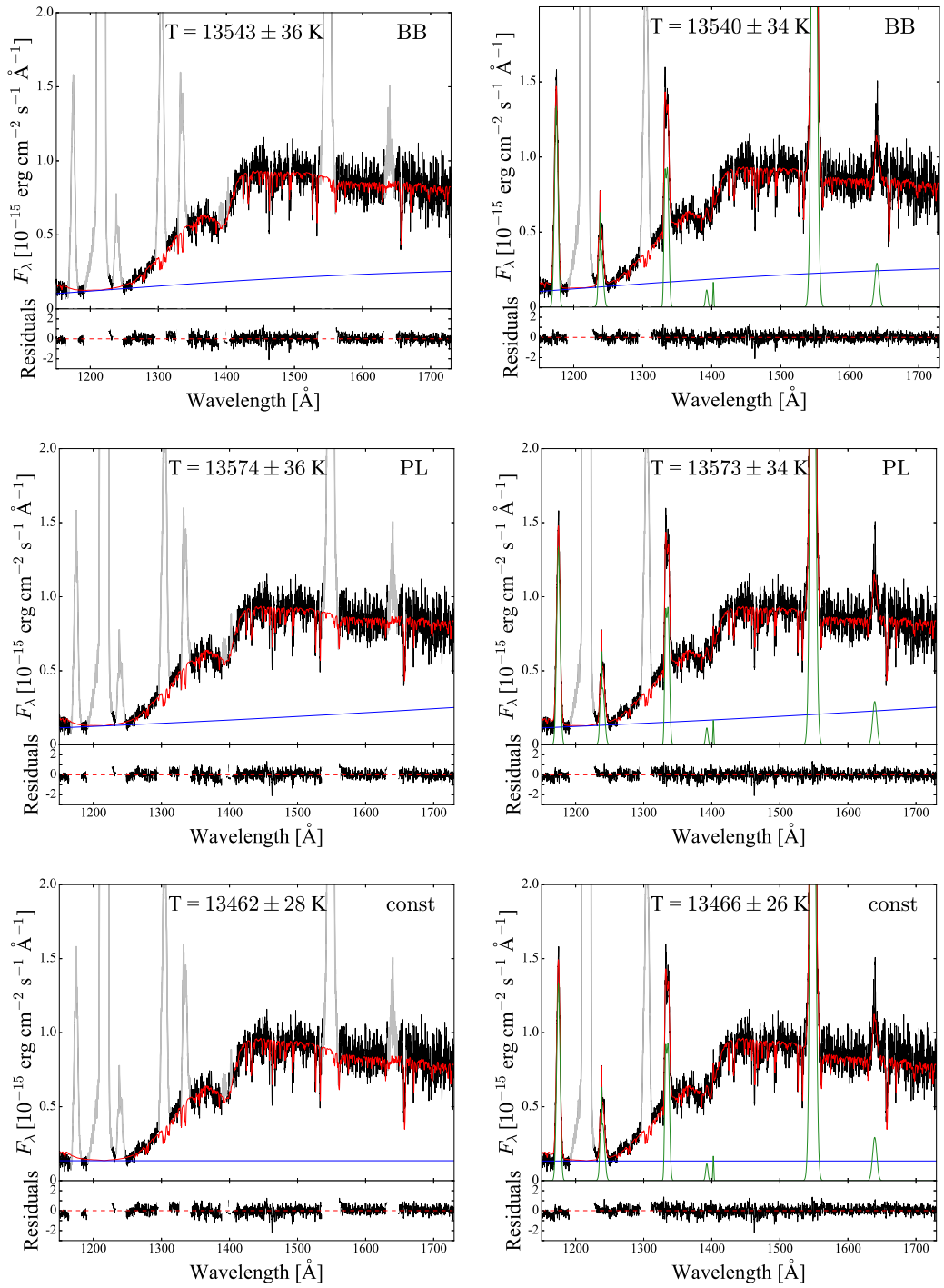

Figure 3.10: *HST*/COS spectrum of 1RXS J023238.8–371812 (black – the disc emission lines of C III (1175 Å), N V (1242 Å), C II (1335 Å), C IV (1550 Å) and He II (1640 Å) are clearly visible; weak emission from Si IV can be identified at $\simeq$ 1400 Å), along with the best–fit model (red) for the two different fitting methods: masking the emission lines (left panels) and including them as Gaussian profiles (right panels). The flux in the core of Lyα does not go to zero, implying the presence of a second continuum component (blue) which has been included in the fit in the form of a blackbody (BB), a power law (PL), or a constant (const). Masking the emission lines from the disc (grey in the left panels) or including them as a Gaussian profile (green in the right panels) returns very similar effective temperatures, within the statistical errors (Table 3.5). Note that the geocoronal emission lines, Lyα (1216 Å) and O I (1302 Å) have always been masked.

Table 3.6: $T_{\rm eff}$ for 1RXS J023238.8–371812 allowing different $\log g$, corresponding to different white dwarf masses. These results have been obtained fitting the data including the emission lines as Gaussian profiles, and using three different models for the second component.

Second component	$T_{\rm eff}$ (K) $\log g = 8.00$ $M_{\rm WD} = 0.6\,{\rm M}_{\odot}$	$T_{\rm eff}$ (K) $\log g = 8.35$ $M_{\rm WD} = 0.8\,{\rm M}_{\odot}$	$T_{\rm eff}$ (K) $\log g = 8.60$ $M_{\rm WD} = 1.0\,{\rm M}_{\odot}$
blackbody	$13\,016 \pm 28$	$13\,540 \pm 34$	$13\,938 \pm 37$
power law	$13\,045 \pm 29$	$13\,573 \pm 34$	$13\,972 \pm 37$
constant	$12\,949 \pm 23$	$13\,466 \pm 26$	$13\,848 \pm 28$
average	$13\,003 \pm 49$	$13\,526 \pm 55$	$13\,919 \pm 64$

The unknown white dwarf mass

As pointed out above, the temperature and mass of a white dwarf correlate. Table 3.6 reports the effective temperatures of 1RXS J023238.8–371812 allowing different $\log g$ (= different white dwarf masses). These results show that an assumption on $\log g$ translates into an accurate measurement of the temperature *for a given mass* ($\simeq 50\,{\rm K}$), while the systematic uncertainty introduced considering different surface gravities is typically an order of magnitude larger ($\simeq 500\,{\rm K}$). Therefore the dominant source of error is the (unknown) white dwarf mass and we used the following approach to evaluate how this systematic uncertainty depends on $T_{\rm eff}$.

As shown by Zorotovic et al. (2011), the average mass of CV white dwarfs is $0.83 \pm 0.23{\rm M}_{\odot}$ and we therefore investigated the correlation between effective temperature and $\log g$ in the mass range $0.6\,{\rm M}_{\odot}(\log g = 8.00)$ to $1.0\,{\rm M}_{\odot}(\log g = 8.60)$. We fitted our *HST* data assuming $\log g = 8.00$, $\log g = 8.35$ and $\log g = 8.60$ for each metallicity and for each type of second component, resulting in 15 effective temperatures (five metallicities × three second components) for each $\log g$, for each object. We define[4] as $T_{8.00} = T_{\rm eff}\,(\log g = 8.00)$, $T_{8.35} = T_{\rm eff}\,(\log g = 8.35)$ and $T_{8.60} = T_{\rm eff}\,(\log g = 8.60)$, and calculated $\Delta^{+}\,T_{\rm eff} = T_{8.00} - T_{8.35}$, and $\Delta^{-}\,T_{\rm eff} = T_{8.60} - T_{8.35}$.

We excluded from this analysis the eclipsing systems IY UMa, SDSS J040714.78–064425.1 and SDSS J100658.41+233724.4 for which disc absorption along the line of sight makes the identification of the continuum flux level difficult (Section 3.4.4). We also did not include CC Scl and SDSS J164248.52+134751.4 for which a reliable effective temperature determination was not possible (Section 3.4.2), and SDSS J153817.35+512338.0 because the core of its narrow Lyα line is strongly con-

[4]We found that the effective temperature derived for different metallicities were consistent within the uncertainties. To simplify our analysis, we do not distinguish between different Z in this discussion.

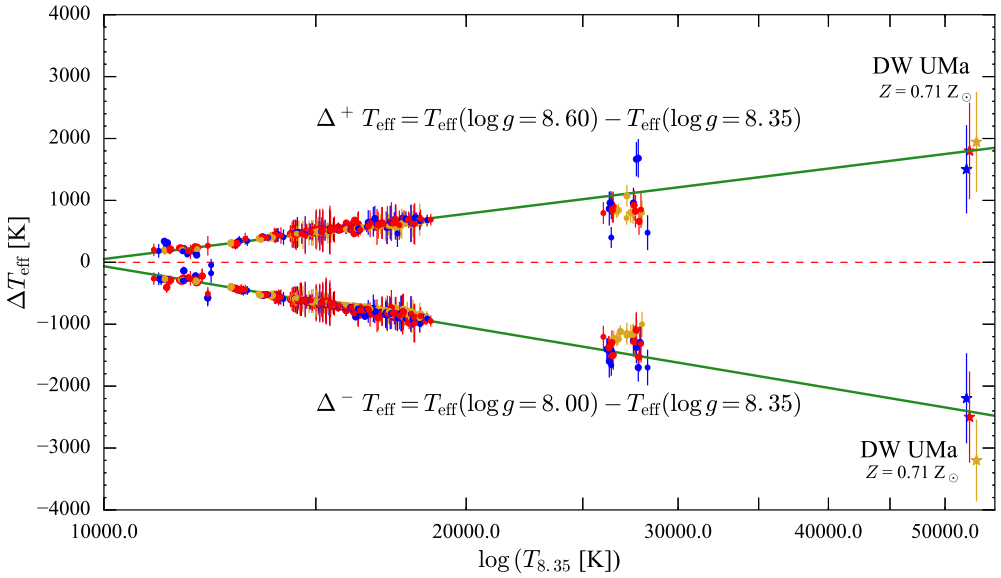

Figure 3.11: Best–fit to $\Delta^+ T_{\rm eff} = T_{\rm eff}(\log g = 8.60) - T_{\rm eff}(\log g = 8.35)$ and $\Delta^- T_{\rm eff} = T_{\rm eff}(\log g = 8.00) - T_{\rm eff}(\log g = 8.35)$, as a function of $T_{\rm eff}(\log g = 8.35)$, for the five metallicities and the three additional continuum second components (red for blackbody, blue for power law and gold for constant). The fit excludes the effective temperatures of (i) the eclipsing systems IY UMa, SDSS J040714.78–064425.1 and SDSS J100658.41+233724.4 for which disc absorption along the line of sight makes the identification of the continuum flux level difficult (Section 3.4.4); (ii) CC Scl and SDSS J164248.52+134751.4 for which a reliable effective temperature determination was not possible (Section 3.4.2); (iii) SDSS J153817.35+512338.0 because the core of its narrow Lyα line is strongly contaminated by geocoronal airglow emission which makes the data less sensitive to a change in the model surface gravity. DW UMa was not included in the fit, but serves as independent test of the fit.

taminated by geocoronal airglow emission which makes the data less sensitive to a change in the model surface gravity.

The remaining objects have typically $T_{\rm eff} \lesssim 21\,000$ K, with the exception of HS2214+2845 ($T_{\rm eff} \simeq 26\,000$ K). To better constrain $\Delta^+ T_{\rm eff}$ and $\Delta^- T_{\rm eff}$ and to verify the validity of this relationship at high temperatures, we included in our analysis two additional hotter objects: SS Aur ($T_{\rm eff} = 34\,000 \pm 2\,000$ K for $\log g = 8.8$, Sion et al. 2008) and DW UMa ($T_{\rm eff} = 50\,000 \pm 1\,000$ K for $\log g = 8.00$ and $Z = 0.71\,{\rm Z}_\odot$, Araujo-Betancor et al. 2003). Both these objects have been observed with STIS, which allows the removal of the contamination from geocoronal emission and therefore, differently from SDSS1538 in our sample, they can be used to constrain the relationship at high temperatures.

We retrieved the STIS spectrum of SS Aur and the out–of–eclipse STIS low–state spectrum of DW UMa (Knigge et al., 2000) from the *HST* data archive. Following the same method as for the CVs in our sample, we fitted these data assuming $\log g = 8.00$, $\log g = 8.35$ and $\log g = 8.60$. For SS Aur we found: $T_{8.00} = 26\,269 \pm 275$ K, $T_{8.35} = 27\,507 \pm 282$ K and $T_{8.60} = 28\,402 \pm 270$ K for $Z = 0.1\,{\rm Z}_\odot$. In

the case of DW UMa, we assumed $Z = 0.71\,Z_{\odot}$, and obtained $T_{8.00} = 49\,900 \pm 844\,K$, in agreement with Araujo-Betancor et al. (2003), $T_{8.35} = 52\,532 \pm 893\,K$ and $T_{8.60} = 54\,282 \pm 986\,K$, respectively.

Figure 3.11 show the trend of $\Delta^+ T_{\rm eff}$ and $\Delta^- T_{\rm eff}$ as a function of $T_{\rm eff}$ ($\log\, g = 8.35$). These correlations are well fit with the following relation:

$$\Delta\, T_{\rm eff} = a \log(T_{\rm eff}\, b) \tag{3.1}$$

where $a = 1054(2)\,K$, $b = 0.0001052(7)\,K^{-1}$ for $\Delta^+ T_{\rm eff}$, and $a = -1417(2)\,K$, $b = 0.0001046(5)\,K^{-1}$ for $\Delta^- T_{\rm eff}$.

We included the SS Aur temperatures in the fit of $\Delta^+ T_{\rm eff}$ and $\Delta^- T_{\rm eff}$ to better constrain the relationship at high temperatures. In contrast, we did not include the DW UMa temperatures and we only overplot them in Figure 3.11 to illustrate that our best–fit is in good agreement with this independent measurement.

The two best–fit curves represent the systematic uncertainty $\sigma_{T_{\rm eff}}$ due to the unknown mass of the white dwarf. The two curves are not symmetric (since the relationship between $\log\, g$ and the white dwarf mass is not linear), resulting in asymmetric error bars with $\Delta^- T_{\rm eff} > \Delta^+ T_{\rm eff}$. In the following, in order to simplify our discussion, we adopted as final uncertainty the larger value between those two, i.e. the one derived from $\Delta^- T_{\rm eff}$:

$$\sigma_{T_{\rm eff}} = 1\,417 \log(0.0001046\, T_{\rm eff}) \tag{3.2}$$

In summary, we found that the systematic uncertainty due to the unknown white dwarf mass lies in the range $300 - 1800\,K$. Once the masses for each system are accurately determined, the degeneracy between $T_{\rm eff}$ and $\log\, g$ will be broken, reducing the uncertainties in $T_{\rm eff}$ to those related to the unknown nature of the second additional component (see Section 3.3.2).

Reddening

Reddening due to interstellar dust along the line of sight can introduce an additional systematic uncertainty in the effective temperature determination as it affects the overall slope of the ultraviolet spectra. However, CVs are intrinsically faint and thus we are observationally biased towards nearby systems, for which extinction is usually negligible. Moreover, owing to their colour similarity with quasars, CVs are often discovered by extragalactic surveys (such as SDSS), which cover high Galactic latitudes, and are therefore not heavily affected by reddening. To verify that reddening is a minor contribution to the total error budget, for all the systems in our sample, we compiled the colour excess of our CVs (Table 3.1 and 3.2) using the three–dimensional map of interstellar dust reddening based on Pan–STARRS 1 and

2MASS photometry (Green et al., 2015) wherever possible, i.e. when the distance is known and the object is inside the field covered by this map. For the remaining objects, we report either the value from the literature where available or the galactic $E(B-V)$ from the NASA/IPAC Extragalactic Database (NED), which only represents an upper limit for the actual reddening. Finally, for CU Vel, we determined its colour excess below (Section 3.4.3).

To establish how the interstellar absorption affects our analysis, we considered one of the systems with zero colour excess, UV Per, and reddened its spectrum using the relationship given by Cardelli et al. (1989) for a range of values in $E(B-V)$. Since we previously determined the effective temperature for this CV white dwarf, $T_{\rm eff}[E(B-V)=0] = 14\,389 \pm 578\,{\rm K}$, we can use this "artificially reddened" dataset to study the variation of $T_{\rm eff}$ as a function of reddening. We fitted the reddened spectra following the prescription from Sections 3.3 and 3.3.2 and show the derived temperatures in Figure 3.12. The interstellar absorption introduces a variation in $T_{\rm eff}$ greater than the systematic uncertainties defined in Section 3.3.2 (blue dashed lines) for $E(B-V) \gtrsim 0.1$, which we assumed as the threshold above which the effect of the reddening cannot be neglected. Only one system in our sample has a colour excess significantly higher than this value: RZ Sge, $E(B-V) = 0.302$, as returned from the NED database. However Sagittarius lies on the Galactic plane and this $E(B-V)$ represents an estimate over the entire Galactic column. Given the typical distances of CVs, the actual reddening of RZ Sge is likely to be lower than that. We assumed the mass–radius relationship from Hamada and Salpeter (1961) and, using the scaling factors from the fit to the STIS data for different surface gravities (Section 3.3.2), we estimated the distance to RZ Sge to lie in the range $262\,{\rm pc} \lesssim d \lesssim 335\,{\rm pc}$, for $0.6\,{\rm M}_\odot \leq M_{\rm WD} \leq 0.8\,{\rm M}_\odot$. From the three–dimensional map of interstellar dust reddening (Green et al., 2015) we found $0.044 \lesssim E(B-V) \lesssim 0.070$, well below the threshold we established above. We therefore considered negligible the reddening for this system.

Finally, interstellar gas along the line of sight can also contaminate the observed spectrum with additional Lyα absorption. Using the relation between interstellar neutral Hydrogen column density and reddening from Diplas and Savage (1994), we determined that this contribution is always of the order of few Ångstrom ($\simeq 3\,$Å for $E(B-V)=0.05$ up to $\simeq 7\,$Å for $E(B-V)=0.3$) and therefore much narrower than the white dwarf Lyα absorption line. In fact, the interstellar Lyα absorption is located in the spectral region that we always masked owing to geocoronal airglow emission, which typically has a width of $\simeq 18\,$Å, and therefore we concluded that interstellar Lyα absorption has no effect on our results.

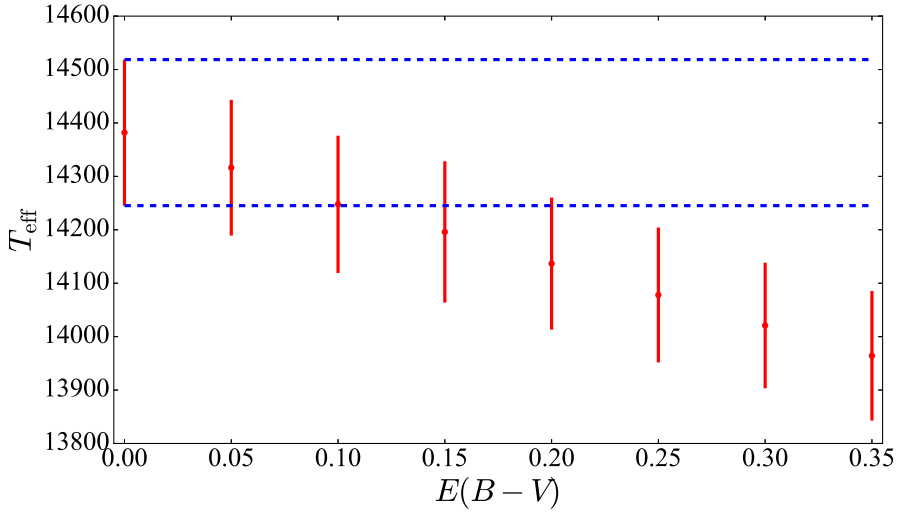

Figure 3.12: Best–fit effective temperatures for UV Per, obtained by reddening the *HST*/STIS data for increasing values of $E(B-V)$. The blue lines show the systematic uncertainties on the effective temperature derived from the fit to the original data ($E(B-V)=0$), following the method described in Section 3.3.2. They establish the threshold above which the effect of interstellar absorption on our $T_{\rm eff}$ is greater than the systematic uncertainties, i.e. $E(B-V)\simeq 0.1$.

Other possible systematic effects

To review all the systematic uncertainties in a way as comprehensive as possible, we need to discuss the possibility of Lyα absorption from the additional non–white dwarf component and inaccuracies in the instrument calibration.

Although not much is known about the physical origin of the second component, it is likely to arise from a hot optically thick (e.g. the bright spot) or a hot optically thin medium surrounding a cooler optically thick layer (e.g. the disc or the boundary layer). It is therefore possible that the second component can contribute, to some extent, to the observed Lyα absorption. The Lyα profile is, along with the spectral slope, the main tracer of the white dwarf temperature, and such a hypothetical contamination could systematically affect our results. Long et al. (2009) investigated an additional Lyβ absorption in VW Hyi finding that it most likely originates from a hot spot region whose emission can be approximated by a stellar model with $\log g \simeq 4$. The Lyman absorption lines arising from such an environment are consequently significantly narrower than the white dwarf Lyα absorption itself, which is broadened by the higher pressure on the white dwarf surface at $\log g \simeq 8.35$. Thus, although the model we used to describe the additional component does not account for the possibility of absorption in the Lyα region, such contamination (if present) would not appreciably affect our effective temperature determination.

Finally, limitations in the instrument calibration may affect our results.

Massa et al. (2014) report that the systematic uncertainties in the COS G140L flux calibration are less than two per cent for $\lambda < 1\,200$ Å and one per cent for $1\,200$ Å $< \lambda < 1\,900$ Å, with an increase up to six per cent at $\lambda = 2\,150$ Å. Owing to a decrease in the detector sensitivity in the red portion of the spectrum, we only considered the wavelength range $1\,150$ Å $< \lambda < 1\,730$ Å, for which systematic uncertainties are less than two per cent. The maximum effect on our results can be evaluated by multiplying the COS spectra with a linear function with a two per cent slope. To assess also for possible dependencies with the temperature of the white dwarf, we choose three systems representative of cool, warm and hot white dwarfs: 1RXS J105010.8–140431, SDSS J123813.73–033932.9 and HS 2214+2845. We fitted their spectra after applying the two per cent slope in flux calibration and find that the resulting $T_{\rm eff}$ values are in agreement, within the uncertainties, with the one we derived from the original COS data. We therefore conclude that our analysis is not affected by the very small uncertainty in the COS instrument calibration.

Three objects in our sample have been observed both with STIS and COS. In Section 3.4.2 we compare the two datasets and, for this comparison to be reliable, we needed to verify that the STIS and COS calibrations agree. To do so, we retrieved from the *HST* archive the STIS and COS data of the flux standard WD 0308–565. We overplot the one available STIS spectrum and the COS data acquired at different epochs, finding that the STIS spectrum matches the flux level of all the COS data. With a linear fit to the ratio between the two datasets, we determined that they differ, on average, by $\simeq 3$ per cent. This comparison proves that uncertainties in the STIS calibration are comparable to the systematic uncertainties of COS and therefore they are negligible in our analysis. Finally, we can also conclude that the differences in the STIS and COS effective temperatures discussed in Sections 3.4.2 are not related to calibration issues of the two instruments.

We followed the procedure outlined in the previous Sections to fit the *HST* data of the 36 CVs and summarize the results in Table 3.7. Figure 3.13 shows three examples of best–fit models obtained with this procedure: 1RXS J105010.8–140431 (top panel), SDSS J123813.73–033932.9 (middle panel) and HS 2214+2845 (bottom panel), which are representative of different temperature regimes (cool, intermediate and hot, respectively).

3.4 Discussion

3.4.1 $\log g$ correction of published $T_{\rm eff}$ values

The two most commonly used techniques to measure effective temperatures of CV white dwarfs are spectroscopy, that is by fitting ultraviolet or optical spectra with

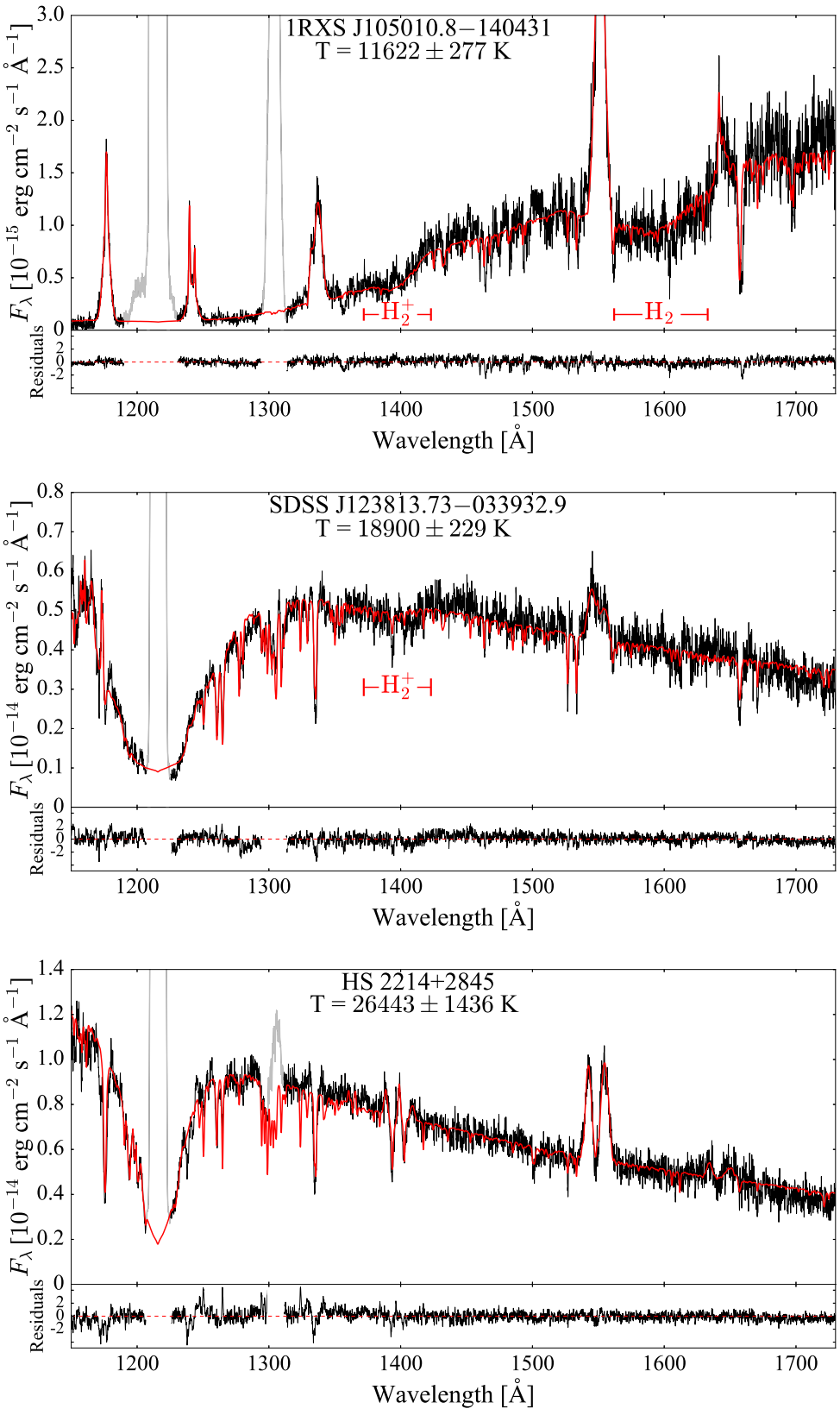

Figure 3.13: Ultraviolet spectra (black) of cool, warm and hot CV white dwarfs in our sample along with the best–fit model (red) assuming a blackbody second component. The quasi–molecular absorption bands of H_2^+ and of H_2 are visible at $\simeq 1\,400$ Å and $\simeq 1\,600$ Å for $T_{\rm eff} \lesssim 19\,000$ K and $T_{\rm eff} \lesssim 13\,500$ K, respectively (Nelan and Wegner, 1985; Koester et al., 1985). The geocoronal emission lines of Lyα (1 216 Å) and O I (1 302 Å) are plotted in grey.

Table 3.7: Characteristics of the 45 CV white dwarfs observed with COS and STIS.

System	$P_{\rm orb}$ (min)	d (pc)	$M_{\rm WD}$ ($M_\odot$)	Ref.	Z ($Z_\odot$)	$T_{\rm eff}$ (K)	$\pm$ (K)	WD contribution	Instrument
V485 Cen	59.03			1	0.5	15 200	655	56%	STIS
GW Lib	76.78	140^{+30}_{-20}		2, 3	0.2	16 995↓	812	85%	COS
SDSS J143544.02+233638.7	78.00			4	0.01	11 940	315	84%	COS
OT J213806.6+261957	78.10			5	0.2	16 292	753	69%	COS
V844 Her	78.69	290 ± 30		3, 6	0.1	14 850	622	61%	STIS
SDSS J013701.06–091234.8	79.71	300 ± 80		7, 8	0.1	14 547	594	77%	COS
SDSS J123813.73–033932.9	80.52	110	0.97(5)	9	0.5	18 900	229*	75%	COS
PU CMa	81.63			10					COS
V1108 Her	81.87	130 ± 30	1.0(2)	11, 12	1.0	14 200	50*	81%	COS
ASAS J002511+1217.2	82.00	130 ± 30		12, 13	0.1	12 830	416	77%	COS
SDSS J103533.02+055158.4	82.22	170 ± 12	0.835(9)	14, 15	0.01	11 620	44*	85%	COS
CC Scl	84.10			16	0.2	16 855:	801	35%	COS
SDSS J075507.70+143547.6	84.76			17	0.5	15 862	716	90%	COS
1RXS J105010.8–140431	88.56	100 ± 50		18, 19	0.1	11 622	277	89%	COS
MR UMa	91.17			20	0.2	15 182↓	654	69%	COS
QZ Lib	92.36	120 ± 50		19	0.01	11 303	238	64%	COS
SDSS J153817.35+512338.0	93.11			17	0.01	33 855	1785	94%	COS
UV Per	93.44			21	0.2	14 389	578	75%	STIS
1RXS J023238.8–371812	95.04	160		22	0.2	13 527	491	78%	COS
SDSS J093249.57+472523.0	95.48			17					COS
RZ Sge	98.32			20	0.5	15 287	663	56%	STIS
CY UMa	100.18			23	0.1	15 232	658	61%	STIS
BB Ari	101.20			24, 25	0.2	14 948↓	632	83%	COS
DT Oct	104.54			24, 25					COS
IY UMa	106.43	190 ± 60	0.79(4)	26, 27	1.0	17 750↓	1000*	77%	COS
SDSS J100515.38+191107.9	107.60			17	0.2	15 944	723	74%	COS
RZ Leo	110.17	340 ± 110		28, 29	0.5	15 014	638	83%	COS
CU Vel	113.04	150 ± 50		29, 30	0.1	15 336	668	89%	COS
AX For	113.04	370^{+20}_{-60}	0.89(8)	25, 31	1.0	16 748↓	99*	68%	COS
SDSS J164248.52+134751.4	113.60			32	1.0	17 710:	871	48%	COS
QZ Ser	119.75	460^{+150}_{-110}		33	0.2	14 481	587	68%	STIS
DV UMa	123.62	504 ± 30	1.098(24)	15, 34	1.0	18 874	182*	92%	STIS
IR Com	125.34	300	0.95(7)	22, 35	1.0	17 015	77*	86%	COS
SDSS J001153.08–064739.2	144.40			36	0.1	13 854	525	63%	COS
OR And	195.70			25					COS
BB Dor	221.90	$1\,500 \pm 500$		37					COS
SDSS J040714.78–064425.1	245.04			38	1.0	20 885	1104	67%	COS
CW Mon	254.30	297		25, 39					COS
V405 Peg	255.81	149^{+26}_{-20}		40					COS
HS 2214+2845	258.02			41	0.5	26 443↓	1436	84%	COS
BD Pav	258.19	500		42, 43	0.5	17 775	876	92%	STIS
SDSS J100658.41+233724.4	267.71	676 ± 40	0.78(12)	44	1.0	16 000	1000*	96%	COS
HM Leo	268.99	350		45					COS
HS 0218+3229	428.02	1 000		46	0.2	17 990	893	70%	COS
HS 1055+0939	541.88			25					COS

Notes. For each object, its orbital period, distance and white dwarf mass are compiled from the literature. The last columns report the results from this work: metallicity, effective temperatures, the systematic uncertainties arising from the unknown white dwarf mass, the percentage of the white dwarf contribution to the total flux and the instrument used. The white dwarf contribution has been calculated assuming a constant flux as second component. For the eight systems highlighted with a star, a precise mass measurement is available and, for the four systems observed with X–shooter, the effective temperatures have been measured assuming the surface gravities reported in Table 3.4. While the uncertainties on the effective temperature of IY UMa and SDSS1006 are dominated by the presence of the curtain of veiling gas (Section 3.4.4), the uncertainties reported for SDSS1035 and DV UMa, are those related the unknown nature of the second additional component (Section 3.3.2). In particular, for DV UMa, we report the effective temperature obtained assuming $\log g = 8.78$ (Section 3.4.3). The values flanked by a downwards arrow represent upper limits for the temperature of the systems. The values flanked by a colon represent unreliable effective temperature and are not considered in the discussion.

References. (1) Augusteijn et al. (1996), (2) Thorstensen (2003), (3) Thorstensen et al. (2002b) (4) Szkody et al. (2007), (5) Chochol et al. (2012), (6) Oizumi et al. (2007), (7) Pretorius et al. (2004), (8) Imada et al. (2007), (9) Aviles et al. (2010), (10) Thorstensen and Fenton (2003), (11) Price et al. (2004), (12) Ishioka et al. (2007), (13) Templeton et al. (2006), (14) Littlefair et al. (2006), (15) Savoury et al. (2011) (16) Chen et al. (2001), (17) Gänsicke et al. (2009), (18) Mennickent et al. (2001), (19) Patterson et al. (2005a), (20) Patterson et al. (2005b), (21) Thorstensen and Taylor (1997), (22) Patterson (2011), (23) Thorstensen et al. (1996), (24) Uemura et al. (2010), (25) Ritter and Kolb (2003), (26) Steeghs et al. (2003), (27) Patterson et al. (2000), (28) Mennickent and Tappert (2001), (29) Mennickent and Diaz (2002), (30) Mennickent and Diaz (1996), (31) Imada et al. (2006), (32) Southworth et al. (2008), (33) Thorstensen et al. (2002a), (34) Feline et al. (2004), (35) Feline et al. (2005), (36) Rebassa-Mansergas et al. (2014), (37) Rodríguez-Gil et al. (2012), (38) Ak et al. (2005), (39) Szkody and Mateo (1986), (40) Thorstensen et al. (2009), (41) Aungwerojwit et al. (2006), (42) Barwig and Schoembs (1983), (43) Sion et al. (2008), (44) Southworth et al. (2009), (45) Thorstensen and Taylor (2001), (46) Rodríguez-Gil et al. (2009)

white dwarf atmosphere models, and photometry, i.e. from the analysis of light curves to study the white dwarf ingress and egress in eclipsing systems. Townsley and Gänsicke (2009, hereafter TG09) present an analysis of CV white dwarf effective temperatures and selected only those systems for which a reliable $T_{\rm eff}$ determination is available. They consider a measurement unreliable when obtained from (i) spectra in which the white dwarf could not be unambiguously detected or, (ii) in the case of eclipse light curve analyses, oversimplified models or data of poor quality were used. Following these criteria, TG09 compiled 43 systems with a reliable temperature measurement (see their table 1).

Among the 43 measurements from TG09, 15 were obtained from light curve analyses (which also delivers the white dwarf mass) or have a white dwarf mass measurements independent from the spectral fit. For the remaining 28 objects an independent mass determination was not available and the white dwarf $T_{\rm eff}$ was evaluated via spectroscopic analyses, following methods similar to the one described here, but assuming $\log g = 8.00$. As discussed in Section 3.3, this assumption does not reflect the average mass in CV white dwarfs, $M \simeq 0.8\,{\rm M}_{\odot}$, corresponding to $\log g = 8.35$. To combine our results with those of TG09, we need therefore to evaluate the corresponding $T_{\rm eff}$ for $\log g = 8.35$ for those 28 objects.

The systematic correction that we need to apply is $\Delta T_{\rm eff} = T_{\rm eff}\,(\log\, g = 8.35) - T_{\rm eff}\,(\log\, g = 8.00)$, which is the opposite of the quantity $\Delta^{-}T_{\rm eff}$ we calculated in Section 3.3.2. Using the relationship $-\Delta^{-}T_{\rm eff} = 1417 \times \log(T_{\rm eff} \times 0.0001046)$, we corrected the $T_{\rm eff}$ values for those 28 systems from TG09 which did not have an independent mass measurement to the average CV white dwarf mass (i.e. $\log\, g = 8.35$), therefore enabling a consistent combinations of these values with the 36 temperatures that we derived for the COS+STIS data.

3.4.2 Notes on individual objects

Systems observed close to an outburst

As explained in Section 3.2, if a CV experienced an outburst shortly before the ultraviolet observation, its spectrum could be contaminated by disc emission. Furthermore the white dwarf photosphere is heated by the increased infall of material and different subtypes of CVs have different cooling time scales on which they return to their quiescent temperature (Sion 1995, Piro et al. 2005). A spectroscopic analysis of these systems can therefore provide only an upper limit on the white dwarf effective temperature.

For each system, we inspected the light curves retrieved from the AAVSO web site plus a total of additional $\sim$ 2 000 images (collected with the Mount John University Observatory OC61 Telescope, the New Mexico State University Observa-

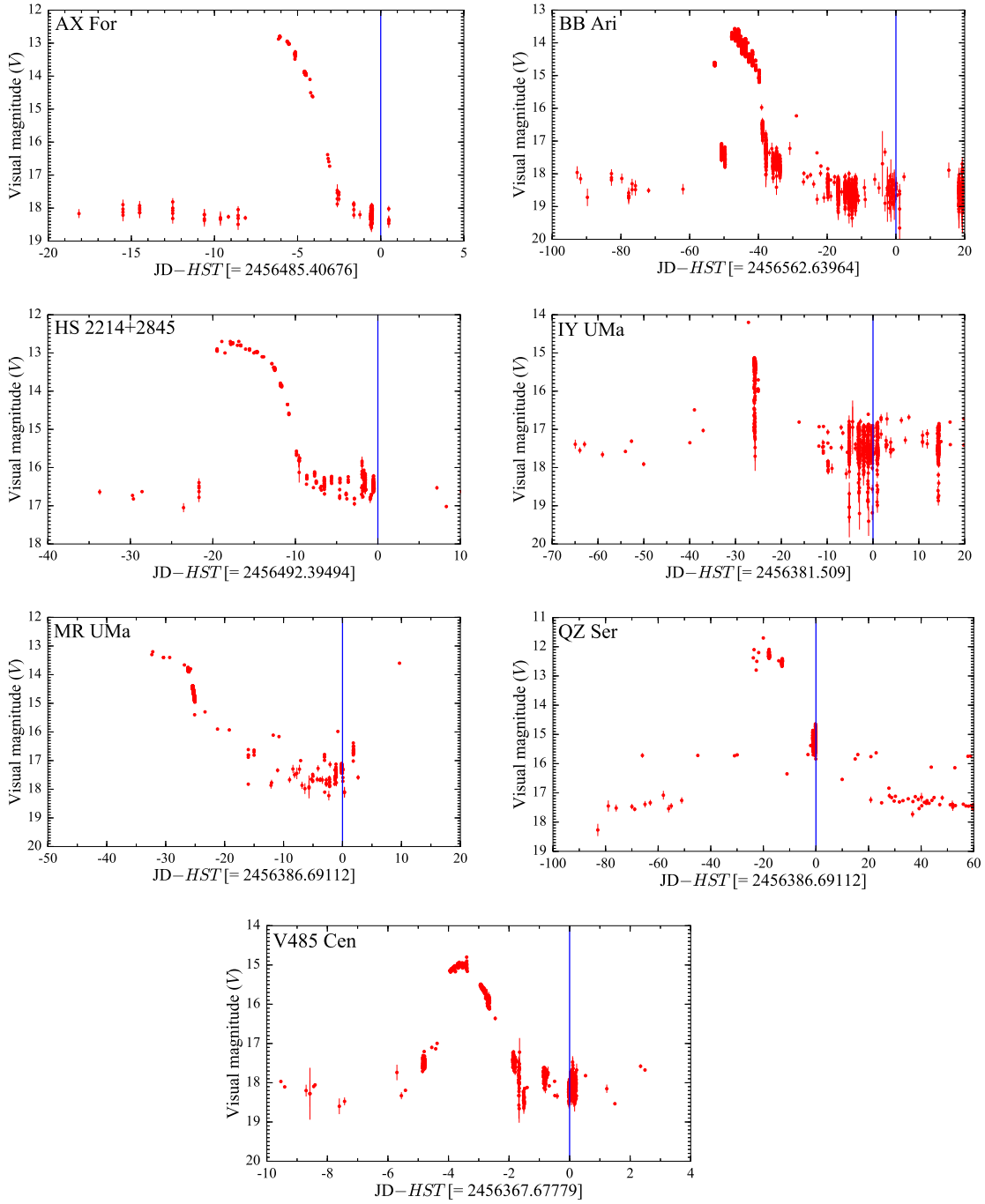

Figure 3.14: Light curves for seven targets in our sample which experienced an outburst within two months before the *HST* observations (indicated with the blue lines). The *HST* observation date has been subtracted from the Julian date. Note the different time range on the x–axis. The data have been retrieved from the AAVSO database.

tory TMO61 telescope and the PROMPT telescopes located in Chile), covering two months before the *HST*/COS observations. We found that nine systems in which the white dwarf dominates the ultraviolet flux went into outburst within this time interval: AX For, BB Ari, HS 2214+2845, IY UMa, MR UMa, QZ Ser, V485 Cen (Figure 3.14), CC Scl (Figure 3.15, left), and SDSS J164248.52+134751.4 (SDSS1642, Figure 3.15, right). QZ Ser and V485 Cen have STIS observations (Section 3.4.2) from which we determined the quiescent temperature while, for the remaining systems, the results that we report here only represent an upper limit for their quiescent $T_{\rm eff}$.

For CC Scl and SDSS1642, we found that the white dwarf contributes only $\simeq$ 35 per cent (Figure 3.16, top) and $\simeq$ 50 per cent of the total flux (Figure 3.16, bottom), respectively. Owing to this strong disc contamination, the derived effective temperatures do not fulfil the requirement of a reliable measurement as defined in TG09, and we do not include them in the following analysis. Furthermore CC Scl is an Intermediate Polar (IP) and its response to accretion and disc instabilities is more complicated than that of a non–magnetic CV. This system is analysed in more detail by Szkody et al. (2017).

Systems with COS and STIS observations

QZ Ser and V485 Cen have been observed both with COS and STIS (Table 3.8). Inspecting their spectra (middle and bottom panel of Figure 3.17), the COS observations have a higher flux compared to the STIS observations, which is also reflected in their effective temperatures; the STIS data return a lower value (QZ Ser: $T_{\rm eff} = 14\,481 \pm 587$ K, V485 Cen: $T_{\rm eff} = 15\,200 \pm 655$ K) compared to the COS data (QZ Ser: $T_{\rm eff} = 15\,425 \pm 676$ K, V485 Cen: $T_{\rm eff} = 16\,208 \pm 746$ K). This difference is not related to difference in the calibration of the two instruments (see Section 3.3.2) and it is rather expected given that the magnitudes derived from the STIS acquisition images suggest that these systems were observed by STIS during the quiescent phase (see Section 3.2.2), whereas the COS spectra were obtained relatively shortly after an outburst (Figure 3.14). Since the temperatures derived from the STIS spectra are representative of the quiescent properties of these systems, we use these values in the discussion below.

COS and STIS observations are available for one additional system: BD Pav (top panel of Figure 3.17). The difference observed among the two data sets (STIS: $T_{\rm eff} = 17\,775 \pm 876$ K, COS: $T_{\rm eff} = 18\,915 \pm 964$ K) could be explained by its eclipsing nature if the STIS snapshot observations were obtained (partly) during the eclipse phase, resulting in a lower observed flux. Unfortunately, a reliable ephemeris is not available for this object and we cannot verify this hypothesis. On the other hand, the two spectra are characterised by a different slope and the derived effective

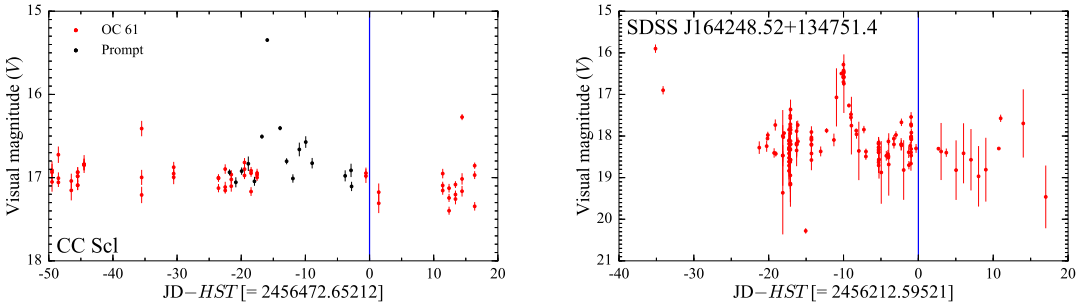

Figure 3.15: *Left*: Prompt and OC61 light curve for CC Scl. *Right*: AAVSO light curve for SDSS J164248.52+134751.4. The blue line represents the date of the *HST* observations which has been subtracted from the Julian date.

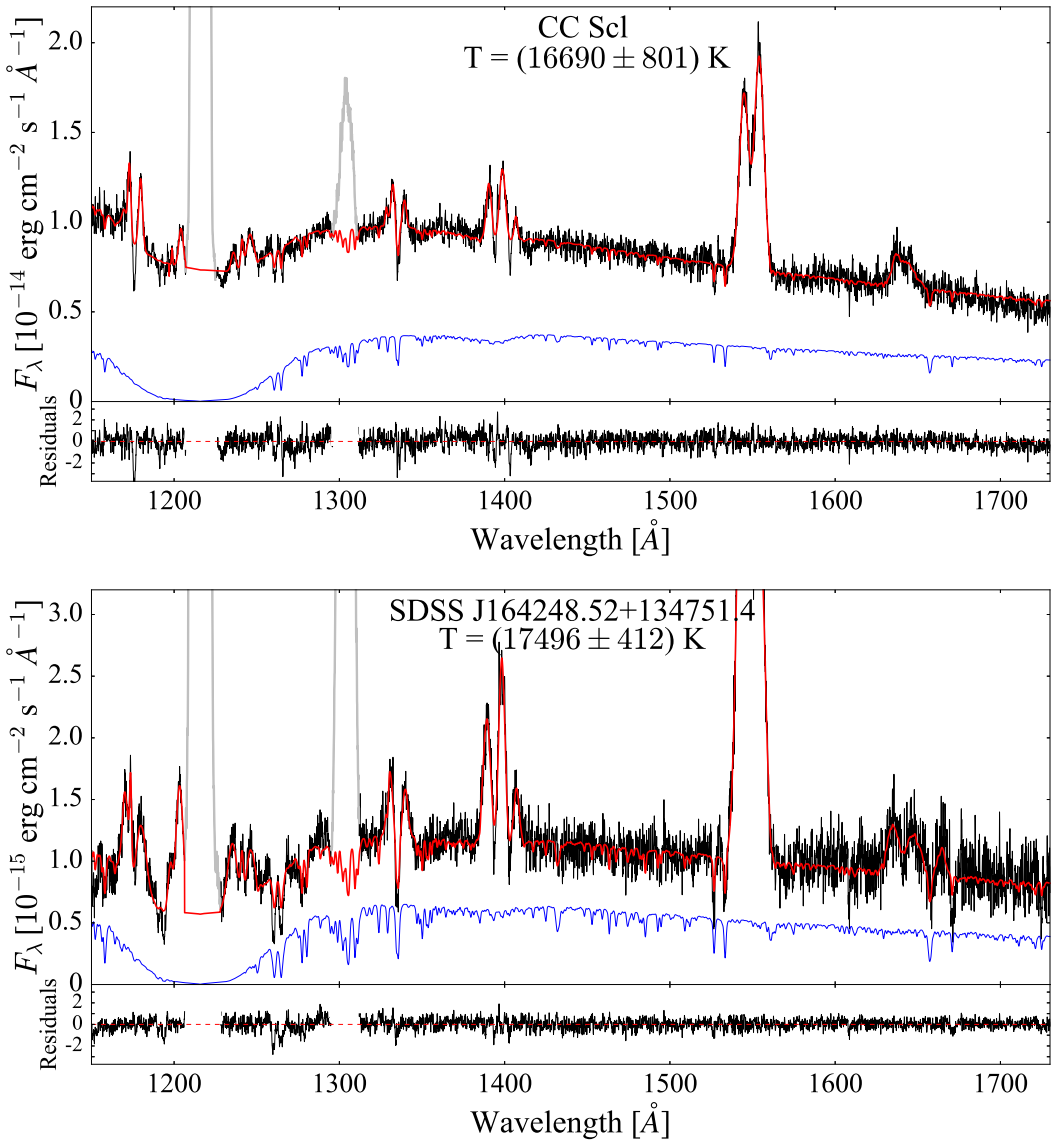

Figure 3.16: *HST*/COS spectra (black) of CC Scl (top) and SDSS J164248.52+134751.4 (bottom) along with the best–fit model (red) assuming a blackbody second component. The white dwarf emission (blue) only contributes $\simeq$ 35 per cent (CC Scl) and $\simeq$ 50 per cent (SDSS1642) of the total flux. The geocoronal emission lines of Lyα (1 216 Å) and O I (1 302 Å) are plotted in grey.

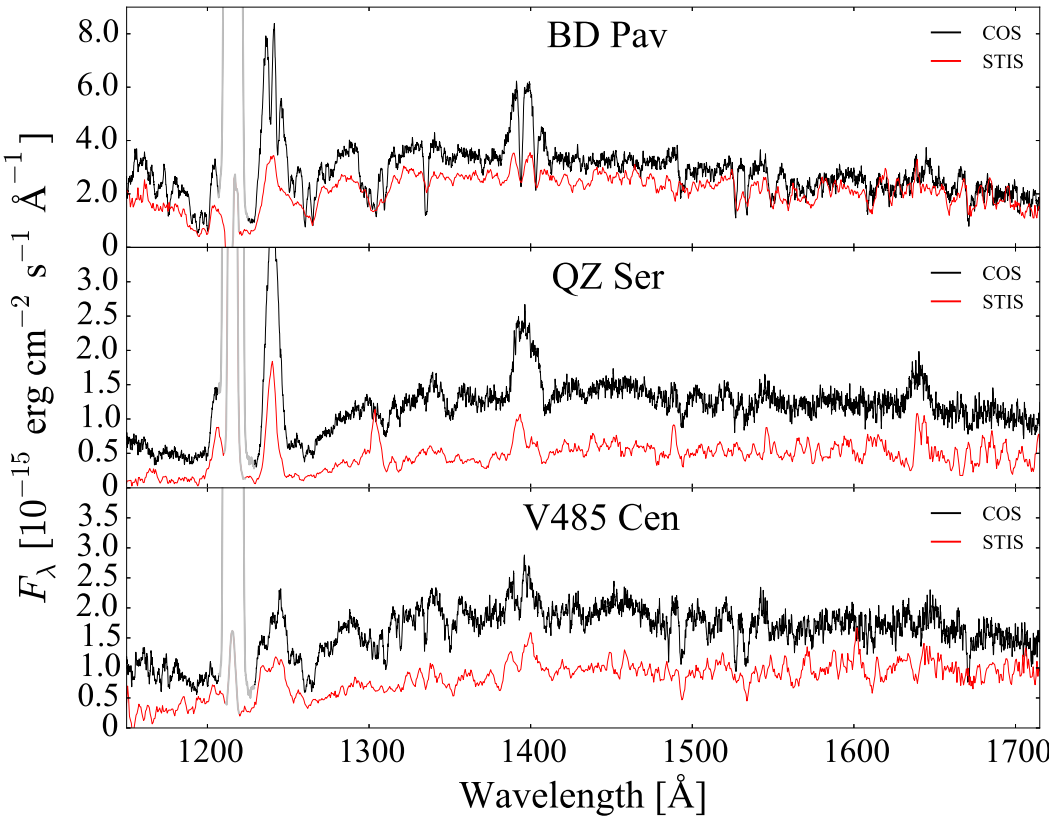

Figure 3.17: *HST*/COS spectra (black) in comparison with the *HST*/STIS spectra (red) of BD Pav, QZ Ser and V485 Cen. The geocoronal Lyα emission (1 216 Å) is plotted in grey.

Table 3.8: Results for BD Pav, QZ Ser and V485 Cen derived from the COS and the STIS data.

Object	Instrument	$T_{\rm eff}$ (K)
BD Pav	STIS	17 775 ± 876
	COS	18 915 ± 964
QZ Ser	STIS	14 481 ± 587
	COS	15 425 ± 676
V485 Cen	STIS	15 200 ± 655
	COS	16 208 ± 746

temperatures differ by $\simeq$ 1 200 K, which could suggest that an outburst occurred before the COS observations. Since BD Pav is a U Gem type CV, its outburst frequency and cooling time are expected to be similar to those of U Gem itself, $\sim$ 120 and $\sim$ 60 days respectively (Sion et al., 1998), i.e. BD Pav is expected to experience a few outbursts every year. In fact, AAVSO observations of BD Pav (available since 1987) show a rough average of one outburst per year, with up to two outbursts observed in years of intense monitoring. No outburst is clearly identifiable

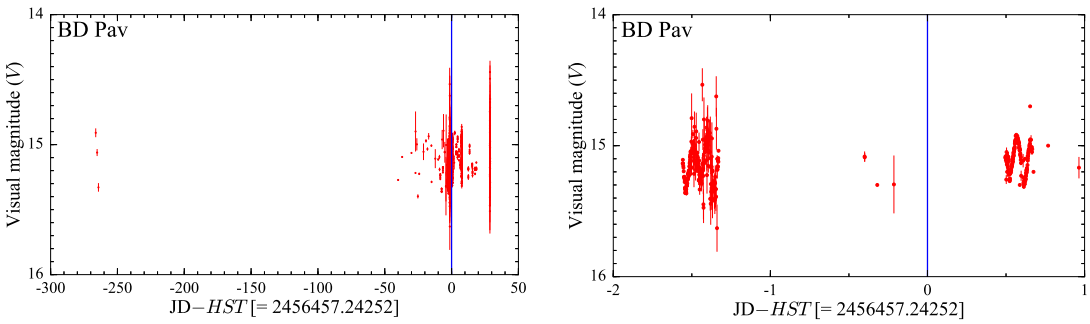

Figure 3.18: *Left*: light curves for BD Pav over the period June 2012 to July 2013. *Right*: close up of the days before the *HST* observations (highlighted with the blue line), which has been subtracted from the Julian date. The system only shows ellipsoidal variations. The data have been retrieved from the AAVSO database.

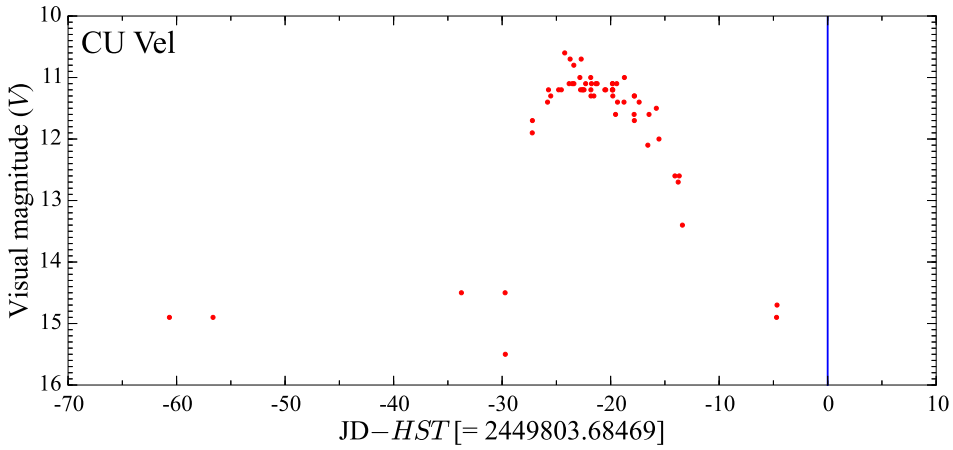

Figure 3.19: Light curve for CU Vel over the period January–April 1995. The blue line represents the date of the *IUE* observations, which has been subtracted from the Julian date. The data have been retrieved from the AAVSO database.

in the AAVSO light curve for the period 2012/2013 (Figure 3.18) but, owing to the relatively sparse sampling, we cannot completely rule out this hypothesis and therefore we consider in the discussion below the lower effective temperature derived from the STIS data.

3.4.3 Systems with previous $T_{\rm eff}$ measurements

Among the 36 systems in our sample, four CVs have a previous $T_{\rm eff}$ determination in the TG09 sample: SDSS J103533.02+055158.4 (SDSS1035), CU Vel, GW Lib and DV UMa, which can be used for comparison with our results. Among them, SDSS1035 and DV UMa have also a previous mass determination and we analyse them in Section 3.4.3.

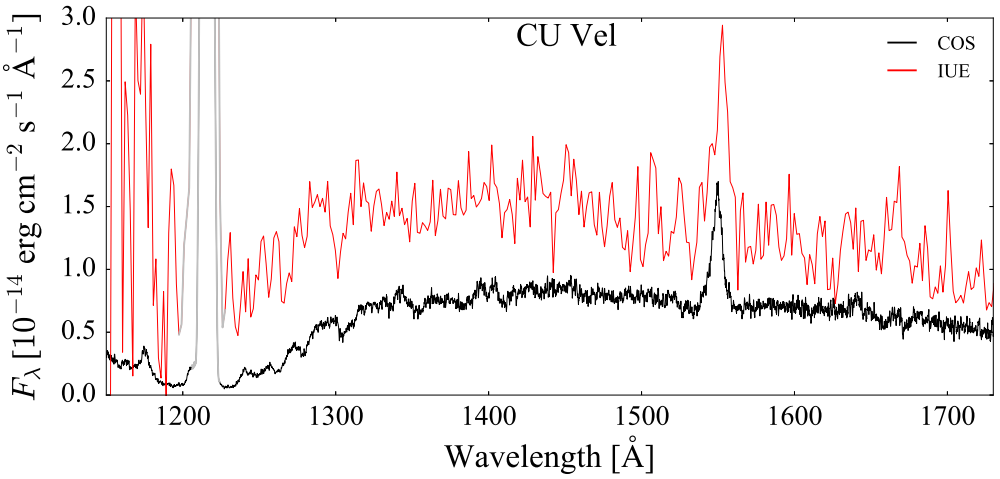

Figure 3.20: *HST*/COS spectrum (black, $T_{\rm eff} = 15\,336 \pm 668$ K) in comparison with the *IUE* spectrum (red, $T_{\rm eff} = 18\,500 \pm 1\,500$ K, Gänsicke and Koester 1999) of CU Vel. The geocoronal Lyα emission (1216 Å) is plotted in grey.

Previous ultraviolet measurements

CU Vel

CU Vel is located in the Vela constellation at a distance of 150 ± 50 pc (Mennickent and Diaz, 2002). Although Vela lies in the galactic plane, given the low distance to the system, CU Vel is not likely severely affected by interstellar reddening. To verify this, we retrieved from the archive the *IUE* spectra of CU Vel, which cover the wavelength range $\simeq 1\,150 - 3\,300$ Å. Inspecting the data, we did not detect the main signature of interstellar dust absorption, i.e. the bump at $\simeq 2\,175$ Å. To estimate the colour excess, we de–reddened the spectrum assuming $E(B-V)$ in the range 0.01 to 0.5. We noticed that for $E(B-V) \gtrsim 0.02$, a positive bump started to be visible in the spectrum, suggesting that we were overestimating the extinction. The low resolution and low signal–to–noise ratio of the *IUE* data did not allow us to accurately measure the colour excess, and we assumed $E(B-V) = 0.02$ as an upper limit, well below the $E(B-V) \simeq 0.1$ threshold defined in Section 3.3.2, concluding that the results for CU Vel are not affected in an appreciable way by interstellar dust absorption.

From the same *IUE* spectrum, Gänsicke and Koester (1999) derived $T_{\rm eff} = 18\,500 \pm 1\,500$ K. This temperature is significantly higher than $T_{\rm eff} = 15\,336 \pm 668$ K derived here from the COS data. To rule out any possible calibration differences among the two instruments, we compared the *IUE* and COS spectra for the flux standard white dwarf WD 0308–565. The flux levels of the different datasets are in good agreement, with an average difference of $\simeq 3$ per cent, and therefore the difference in the effective temperatures are not related to instrument calibration issues. Inspecting the AAVSO light curve of CU Vel, we find that the system ex-

perienced an outburst 20 days before the *IUE* observations (Figure 3.19), which explains the higher ultraviolet flux observed with *IUE* compared to that of our new *HST*/COS data (Figure 3.20), and the higher temperature determined by Gänsicke and Koester (1999).

GW Lib

GW Lib has been observed with *HST* before (January 2002, Szkody et al. 2002b) and after (March 2010 and April 2011, Szkody et al. 2012) its superoutburst in April 2007. In these works, the authors assume $\log g = 8.0$ and $\log g = 8.7$, respectively, so we cannot directly compare our and their results.

Toloza et al. (2016) present a new analysis of all these *HST* observations. They re–fit the data assuming $\log g = 8.35$ and find $T_{\rm eff} = 14\,695^{+13}_{-11}$ K for the 2002 dataset, $T_{\rm eff} = 17\,980 \pm 14$ K and $T_{\rm eff} = 15\,915 \pm 9$ K for the 2010 and 2011 observations, respectively.

GW Lib is a very peculiar system and a comparison between our ($T_{\rm eff} = 16\,995 \pm 813$ K) and these previous temperature measurements has to be considered with some caution. Indeed, GW Lib not only hosts a pulsating white dwarf but it also showed variations in $T_{\rm eff}$ of $\simeq 3000$ K throughout the course of the *HST* observations (Toloza et al., 2016). Moreover, assuming $\log g = 8.35$, Szkody et al. (2016) derived $T_{\rm eff} = 17\,560 \pm 9$ K from 2015 *HST*/COS data, showing that the system has not cooled back to its quiescent temperature yet. Therefore the $T_{\rm eff}$ derived here is only an upper limit for the quiescent white dwarf temperature and therefore, in the following analysis, we assume as $T_{\rm eff}$ for GW Lib the one derived for the 2002 dataset by Toloza et al. (2016) for $\log g = 8.35$, $T_{\rm eff} = 14\,695$ K. The mass of the white dwarf in GW Lib has been measured by Szkody et al. (2012, $M_{\rm WD} = 0.79 \pm 0.08\,{\rm M}_{\odot}$) and van Spaandonk et al. (2010, $M_{\rm WD} = 0.84 \pm 0.02\,{\rm M}_{\odot}$). However, these mass estimates depend on using velocity amplitude of the secondary star derived from the narrow Ca II emission lines during outburst (assuming they originate on the irradiated face of the donor star), and do not fulfil the accuracy requirement to be included in the sample from Zorotovic et al. (2011), which represents the reference for our analysis. We therefore preferred a more conservative approach and assumed as uncertainty of the effective temperature, the one related to the unknown mass of the white dwarf, ± 812 K (Section 3.3.2).

Systems with a measured mass

As discussed in Section 3.3, it is not possible to break the degeneracy between $T_{\rm eff}$ and $\log g$ solely from the fit to the *HST* data and therefore we assumed $\log g = 8.35$ ($M_{\rm WD} = 0.8\,{\rm M}_{\odot}$). Although several CVs in our sample have published mass estimates (e.g. BD Pav, QZ Ser), only four of them have a mass measure-

ment that is accurate enough to be included in the study of Zorotovic et al. (2011, see their table 1): SDSS J103533.02+055158.4 (SDSS1035), IY UMa, DV UMa and SDSS J100658.41+233724.4 (SDSS1006). A previous $T_{\rm eff}$ that can be considered reliable is only available for SDSS1035 and DV UMa, which we discuss in the following.

Littlefair et al. (2006) carried out a colour analysis of the SDSS1035 light curves during the white dwarf eclipse. From the observed shape of the white dwarf and bright spot eclipses, they measured a white dwarf mass of $M_{\rm WD} = 0.835 \pm 0.009\,{\rm M}_{\odot}$ and an effective temperature of $T_{\rm eff} = 10\,100 \pm 200\,{\rm K}$. The effective temperature we derived here, $T_{\rm eff} = 11\,620 \pm 44\,{\rm K}$, is $\simeq 1500\,{\rm K}$ higher than the temperature measured by Littlefair et al. (2006). Since our assumption of $\log g = 8.35$ is consistent with the measured white dwarf mass, we can conclude that this difference is related to the different methods used (light curves analysis vs. spectroscopic analysis).

While the masses of SDSS1035 correspond, within the errors, to $\log\, g = 8.35$, the mass of DV UMa is substantially higher: $M_{\rm WD} = 1.098 \pm 0.024\,{\rm M}_{\odot}$ (Savoury et al., 2011), which corresponds to $\log\, g = 8.78$. To take into account the independently measured surface gravity, we repeated the fit assuming $\log\, g = 8.78$, which returned $T_{\rm eff}(\log\, g = 8.78) = 18\,874 \pm 182\,{\rm K}$. As expected, this value is higher than the temperature we obtained for $\log g = 8.35$, i.e. $T_{\rm eff}(\log g = 8.35) = 18\,176 \pm 108\,{\rm K}$, and demonstrates that, if the masses were known, we could measure effective temperatures with an accuracy of $\simeq 200\,{\rm K}$, appreciably more accurate than the uncertainty estimate recommended here for all systems without measured masses.

Feline et al. (2004) and Savoury et al. (2011) measured the temperature of DV UMa from light curve analyses and report $T_{\rm eff} = 20\,000 \pm 1\,500\,{\rm K}$ and $T_{\rm eff} = 15\,500 \pm 2\,400\,{\rm K}$. Our result is in agreement with the temperature from Feline et al. while it is hotter than the measurement from Savoury et al. (2011). Comparing the DV UMa spectrum (Figure 3.2, bottom) to the spectra of cooler systems (Figure 3.2, top and middle panels), it is easily recognizable that the narrower Lyα profile and the absence of quasi–molecular bands require $T \gtrsim 19\,000\,{\rm K}$. Thus we are confident that our measurement is a realistic measure of the temperature of the white dwarf. DV UMa exemplifies how space–based ultraviolet spectroscopic measurements can give $T_{\rm eff}$ to about one per cent accuracy compared to the $\simeq 10-15$ per cent accuracy achievable from ground–based optical light curve analysis.

As a final caveat, we have to bear in mind that comparing effective temperatures measured at different epochs is always a delicate matter since a genuine temperature change can occur owing to increases of the system mass–transfer rate above its quiescent value.

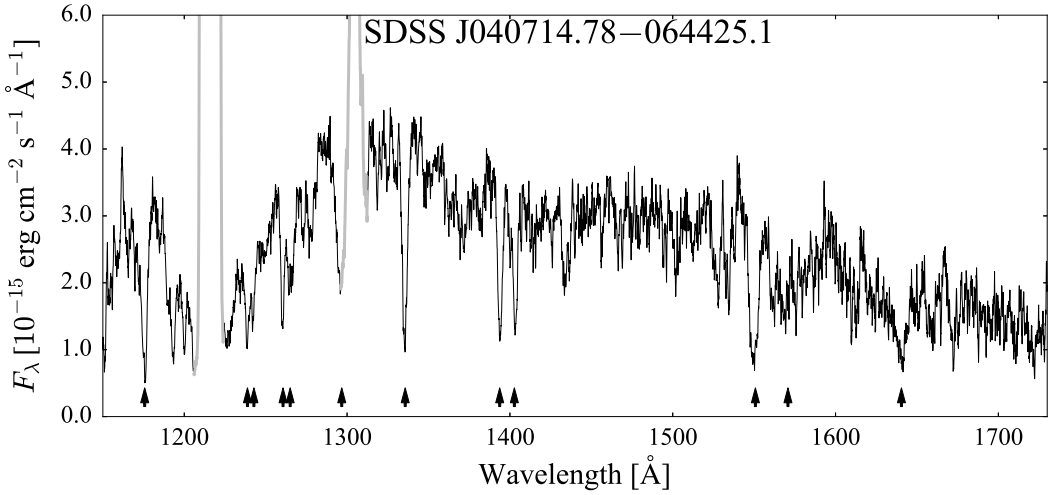

Figure 3.21: *HST*/COS spectrum of SDSS J040714.78–064425.1. The arrows highlight the position of those lines which are contaminated by or arise from absorption within the veiling gas: C III (1 175 Å), N V (1 242 Å), Si II (1 260 Å), Si III (1 298 Å), C II (1 335 Å), Si IV (1 400 Å), C IV (1 550 Å) and broad absorption bands from Fe II (1 568 Å and 1 636 Å). The geocoronal emission lines of Lyα (1 216 Å) and O I (1 302 Å) are plotted in grey.

3.4.4 Eclipsing systems

In eclipsing CVs, the line of sight can pass through material extending above the disc, giving rise to strong absorption features. This has been observed for example in OY Car, where a forest of blended Fe II absorption lines (the so–called "iron curtain") veil the white dwarf emission (Horne et al., 1994). Our sample contains seven eclipsing systems: BD Pav, DV UMa IR Com, IY UMa, SDSS J040714.78–064425.1 (SDSS0407), SDSS1006 and SDSS1035. While the observations of BD Pav, IR Com and SDSS1035 are not strongly affected by the veiling gas, in the spectra of the remaining systems the curtain signature is revealed by several absorption features (Figure 3.21), which modify the overall slope of the spectrum and contaminate the core of the Lyα line, the main tracers for the white dwarf effective temperature.

In order to estimate how our measurements and their uncertainties are affected by the presence of the veiling gas we carried out an exploratory study of each eclipsing CV. Inspecting their spectra, we identify strong C IV (1550 Å) lines, suggesting the presence of hot gas along the line of sight, but also broad absorption bands from Fe II ($\simeq$ 1568 Å and $\simeq$ 1636 Å), which instead imply cold veiling gas. We therefore assumed that the white dwarf spectrum is attenuated by two homogeneous slabs, one cold ($T \simeq 10\,000$ K) and one hot ($T \simeq 80\,000 - 100\,000$ K). We used SYNSPEC to generate models for the monochromatic opacity of the slabs which, combined with the column densities, returns the absorption due to the curtain.

The purpose of this study is not to determine the best–fitting model for the curtains but to determine the white dwarf effective temperature and realistic

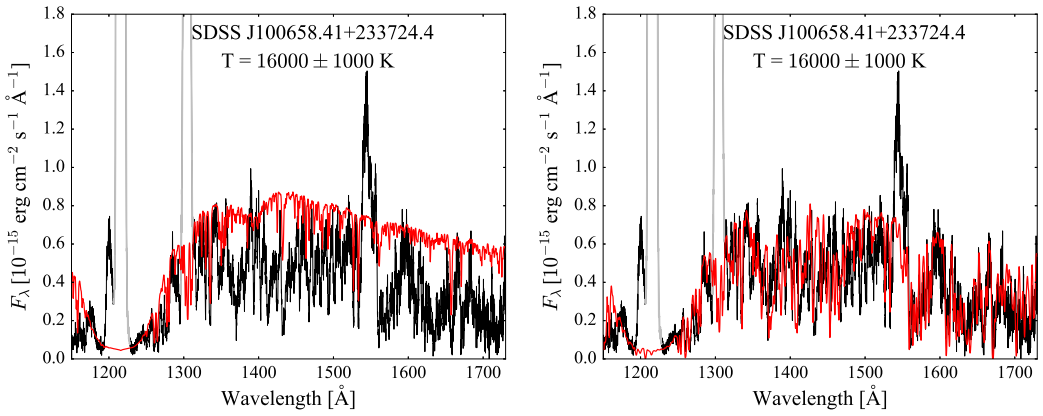

Figure 3.22: *HST*/COS spectrum (black) of SDSS J100658.41+233724.4 along with the best model (red) assuming a constant second component, with (right) and without (left) absorption from two slabs with different temperatures. The geocoronal emission lines of Lyα (1 216 Å) and O I (1 302 Å) are plotted in grey.

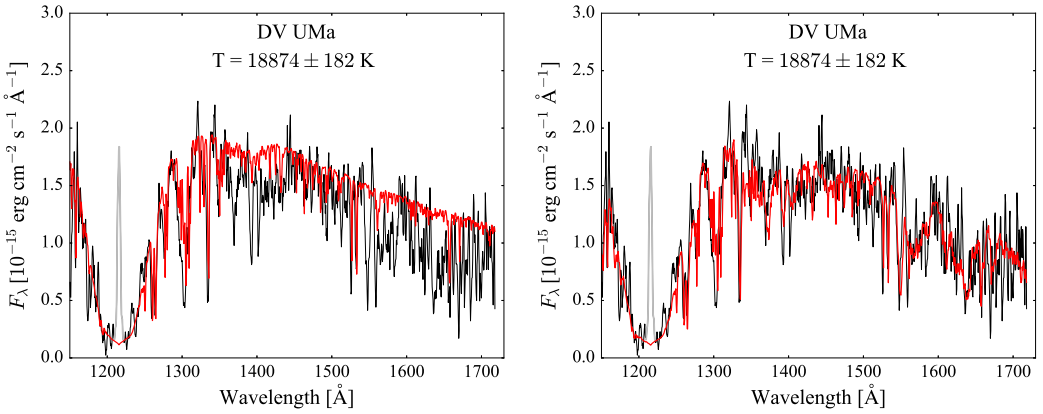

Figure 3.23: *HST*/STIS spectrum (black) of DV UMa along with the best model (red) assuming a constant second component, with (right) and without (left) absorption from two slabs with different temperatures. The geocoronal emission line of Lyα (1216 Å) is plotted in grey.

Table 3.9: Optimal set of parameters for the two homogeneous slabs, one cold and one hot, veiling the white dwarf spectrum in the eclipsing systems.

System	Cold slab parameters				Hot slab parameters			
	$T_{\rm eff}$ (K)	$\log(n_{\rm e} \cdot {\rm cm}^3)$	$\log(N_{\rm H} \cdot {\rm cm}^2)$	$V_{\rm t}$ (km s^{-1})	$T_{\rm eff}$ (K)	$\log(n_{\rm e} \cdot {\rm cm}^3)$	$\log(N_{\rm H} \cdot {\rm cm}^2)$	$V_{\rm t}$ (km s^{-1})
IY UMa	10 000	12.0	20.5	200	100 000	18.7	20.3	200
DV UMa	10 000	12.0	19.8	50	80 000	18.0	20.7	20
SDSS0407	10 000	12.0	19.9	250	100 000	18.7	19.9	200
SDSS1006	10 000	12.0	21.6	200	100 000	18.0	21.8	200

uncertainties. We varied the curtain parameters manually, exploring the space of four free parameters defining each slab (effective temperature $T_{\rm eff}$, electron density $n_{\rm e}$, turbulence velocity $V_{\rm t}$ and column density $N_{\rm H}$) and the white dwarf $T_{\rm eff}$ and

scaling factor. We started from the white dwarf effective temperature determined following the prescription from Section 3.3. Since the problem already contains a large number of free parameters, we used a constant as second additional component. We attenuated the white dwarf emission using the best matching model for the curtain we could identify and then changed the white dwarf temperature and scaling factor to better reproduce the observed spectrum. We repeated this procedure iteratively until we found the optimal set of parameters (Table 3.9), which define the final white dwarf $T_{\rm eff}$. This exercise allowed us to estimate that the systematic uncertainties introduced by the curtain are of the order of $\simeq 1\,000$ K for IY UMa, SDSS0407 and SDSS1006. Except for SDSS0407, this uncertainty is bigger than the systematic due to the unknown mass of the white dwarf and it is the value we use in the following analysis. In Figure 3.22, we show the spectrum of SDSS1006 (black), which is dominated by several strong absorption bands. A white dwarf model alone (red, left) cannot adequately reproduce the observed flux level, which instead is well modelled including additional absorption from two slabs with different temperatures (red, right).

Finally, in the case of DV UMa (Figure 3.23), the main source of contamination comes from the iron bands in the red portion of the spectrum. Weaker absorption features are present at shorter wavelengths but they do not contaminate the Lyα region. For this reason we found that the veiling gas has no effect on the white dwarf temperature and therefore our result from Section 3.4.3 remains unchanged.

3.4.5 Effective temperature of CV white dwarfs as a probe of their evolution

In Figure 3.24 we show our sample (circles, red for COS data and blue for STIS data) and the corrected effective temperatures for the non–magnetic systems from TG09 (green triangles). While TG09 also included magnetic CVs observed in low state, we only observed non–magnetic systems (except for CC Scl, which is an Intermediate Polar). We exclude the magnetic systems from the following discussion, as their evolution may differ from that of non–magnetic CVs due to (potential) suppression of magnetic braking (Webbink and Wickramasinghe, 2002; Araujo-Betancor et al., 2005a; Ferrario et al., 2015).

The uncertainties in the two samples are dominated by the unknown white dwarf mass. It is important to notice that these uncertainties are of the order of $\simeq 300 - 1\,800$ K (see Section 3.3.2), therefore the overall shape of the distribution is unlikely to change once the white dwarf masses are accurately determined.

The white dwarf $T_{\rm eff}$ is set by the compressional heating of the accreted material (Townsley and Bildsten, 2004) and provides a measurement of the secular

mean accretion rate $\langle \dot{M} \rangle$ as defined by Townsley and Bildsten (2003). By comparing the distribution shown in Figure 3.24 with results from population synthesis calculations (see e.g. the $\dot{M} - P_{\rm orb}$ plane in figure 2b from Goliasch and Nelson 2015), we can test the models for the present day CV population.

Our results show that long period systems have typical mass transfer rates of $\dot{M} \simeq 10^{-10}$ to $\simeq 10^{-9}\,{\rm M_\odot yr^{-1}}$, while systems below the period gap are characterised by a lower average, $\dot{M} \simeq 5\times10^{-11}\,{\rm M_\odot yr^{-1}}$. This difference is in accordance with the angular momentum loss mechanisms which are thought to dominate the different phases of CV evolution (magnetic braking above and gravitational wave radiation below the period gap[5]).

Nonetheless, the presence of clear discrepancies with the standard model of CV evolution are highlighted by comparing our results with the evolutionary track[6] (Figure 3.24, red line) computed for a system with a $0.8\,{\rm M_\odot}$ white dwarf accreting from a donor with an initial mass of $M_2 = 0.65\,{\rm M_\odot}$ and an initial orbital period of 12 hours, representative of a typical CV. Above the period gap, several systems with $T_{\rm eff} \simeq 40\,000 - 50\,000\,{\rm K}$ are present in the range $P_{\rm orb} \simeq 180 - 240\,{\rm min}$. These objects are known as VY Scl systems and are usually characterised by high temperatures, which indicate very high accretion rates onto the white dwarf, with $\langle \dot{M} \rangle$ about ten times above the value predicted by the standard evolution theory (TG09, Howell et al. 2001). Goliasch and Nelson (2015) suggested that these objects could arise naturally from systems close to the regime of unstable mass transfer – where the mass of the donor star is similar to the white dwarf mass – but this hypothesis needs to be investigated in more detail.

The effective temperatures at $P_{\rm orb} \gtrsim 3\,{\rm h}$ indicate that there is more diversity above the period gap than expected from the results of TG09. Considering only the green points (non–magnetic CV from TG09), the systems above the period gap present clearly higher temperatures than the systems below. In contrast, the new systems from this work (red and blue circles) are characterised by surprisingly low temperatures, and the difference between CVs above and below the gap is not as pronounced as before. Our selection criteria, particularly the requirement that the white dwarf and/or the secondary should be detectable in the optical spectrum of the system, could favour the selection of such low mass accretion rate CVs,

[5]When the secondary star becomes fully convective ($P_{\rm orb} \simeq 3$h), it loses its radiative core, and the magnetic stellar wind, which sustains magnetic braking, is thought to be greatly reduced. In fact, there is good observation evidence for a decrease in the efficiency of magnetic braking in CVs (Schreiber et al., 2010) as well as in single stars (Reiners and Basri, 2008). At this point, in the standard model of CV evolution, the evolution of the system is thought to be driven only by gravitational wave radiation. However, there are arguments for an angular momentum loss that is larger than produced by pure gravitational wave radiation below the period gap, suggesting the presence of a 'residual' magnetic braking at short periods (Patterson 1998, Knigge et al. 2011).

[6]Evolutionary track computed using MESABINARY revision 8845 and inlists provided by Paxton et al. (2015) for the cataclysmic variable case (their figure 5).

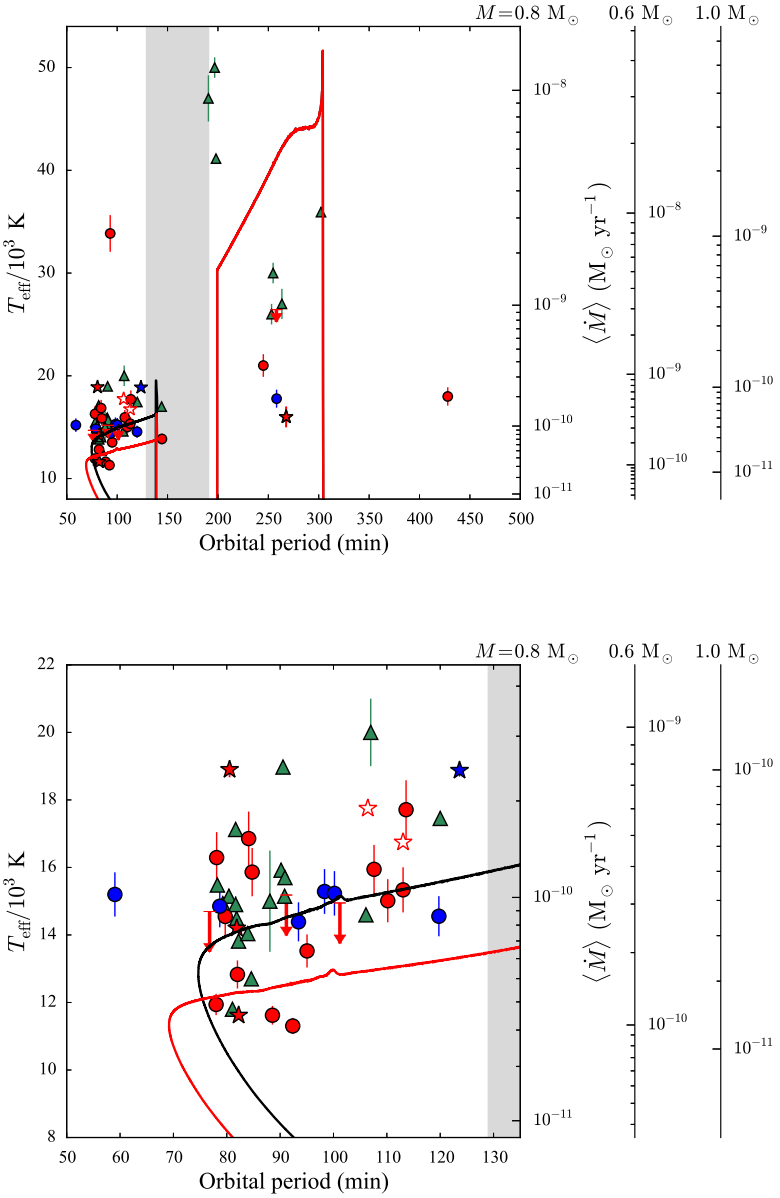

Figure 3.24: *Top:* effective temperature as function of the orbital period from this work (circles, red for COS data, blue for STIS data) and for the non–magnetic system from Townsley and Gänsicke (2009, green triangles). Systems for which only an upper limit has been determined are shown with a downward arrow. The systems for which a mass measurement is available are shown with a starred symbol. IY UMa and AX For, for which a mass measurement is available but only an upper limit on their effective temperatures has been determined, are shown with an empty star. Some temperatures in the TG09 sample do not have an associated error. In these cases, we estimated the corresponding uncertainty using our Equation 3.2 as described in Section 3.4.1. The solid lines represent the evolutionary tracks for a system with a $0.8\,M_\odot$ white dwarf accreting from a donor with an initial mass $0.65\,M_\odot$, and an initial orbital period of 12 hours. The red track has been generated with the classical recipe for CV evolution (gravitational wave radiation only below the period gap) while the black track includes a "residual" magnetic braking equal to the gravitational wave radiation AML when the donor has no radiative core. The two tracks overlap above the period gap. The small bump at $P_{\rm orb} \simeq 100$ min is a computational artefact arising in the change of equation of state table describing the secondary internal structure. The grey band highlights the period gap while, on the right, a mapping to $\langle \dot{M} \rangle$ calculated through equation 1 from TG09 is shown for $M = 0.8$, 0.6 and $1.0\,M_\odot$, respectively. *Bottom:* closeup of the systems below the period gap.

thus potentially introducing an observational bias. Nonetheless, the mere existence of cold CV white dwarfs at these long orbital periods is clearly in contrast with the currently available models of CV evolution. However, the currently still small number of effective temperatures available in this period range makes it difficult to draw any definitive conclusions on these results. The overall picture is additionally complicated by the presence of the unexpectedly hot novalike systems. Novalikes are non–magnetic CVs and are further sub–divided into VY Scl systems, which have been detected at least once during a state of low accretion activity, and UX UMa systems, which have no recorded low states (Dhillon, 1996). This dichotomy is naturally subject to observational biases. Since the white dwarfs in novalike CVs are always/often hidden by the disc emission, it is difficult to measure their effective temperature and more observations are needed to increase the number of systems with an accurate $T_{\rm eff}$ above the period gap. Additional constraints will be provided in the next few years by *Gaia*: from its accurate parallaxes, we will determine an upper limit on the white dwarf effective temperatures of all disc–dominated CVs for which ultraviolet spectroscopy is available, improving our understanding of CV evolution above the period gap.

At short orbital periods, we note the presence of an extreme outlier, SDSS J153817.35+512338.0, with an effective temperature of $T_{\rm eff} = 33\,855 \pm 1\,785$ K. This is *much hotter* than expected given its short orbital period ($P_{\rm orb} = 93.11$ min), i.e. for CVs with $P_{\rm orb} \lesssim 2$h, $T_{\rm eff} \simeq 15\,000$ K. This temperature is incompatible with mere accretion heating, but suggests that the system is either a young CV which just formed at this orbital period, that it had a recent period of sustained high mass transfer, or that it recently experienced a nova explosion and the white dwarf has not cooled down yet.

The bottom panel of Figure 3.24 shows a closeup of the systems below the period gap. We note two unexpected features: (i) there is a large scatter near $P_{\rm orb} \simeq 80$ min, in contrast to theoretical predictions that suggest a well defined $T_{\rm eff}$ at the period minimum and, (ii) the effective temperatures show a steeper decrease towards short periods, and a mean accretion rate about twice above that expected from pure GWR AML. For comparison, we overplot a second evolutionary track (black) computed including a "residual" magnetic braking equal to the gravitational wave radiation AML when the donor has no radiative core. The new track agrees better with the observed $T_{\rm eff}$ decrease and the observed orbital period minimum than the standard recipe for CV evolution. Although the new track does not accurately reproduce the observed slope towards the period minimum, its better match to the measured effective temperatures strongly supports the ideas of additional AML mechanisms than GR below the period gap, which have been suggested as "residual magnetic braking" by Patterson (1998) and Knigge et al. (2011) and, more recently,

as consequential angular momentum loss (CAML) by Schreiber et al. (2016) and Nelemans et al. (2016).

Finally, reaching the minimum period, CVs are expected to evolve back towards longer periods with mean accretion rates of $\dot{M} \lesssim 2 \times 10^{-11}\,\mathrm{M}_{\odot}\,\mathrm{yr}^{-1}$, corresponding to $T_{\rm eff} \lesssim 11\,500\,\mathrm{K}$ and the standard model of CV evolution predicts that about 70 per cent of the present day CVs should be found in this phase (Section 1.4.1). However, we find only two period bouncer candidates in our sample: 1RXS J105010.8–140431 ($P_{\rm orb} = 88.56\,\mathrm{min}$, $T_{\rm eff} = 11\,622 \pm 277\,\mathrm{K}$) and QZ Lib ($P_{\rm orb} = 92.36\,\mathrm{min}$, $T_{\rm eff} = 11\,303 \pm 238\,\mathrm{K}$) which are characterised by effective temperatures $\simeq 3\,000 - 4\,000\,\mathrm{K}$ lower than those of the other systems at similar orbital periods, and both have also been identified as possible period bouncers by Patterson (2011). However these two systems have still higher temperatures than predicted by the theory and do not fall onto either of the lower two branches of the evolutionary tracks in Figure 3.24. This could suggest the presence of enhanced AML in the post–bounce regime. This would consequently imply faster evolution than predicted by the standard theory, which could be a possible explanation for the dearth of this component of the CV population in the observed samples.

The lack of unambiguous period bouncers in our sample cannot be explained by selection biases: we selected our targets among CVs that experience rare outbursts and for which the white dwarf is visible in their optical spectra. However, given their extremely low mass–transfer rate, period bouncers are expected to be intrinsically faint. In fact, assuming the average distance of the CVs in our sample $\langle d \rangle \simeq 320\,\mathrm{pc}$, the expected apparent V–band magnitude for a period bouncer with $T_{\rm eff} \simeq 9\,000\,\mathrm{K}$ and $\log g = 8.35$ would be $V \simeq 20.5\,\mathrm{mag}$ (calculated using synthetic colours and evolutionary sequences of Hydrogen atmosphere white dwarfs[7], Holberg and Bergeron 2006, Kowalski and Saumon 2006, Tremblay et al. 2011, Bergeron et al. 2011) and therefore it is possible that we are limited by the present observational technologies which are not sensitive enough to identify these elusive systems.

3.4.6 CV white dwarf masses

Our results exemplify how the combination of accurate mass measurements and space–based ultraviolet spectroscopic during the quiescent state allows to measure CV white dwarf $T_{\rm eff}$ to about one per cent accuracy, thus allowing to test the present model of CV evolution. Furthermore, obtaining accurate mass measurements is important in order to test the mass erosion versus mass growth hypotheses (Section 1.6.2). Our results have unveiled the presence of high–mass ($\simeq 0.9\mathrm{M}_{\odot}$) white dwarfs in the four systems we observed. These results are in agreement with the

[7] http://www.astro.umontreal.ca/~bergeron/CoolingModels

findings from Zorotovic et al. (2011) and show how, using phase–resolved medium resolution optical observations, we are able to accurately measure the masses of accreting white dwarfs. However, this method has some limitations since optical spectra are often contaminated by strong disc emission, making the identification of both the white dwarf and secondary signature challenging. In fact, out of the 23 CV for which we acquired phase–resolved observations, we were able to reconstruct the radial velocity curve for only four of them.

A more successful method which does not require the identification of the secondary consists in combining ultraviolet spectroscopy with the distance to the system. If the distance is known, then the scaling factor between the best–fit model and the ultraviolet spectrum returns the white dwarf radius; by assuming a mass–radius relationship it is then possible to measure the mass of the white dwarf. (Section 2.4.4). Next year, the ESA *Gaia* mission will provide accurate parallaxes in the second data release DR2 for all the targets in our *HST* sample. Moreover this method can be applied to all CVs for which ultraviolet spectroscopy is available and will allow to quadruple the current number of systems with an accurate mass determination.

While waiting for DR2, several tools developed by the *Gaia* Data Processing and Analysis Consortium (DPAC) are available that allow to perform simulations on the results that can be achieved with *Gaia*. Particularly, the PyGaia Python toolkit[8] provides Python modules to simulate the expected errors on the parallaxes.

In order to estimate the accuracy that we will be able to achieve on the CV white dwarf masses once the *Gaia* DR2 and final (DR4) releases will be available, we selected the 20 CVs in our sample for which (i) a distance estimate is available (Table 3.7) and (ii) the ultraviolet emission is dominated by the white dwarf, and performed a simulation with PyGaia. For each system, we convolved the best fit model to the ultraviolet *HST* data with the V and I filter profiles, thus obtaining their magnitudes in those passbands. Similarly, we computed the corresponding magnitude for the G_p *Gaia* filter (central wavelength of 5 044.37 Å and full width at half–maximum of 2 529.83 Å), useful to compare the brightness of each system with the *Gaia* limiting magnitude ($G_p \simeq 20$ mag). The inputs for the simulation are: the right ascension and declination, the G_p and I magnitudes, the $V - I$ colour and the distance d and its relative uncertainty. Using the coordinates to establish the number of observations that *Gaia* will obtain in that direction, and the photometry and distance to simulate the brightness and the expected displacements during the duration of the *Gaia* mission, PyGaia returns the uncertainties on the parallaxes for DR2 and DR4 (σ_π, Table 3.10).

The results of the simulation are shown in Figure 3.25: the uncertainties

[8] https://pypi.python.org/pypi/PyGaia/

Table 3.10: Simulated accuracy on the *Gaia* parallaxes estimated with PyGaia and the corresponding accuracy on the mass determination.

System	distance	V	G_p	Parallax accuracy (%)		Mass accuracy (%)	
	(pc)	(mag)	(mag)	DR2	DR4	DR2	DR4
GW Lib	140	17	17.1	2	1	2	1
V844 Her	290	18.7	18.7	12	7	14	9
SDSS J013701.06–091234.8	300	19.4	19.4	16	9	18	11
SDSS J123813.73–033932.9	190	18.7	18.7	7	5	6	4
V1108 Her	130	18.2	18.2	2	1	1	1
ASAS J002511+1217.2	130	18.6	18.6	4	3	5	3
SDSS J103533.02+055158.4	170	19.3	19.3	11	7	13	8
1RXS J105010.8–140431	100	17.4	17.4	1	1	1	1
QZ Lib	120	19.6	19.6	7	4	8	5
1RXS J023238.8–371812	160	19.3	19.4	7	4	8	5
IY UMa	190	18.5	18.5	4	3	5	3
RZ Leo	340	19.4	19.4	23	14	24	16
CU Vel	150	17.3	17.4	2	1	2	1
AX For	370	19.1	19.2	16	10	15	10
QZ Ser	460	20.3	20.3	69	42	30	28
DV UMa	504	19.6	19.7	28	17	10	8
IR Com	300	18.7	18.7	8	5	7	4
BD Pav	500	19.1	19.1	29	18	28	20
SDSS J100658.41+233724.4	676	20.5	20.5	76	46	29	28
HS0218+3229	1000	19.7	19.7	96	58	30	27

on the parallaxes increase with the distance and with G_p magnitudes. Systems close the *Gaia* limiting magnitude and with large uncertainty on the distance (such as BD Pav, SDSS1006 and HS0218), have the largest uncertainties on the *Gaia* parallaxes.

This correlation of σ_π with distance and brightness reflects in the mass accuracy than can be achieved (Figure 3.26): $\lesssim 10\,\%$ for $d \lesssim 300\,\mathrm{pc}$ and $G_p \lesssim 18.7\,\mathrm{mag}$ with DR2. DR4 will improve this limit by typically $\simeq 60\%$ and will allow to achieve accuracy of $\lesssim 10\,\%$ for $d \lesssim 500\,\mathrm{pc}$ and $G_p \lesssim 19.5\,\mathrm{mag}$. Given that the average distance and magnitude of the CVs in our sample are $\langle d \rangle \simeq 320\,\mathrm{pc}$ and $\langle V \rangle \simeq 17.8\,\mathrm{mag}$, we expect to achieve an accuracy on the masses of $\simeq 2\,\%$ with the *Gaia* DR2 data, which will be further reduced to $\simeq 1\,\%$ with the final data release.

3.5 Conclusions

From a large *HST* survey of 45 cataclysmic variables we find 36 systems in which the white dwarf dominates the ultraviolet flux, as revealed by broad Lyα absorption. We determine the white dwarf effective temperatures by fitting the *HST* data with atmosphere models.

Combining our results with the 43 CVs from Townsley and Gänsicke (2009), we almost double the number of objects with an accurate temperature measure-

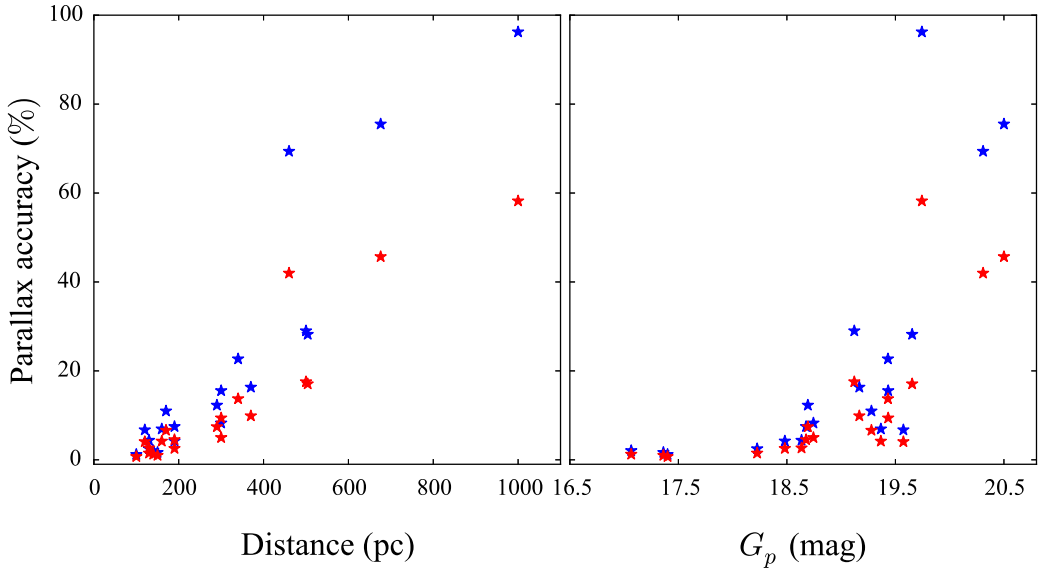

Figure 3.25: *Gaia* parallax accuracy simulated using PyGaia for DR2 (blue) and DR4 (red) as a function of the distance (left) and the G_p *Gaia* magnitude (right). There is a clear correlation of the parallax accuracy with the distance and the G_p magnitude, which reflects in the mass accuracy that can be achieved (Figure 3.26).

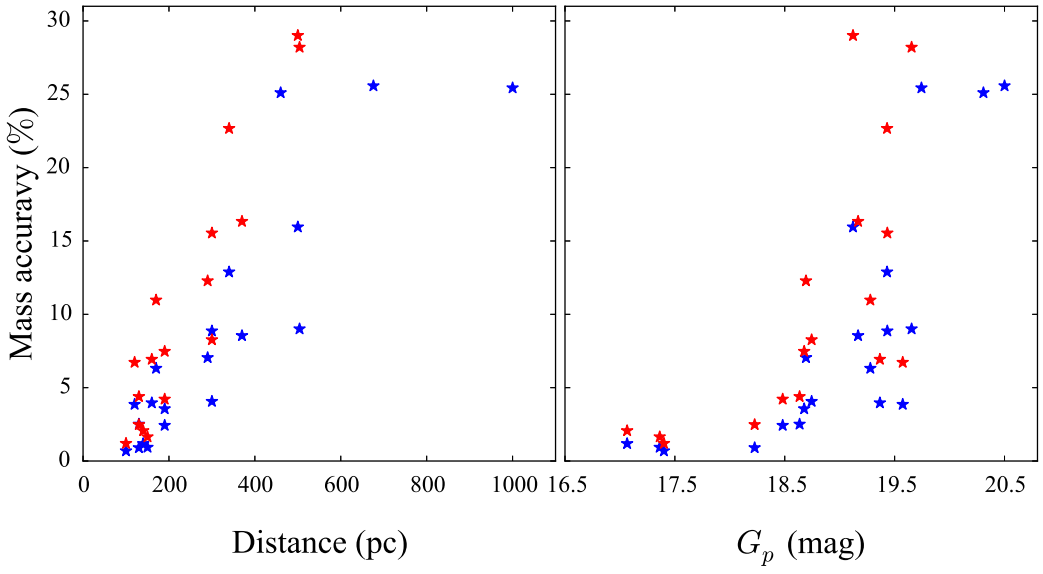

Figure 3.26: Mass accuracy from the uncertainties on the *Gaia* parallaxes simulated using PyGaia for DR2 (blue) and DR4 (red) as a function of the distance (left) and the G_p *Gaia* magnitude (right). With DR2, a mass accuracy of $\lesssim 10\,\%$ will be achieved for systems closer than $\simeq 300\,\mathrm{pc}$ and brighter than $G_p \simeq 18.7\,\mathrm{mag}$. Similar accuracies will be reached in DR4 for systems closer than $\simeq 500\,\mathrm{pc}$ and brighter than $G_p \simeq 19.5\,\mathrm{mag}$.

ment. Comparing the $T_{\rm eff}$–$P_{\rm orb}$ distribution with the mean accretion rate $\dot{M}$–$P_{\rm orb}$ distribution from population models, we test the model for the present day CV population. The systems above the period gap have, on average, mean accretion rates about one order of magnitude higher than those of the systems below the period gap. This is in accordance with the angular momentum loss mechanisms which are thought to dominate the different phases of CV evolution (magnetic braking above and gravitational wave radiation below the period gap).

However, besides this qualitative agreement between observations and theoretical predictions, some clear discrepancies are present:

- VY Scl systems dominate the orbital period range $P_{\rm orb} \simeq 180 - 240\,{\rm min}$, with $T_{\rm eff} \simeq 40\,000 - 50\,000\,{\rm K}$. These temperatures correspond to a $\langle\dot{M}\rangle$ about ten times above the value predicted by the standard evolution theory.

- The results at $P_{\rm orb} \gtrsim 3\,{\rm h}$ present a much more variegated scenario than in the smaller sample analysed by Townsley and Gänsicke (2009), with the new systems showing surprisingly low temperatures. To improve our understanding of CV evolution above the period gap, we need to increase the number of well–characterised systems in this period range.

- At short orbital periods, the temperatures imply higher mass transfer rates than predicted by pure GWR. Moreover, near the period minimum the data show a large scatter that is not accounted for by the models.

- The standard model of CV evolution predicts that period bouncers should make up for $\simeq 40 - 70$ per cent of the present day CV population. We identify only two period bouncer candidates in our sample and, since the lack of these systems cannot be explained by selection effects, we conclude that the present methods used to identify CVs are not sensitive enough to spot these faint systems.

We note that our results are dominated by a systematic uncertainty of $\sim 300 - 1800\,{\rm K}$ due to the unknown white dwarf mass. Once additional constraints on the masses – dynamical and/or distances – become available, the white dwarf effective temperatures will be known with an accuracy of about $\simeq 200\,{\rm K}$. While a significant improvement, the overall shape of the distribution will not drastically change and our conclusions will remain unchanged.

We identify an exceptional outlier (SDSS J153817.35+512338.0) below the period gap, whose extremely high temperature ($T_{\rm eff} = 33\,855 \pm 1\,785\,{\rm K}$) for its short orbital period ($P_{\rm orb} = 93.11\,{\rm min}$) could be explained by a young CV just formed at this $P_{\rm orb}$.

Finally, recent studies (Zorotovic et al., 2011) have shown that the average mass of white dwarf in CVs is substantially higher ($\simeq 0.8\,M_{\odot}$) than that of single white dwarfs ($\simeq 0.6\,M_{\odot}$, Liebert et al. 2005). This finding re–opened the long–standing debate on whether mass growth in CV white dwarf is real or not and on their potential as SN Ia progenitors. Given the fundamental importance of the mass evolution of accreting white dwarfs, it is crucial to enlarge the sample of CV white dwarfs with an accurate mass determination, presently limited to $\simeq 50$. Our results from X–shooter phase–resolved observations for four CVs (SDSS J123813.73–033932.9, V1108 Her, AX For and IR Com) show that we can accurately measure the masses of accreting white dwarfs from their reflex motions. However, this method is limited to those CVs in which the optical emission is not strongly contaminated by the accretion disc. For the remaining systems in our sample, we will combine ultraviolet spectroscopy from *HST* with the distances from *Gaia*. This method can be applied to all CVs for which ultraviolet observations are available and will allow to quadruple the he number of systems with an accurate mass measurements and test, in this way, the mass erosion versus mass growth hypotheses.

Chapter 4

Evidence for spiral density waves in the accretion disc of SDSS J123813.73–033933.0

4.1 Introduction

Among the over 300 CVs identified by SDSS in the last decades, SDSS J123813.73–033933.0 (aka, V406 Vir, hereafter SDSS1238) stood out because of its particular optical variability. SDSS1238 was identified as a CV in 2003 by Szkody et al. (2003), who first estimated its orbital period from seven phase–resolved spectra, finding $P_{\rm orb} \simeq 76\,{\rm min}$. This value was later refined to $P_{\rm orb} = 80.5 \pm 0.5\,{\rm min}$ by Zharikov et al. (2006), locating SDSS1238 at the period minimum. The short orbital period, the absence of normal disc outburst in the SDSS1238 light curve and its recent superoutburst (31st of July 2017, VSNET–alert 21308), make it a member of the the WZ Sge CV subclass.

The peculiarity of SDSS1238 resides in its light curve, in which Zharikov et al. (2006) discovered two types of variability: the first is a sudden increase in brightness, up to $\simeq 0.45\,{\rm mag}$, occurring quasi–periodically every 8–12 hours (called "brightenings"). The second is a double–humped variation at half the orbital period. Aviles et al. (2010) suggested that these double–humps are caused by spiral arms in the accretion disc, which should arise in the disc extending permanently at the 2:1 resonance radius in a system with mass ratio $q \leq 0.1$ (Lin and Papaloizou, 1979). Similar double–humped light curves have also been observed in other WZ Sge CVs, such as V455 And (Araujo-Betancor et al., 2005b), GW Lib (Woudt and Warner, 2002) and SDSS J080434.20+510349.2 (hereafter SDSS0804, Zharikov et al. 2008). Moreover, GW Lib and SDSS0804 share with SDSS1238 also the occurrence of simi-

lar brightening events (Zharikov et al., 2008) which, in GW Lib, have been observed simultaneously with non–radial white dwarf pulsations (Toloza et al., 2016; Chote and Sullivan, 2016).

In the case of GW Lib, it has been suggested that the brightenings could arise from retrograde pulsation modes in the rapidly rotating white dwarf (Toloza et al., 2016) and a possible link between the brightening events and pulsations is the recent detection of a similar phenomenon in isolated pulsating white dwarfs (DAVs, Bell et al. 2015; Hermes et al. 2015; Bell et al. 2016, 2017).

We present new photometric and spectroscopic observations of SDSS1238 obtained during quiescence using *HST*, VLT and *Kepler*, and we report an analysis of the first superoutburst of SDSS1238. By investigating the system variability in a wide range of wavelengths (from the far–ultraviolet into the near–infrared), we reveal a fast heating and cooling of a fraction of the white dwarf as the origin of the peculiar light curve of SDSS1238. We discuss these results in the framework of accretion rate modulation and non–radial pulsations of the white dwarf.

4.2 Observations

4.2.1 Photometry

K2 observations

SDSS1238 was observed by the *Kepler* Space Telescope during Campaign 10 of the *K2* mission. It is designated EPIC 228877473 in its Ecliptic Plane Input Catalogue. The Campaign 10 observations, taken between 2016 July 6 and September 20, suffered from an initial pointing error as well as the failure of one of the CCD modules on the spacecraft. As a result, the first six days of data were lost and the remaining observations have a 14–day gap during which the photometer powered itself down in response to the failure of Module #4.

SDSS1238 was observed in short cadence mode (58.9 s exposures) between July 13 – 20 (MJD 57 582.1 – 57 589.3) and then uninterrupted between August 3 and September 20 (MJD 57 603.3 - 57 651.2). It is the only object in the image stamp, so we extracted the flux using a three pixel radius aperture centred on the target. We then removed all exposures flagged with non-zero error codes. The flags indicate that these were mostly due to cosmic ray strikes. Finally, we identified all times corresponding to thruster firings, by comparing the centroid positions of the target in adjacent exposures. Deviations of more than 4σ were assumed to be due to the regular small adjustments that have to be made to the spacecraft position to correct for drift, and were removed from the light curve. We converted the summed counts f to an approximate *Kepler* magnitude K_p, using $K_p = 25.3 - 2.5\log_{10}(f)$

Table 4.1: Summary of the ground–based CCD observations for the monitoring of the superoutburst of SDSS1238.

Telescope	Location	Diameter (cm)	Filter	Exposure time (s)
ROAD observatory[a]	Chile	40	–	60
Klein Karoo Observatory	South Africa	30	–	60
Prompt 8	Chile	61	V	15–30
Ellinbank Observatory	Australia	32	–	60
Tetoora Road Observatory	Australia	55	Vis	30
Siding Spring	Australia	50	V	30
LCO[b]	Australia	40	V	60

Notes. *(a)* Remote Observatory Atacama Desert. *(b)* Las Cumbres Observatory.

(e.g. Lund et al., 2015; Huber et al., 2016).

Superoutburst: ground–based photometry

On 2017 July 31 K. Stanek reported the outburst (VSNET–alert 21308) of SDSS1238, detected by the All-Sky Automated Survey for Supernovae (ASAS–SN, Pojmanski 1997). SDSS1238 brightened from a quiescent magnitude $V \simeq 17.8$ mag to $V \simeq 11.86$ mag. This was the first outburst ever detected for this system. Following the detection of the outburst, an intensive monitoring was carried out by the global amateur community. Unfortunately the superoutburst occurred at the very end of the observational season of SDSS1238, when the star was only visible for about 1.5 hours after the sunset and only from the southern hemisphere. Time–resolved photometry was obtained using seven telescopes around the world for about two weeks after the event. In order to maximise the number of data acquired, the observations were often started in twilight and continued up to very high airmass (up to $\simeq 3$). In this cases, sufficiently blue stars were used to compute the differential photometry in order to account for differential extinction. A summary of the observations is reported in Table 4.1.

4.2.2 Spectroscopy

HST/COS observations

SDSS1238 was observed for three consecutive spacecraft orbits for a total exposure time of 7 183 s as a part of a large *HST* programme in Cycle 20 (programme ID 12870) on 2013 March 1 using COS (see Section 3.2.1 and Table 3.2.1). In Chapter 3 we report on the results of this large programme and verify that the *HST*

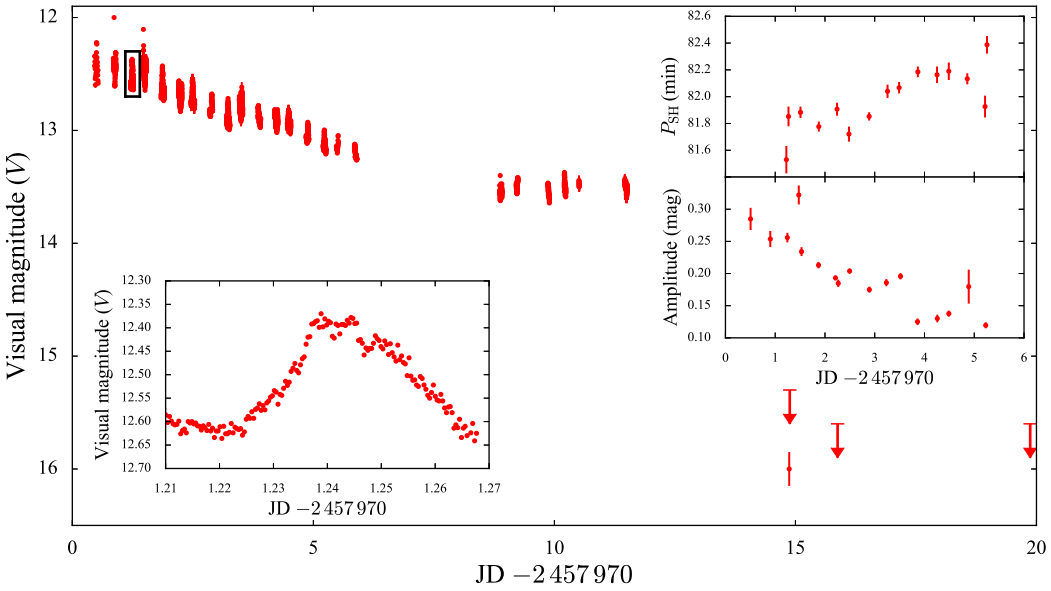

Figure 4.1: Superoutburst light curve of SDSS1238. The bottom left inset shows a close–up of the region highlighted with the black rectangle in the main plot; the top right insets show the P_{SH} (top) and the amplitude (bottom) variation of the superhumps detected before the observing gap.

observations were carried out during the quiescent phase of SDSS1238 (Pala et al., 2017).

The data were collected in TIME–TAG mode, i.e. recording the time of arrival and the position on the detector of each detected photon, which also allows to construct light curves.

VLT/X–shooter observations

Phase–resolved spectroscopy of SDSS1238 was carried out on 2015 May 12 with X–shooter (see Section 3.2.3 and Table 3.3). We used the 1.0″, 0.9″ and 0.9″ slits for the UVB, VIS and NIR arm, respectively, in order to match the seeing, which was stable at $\simeq 1.0''$ during the observations. The sky was not clear and some thick clouds passed over, consequently we had to discard two spectra for each arm owing to their extremely low SNR.

4.3 Results

4.3.1 Superoutburst and superhumps

The superoutburst of SDSS1238 lasted about 15 days (Figure 4.1), although the decline to quiescence could not be followed because of the decreasing visibility of SDSS1238. Because of adverse weather condition, the photometric observations

have a gap of about three days. Superhumps were detected beginning on August 5, but their amplitude results greatly reduced after the gap in the observations.

We analysed the superoutburst light curve using the MIDAS/TSA package implemented by Schwarzenberg-Czerny (1996). A first cursory analysis showed that the superhump period ($P_{\rm SH}$) has been evolving throughout the outburst, and that due the lower amplitude of the superhumps after the three-day gap, the quality of the data was insufficient to derive reliable results for these final six observing runs. We therefore restricted the following analysis to the observations obtained in the first $\simeq 5.5$ d of the outburst, computing discrete Fourier transforms for groups of three consecutive observing runs, typically spanning $\sim 0.25 - 0.5$ d, stepping through the entire data set. For each group of observations, we determined the period of the strongest signal in the power spectrum, and subsequently fitted a sine wave to the data to derive an uncertainty on the period. The resulting superhump periods and their amplitudes are shown in the inset panels in Figure 4.1. Given the overlap between the grouping of the observing runs, adjacent measurements are not statistically independent. Following the definition of stage A, B and C of superhump evolution from Kato et al. (2009), we concluded that stage A, during which the superhump period is the longest, was missed and that the observations were carried out during the middle/late stage B, during which $P_{\rm SH}$ is growing and the superhump amplitude is decreasing (see insets in Figure 4.1), and we adopted the average superhump period throughout this phase, $P_{\rm SH} = 81.987 \pm 0.005$ min. Assuming this value and an orbital period of $P_{\rm orb} = 80.5200 \pm 0.0012$ min (see Section 4.3.3 and Zharikov et al. 2006), we used equation 10 and equation 5 from Kato and Osaki (2013) for mean stage B superhumps to estimate the system mass ratio, which results $q = 0.08 \pm 0.01$.

4.3.2 System parameters and optical spectral fitting

As described in Section 3.3.1, we used the K I (12 432/12 522 Å) lines and the Mg II (4 481.25 Å) absorption feature to track the reflex motion of, respectively, the secondary and the white dwarf in SDSS1238. In order to achieve more robust radial velocity measurements, we simultaneously fitted all the spectra.

We first fitted the K I absorption lines using a combination of a constant and a double Gaussian of fixed separation. We allowed the position of the Gaussians to vary as Equation 2.4. From this fit, we determined the gamma velocity ($\gamma_{\rm sec} = -11 \pm 9\,{\rm km\,s^{-1}}$) and the velocity amplitude ($K_2 = 428 \pm 12\,{\rm km\,s^{-1}}$) of the secondary. Combining K_2 with the mass ratio determined from the superhump analysis returns the white dwarf velocity amplitude $K_1 = 34 \pm 5\,{\rm kms^{-1}}$. To better constrain the fit to the Mg II absorption line, we assumed K_1 to be normally distributed around this value and fitted the Mg II feature using a combination of a constant and a

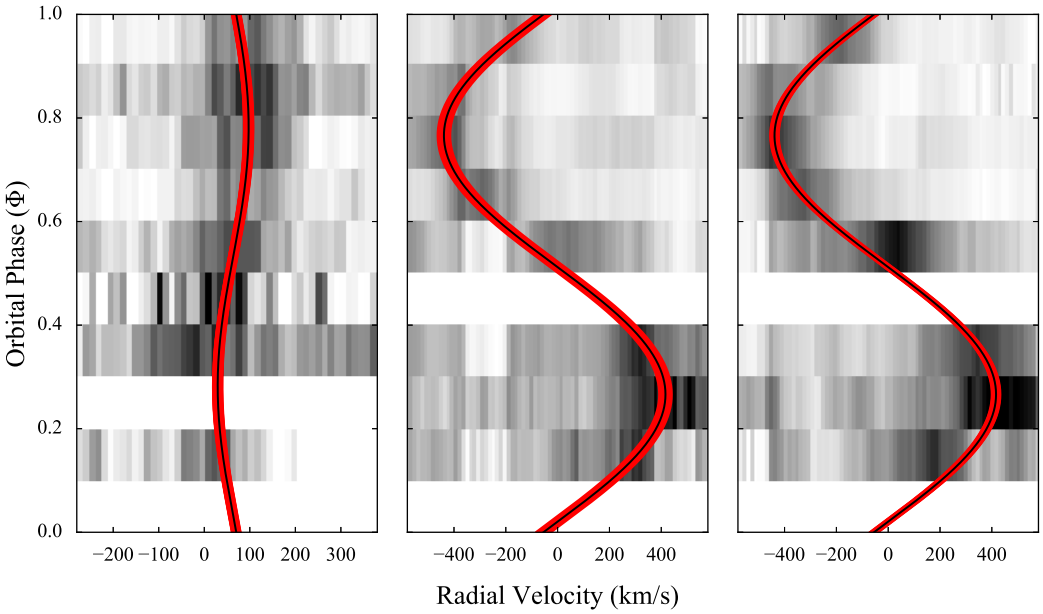

Figure 4.2: Trailed spectra for the Mg II line (4 481 Å, left) and the K I lines (12 432/12 522 Å, middle and right). The black lines represent the best fit models along with their uncertainties (red).

single Gaussian, thus obtaining the gamma velocity of the white dwarf, $\gamma_{\mathrm{WD}} = 63 \pm 4\,\mathrm{km\,s^{-1}}$. The results of these fits are shown in Figure 4.2.

The gamma velocities of the white dwarf and the secondary carry information on the white dwarf mass, since their difference is a measurement of the white dwarf gravitational redshift (Equation 2.5). Using the mass–radius relationship from Hamada and Salpeter (1961), which is justified for the low white dwarf temperature, we found that the mass and the radius of the white dwarf in SDSS1238 are $M_{\mathrm{WD}} = 0.97 \pm 0.05\,\mathrm{M_\odot}$ and $R_{\mathrm{WD}} = 0.0085 \pm 0.0006\,\mathrm{R_\odot}$, corresponding to $\log(g) = 8.56 \pm 0.06$, where g is expressed in *cgs* units.

The secondary mass can then be calculated from the system mass ratio, $M_2 = 0.08 \pm 0.01\mathrm{M_\odot}$. From Kepler's third law a measurement of the orbital separation is obtained, $a = 0.62 \pm 0.01\,\mathrm{R_\odot}$. The presence of strong emission lines suggests that accretion was ongoing at the time of the X–shooter observations and thus the secondary must fill its Roche–lobe. The mass–ratio and the orbital separations yield the Roche–lobe radius which corresponds to the secondary radius (Equation 1.4), $R_2 = 0.123 \pm 0.005\,\mathrm{R_\odot}$.

Finally, the light curve of SDSS1238 does not show the eclipse of the white dwarf, nonetheless the presence of double peaked emission lines suggests a relatively high inclination of the system, which can be estimated from the white dwarf mass function (Equation 2.7) and results $i = 55 \pm 3°$.

The night of the X–shooter observations was characterized by the passing

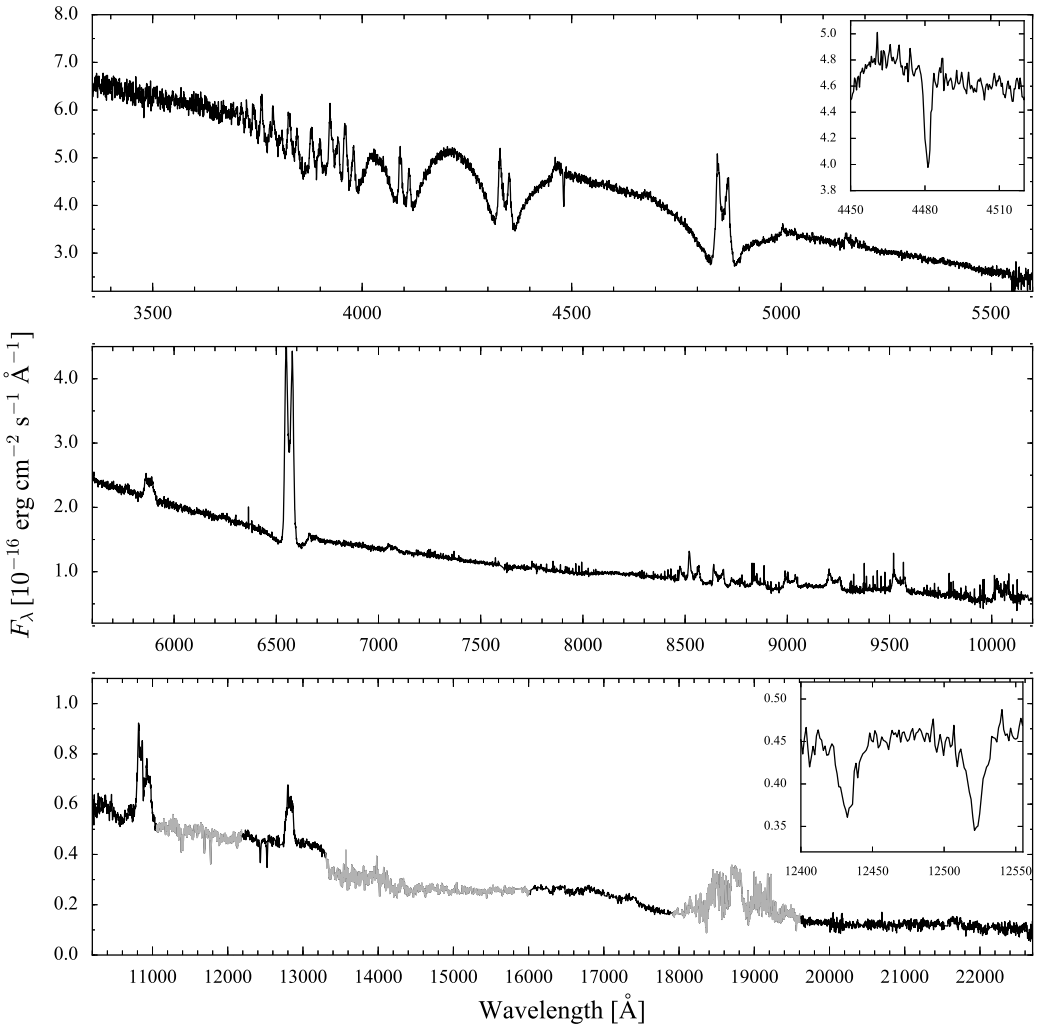

Figure 4.3: VLT/X–shooter average spectrum (upper panel UVB, central panel VIS, bottom panel NIR) of SDSS1238, shifted into the rest frame of the centre of mass. Regions strongly affected by residuals of the telluric correction are drawn in gray. The two insets show the white dwarf Mg II (4 481 Å) and the secondary K I (12 432/12 522 Å) absorption features used to measure the radial velocities.

over of some thick clouds which, combined with the intrinsic variability of SDSS1238 (see Section 4.3.4), makes it impossible to reconstruct a reliable flux–calibrated average spectrum. To reconstruct the system SED we selected the three spectra with the highest flux for each arm, which correspond to an orbital phase $\phi \simeq 0.75$, and shifted them into the reference frame of the centre of mass[1]. We then computed the average spectrum, which well agrees with the available photometry of SDSS1238 from 2MASS (Two Micron All–Sky Survey) and SDSS. We scaled each individual

[1]We used the radial velocities we measured from the Mg II line to shift the UVB spectra and the ones from the K I lines to shift the NIR spectra. No absorption features were detected in the VIS spectra, for which no shift was applied.

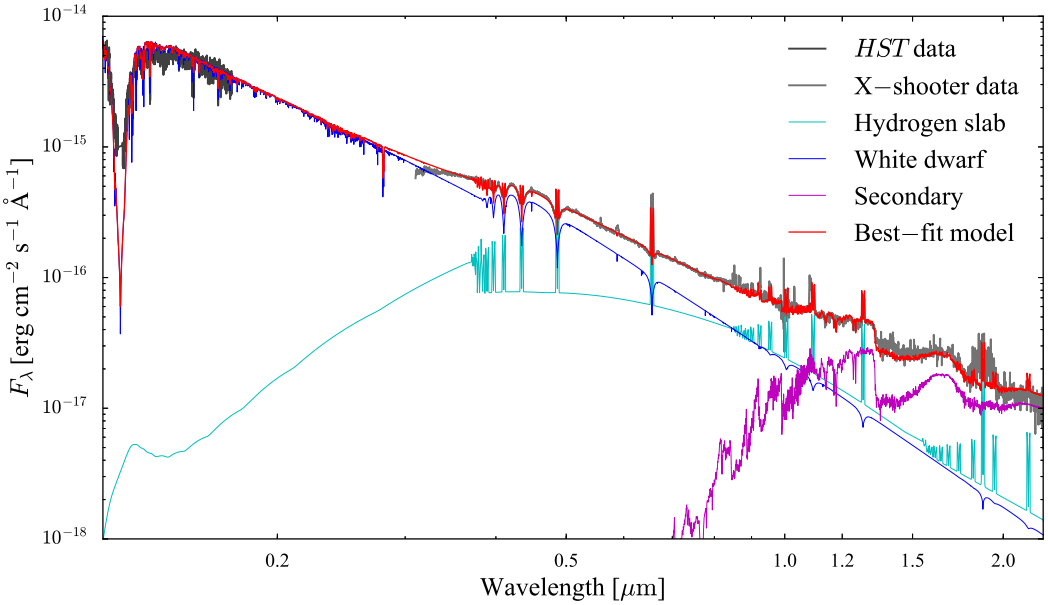

Figure 4.4: *HST*/COS average (dark grey) and X–shooter average spectrum (light grey, reconstructed as described in the text) of SDSS1238, along with the best–fit model (red), which is composed of the sum of a white dwarf (blue), an isothermal and isobaric pure–hydrogen slab (cyan) and a late–type star (magenta). The *HST* data were not included in the fit but are overplotted to show the agreement between the best–fit model and the observed flux level in the ultraviolet (note that the *HST* spectrum is the average of the intrinsic variability of SDSS1238, see Section 4.3.4).

spectrum to the flux level of this high–flux spectrum and calculated the weighted average, thus obtaining the SED shown in Figure 4.3. The white dwarf contribution can be recognized from the broad Balmer absorption lines in the UVB arm (upper panel); strong double peaked emission lines reveals the presence of an accretion disc and the donor star contribution can be identified in some absorption features (such as the K I doublet at 12 432/12 522 Å) in the NIR portion of the spectrum (bottom panel).

Aviles et al. (2010) reported a distance to SDSS1238 of $d = 110$ pc, for which the interstellar reddening results $E(B-V) = 0.006$ mag. As we have discussed in Chapter 3, spectral fits in the ultraviolet are affected by interstellar reddening for $E(B-V) \gtrsim 0.1$ mag, and given that optical observations are less sensitive to interstellar extinction we did not apply any reddening correction.

Fundamental system parameters, such as the distance and effective temperatures, can be measured from a spectral fit to the SED. A model to fit the data has to take into account the three light sources in the system, i.e. the white dwarf, the disc and the donor star. We therefore generated a grid of white dwarf models using TLUSTY and SYNSPEC (Hubeny, 1988; Hubeny and Lanz, 1995), covering the effec-

Table 4.2: Best-fit parameters and their range of variations for the model used to fit the SED of SDSS1238.

Parameter	Model	Range of variation	Best–fit result
$T_{\rm WD}$ (K)	TLUSTY and SYNSPEC	$10\,000 - 49\,000$	$18\,600 \pm 1\,400$
White dwarf scaling factor	TLUSTY and SYNSPEC	> 0	$1.3(2) \times 10^{-23}$
$T_{\rm slab}$ (K)	Gänsicke et al. (1997, 1999)	$5\,700 - 8\,000$	$6\,000 \pm 300$
Pressure (dyn cm^{-2})	Gänsicke et al. (1997, 1999)	$0 - 1\,000$	300 ± 80
Rotational velocity (km s^{-1})	Gänsicke et al. (1997, 1999)	$0 - 3\,000$	$1\,200 \pm 700$
Geometrical height (cm)	Gänsicke et al. (1997, 1999)	$10^6 - 10^{12}$	$7.0(8) \times 10^7$
Slab scaling factor	Gänsicke et al. (1997, 1999)	> 0	$5.9(3) \times 10^{-21}$
T_2 (K)	BT–DUSTY	$1\,000 - 3\,600$	$1\,770 \pm 140$
Secondary scaling factor	BT–DUSTY	> 0	$9.4(3) \times 10^{-22}$

tive temperature range $T_{\rm eff} = 10\,000 - 40\,000$ K in steps of 100 K, for $Z = 0.5\,{\rm Z}_\odot$ (as measured in Chapter 3 from the analysis of the *HST* data) and fixing $\log g = 8.56$ (as determined in the previous Section). We used an isothermal and isobaric pure–hydrogen slab model to approximate the disc emission. The model is described in Gänsicke et al. (1997, 1999) and is defined by five free parameters: temperature, gas pressure, rotational velocity, inclination and geometrical height. Finally, we retrieved from the Theoretical Spectra Web Server[2] a grid of BT–DUSTY (Allard et al., 2012) models for late–type stars, covering $T_{\rm eff} = 1\,000 - 3\,600$ K in steps of 100 K, for $\log g = 5$ (as derived from the secondary mass and radius in the previous Section) and $Z = 0.3\,{\rm Z}_\odot$, since no models are available for $Z = 0.5\,{\rm Z}_\odot$.

We used a χ^2 minimization routine to fit the data assuming the system inclination, $i = 55 \pm 3$, as determined in the previous Section and constraining the white dwarf and the secondary to be located at the same distance. Moreover, since the secondary is irradiated by the hotter white dwarf, its intrinsic flux is only a fraction of the observed one (Rebassa-Mansergas et al., 2013):

$$\frac{F_{\rm int}}{F_{\rm irr}} = \left(\frac{T_{\rm sec}}{T_{\rm WD}}\right)^4 \left(\frac{a}{R_{\rm WD}}\right)^2 \tag{4.1}$$

where $F_{\rm int}$ and $F_{\rm irr}$ are the intrinsic and the irradiated flux of the secondary, respectively. To take into account the effect of irradiation in our fitting procedure we scaled the secondary model accordingly to this relationship. Finally, to better constrain the fit, we included as free parameter the areas of the disc emission lines of Hα, Hβ and Hγ. The result of this fitting procedure are summarised in Table 4.2 and the best–fit model is shown in Figure 4.4.

[2] http://svo2.cab.inta-csic.es/theory/newov/index.php?model=bt-settl.

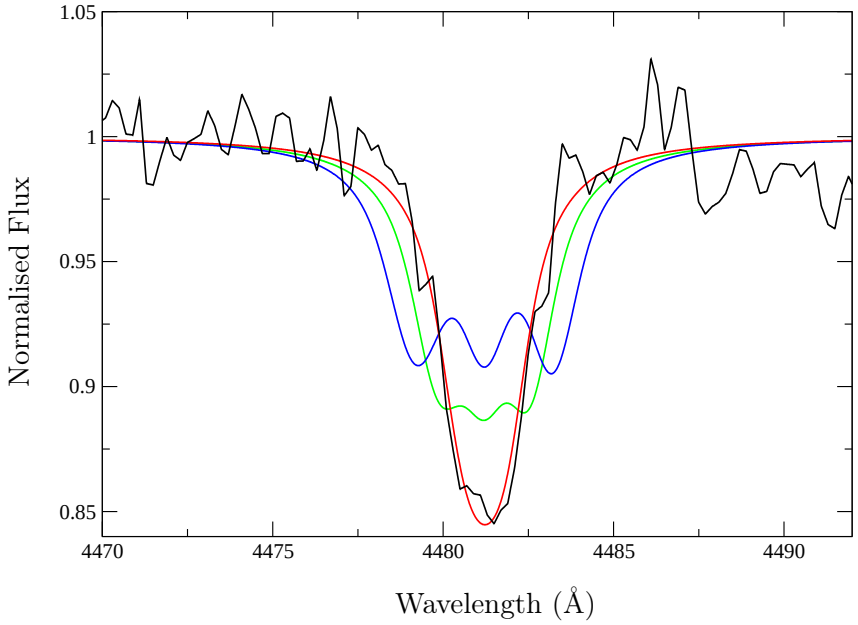

Figure 4.5: White dwarf Mg II absorption line at 4 481 (black) along with the theoretical line profile computed for different strenghts of the magnetic field and assuming zero rotation for the white dwarf: $\langle B \rangle = 71\,\mathrm{kG}$ (red), $\langle B \rangle = 143\,\mathrm{kG}$ (green) $\langle B \rangle = 216\,\mathrm{kG}$ (blue).

The scaling factor between the data and the best–fit model to the white dwarf spectrum (Equation 2.2) yields the distance to the system, $d = 190 \pm 29\,\mathrm{pc}$. This value is larger than the one previously estimated by Aviles et al. (2010) and corresponds to an interstellar reddening of $E(B-V) \lesssim 0.01\,\mathrm{mag}$ (Lallement et al., 2014), well below the threshold established in Section 3.3.2, and we therefore conclude that our assumption of negligible interstellar reddening remains correct.

The resolution of the X–shooter spectra allows to measure the rotational velocity of both stellar components and to put an upper limit on the strength of a possible magnetic field of the white dwarf. In Figure 4.5 we show the white dwarf Mg II absorption line at 4 481 Å, which is broadened by the rotation of the white dwarf and (possibly) by its magnetic field. Assuming a zero magnetic field, the observed line broadening corresponds to a rotational velocity of $v_{\mathrm{rot}} = 110 \pm 30\,\mathrm{km\,s^{-1}}$, and a spin period of $P_{\mathrm{spin}} = 6 \pm 1$ min. On the contrary, assuming zero rotation for the white dwarf and fitting the line with magnetic atmospheric models, the observed line broadening is reproduced by $\langle B \rangle \lesssim 100\,\mathrm{kG}$ (red line in Figure 4.5). However, given that the white dwarf is accreting mass and angular momentum, rotation very likely contributes to the broadening of the observed line profile (King et al., 1991). White dwarf rotation velocities have been measured for a handful of CVs, and range from $\simeq 100\,\mathrm{km\,s^{-1}}$ (Sion et al., 1994, 1998; Long et al., 2006) to $\simeq 500\,\mathrm{km\,s^{-1}}$ (Sion et al., 1995, 2001; Long et al., 2004, 2009). Therefore

Table 4.3: Stellar and binary parameters for SDSS1238.

System parameter	Value
$P_{\rm orb}$ (min)	80.5200 ± 0.0012
q	0.08 ± 0.01
i (°)	55 ± 3
a ($R_\odot$)	0.62 ± 0.01
d (pc)	190 ± 29
$E(B-V)$ (mag)	$\lesssim 0.01^a$
White dwarf parameter	**Value**
T (K)	$\lesssim 14\,200^b$
M ($M_\odot$)	0.97 ± 0.05
R ($R_\odot$)	0.0085 ± 0.0006
$\log(g)$	8.56 ± 0.06
$v_{\rm rot}$ (km s^{-1})	110 ± 30
$P_{\rm spin}$ (min)	6 ± 1
$\langle B \rangle$ (kG)	< 100
γ (km s^{-1})	63 ± 4
K (km s^{-1})	34 ± 5
$v_{\rm grav}$ (km s^{-1})	74 ± 10
Secondary parameter	**Value**
T (K)	1770 ± 140
M ($M_\odot$)	0.08 ± 0.01
R ($R_\odot$)	0.123 ± 0.005
$\log(g)$	5.17 ± 0.07
$v_{\rm rot}$ (km s^{-1})	136 ± 24
$P_{\rm spin}$ (min)	73 ± 11
Sp2	L3 $\pm$ 0.5
γ (km s^{-1})	-11 ± 9
K (km s^{-1})	428 ± 12

Notes. *(a)* From Lallement et al. (2014), for $d = 190$ pc. *(b)* From *HST*/COS spectrum at minimum (see Section 4.3.4).

the assumption of zero rotational velocity seems quite unlikely and the value we determined only represent an upper limit for the actual strength of the magnetic field.

Finally, from a Gaussian fit of the K I lines, we measured the secondary rotational velocity, $v_{\rm spin} = 136 \pm 24$ km s^{-1}. This yields a spin period of $P_{\rm spin} = 73 \pm 11$ min, indicating that the donor star is tidal locked, as expected for a Roche–lobe filling secondary star.

The system and stellar parameters as derived from the analysis of the X–

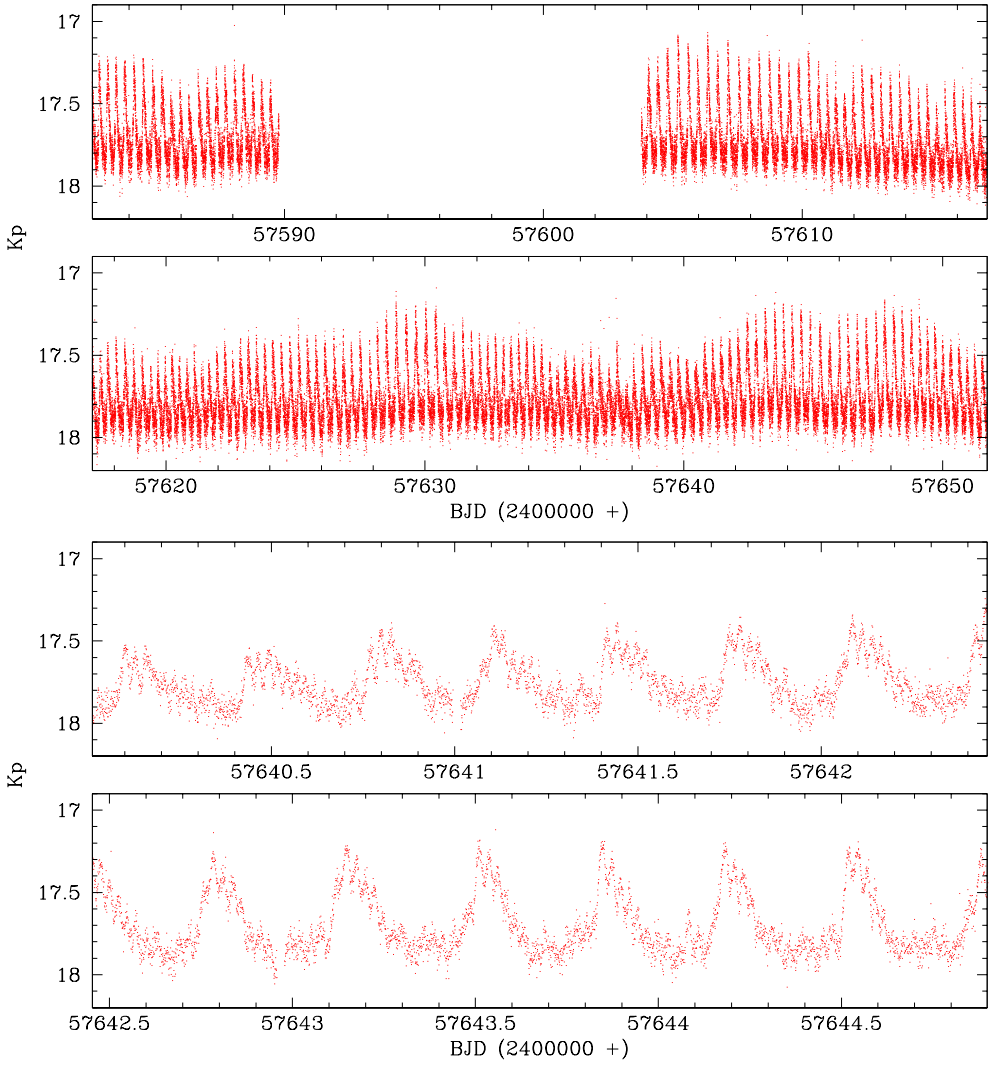

Figure 4.6: The top two panels show the entire *K2* light curve, the bottom two panels zoom in on a five-day segment. The 14 d gap is related to the loss of CCD Module #4. The *K2* light curve is dominated by quasi–periodic brightenings recurring every $\simeq 8.5$ h with a typical amplitude of $\simeq 0.5$ mag, though a significant modulation of this amplitude is seen throughout the *K2* Campaign. Superimposed on the $\simeq 8.5$ h brightenings is a photometric modulation with a coherent period of 40.26 min, i.e. half the orbital period, the amplitude of these double–humps increases during the brightenings.

shooter data are summarised in Table 4.3.

4.3.3 Light curve analysis

The *K2* light curve shows the two main characteristics identified in ground-based photometry of SDSS1238 (Zharikov et al., 2006; Aviles et al., 2010), i.e the quasi–periodic brightening events recurring every $\simeq 8.5$ h (Figure 4.6, top panels) with a

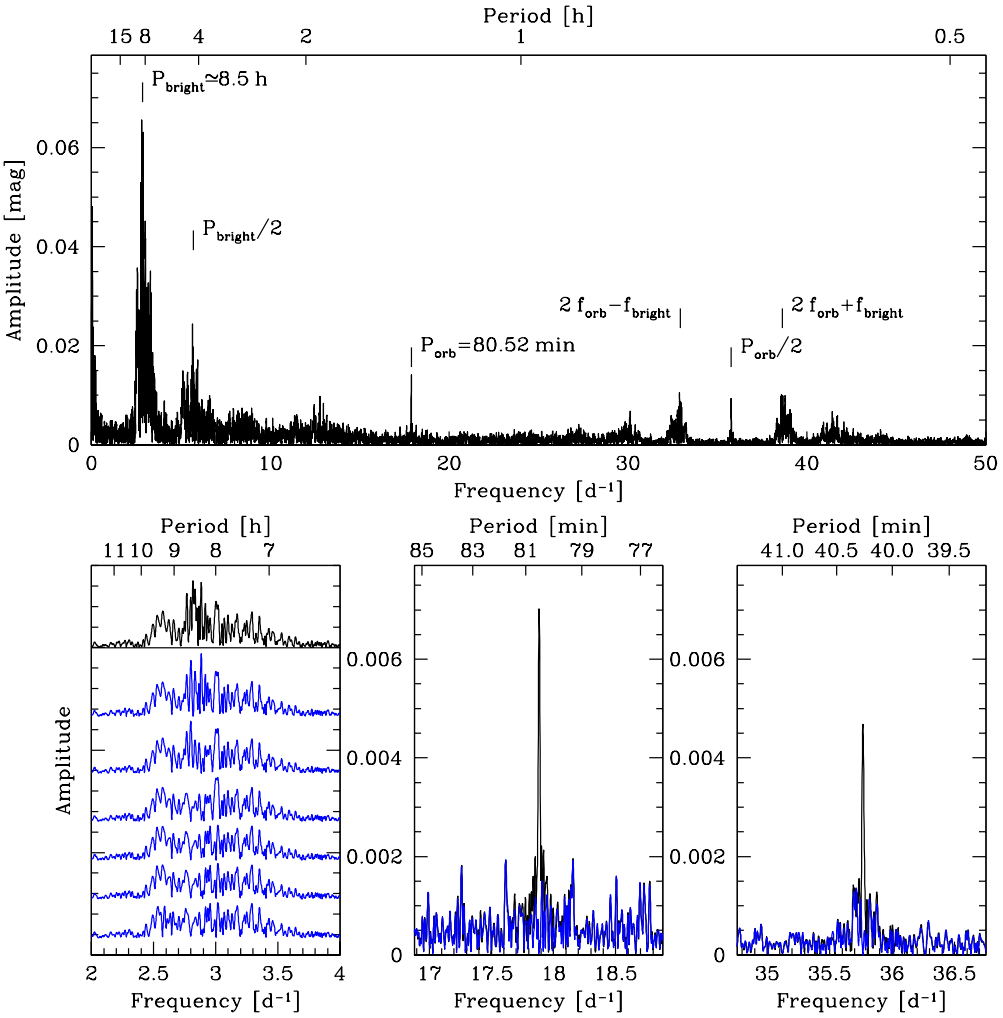

Figure 4.7: Top panel: amplitude spectrum of the full *K2* light curve. The brightenings are non-coherent, resulting in a broad forest of signals centred on $\simeq 8.5\,\mathrm{h}$. Subsequent pre-whitening of the *K2* data with the strongest signal near $\simeq 8.5\,\mathrm{h}$ (blue amplitude spectra on the bottom left panel) leaves significant structure, confirming the non-periodic nature of the brightenings. In contrast, the modulation at half the orbital period produces a sharp signal at P_{orb} in the amplitude spectrum, both signals can be cleanly removed (bottom middle/right, blue curves).

typical amplitude of $\simeq 0.5\,\mathrm{mag}$ which, however, varies on time scales of days. In addition, the light from the system is modulated at 40.26 min, i.e. half the orbital period (Figure 4.6, bottom). These double–humps are persistently detected, but increase in amplitude during the brightenings.

We computed discrete Fourier transforms of the *K2* data using again the MIDAS/TSA package. As expected, the power spectrum is dominated by a forest of signals near $P_{\mathrm{bright}} \simeq 8.5\,\mathrm{h}$ ($f_{\mathrm{bright}} \simeq 2.8\,\mathrm{d}^{-1}$, Figure 4.7, top panel), corresponding to the brightening events, and additional power is seen at the harmonic of that

signal. Iteratively pre–whitening the *K2* light curve with the strongest signal and re–computing a Fourier transform shows that multiple strong signals remain in the range $\simeq 7-9\,\mathrm{h}$ ($\simeq 2.5-3.5\,\mathrm{d}^{-1}$), underlining the incoherent nature of P_{bright} (Figure 4.7, bottom left panel). In addition, the power spectrum contains two sharp signals at $P_{\mathrm{orb}} = 80.52\,\mathrm{min}$ ($f_{\mathrm{orb}} \simeq 17.9\,\mathrm{d}^{-1}$) and $1/2\,P_{\mathrm{orb}} = 40.26\,\mathrm{min}$. Both signals are cleanly removed by pre–whitening the *K2* data (Figure 4.7, bottom middle and right panel), as expected for the stable signal of the orbital period. Noticeable are the two sidebands seen at $2f_{\mathrm{orb}} \pm f_{\mathrm{bright}}$, which are the result of the strong amplitude modulation of the double–hump signal during the brightenings (see Section 4.3.3).

Brightening analysis

The strongest signal in the periodogram of the *K2* light curve corresponds to a period of $\simeq 8.5\,\mathrm{h}$ and arises from the 162 brightenings occurring during the *Kepler* observations. This signal is quasi–periodic, but not strongly coherent (lower left panel of Figure 4.7). In order to study the recurrence time and the amplitude of these phenomena in more detail, we used a χ^2 minimisation routine to fit the data with a sum of a constant value, to reproduce the quiescent flux, and 162 Gaussians to reproduce the shape of each individual brightening. The free parameters of this model are the quiescent level and the central time, the amplitude and the width of each Gaussian. A portion of the *K2* light curve along with the best fit model is shown in the top left panel of Figure 4.8.

From the width of each Gaussian we estimated the average brightening duration, $\delta t_{\mathrm{bright}} = 1.0 \pm 0.1\,\mathrm{h}$ (middle right panel of Figure 4.8). By measuring the delay time between two consecutive brightenings (middle left panel of Figure 4.8), we determined the average recurrence time of the brightenings, $t_{\mathrm{rec}}^{\mathrm{brigth}} = 8.2 \pm 1.3\,\mathrm{h}$. Assuming this value, we calculated the $O-C$ diagram for the long period modulation (top right panel of Figure 4.8).

The smooth variation of the slope observed in the $O-C$ diagram implies that the brightnenings do not occur randomly but seem to evolve in a small number of preferred states. Further correlations are seen between their amplitudes, recurrence times and durations: the longer is the delay between a brightening and the preceding one, the larger is its amplitude and the longer it lasts (bottom panels of Figure 4.8). These correlations highlight the presence of a systematic mechanism acting behind the brightenings, whose origin will be discussed in detail in Section 4.4.

Double–hump analysis

The coherent $40.26024 \pm 0.00060\,\mathrm{min}$ signal detected in the Fourier transform of he *K2* data, which we dubbed "double–humps", is consistent with half the spectroscopically measured orbital period. In order to investigate possible correlations between

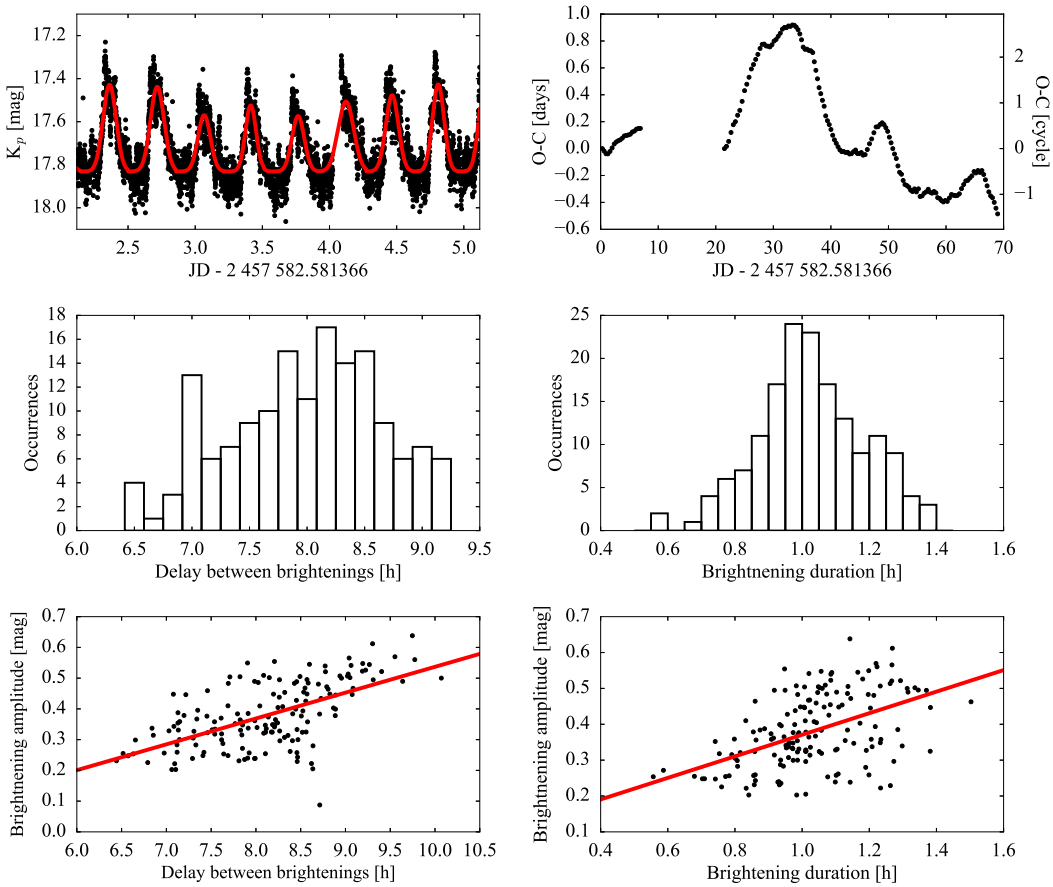

Figure 4.8: **Top.** *Left:* Close–up of the *K2* light curve (black) along with the best–fit model to the long period modulation (red), which is the sum of a constant and 162 Gaussians. *Right:* $O-C$ diagram for the brightenings observed in the *K2* light curve, calculated using the recurrence time $t_{\rm rec} \simeq 8.2\,$h. **Middle.** Histogram of the time difference between two consecutive brightenings (left) and the brightening durations (right). The medians and the standard deviations of these distributions are the average duration and recurrence time of the brightenings reported in the text. **Bottom.** Correlation between the amplitude and the delay between two consecutive brightnenings (left) and between the amplitude and the brightening duration (right). The straight line best–fit models (red) show the positive correlations, which have Pearson coefficients of $\rho \simeq 0.6$ and $\rho \simeq 0.5$, respectively.

the 8.5 h brightenings and the double–humps, we divided the *K2* light curve into 9.6 h long chunks, each of them centred onto the peak of one of the 162 brightening events (as measured from the Gaussian fits described in Section 4.3.3), and shifted the time axes of each chunk so that these peaks align – however, these shifts in time were carried out in steps of 40.26025 min, so that also the double-humps align in phase. The resulting average light curve reveals that the brightenings repeat remarkably well in time, with a fast rise and a slow decline, and that the double–humps grow in amplitude during the brightening (Figure 4.9, right panel).

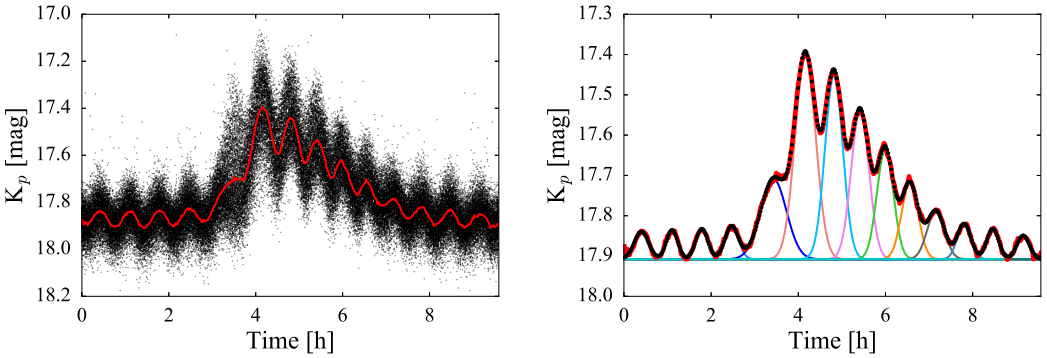

Figure 4.9: The 162 brightenings superimposed with respect to the 40.26 min ephemeris of the double–humps (left, black dots). The double–humped structure is clearly coherent throughout the *K2* campaign, and shows an increase in amplitude during the brightenings. The red line represents the data binned over an interval of five seconds. The binned light curve is shown again on the right (red line, note the different scale of the y–axis) along with it best fit model (black, dotted), which is composed by a series of 14 Gaussians of different weights and amplitudes.

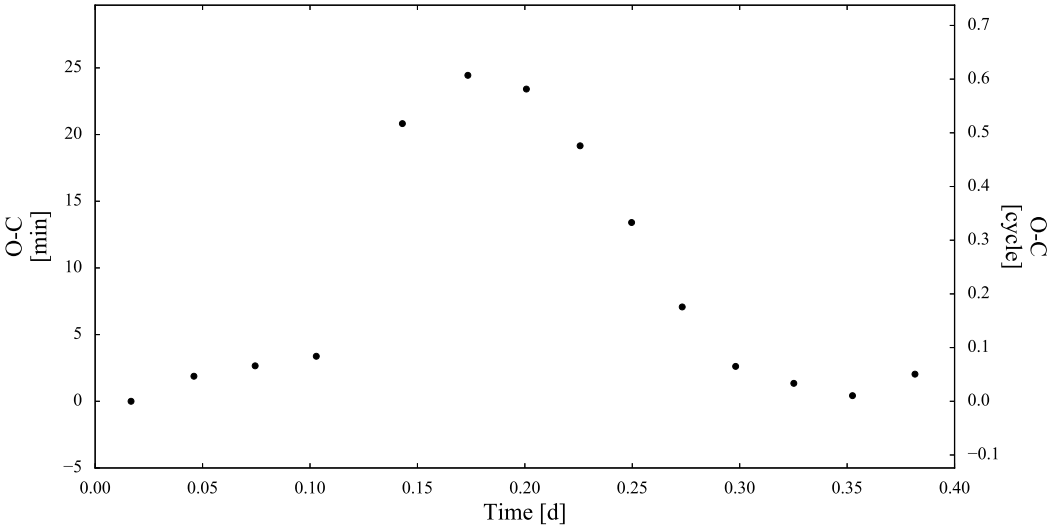

Figure 4.10: $O-C$ diagram for the humps observed in the shifted *K2* light curve (see Figure 4.9). During the brightening the humps result phase shifted by about half cycle.

As done for the brightenings, we fit the double–humps in the average brightening light curve with a model which is the sum of 14 Gaussians (one for each hump detected) and a constant, to reproduce the quiescence level. The free parameters of the model are hence the quiescent magnitude, the amplitude, the weight and the central time of the 14 Gaussians describing the humps. The best–fit model to the average brightening light curve is shown in the right panel of Figure 4.9.

By measuring the time difference between two consecutive humps, we calculated the $O-C$ diagram for this short period modulation (bottom panel of Fig-

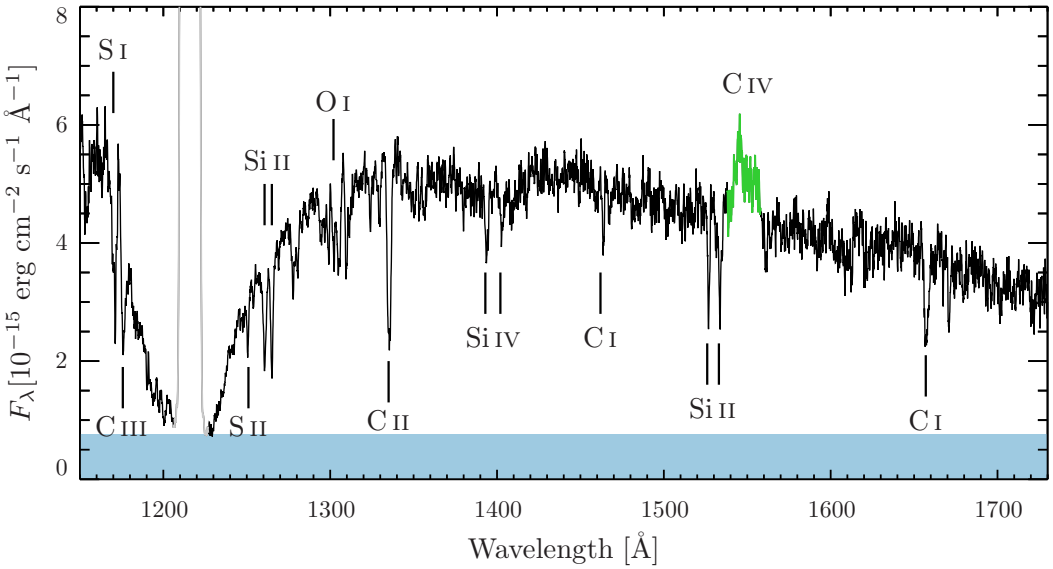

Figure 4.11: *HST*/COS average spectrum of SDSS1238. The unmistakable white dwarf signature is the broad Lyα absorption, the quasi–molecular absorption band of H_2^+ at $\lambda \simeq 1\,400$ Å and several sharp metal absorption lines. Plotted in green is the disc emission line of C IV (1 550 Å). The blue band illustrates the presence of a second continuum component which contributes $\simeq 15$ per cent of the observed flux and which we assume to be flat in F_λ. The geocoronal emission lines of Lyα (1 216 Å) is plotted in grey.

ure 4.10). During the brightening, the humps undergo a phase shift, as can be seen by the sharp increase and subsequent smooth decrease of the $O - C$ values.

4.3.4 Ultraviolet spectroscopy and light curve

Figure 4.11 shows the average ultraviolet spectrum of SDSS1238 from the *HST*/COS observations. The emission is dominated by the white dwarf, recognisable in the broad Lyα absorption profile at 1 216 Å. Some contribution from the disc can be identified in the C IV emission at 1 550 Å. Moreover, the non–zero flux in the core of the Lyα unveils the presence of an additional continuum component, which contributes to $\simeq 15$ per cent of the observed flux[3]. From a fit to this spectrum, we determined an effective temperature of the white dwarf of $T_{\rm WD} = 18\,900 \pm 229$ K for $\log g = 8.56$ and $Z = 0.5\,Z_\odot$ (Table 3.7, middle panel of Figure 3.13).

The *HST*/COS data were collected in TIME–TAG mode, i.e. by recording the time of arrival and the position on the detector of each event, and it is therefore possible to reconstruct the ultraviolet light curve of SDSS1238 (Section 2.4.1).

[3]The origin of this additional emission source is unclear and it has been suggested that it could arise from (i) the disc, or (ii) the region of intersection between the ballistic stream and the disc or (iii) the interface region between the disc and the white dwarf surface, see Section 3.3.2 for a more detailed discussion.

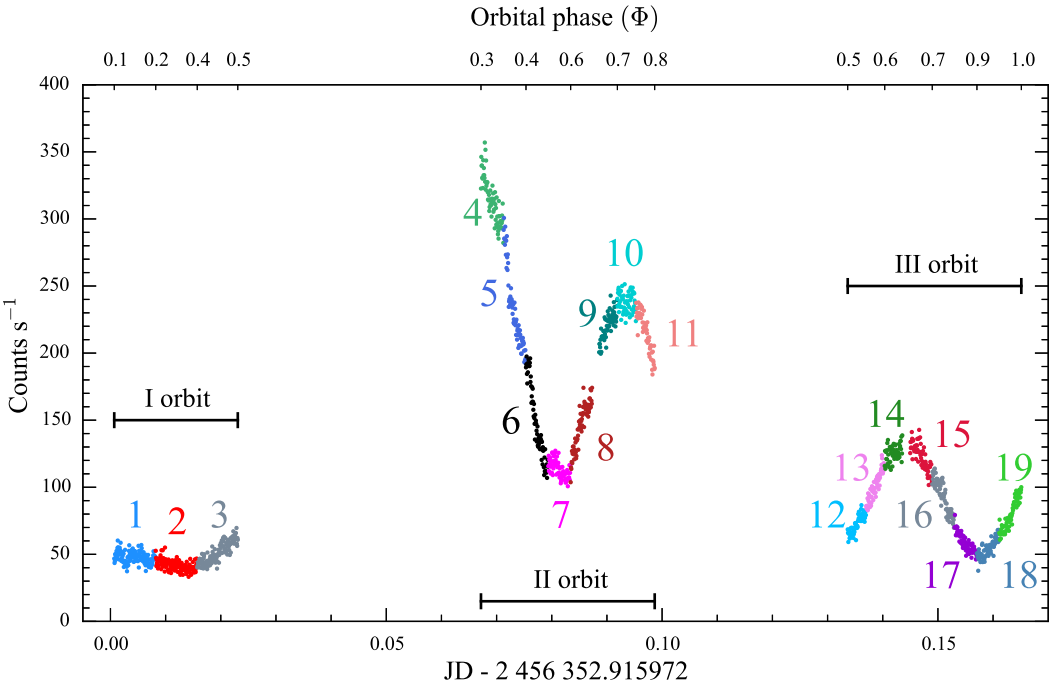

Figure 4.12: *HST*/COS light curve of SDSS1238, obtained over three consecutive spacecraft orbits, the gaps result from the target being occulted by the Earth. The colours highlight the different exposures from which the 19 sub–spectra have been extracted.

The COS light curve (Figure 4.12) shows a significant variability of the ultraviolet flux on time scales close to half of the orbital period. Therefore, the spectrum in Figure 4.11, obtained averaging over the three spacecraft orbits, is not representative of this temporal evolution of the system. In order to investigate the temporal evolution of the white dwarf spectral appearance, we used the splitcorr routine from the CALCOS pipeline to split the observations into 19 shorter exposures, from which we extracted the corresponding spectra using the CALCOS x1dcorr routine.

Figure 4.13 shows the *HST* spectra corresponding to the minimum (#18, blue) and the maximum (#4, red) ultraviolet flux of SDSS1238. The spectral shape varies from that of a cool white dwarf (#18, with a very broad Lyα absorption extending to $\simeq 1\,600$ Å) to that of a hot white dwarf (#4, with a narrow Lyα profile and a steep blue continuum), revealing the heating and subsequent cooling of the white dwarf in SDSS1238.

We carried out spectral fits to the ultraviolet spectra to study the evolution of the white dwarf effective temperature throughout the *HST*/COS observations. Using the grid of white dwarf models described in the previous Section, we fitted the *HST* data and determined the white dwarf effective temperature for each of the 19 sub–spectra. To account for the presence of the additional continuum component,

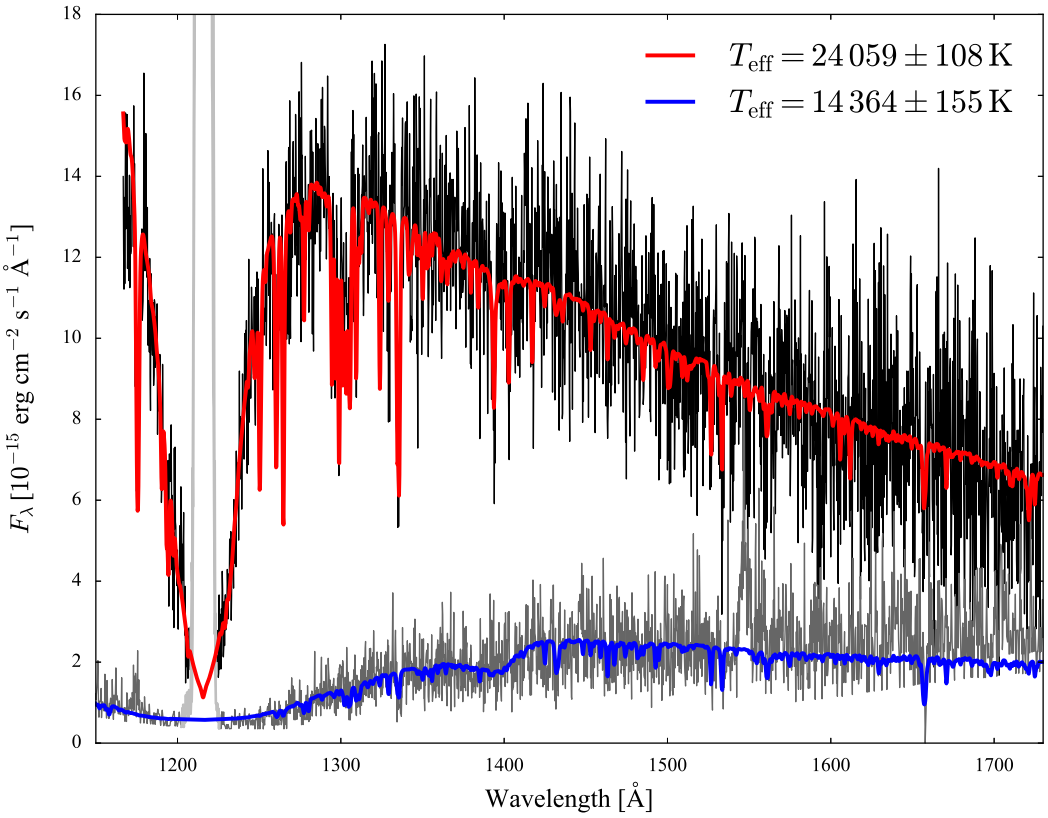

Figure 4.13: *HST*/COS spectra of SDSS1238 extracted at the minimum (#18, dark grey) and at the maximum (#4, black) brightness level (see Figure 4.12) along with the best fit models (blue and red, respectively). The geocoronal Lyα (1 216 Å) emission lines are plotted in grey.

we included a constant flux (in F_λ) in the fit. Although different approximations can be used to model this second component (such as a power law or a black body, see Section 3.3.2), we chose to use a constant flux since it is the simplest model and it introduces only one additional free parameter in the fit. Hereafter, we refer to this fitting method as the two–component fit (one white dwarf plus a constant).

We performed the spectral fit using the Markov chain Monte Carlo (MCMC, Section 2.4.3) implementation for Python EMCEE (Foreman-Mackey et al., 2013). We assumed a flat prior for the white dwarf effective temperature in the range $9\,000\,{\rm K} < T_{\rm eff} < 40\,000\,{\rm K}$ and constrained the white dwarf scaling factor and the additional second component to be positive. The best–fit results are summarised in Table 4.4.

Assuming the distance derived from the analysis of the X–shooter data, $d = 190\,{\rm pc}$, the scaling factor for each sub–spectrum corresponds to an *apparent* white dwarf radius (Figure 4.14, blue points, second panel), which varies from $\simeq 0.005\,{\rm R}_\odot$ to $0.009\,{\rm R}_\odot$ as a function of the heating and cooling.

This $\simeq 50$ per cent variation in the apparent radius implies that the heating

Table 4.4: Effective temperature variation of the white dwarf in SDSS1238.

		Two–component fit		Three–component fit	
Spectrum	Exposure time (s)	$T_{\rm WD}$ (K)	$\pm$ (K)	$T_{\rm hot}$ (K)	$\pm$ (K)
# 1	648	14 602	87	16 803	1 107
# 2	648	14 380	102	16 181	1 408
# 3	648	15 104	97	16 292	594
# 4	350	24 059	108	24 501	200
# 5	350	23 193	130	23 420	199
# 6	350	21 191	176	22 284	369
# 7	350	18 899	184	20 849	391
# 8	350	19 229	130	20 121	273
# 9	293	20 506	120	21 235	246
# 10	293	20 771	115	21 374	257
# 11	293	20 686	123	21 422	275
# 12	288	15 083	157	16 936	887
# 13	288	16 359	130	17 107	445
# 14	288	17 106	125	17 950	401
# 15	350	17 596	112	18 605	297
# 16	350	16 989	126	18 240	424
# 17	350	14 943	157	17 389	1 226
# 18	350	14 364	155	16 442	1 841
# 19	350	15 580	115	16 413	482

occurs only over a fraction of the visible white dwarf surface. To account for the presence of a hotter region, we repeated the fit to the 19 *HST* sub–spectra including two white dwarf models. In this procedure, we assumed an underlying white dwarf with $T_{\rm cool} = 14\,000\,{\rm K}$, slightly cooler than the minimum temperature measured from spectrum #18 ($T_{\rm eff} = 14\,364\,{\rm K}$), and allowed the presence of an additional hotter white dwarf. We assumed a flat prior on its effective temperature, constraining its value in the range $T_{\rm cool} < T_{\rm hot} < 40\,000\,{\rm K}$. As before, we included an additional flat F_λ continuum component. We constrained the flux scaling factors for the two white dwarf models and the F_λ component to be positive. Following the same nomenclature as before, we refer to this prescription as three–components fit (two white dwarfs plus a constant).

We find that this three–component fit successfully describes the observed variation of the ultraviolet flux, and the accompanying change of the white dwarf temperature, by heating and cooling of a region on the white dwarf surface. The area covered by the hotter region varies from $\simeq 5$ per cent up to $\simeq 80$ per cent of the visible white dwarf surface. The flux contribution of the flat F_λ component results

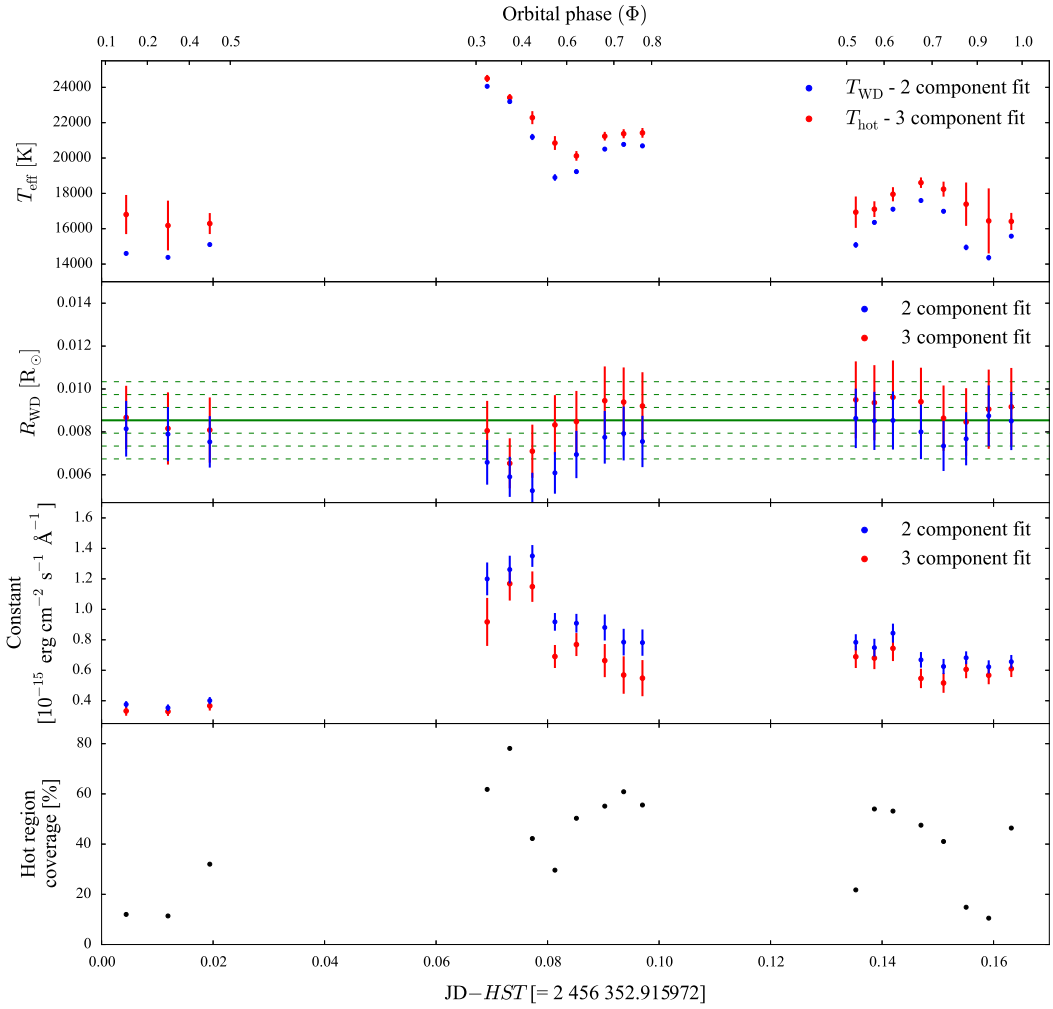

Figure 4.14: Best–fit results for the 19 *HST* sub–spectra for the two–component fit (blue dots) and the three–component fit (red dots). In the second panel, the solid green line represents the white dwarf radius as determined from the analysis of the X–shooter data. The dashed green lines are the relative 1σ, 2σ and 3σ uncertainties. The large change of the (apparent) white dwarf radius in the two–component fit (blue dots) rules this model out as a physically meaningful description. The bottom panel shows the coverage percentage of the hotter region from the three–component fit compared to the whole white dwarf surface.

almost unchanged between the two and the three–component fits (Figure 4.14, third panel).

In the three-component fit, the radius of the white dwarf (red points in Figure 4.14, second panel) can be calculated using Equation 2.2, where S is now the sum of the two scaling factors of the cold and hot white dwarf models. In contrast to the two-component fit, the white dwarf radius is in a better agreement with the value measured from the X–shooter data. Since the three-component fit does not implies a significant variation in the white dwarf size, we consider this a

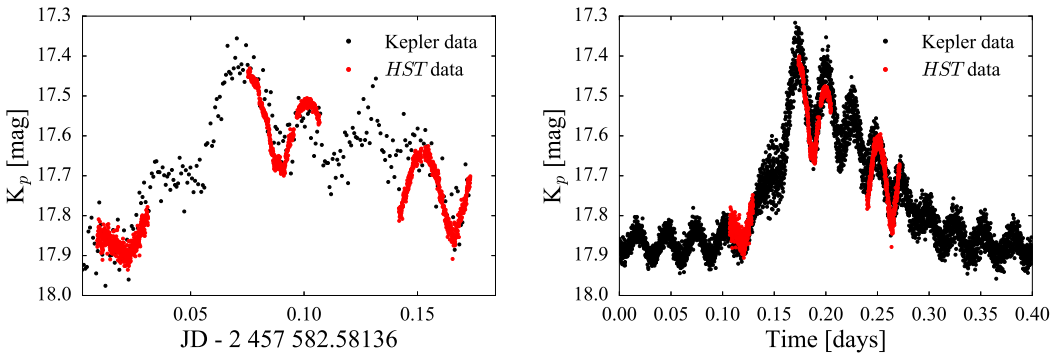

Figure 4.15: *HST* light curve (red) in comparison with *K2* data (black) of a sample brightening (right) and the *K2* light curve folded with respect to the 40.26 min ephemeris of the double-humps (left). The *HST* data are arbitrarily shifted in time to overlap with the *Kepler* observations. The perfect agreement between the two set of data demonstrates that the brightenings and humps detected in the optical light curve arise from the heating and the cooling of the white dwarf unveiled by the *HST* observations.

more physical and realistic model of the behaviour of SDSS1238.

4.3.5 Energetics of the brightenings

The photometric variability of SDSS1238 observed in the ultraviolet closely resembles the shape of the optical lightcurve. In order to compare the *HST* and *Kepler* observations, we converted the *HST* count rate light curve shown in Figure 4.12 into magnitudes and then we scaled and shifted them in order to match the *K2* data (Figure 4.15). The perfect agreement we found between the *HST* and *Kepler* dataset clearly demonstrates that the heating and the cooling of the white dwarf detected in the ultraviolet is the origin of both the brightenings and the double–humps detected in the optical light curve of SDSS1238.

Moreover, we convolved the best–fit models obtained from the three–component fit to the *HST* data with the K_p filter passband, obtaining the corresponding magnitudes of the white dwarf (Figure 4.16). While the ultraviolet emission is dominated by the white dwarf, its contribution in the optical varies from $\simeq$ 40 per cent in quiescence up to $\simeq$ 60 per cent during the brightening. The accretion disc and, potentially, the second component detected in the ultraviolet and extending into the optical, make up to the remaining half of the emission.

Finally, to calculate the energy excess associated with the brightenings, we first computed the average counts associated with each *HST* subspectrum, scaling the value accordingly to the percentage of white dwarf contribution with respect to the additional second component. We found an analytical expression for the relationship between the average counts and the effective temperature of each *HST*

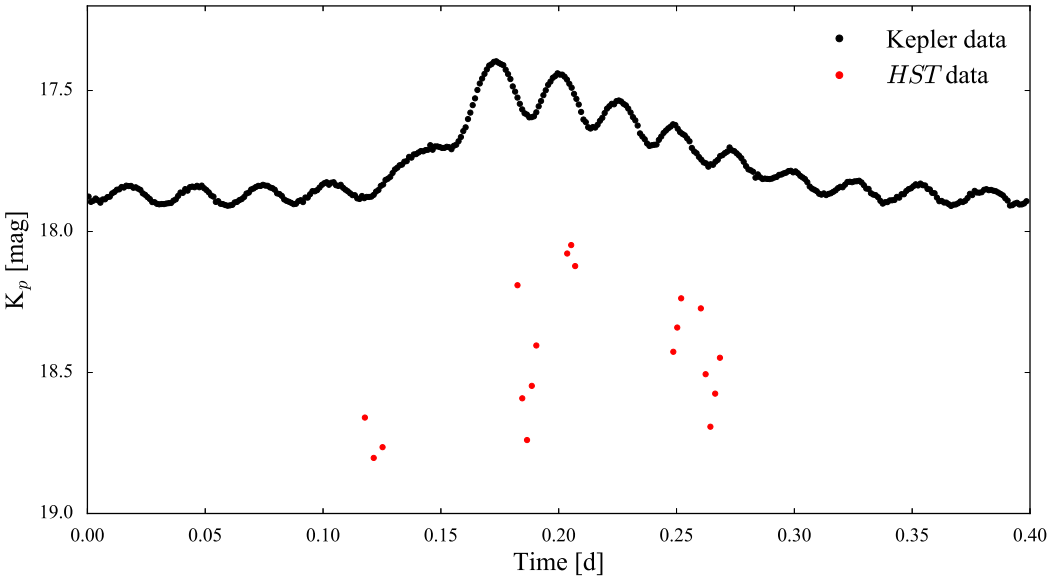

Figure 4.16: The *HST* synthetic K_p magnitudes, computed from the convolution of the best–fit models to the *HST* subspectra with the K_p filter curve, are shown in comparison with the *K2* light curve folded with respect to the 40.26 min ephemeris of the double–humps (black). The white dwarf contribution in the optical varies from $\simeq$ 40 per cent in quiescence up to $\simeq$ 60 per cent during the brightening.

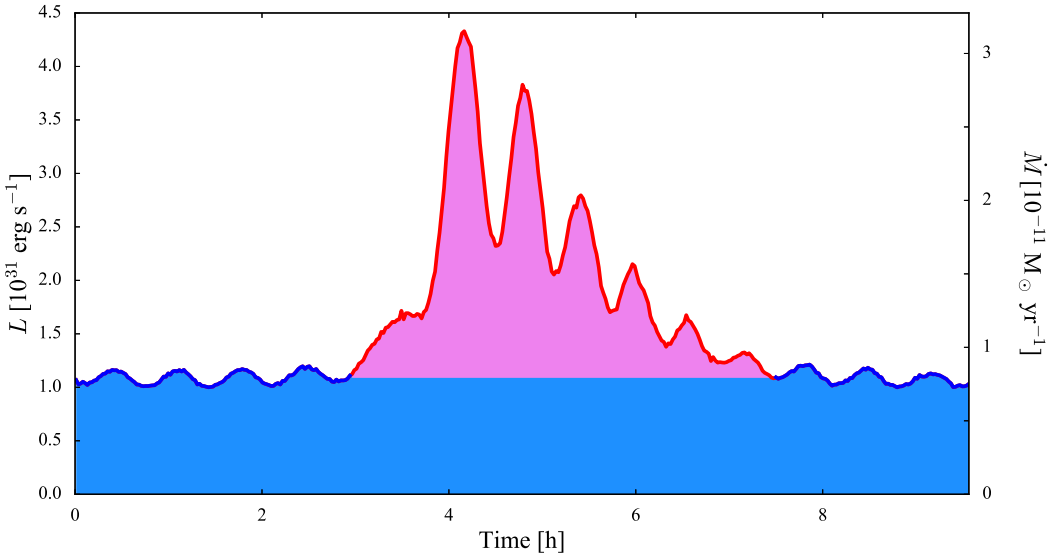

Figure 4.17: Luminosity of SDSS1238 calculated from the average brightening light curve. The blue line highlights the quiescent level, which corresponds to an energy of $\simeq 4 \times 10^{30}$ erg (light blue area). The excess of energy during the brightening (magenta area beneath the red line) corresponds to $\simeq 2 \times 10^{35}$ erg.

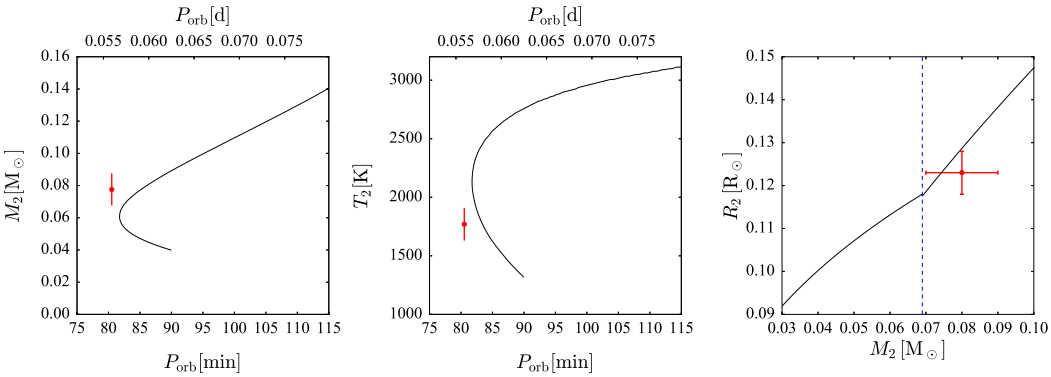

Figure 4.18: The mass and effective temperature of the secondary in SDSS1238 (left and middle panel respectively) are plotted in comparison with the evolutionary track for the revised model from Knigge et al. (2011). The right panel shows the comparison between the secondary mass and radius with the mass–radius relationship for CV donor from Knigge et al. (2011). The vertical dotted line represent the mass at which the bounce should occur. All the error bars represent 1σ uncertainties. Given the location of SDSS1238 at the period minimum and the uncertainties on our results, we cannot draw any definitive conclusion on the period bouncer nature of this system.

subspectrum. Using the *HST* data as a reference, we converted the average brightening light curve in counts/s. We then used the relation between the average *HST* counts and effective temperature to calibrate the *Kepler* data and, from the knowledge of the temperature, we computed the luminosity (Figure 4.17). After subtracting the quiescence level, which we approximated with a constant, the energy excess released during the average brightening corresponds to $\simeq 2 \times 10^{35}$ erg.

4.4 Discussion

4.4.1 SDSS1238 as a period bouncer

Aviles et al. (2010) fitted the optical spectrum of SDSS1238 with a combination of a white dwarf and an accretion disc model. Extending the best–fit model into the infrared and comparing the photometric observations with the predicted flux at these wavelengths resulted in the detection of an infrared excess from which Aviles et al. (2010) inferred that the secondary is a brown dwarf of spectral type L4 and argued that SDSS1238 is a period bouncer.

From the analysis of the X–shooter data we have spectroscopically confirmed the presence of a brown dwarf companion. However, given the location of SDSS1238 near the period minimum, it is difficult to establish whether this system is a period bouncer or not. In fact a brown dwarf companion is a condition necessary but not sufficient for the system to be a post–bounce CV. The other fundamental ingredient

is that $\tau_{\dot{M}_2} \ll \tau_{\rm kh}$ and thus the secondary must be driven considerably out of thermal equilibrium. Although the currently available observations of SDSS1238 do not allow a direct measurement of the secondary mass loss rate, we can make the rough assumption that the secondary is losing mass at the same rate at which the white dwarf is accreting. A direct measurement of the latter is provided by the white dwarf effective temperature (Townsley and Bildsten, 2003; Townsley and Gänsicke, 2009) and the temperature of SDSS1238 derived from the *HST* spectrum obtained near the flux minimum ($T_{\rm eff} \simeq 14\,000\,{\rm K}$) corresponds to $\simeq 3.4 \times 10^{-11}\,{\rm M}_{\odot}\,{\rm yr}^{-1}$. This is typical value for a system near the period minimum (Townsley and Gänsicke, 2009; Pala et al., 2017) and it is actually higher compared to those of period bouncer CVs (see Figure 3.24). In addition, comparing the system parameters obtained in Section 4.3.2 with the theoretical predictions, we found conflicting results. While the secondary effective temperature suggests a post–bounce CV, its mass and radius are in good agreement with the mass–radius relationship for CV donors computed by Knigge et al. (2011), accordingly to which, the bounce should occur at $M_2 \simeq 0.07\,{\rm M}_{\odot}$ (see Figure 4.18). Therefore we cannot determine whether this system has already evolved through the period minimum or not.

4.4.2 The origin of the optical and ultraviolet variability in SDSS1238

The optical lightcurve of SDSS1238 shows quasi–sinusoidal double–humps at half the orbital period, and quasi–periodic brightenings every $\simeq 8.5\,{\rm h}$, during which the system brightness increases by $\simeq 0.5\,{\rm mag}$. Moreover, the double–humps grow in amplitude and undergo phase shifts during the brightenings. We have detected the same behaviour in the ultraviolet data and shown that these photometric modulations originate from heating and cooling of a fraction of the white dwarf.

Two physical processes, accretion and non–radial pulsations, are plausible physical mechanisms causing the observed variations in the white dwarf effective temperature. In the following, we discuss in detail the possible scenarios for the origin of the observed variability of SDSS1238.

The double–humps

The fact that the double-humps are modulated at half the orbital period implies the presence of two heated regions that become alternatingly visible to the observer every half orbital period. One or two hot spots on the white dwarf are commonly observed in polars and intermediate polars, CVs hosting magnetic white dwarfs (e.g. Stockman et al., 1994; Eracleous et al., 1994; Gänsicke et al., 1995; Araujo-Betancor et al., 2005a; Gänsicke et al., 2006). In these systems, the accreting material couples to the magnetic field lines resulting in localised heating near the white dwarf magnetic poles. As the white dwarf rotates, these spots become periodically visible thus

resulting in a flux modulation at the white dwarf spin period. However, although the time resolution of the *K*2 data ($\simeq 1$ min) would easily allow the detection of the white dwarf spin ($\simeq 6$ min), we do not detect such signal in the periodogram of the *K*2 light curve (Figure 4.7). Therefore the only way in which a magnetic white dwarf could explain the observational properties of SDSS1238 would require that the white dwarf spin period is equal to the orbital period. Spin–orbit locking of the white dwarf is a key defining feature of polars, having magnetic fields of $10 \lesssim B \lesssim 200$ MG (Ferrario et al., 2015). For lower field strengths, the white dwarf is always spinning faster than the orbital period (Mukai, 2017). Given our stringent upper limit on the field strength of SDSS1238, $B < 100$ kG, we can rule out that the white dwarf is spinning at the orbital period. Hence the non–detection of the white dwarf spin implies that the hot spots must be symmetric with respect to the white dwarf rotation axis.

The analysis of the *K*2 data provides additional constraints on the geometry of these regions. In fact, the hot spots must be limited in their azimuthal extension but spread vertically, in order to give rise to the observed quasi–sinusoidal modulation also during the brightenings, when they cover $\simeq 80$ per cent of the visible white dwarf surface (Figure 4.14, bottom). Such a vertical extension is plausible if the inner disc is evaporated in a hot diffuse corona that extends vertically above the disc (Meyer and Meyer-Hofmeister, 1994). This hot corona could, in turn, be also at the origin of the continuum second component detected in the ultraviolet spectra. Furthermore, given that the white dwarf spin period is much shorter than the orbital period, the cooling time of the hot spots must be shorter than the spin period of the white dwarf, in such a way that the hotter regions are not spread into an accretion belt which would suppress the photometric humps.

Double–humps during quiescence have been identified in many other short period CVs (see for example Patterson et al. 1996; Augusteijn and Wisotzki 1997; Rogoziecki and Schwarzenberg-Czerny 2001; Pretorius et al. 2004; Dillon et al. 2008) and are thought to arise from spiral arms in the accretion disc, giving rise to photometric humps locked with the orbital period of the system (Osaki and Meyer, 2002). Spiral arms have been detected in the first phases of the outbursts of IP Peg (Steeghs et al., 1997), EX Dra (Joergens et al., 2000), WZ Sge (Steeghs et al., 2001), and U Gem (Groot, 2001), when the enhanced mass transfer rate and angular momentum transfer through the disc (Section 1.5.3) allow its expansion up to the 2:1 resonance radius, giving rise to the spiral structure (Lin and Papaloizou, 1979). On the contrary, in quiescence, the disc is smaller and it is quite unlikely that it extends up to the 2:1 resonance radius (at least in systems with $q > 0.06$, Matthews et al. 2006). In this case, spiral arms can develop as consequence of a shock due to the tidal interaction with the secondary. Owing to the relative supersonic velocities

between different disc orbits, the presence of such a shock would allow the accreting matter to spiral inward, developing (at least) two spiral density waves (Spruit, 1987).

As already suggested by Aviles et al. (2010), spiral density waves can well explain the peculiar light curve of SDSS1238. In this case, two spiral shocks originate in the outer disc and then propagates into the inner region. The interface between the white dwarf and the inner edge of these spiral arms are two hot spots that, every half orbital period, are visible to the observer. The spiral density waves could modulate the accretion onto the white dwarf through these hot spots (Rafikov, 2016) causing the detected heating and cooling of the white dwarf in the *HST* data.

To investigate the presence of spiral shocks, we computed the Doppler maps from the X–shooter data (Figure 4.19). Our results are similar to the maps presented by Aviles et al. (2010, see their figure 4). The four regions of enhanced emission detected in the Hα Doppler map may be associated with the tidal shocks expected in the accretion disc of low mass ratio CVs (Kononov et al., 2015). Moreover, the two symmetric dips observed in the Hδ map resemble those observed on the Doppler maps of IP Peg (see figure 1 from Steeghs et al. 1997), suggesting the presence of spiral density waves.

The brightnenings

Thermal instabilities in the disc

During the brightenings, the hot regions become larger as a bigger fraction of the white dwarf is heated. These events are not random as, from the analysis of the *K2* lightcurve, we have identified the presence of a *systematic* mechanism, similar to that driving dwarf nova outbursts.

As described in Section 1.5.3, accretion discs experience a thermal instability once they undergo partial ionisation of hydrogen, increasing the viscosity and resulting in a temporary increase of the mass flow rate through the disc. This phenomenon is observed in the form of dwarf nova outbursts, during which the white dwarf in heated by the increased accretion rate (Gänsicke and Beuermann, 1996; Sion et al., 1998; Godon et al., 2004b; Long et al., 2004; Piro et al., 2005). In the hot state, the mass flow rate through the disc is higher than the mass loss rate of the secondary, so eventually the column density in the disc drops below a critical rate, resulting in the recombination of hydrogen, a drop in viscosity, and a decrease in the accretion rate onto the white dwarf, which subsequently cools back to its quiescent temperature. Regular dwarf nova outbursts last days to weeks, i.e. much longer than the $\simeq 8.5$ h brightening events in SDSS1238. However, a similar phenomenon, on shorter time scales and with smaller amplitudes, could be occurring in SDSS1238. Furthermore, thermal instabilities in the accretion disc would also be

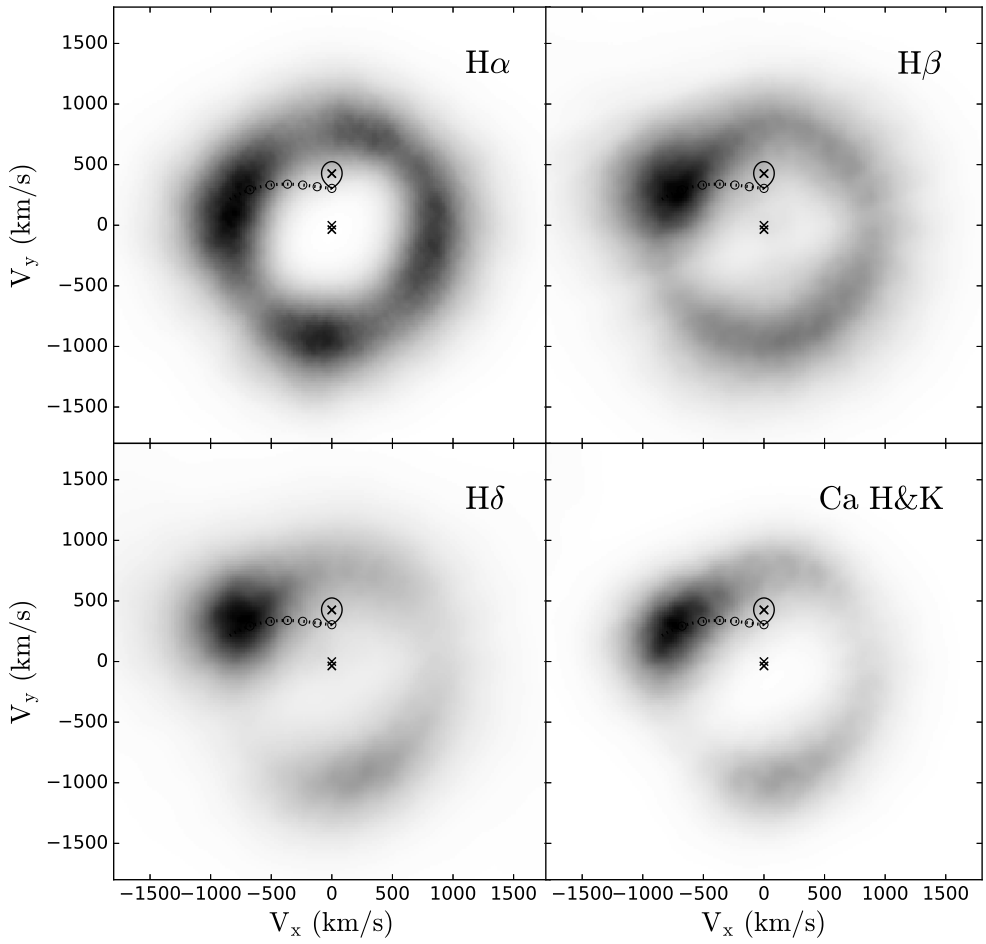

Figure 4.19: Doppler maps of SDSS1238 computed from the Balmer and the Calcium H & K emission lines detected in the X–shooter data. Four regions of enhanced disc emission are clearly visible in the Hα map and can be interpreted as the tidal shocks expected in the accretion discs of WZ Sge stars (Kononov et al., 2015). The symmetric dips detected in the Hδ and Ca H & K lines, resembles those detected in the Doppler maps of IP Peg (see figure 1 from Steeghs et al. 1997), suggesting the presence of spiral density waves.

consistent with the rise of the emission of the second component observed in the *HST* spectra at the inset of the brightening (see the third panel of Figure 4.14), as its temperature increases following the enhanced accretion onto the white dwarf.

Our measurement of the increased luminosity during the brightening (Section 4.3.5) is consistent with an accretion event. After subtracting the quiescence level, the mass accreted on a single average brightening results in $\simeq 1 \times 10^{-13}\,M_{\odot}$. Assuming an occurrence of three brightenings per day, this corresponds to a mass accretion rate of $\simeq 1 \times 10^{-10}\,M_{\odot}yr^{-1}$, a value not too different from the typical mass accretion rate of CVs at the period minimum (Townsley and Gänsicke, 2009;

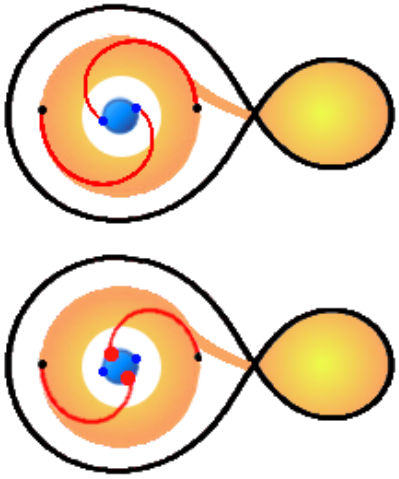

Figure 4.20: Schematic drawing of the phase shifts of the double humps during the brightenings. The secondary is filling its Roche lobe and is transferring matter onto the white dwarf via an accretion disc. Owing to instability in the accretion disc, probably due to the tidal interaction of the secondary, spiral shocks originating in the outer disc (black dots) propagate towards the centre. In order to generate the humps observed in the light curve during the brightenings, the inner part of the disc must be hot and optically thin, extending vertically far from the orbital plane. In this cartoon, this is illustrated as the white region in the inner part of the disc (the scale is exaggerated). *Top:* during quiescence the spiral arms are phase locked. The corresponding hot spots occupy $\simeq 10$ per cent of the white dwarf surface. *Bottom:* during the brightenings, the speed of sound increases in the disc and the opening angle of the spiral arms becomes larger. The area of the bright spots increases and their undergo phase shifts by $\simeq 90°$(red dots) with respect to their location in quiescence (blue dots), owing to the enhanced mass transfer rate.

Pala et al., 2017).

The combination of thermal instabilities and spiral shocks in the accretion disc might also be the origin of the phase shifts detected during the brightenings in the $O - C$ diagram of the double–humps (Figure 4.10). This is because the opening angle of the spiral shocks is determined by the Mach number, i.e. the ratio between the orbital velocity and the speed of sound in the gas at a given disc radius. During an outburst, the density increases and the speed of sound decreases. With a higher Mach number, the opening angle is bigger and the shocks result phase shifted (Figure 4.20), up to about $\simeq 90°$ at the maximum of the brightening.

In conclusion, the brightenings observed in the light curve of SDSS1238 can arise from thermal instabilities occurring in the disc every $\simeq 8.5$ h. These can periodically drain the disc of material and prevent the onset of normal dwarf nova outbursts, explaining the long outburst recurrence time of SDSS1238, which is of the order of decades. The disappearance of the brightenings in SDSS0804 after its superoutburst in 2006 (Zharikov et al., 2008) further reinforces the idea of a

disc origin for these events. It is possible that after the superoutburst, the delicate equilibrium for the brightening occurrence has been broken and, following also a second superoutburst of SDSS0804 in 2010 (Isogai et al., 2015), this has not been restored yet. Additional support to this hypothesis can be provided by photometric observation of SDSS1238 in order to verify whether, as in the case of SDSS0804, the brightenings are still occurring in this CV after its recent superoutburst.

White dwarf pulsations

Given that the period of the humps is half the orbital one, it is quite unlikely that they are related to pulsations in the white dwarfs. However, the correlations we have identified between the amplitude, the recurrence time and the duration of the brightenings, do not allow us to draw the same conclusion in the case of the brightenings.

ZZ Ceti white dwarfs exhibit non–radial pulsations that are driven by opacity instabilities of a partially ionised layer of hydrogen in their envelopes, occurring in the temperature range of $T_{\rm eff} \simeq 10\,500 - 12\,000$ K (Althaus et al., 2010). Brightenings similar to those observed in SDSS1238 have been discovered recently in *Kepler* observations of ZZ Ceti white dwarfs (Bell et al., 2015; Hermes et al., 2015; Bell et al., 2016, 2017). These DAV (hydrogen dominated pulsating) white dwarfs are characterised by a sudden increase in brightness, during which their flux increases typically by $\simeq 15$ per cent above the quiescent level (although in the extreme case of PG 1149+057, flux increases of $\simeq 45$ per cent above the quiescent level have been observed, Hermes et al. 2015). The recurrence time and duration of these events vary among different objects and, on average, they occur every five days and last $\simeq$ 12h (Bell et al., 2017). Since none of these DAVs is part of a binary system, the brightenings must arise from the white dwarfs themselves. All six ZZ Ceti white dwarfs known to show these brightenings are located at the red edge of the instability strip, and it has been suggested that the brightenings originate from the change in the physical condition of the convective layer of the white dwarfs as they cool and move out of the red edge of the instability strip for ZZ Ceti stars (Bell et al., 2015). The physics behind the brightenings is not well understood yet but it appears to be firmly related to the non–radial pulsations of these stars.

Although SDSSS1238 is too hot to fall inside the canonical ZZ Ceti instability strip, ongoing accretion implies that its atmosphere is helium–rich and, with an effective temperature of $T_{\rm eff} \simeq 14\,000$ K, SDSS1238 is located in the regime where many CV white dwarfs exhibit pulsations. It is thus possible that SDSS1238 exhibits helium driven pulsations (arising from opacity instabilities in a partially ionised layer of helium in its envelope, Arras et al. 2006; Szkody et al. 2010; Van Grootel et al. 2015). Therefore, it is conceivable that the brightenings in SDSS1238 are, as those

in the isolated DAVs, produced by non–linear mode coupling. This hypothesis is further corroborated by the identification of similar correlation as observed for DAVs (Bell et al., 2015) between the amplitude, the duration and the recurrence time of the brightenings in SDSS1238 (see Section 4.3.3).

Similar temperature variations as those observed in SDSS1238 during the brightenings (from $T_{\rm eff} \simeq 14\,000$ K up to $T_{\rm eff} \simeq 24\,000$ K, Figure 4.13) have also been seen in the pulsating CV white dwarf GW Lib. Toloza et al. (2016) argued that the heating and cooling of GW Lib by 3 000 K on timescales of $\simeq 4$ h can be explained by a retrograde pulsation wave in a rapid rotating white dwarf. Interestingly, SDSS1238 heats and cools in comparable timescales and its spin period ($\simeq 360$ s) is similar to that of GW Lib ($100 - 200$ s, van Spaandonk et al. 2010; Szkody et al. 2012).

A caveat to this interpretation is that we do not detect short–period pulsations (Figure 4.7) in the *K2* data, however, it is possible that the amplitude of these pulsations is too low to be detected in the *K2* light curve.

The recent superoutburst of SDSS1238 offers the unique possibility to test this hypothesis. In fact, the temporarily enhanced accretion rate during the outburst likely heated the white dwarf by $\simeq 10\,000$ K above its quiescent temperature (see e.g. the case of WZ Sge, Long et al. 2003), thus moving the system to the blue edge of the accreting white dwarf instability strip. In a hotter white dwarf, non–radial pulsations are expected to have much larger amplitude and thus high–time resolution photometric observations of SDSS1238 in the next years can potentially reveal the inset of pulsations during the cooling of the white dwarf, as in the case of SDSS0804 after its 2006 and 2010 superoubursts (Pavlenko, 2009; Pavlenko et al., 2014). If pulsations are detected also in SDSS1238, this will be the third CV, together with SDSS0804 and GW Lib, showing brightenings and pulsations thus providing additional support to the presence of a correlation between the two phenomena.

4.5 Conclusions

SDSS1238 is a short period CV of the WZ Sge class, located near the period minimum. We have observed the first detected superoutburst of this system, which occurred on 2017 July 31. Superhumps are clearly visible in the light curve of this event, from which we measure the system mass ratio: $q = 0.08 \pm 0.01$.

From the analysis of phase–resolved X–shooter observations, we determine the physical parameters of the two stellar components. We find that SDSS1238 hosts a relatively massive white dwarf ($M_{\rm WD} = 0.97 \pm 0.05\,{\rm M}_{\odot}$) and a brown dwarf donor ($M_2 = 0.08 \pm 0.01\,{\rm M}_{\odot}$) of L3 $\pm$ 0.5 spectral type. Given the location of this system at the period minimum ($P_{\rm orb} = 80.5200 \pm 0.0012$ min), it is difficult to

unambiguously establish whether this CV is a period bouncer.

The high resolution of the X–shooter observations allow us to determine an upper limit on the magnetic filed of the white dwarf: $\langle B \rangle \lesssim 50 - 100\,\mathrm{kG}$. This is a conservative upper limit since it has been obtained assuming a non–rotating white dwarf. However, owing to the mass transfer process, the white dwarf is also accreting angular momentum and it is therefore likely that it is a fast rotator. Consequently, SDSS1238 probably hosts a non–magnetic white dwarf.

The *Kepler* lightcurve of SDSS1238 is characterised by two types of variability: the brightening and the double–humps. The first occur every $\simeq 8.5\,\mathrm{h}$, during which the white dwarf brightness increases by $\simeq 0.5\,\mathrm{mag}$ for about one hour. The latter are smaller amplitude sinusoidal modulations with a period of half the orbital one. The two modulations are also clearly visible in the ultraviolet light curve obtained from *HST*/COS TIME–TAG observations and correspond to the heating of two regions at the white dwarf surface.

Analysing the high–time resolution photometry of SDSS1238 obtained with *Kepler*, we detect a correlation between the amplitude, the duration and the recurrence time of the brightenings and we argue that these events arise most likely from thermal instabilities in the accretion disc. Moreover, by periodically draining the disc of material, the thermal instabilities would also explain the long recurrence time of the outbursts in SDSS1238.

The double humps can be explained by shocks originating at the outer edge of the disc due to the secondary tidal interaction. Owing to the supersonic velocity difference between different orbits, the shocks spiral inward, generating two wound–up density waves and creating two hot spots at the white dwarf surface. The $O-C$ diagram of this photometric modulation shows that, during the brightenings, the double humps undergo phase shifts. We suggest that the phase shifts originate from the change in the speed of sound of the gas in the accretion disc during the brightening. During the thermal instabilities, the disc density increases and the opening angle of the spiral arms becomes bigger, causing a shift of the hot spot by $\simeq 90^\circ$ with respect to their position at the white dwarf surface during quiescence.

By modulating the accretion rate onto the white dwarf, the spiral density wave and the thermal instabilities can explain the heating and cooling of the white dwarf observed in the *HST* data.

An alternative possibility is that the brightenings are caused by a similar mechanisms acting at the origin of the flares in isolated pulsating white dwarf (Bell et al., 2015), i.e. the changing in the physical condition of the convective layer while the white dwarf cools and crosses the edge of the instability strip. Although we do not identify pulsations in the *K2* data, it is possible that they have low amplitudes which are below the *Kepler* detection threshold. In order to test this hypothesis,

high–time resolution photometry observations of SDSS1238 are required in the next year. Now that the system is cooling after the recent superoutburst, the white dwarf is located at the blue edge of the instability strip and the detection of the onset of pulsation during the cooling of the white dwarf would reveal a connection between the brightening phenomena in isolated and accreting white dwarfs.

Chapter 5

The SU UMa QZ Lib: a period bouncer

5.1 Introduction

The lack of period bouncers in the present day CV population is an outstanding problem that only recently has started to be addressed thanks to the advent of large telescopes and deep surveys. However, the handful of period bouncers identified so far is still far from making up the predicted fraction ($\simeq 40-70\%$, Kolb 1993; Knigge et al. 2011; Goliasch and Nelson 2015) of the Galactic CV population. Therefore enlarging the sample of post–bounce CVs is important in order to validate a fundamental prediction of the current models of compact binary evolution (see Section 1.6.3).

One of the best parameters to identify a period bouncer is the mass ratio $q = M_{\rm sec}/M_{\rm WD}$. In fact, during the system evolution, donor stars in CVs continuously lose mass and, since the typical mass of CV white dwarfs is $\simeq 0.8\,{\rm M}_{\odot}$ (Zorotovic et al., 2011), the mass ratio reflects the evolutionary stage of the system (Figure 1.14b, Patterson et al. 2005a; Knigge et al. 2011). In particular, for systems with $P_{\rm orb} \simeq 90\,{\rm min}$ that have not yet evolved through the period minimum (pre–bounce CVs), the expected mass ratio is $q \simeq 0.13$ while period bouncers at the same orbital period are expected to have $q \simeq 0.03$ (Knigge, 2006). Given the bifurcation of the CV evolutionary track at the period minimum, this difference further increases for longer period CVs. Therefore the mass ratio is a discriminant between pre and post–bounce systems (see for example figure 6 from Howell et al. 2001) and provides a powerful tool to successfully identify period bouncer candidates when a direct spectroscopic detection of the secondary is not possible (Patterson, 2011; Kato et al., 2015, 2016).

A measurement of the mass ratio can be obtained from superhumps, i.e. low–amplitude modulations observed in the lightcurve of short–period CVs during

superoutburts, using the empirical relationship calibrated by Kato and Osaki (2013, Section 1.5.3).

In February 2004, Pojmanski (VSNET–alert 7982) detected the outburst of a new eruptive star in Libra, QZ Lib (aka ASAS 153616–0839.1). Lightcurves taken all over the world revealed that the object showed periodic variability with a probably increasing period (Kiyota, 2004), which was thus interpreted as growing superhumps with a final period of $P_{\rm sh} = 0.06501(3)$ d (Kato, 2004). Schmidtobreick et al. (2004) confirmed the SU UMa classification spectroscopically.

QZ Lib was included by Patterson (2011) in his list of period bouncer candidates (see their table 3 and table 5) owing to its low tentatively derived mass ratio ($q = 0.035 \pm 0.020$, Patterson et al. 2005a). However, Patterson et al. (2005a) obtained this measurement from unpublished CBA (Center for Backyard Astrophysics) data and hence it is not clear either the accuracy or the significance of this measurement. Here, we present new phase–resolved photometric and spectroscopic observations of this system, from which we derive a more reliable mass ratio that, combined with the spectral energy distribution analysis, demonstrates the likely period bouncer nature of the system.

5.2 Observation and data reduction

5.2.1 Spectroscopic observations

Low resolution spectra and medium resolution time–series spectra were obtained at several epochs in 2004 using EFOSC2 at the 3.6–meter telescope on La Silla Observatory, Chile. The details of the observations are given in Table 5.1.

The standard reduction of the data was performed using IRAF[1] (Tody, 1986, 1993). The bias level has been subtracted and the data have been divided by a flat field, which was normalised by fitting Chebyshev functions of high order to remove the detector specific spectral response. All spectra have been optimally extracted following the method of Horne (1986) and the low resolution spectra of each night have been averaged. Wavelength calibration yielded a final FWHM resolution of 12.8 Å for the low resolution data (grism # 6) and 5.5 Å for the medium resolution data (grism #10). All further analysis has been done using the ESO–MIDAS toolkit.

For the low resolution data, the instrument response function was corrected using spectroscopic standards at low airmass. Since the nights have been clear but not photometric, we performed differential photometry on the acquisition files to determine the relative flux values of our object with respect to four comparison

[1]IRAF is distributed by the National Optical Astronomy Observatories, which are operated by the Association of Universities for Research in Astronomy, Inc., under cooperative agreement with the National Science Foundation.

Table 5.1: Summary of the observational details.

Date (UT)	Tel./Inst.	Grism/Slit/Filter	$N_{\rm Exp}$	$t_{\rm Exp}$[s]
2004-03-15	3.6/EFOSC2	Gr #6, 1.0"	3	600
2004-03-16	3.6/EFOSC2	Gr#10, 1.0"	30	400
2004-03-17	3.6/EFOSC2	Gr#10, 1.0"	15	300
2004-05-01	3.6/EFOSC2	Gr#6, 1.0"	3	600
2004-08-27	3.6/EFOSC2	Gr#6, 1.0"	3	900
2004-08-28	3.6/EFOSC2	Gr#10, 1.0"	6	400
2004-08-29	3.6/EFOSC2	Gr#10, 1.0"	26	400
2004-08-30	3.6/EFOSC2	Gr#10, 1.0"	11	400
2005-02-07	1.0–m SMARTS	V	12	300
2005-02-09	1.0–m SMARTS	V	19	300
2005-02-10	1.0–m SMARTS	V	21	300
2005-02-11	1.0–m SMARTS	V	17	300
2005-02-12	1.0–m SMARTS	V	20	300
2005-02-13	1.0–m SMARTS	V	22	300
2005-02-13	3.6/EFOSC2	V	145	20
2012-08-13	VLT/X–shooter	UVB,VIS,NIR	6,6,7	244,252,249
2012-08-15	VLT/X–shooter	UVB,VIS,NIR	4,4,4	244,252,249
2013-04-21	VLT/X–shooter	UVB,VIS,NIR	24,24,24	244,252,249
2015-05-12	VLT/X–shooter	UVB,VIS,NIR	9,7,7	410,465,510

stars. The spectra were scaled accordingly. Hence, while the absolute zero–point is more uncertain, the relative flux calibration of the individual spectra and the flux differences between the three spectra have an accuracy of about 4%.

High–resolution time–series spectroscopy was obtained with X–shooter at four epochs in 2012, 2013, and 2015. The data processing was performed with the ESO Reflex pipeline.

QZ Lib is located at a galactic latitude of about 34° and, assuming a distance of $d = 120 \pm 50$ pc (Patterson et al., 2005a), in Chapter 3 we determined an interstellar extinction of $E(B-V) = 0.054$ from the three–dimensional map of interstellar dust reddening based on Pan–STARRS 1 and 2MASS photometry (Green et al., 2015). Thus the interstellar extinction can be considered low and we present the spectra as observed, i.e. without reddening correction.

5.2.2 Photometric observations

Differential photometry at five minute cadence was performed using a V–band filter in front of a 512x512 CCD mounted on the 1.0 m SMARTS telescope at CTIO in February 2005. 1.5 h of photometry with higher time resolution (20 s) were observed with EFOSC2 on February 2013. The details of the observations are given in Table 5.1. The reduction was done with IRAF and included the usual steps of bias

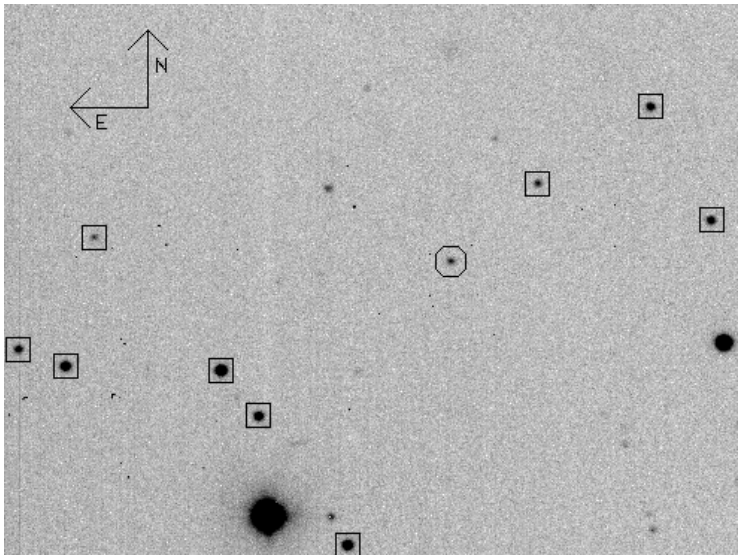

Figure 5.1: Finding chart of QZ Lib (circle, RA = $15^{\mathrm{h}}\,36^{\mathrm{m}}\,16\overset{\mathrm{s}}{.}0$, Dec. = $-08^{\circ}\,39'\,07\overset{''}{.}6$) and the nine reference stars used for the differential photometry (squares). The field of view is $4' \times 3'$, north is up, east to the left.

subtraction and division by skyflats. Aperture photometry for all stars on the CCD field was computed using the stand–alone version of DAOPHOT and DAOMASTER (Stetson, 1992). Differential light curves were established with respect to an average light curve of nine comparison stars (see Figure 5.1), which were present on all frames and were checked to be non–variable.

5.3 The lightcurve

The SMARTS and EFSOC2 lightcurves are plotted in Figure 5.2. The zero point for the differential magnitude corresponds to the average magnitude $V = 18.2 \pm 0.1$ of QZ Lib that was calculated using the USNO (United States Naval Observatory) magnitudes of the comparison stars.

The brightness of QZ Lib is clearly varying, however, this variation is more of an irregular nature, with flickering and long–time variations dominating the light curves. We searched for periodic modulation using various Fourier techniques but did not find any persistent signal. Similar results can be derived from the photometric observations in the AAVSO database (Figure 5.3). In the last ten years, four outbursts reaching about 16 mag have been observed but no orbital variation is detected even for those nights that are covered with ample data points (Figure 5.4).

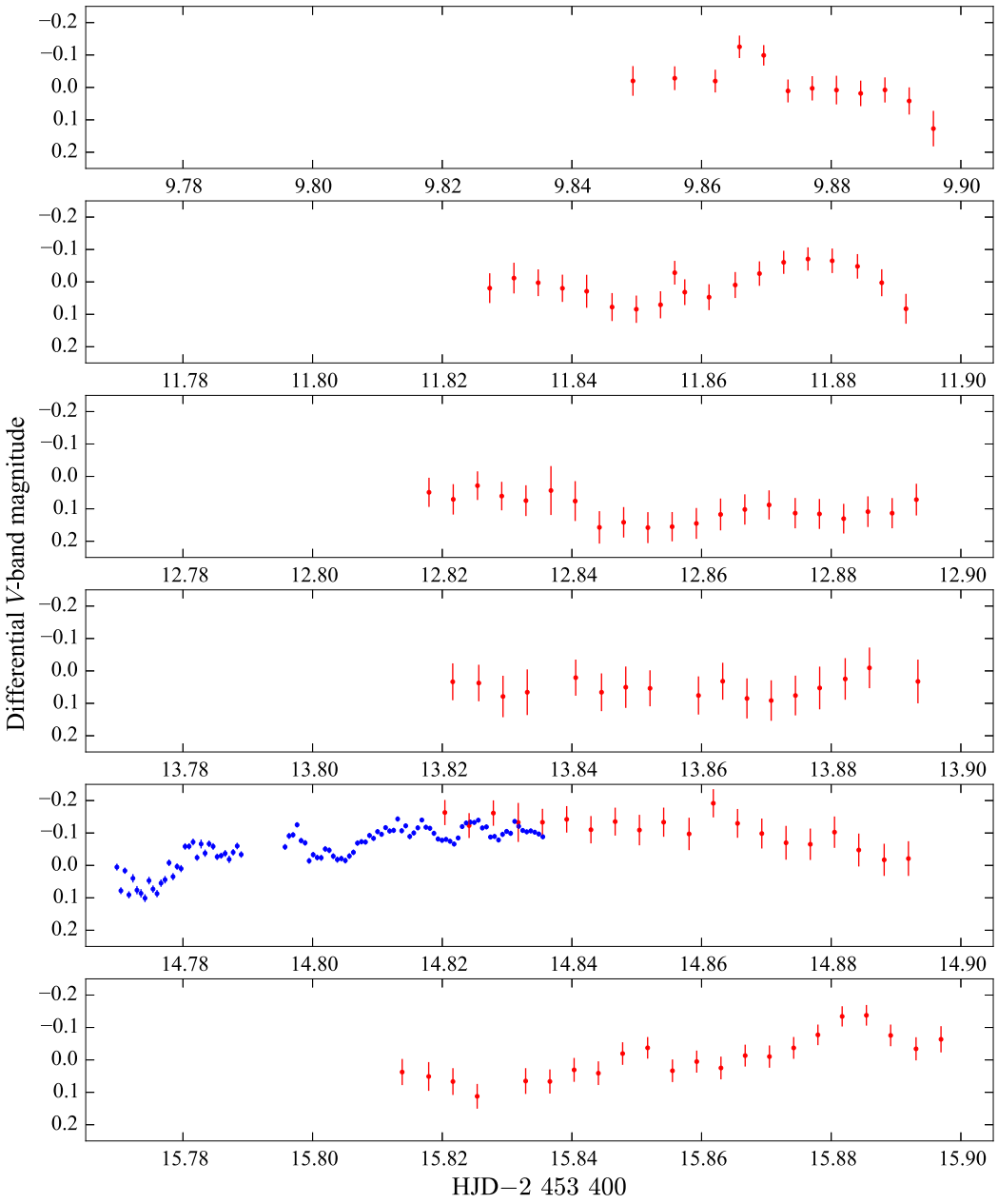

Figure 5.2: SMARTS (red) and EFOSC2 (blue) light curves obtained in February 2005. A differential V–band magnitude with respect to the average magnitude $V = 18.2 \pm 0.1$ of QZ Lib is reported.

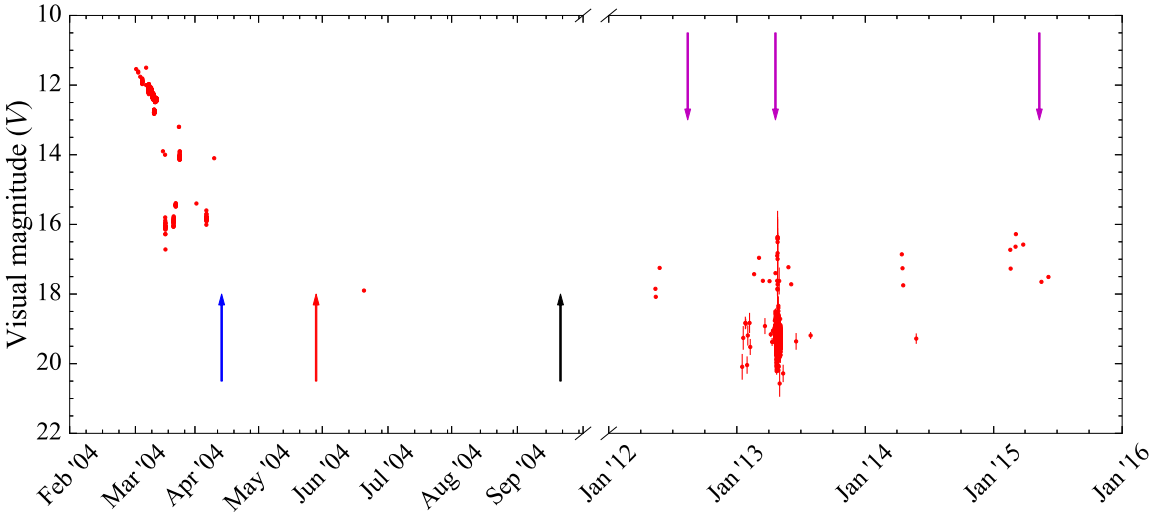

Figure 5.3: AAVSO ligthcurve for QZ Lib from its first detection (superoutburst on February 2004) up to 2016. The arrows highlight the epochs of the EFOSC2 observations one month (blue), two months (red) and six months (black) after the superoutburst. The purple arrows highlight the three epochs in which X–shooter spectroscopy has been acquired.

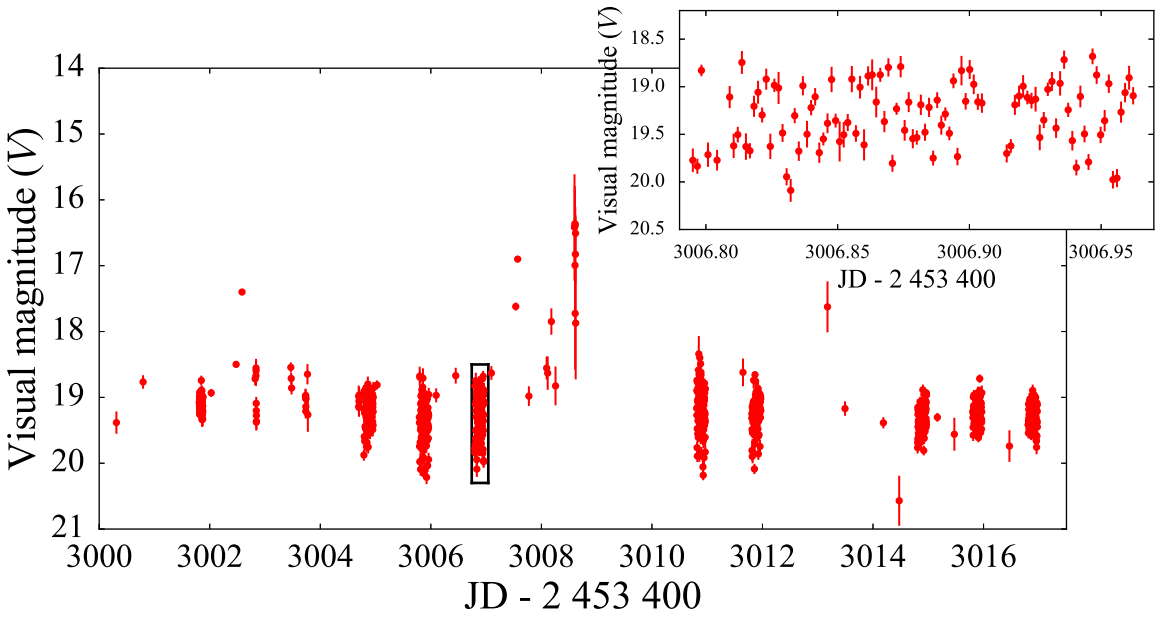

Figure 5.4: AAVSO ligthcurve of QZ Lib in a period of particular intense monitoring (17 April 2013 – 5 May 2013, the x–axis scale is similar to that of Figure 5.2 for an easier comparison), during which the system showed one outburst reaching $\simeq$ 16 mag. The inset shows a sample close–up of the night of 24–04–2013 (highlighted with a black box in the main plot): the system variability is dominated by flickering and no periodic variation is detected.

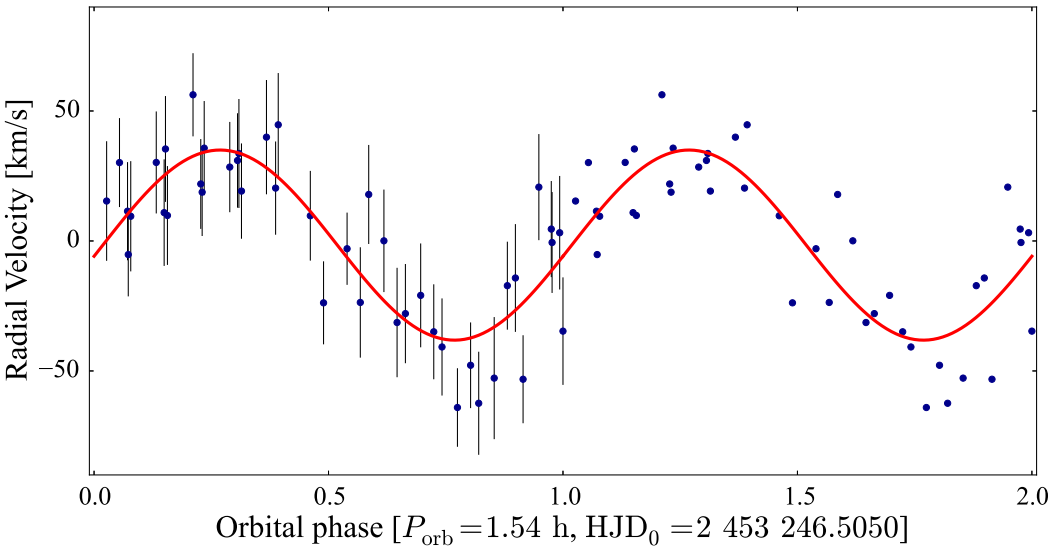

Figure 5.5: The EFOSC2 August data are plotted in phase using the orbital period $P_{\rm orb} = 0.06416(20)$ d; the zero-phase corresponds to HJD = 2 453 246.5050. Two phases are plotted for clarity, the first one has the uncertainties of the individual measurements overplotted. The red line gives the best sinusoidal fit to the data.

5.4 Time resolved spectrosopy

Medium resolution time–resolved optical spectroscopy of QZ Lib was obtained with the EFOSC2 grism # 10 on March and August, 2004 on 2 × 2 nights. About 1.5 orbits were covered each night. We measured the radial velocity of Hα emission line by fitting a broad Gaussian to it. A clear periodicity was found using Scargle and AOV Fourier techniques. The periodograms of both data sets show several alias peaks but only one frequency yields a strong signal in both, which we concluded to belong to the orbital period. Since the August dataset has higher SNR and is slightly longer than the March dataset, we used this to determine the orbital period, which results $P_{\rm orb} = 0.06416(20)$ d or 1.540 ± 0.005 h. Unfortunately, the two sets are too far apart in time to allow the combination of the data to increase the accuracy. In addition, some time–series high resolution spectroscopy was taken with X–shooter during three epochs in 2012, 2013 and 2015 which we used to verify the orbital period. However, only parts of an orbit were observed in most cases and again, the data sets are too far apart in time to be combined and thus to improve the uncertainty of the period determination.

Given the higher quality of the August EFOSC2 dataset, we used these time–resolved observations to compute the systemic velocity ($\gamma_{\rm WD}$) and the radial velocity amplitude (K_1) of the white dwarf. From a least squares fit to the data, we found the system velocity, $\gamma = -1.6 \pm 1.5$ km/s, and the white dwarf radial velocity amplitude, $K_1 = 37 \pm 2$ km/s. The uncertainties on these quantities were

determined by computing Monte–Carlo simulations of the fit. The best fit returns the following ephemeris for the red to blue crossing of the emission lines:

$$\phi = \frac{\mathrm{HJD_{obs}} - 2\,453\,246.5050}{P_{\mathrm{orb}}} + N \tag{5.1}$$

We then used this ephemeris to calculate the orbital phase for all data points of the August 2004 data set (Figure 5.5).

Finally, using the orbital period $P_{\mathrm{orb}} = 0.06416(20)$ d and the reported stage A superhump period of QZ Lib from Kato et al. (2015, $P_{\mathrm{SH}} = 0.06557(14)$ d), we derive a period excess of $\epsilon = 0.02198(1)$ d and, using Equation 1.20 and 1.21, we obtained the system mass ratio $q = 0.057 \pm 0.006$. Within the uncertainties, this value is consistent with the previously determined one by Patterson et al. (2005a, $q = 0.035 \pm 0.020$). However, we consider our measurement a more reliable result since their orbital period was tentatively derived from photometric variations (Patterson, private communication) which we consider problematic due to strong non–periodic contributions like flickering and long–term variability.

5.5 Doppler Tomography

Doppler tomography makes use of the orbital variation of the emission line profiles. Each point of the emission line can be attributed to a radial velocity, which can be transformed to (v_x, v_y) for a given phase. The Doppler maps $I(v_x, v_y)$ display the flux emitted by gas moving with the velocity (v_x, v_y) and thus show the emission distribution in velocity coordinates with the centre of mass at (0,0). We used the code of Spruit (1998) with a MIDAS interface replacing the original IDL (Interactive Data Language) routines (Tappert et al., 2003). To correct for the variation of the equivalent width, the input spectra have been normalised by the respective emission line flux. The intensity values in the Doppler map are hence to be interpreted as relative flux values only.

We used the largest contiguous high–resolution data set – the X–Shooter data from April 2013 – for these computations. The final Doppler maps for Hα and Hβ are shown in Figure 5.6, illustrating the distribution of the emission sources in velocity coordinates. The orientation of the map is chosen in such a way that the phase angle ϕ_r with respect to the zero point of radial velocities is zero towards the top and increases clockwise. Apart from the disc itself, which is clearly visible, a significant additional source of emission can be seen in the upper left quadrant, located a phase angle $\phi_r \approx 0.75$, which can be interpreted as emission from the hot spot, the point where the accretion stream connects with the disc. The emission from the bright spot is also visible as a thin S–curve with a velocity amplitude consistent with the outer disc velocity in the trailed spectra shown in the right–

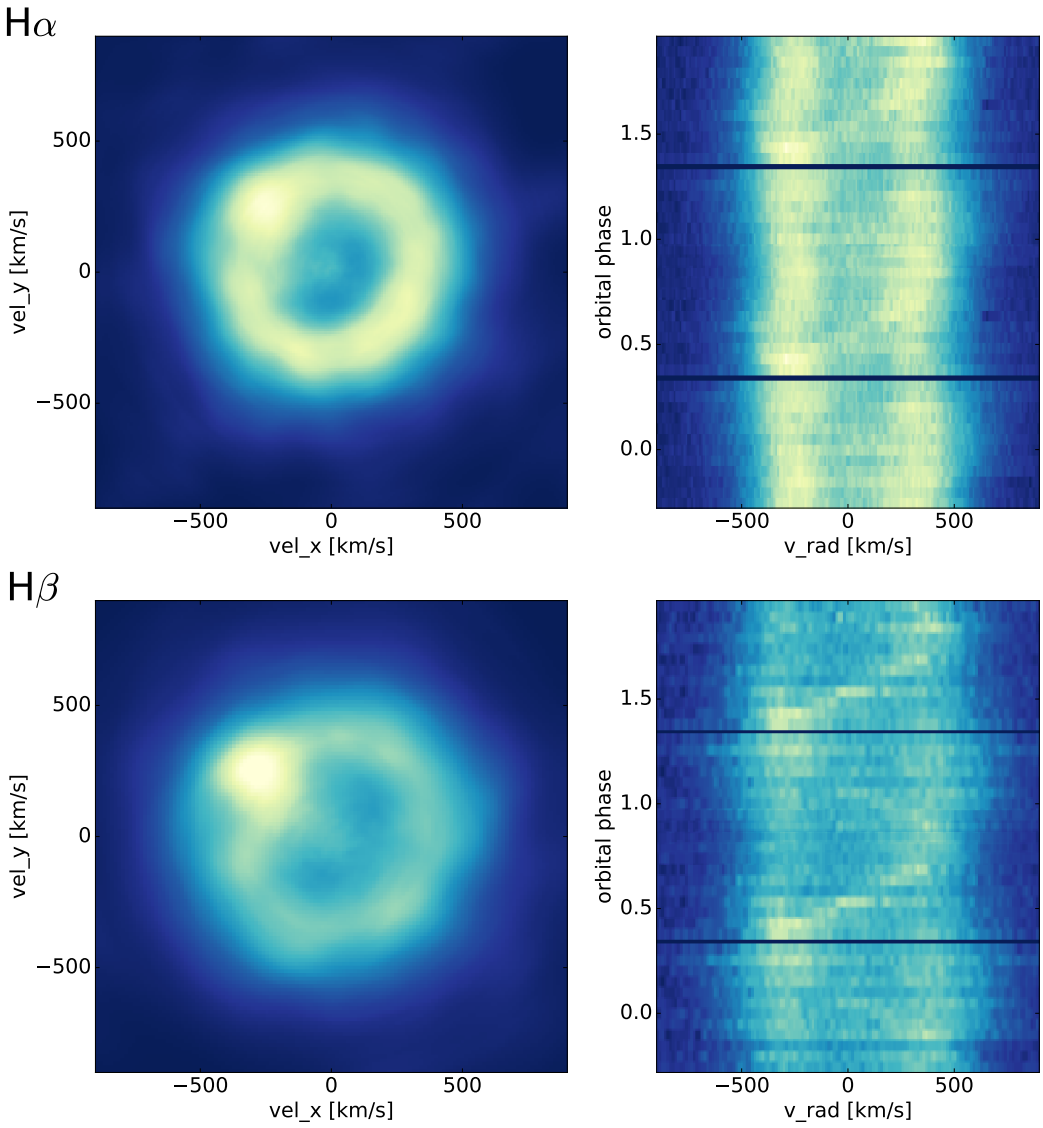

Figure 5.6: The Doppler maps show the emission line distribution in velocity coordinates for Hα (upper plot) and Hβ (lower plot). In the panel on the right, the trailed spectra of the respective emission line are plotted in velocity coordinates. Two phase cycles are plotted for clarity.

hand side panels.

5.6 The spectra

5.6.1 The model

From a spectral fit to a CV spectrum with models accounting for the contribution of the white dwarf, the secondary and the accretion disc, it is possible to determine the effective temperatures of the white dwarf and the secondary star. We therefore used

Table 5.2: Range of variations for the free parameters in the slab model.

Parameter	Value
Effective temperature (K)	$5\,700 - 8\,000$
Pressure ($\mathrm{dyn\,cm^{-2}}$)	$0 - 1\,000$
Radial velocity ($\mathrm{km\,s^{-1}}$)	$0 - 2\,000$
Inclination (°)	$0 - 60$
Geometrical height (cm)	$0 - 10^{10}$

Notes. The upper limit on the inclination is set by the fact that no eclipse is detected in the lightcurve of QZ Lib.

TLUSTY and SYNSPEC (Hubeny 1988, Hubeny and Lanz 1995) to compute a grid of white dwarf atmosphere models covering the range $T_{\rm eff} = 9\,000 - 40\,000$ K in steps of 100 K and assuming $Z = 0.01\,Z_{\odot}$, (as determined from the analysis of ultraviolet *HST* data of QZ Lib, see Chapter 3). Since the white dwarf effective temperature and surface gravity correlate (Section 3.3.2) and the Balmer line cores, commonly used to simultaneously constrain the effective temperature and the surface gravity of isolated white dwarfs (see for example Gianninas et al. 2011), are contaminated by strong disc emission lines, it is not possible to constrain both $T_{\rm eff}$ and $\log g$ of QZ Lib from the analysis of the optical data. We therefore generated our grid of models assuming $\log g = 8.35$, corresponding to the average mass of CV white dwarfs ($M_{\rm WD} \simeq 0.8 \mathrm{M}_{\odot}$, Zorotovic et al. 2011).

To approximate the disc emission, we used an isothermal and isobaric pure–hydrogen slab model, as described in Gänsicke et al. (1997) and Gänsicke et al. (1999). The free parameters of this model and their allowed ranges are reported in Table 5.2.

Finally, the last contribution that needs to be taken into account is the emission from the donor star. From the knowledge of the orbital period and the system mass ratio, and from our previous assumption of $M_{\rm WD} = 0.8\,\mathrm{M}_{\odot}$, we determined the mass ($M_{\rm sec} = 0.04 \pm 0.01\,\mathrm{M}_{\odot}$), the radius ($R_{\rm sec} = 0.11 \pm 0.01\,\mathrm{R}_{\odot}$) and the surface gravity ($\log(g[\mathrm{cm\,s^{-2}}]) = 4.9 \pm 0.1$) of the donor star. The typical effective temperature of donor stars in short–period CVs are $500\,\mathrm{K} \lesssim T_{\rm eff} \lesssim 3000\,\mathrm{K}$ (Knigge, 2006). The metallicity of the white dwarf represents a lower limit on the metallicity of the accreted material, which is stripped from the secondary photosphere. We therefore assumed that the secondary has the same metallicity as the white dwarf, $Z = 0.01\,Z_{\odot}$. However, at present, none of the available model grids for late–type stars for $Z = 0.01\,Z_{\odot}$ cover the required range in temperature. We therefore retrieved a grid of BT–Dusty (Allard et al., 2012) models for late–type stars from the

Table 5.3: Cooling sequence for the white dwarf in QZ Lib after its 2004 super–outburst.

Date	$T_{\rm eff}$ (K)
2004–03–15	$17\,000 \pm 2\,000$
2004–05–01	$13\,200 \pm 600$
2004–08–27	$11\,530 \pm 250$

Theoretical Spectra Web Server[2], extending from $T_{\rm eff} = 1\,000$ K (T6 spectral type) up to $T_{\rm eff} = 3\,600$ K (M2 spectral type), for $\log g = 5$ and $Z = 0.3\,Z_{\odot}$, which is the widest grid of models with the lowest metallicity value we could find.

We then used a χ^2 minimisation routine to fit our grid of models to the optical spectra. In the fitting procedure, we did not include the wavelength ranges of the telluric absorption features arising in the Earth's atmosphere and, to better constrain the contribution of the disc to the overall emission, we allowed as free parameters the areas of the emission lines Hβ, Hγ, Hδ and Hϵ. In the case of the X–shooter spectra we included also the areas of the emission lines Hα, Paδ and Paζ.

5.6.2 The spectra after outburst

The spectrophotometric calibrated low resolution EFOSC2 spectra of three epochs are plotted in Figure 5.7. The white dwarf is dominating the continuum in all of them, as seen from the clear presence of its broad Balmer absorption lines. The spectrum taken on 2004–03–15 still has a noticeable contribution of the accretion disc which then decreases at the later epochs.

From a spectral fit to the spectra obtained one, two and six month after the super–outburst, we measured the effective temperatures of the white dwarf cooling towards quiescence (Table 5.3). The strong continuum contribution arising from the disc and the contamination from the emission lines in the 2004–03–15 spectrum prevent an accurate measurement of the white dwarf effective temperature, which we estimated to be about 17 000 K.

We used the spectrum taken on 2004–08–27 to fit the contributions from the white dwarf, the accretion disc, and the secondary star to the spectrum of the object. Unfortunately, we noticed after the observations that the grism of EFOSC2 is affected by a second–order contamination starting around 6000 Å. Hence, no conclusions can be made for the cool donor star and only the blue part of the spectrum was used for the fit of the white dwarf and the accretion disc. Following the methodology described in the previous section, we fitted the EFOSC2 data and we found that the white dwarf has a temperature of $\simeq 11\,500$ K. Assuming

[2] http://svo2.cab.inta-csic.es/theory/newov/index.php?model=bt-settl

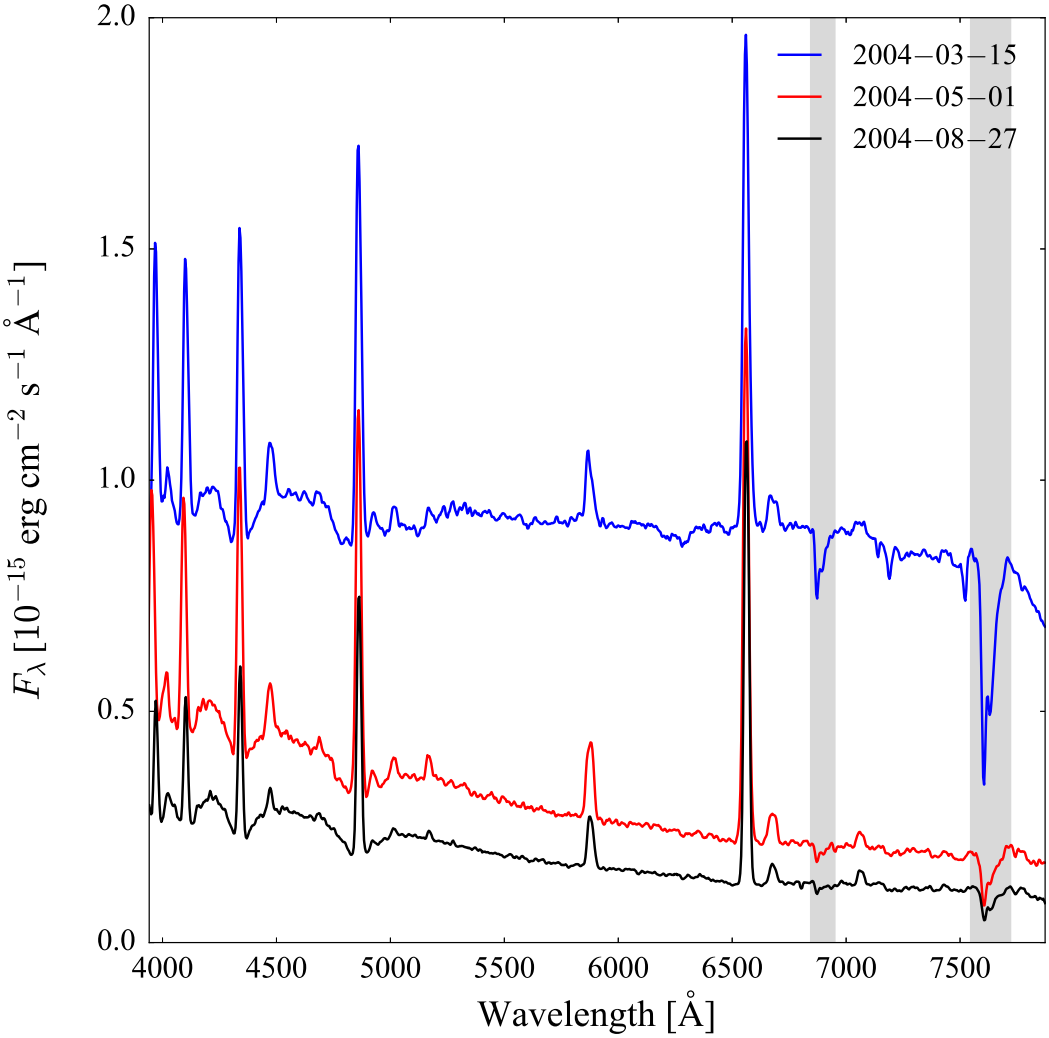

Figure 5.7: EFOSC2 spectrophotometric calibrated spectra of QZ Lib obtained one (blue), two (red) and six (black) months after its 2004 superoutburst. The regions contaminated by telluric absorption bands are highlighted in grey.

the mass–radius from Hamada and Salpeter (1961), we estimated the radius of the white dwarf $R_{\rm WD} = 0.01 {\rm R}_\odot$ which, combined with the ratio between the best–fit model and the observed spectrum (Equation 2.2), yields the distance to the system, $d = 180 \pm 80$ pc, in agreement with Patterson et al. (2005a, $d = 120 \pm 50$ pc). From the best fit model of the isothermal hydrogen slab, we found that the accretion disc is typical for a dwarf nova system (Williams, 1980; Tylenda, 1981), optically thin and with a temperature of about 6 200 K.

5.6.3 The quiescent spectra

The X–shooter average spectrum of QZ Lib, taken about ten years after its super–outburst is shown in Figure 5.9. We compared the X–shooter spectra from the

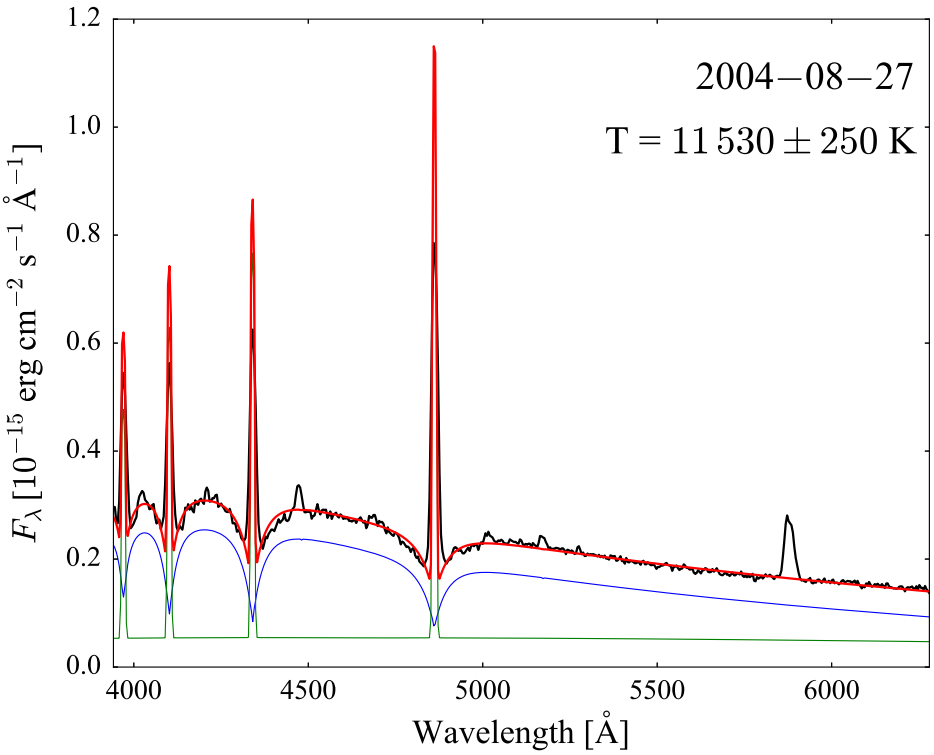

Figure 5.8: EFOSC2 spectrum of QZ Lib taken on 2004–08–27. The #6 grism is affected by a second–order contamination which reduces the useful wavelength range to 6 200 Å. At these wavelengths the possible contribution of the donor is negligible and thus we fitted the data including the contribution of a white dwarf (blue line) and an isothermal and isobaric pure hydrogen slab (green line) to approximate the disc emission. The sum is given by the red line.

different years, i.e. 2012, 2013, and 2015 but found no difference and hence combined them to increase the S/N. This late spectrum differs from the spectra obtained within the first year of the outburst, showing narrower Balmer and helium emission lines, typical of a dwarf nova disc in quiescence (see Table 5.4).

We inspected the red part of the spectrum for absorption features arising from the secondary photosphere. Typically, when the donor star dominates the near–infrared emission, the most prominent absorption lines are Na I 11 381/11 403 Å, K I 11 690/11 769 Å and 12 432/12 522 Å. However we could not identify any of those and therefore we assumed that the companion star contribution is negligible and performed a spectral fit to the X–shooter data including a white dwarf and an hydrogen slab in the model. The best–fit model is shown in the top panel of Figure 5.10 and returns a white dwarf effective temperature of $T_{\rm eff} = 10\,500 \pm 1500$ K, in agreement with the value we determined from the analysis of ultraviolet data ($T_{\rm eff} = 11\,303 \pm 238$K, Table 3.7, Pala et al. 2017). The best–fit parameter for the hydrogen slab are listed in Table 5.5 while the overall system parameters de-

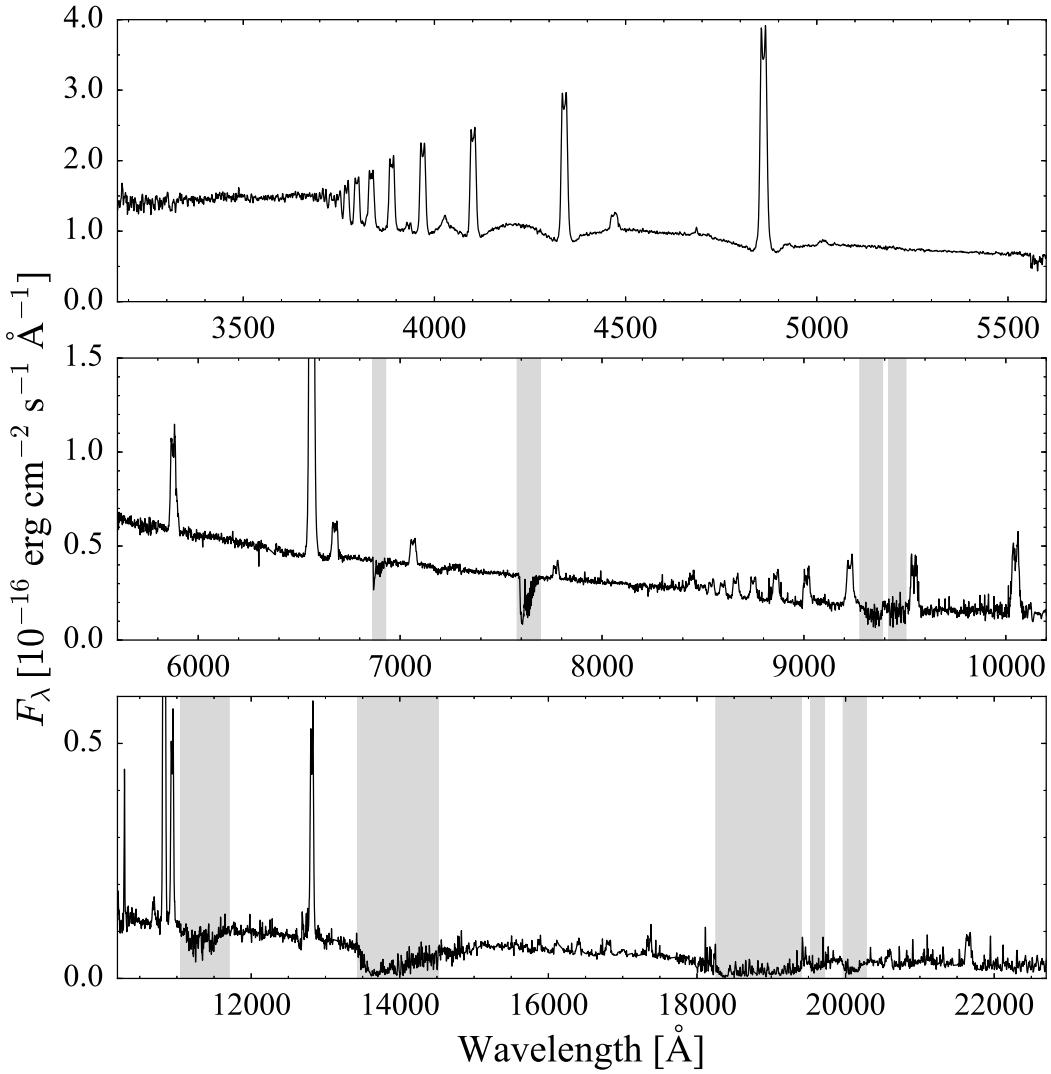

Figure 5.9: Averaged X–shooter spectrum of QZ Lib (UVB, top panel; VIS middle panel; NIR, bottom panel). The white dwarf signature is recognisable in the broad Balmer lines in the UVB arm. Strong emission lines arise from the accretion disc. No features from the secondary are detected in the near–infrared, which is contaminated by broad telluric absorption bands (highlighted in grey) and residuals from the sky line removal.

rived from the analysis of the EFOSC2 and X–shooter data are listed in Table 5.6. Although a clear signature of the companion star cannot be identified in the X–shooter data, only accounting for the white dwarf and the slab emission does not allow to adequately reproduce the observed flux level for $\lambda \gtrsim 10\,000$ Å. We therefore subtracted the white dwarf and the slab model to the X–shooter data and fit the grid of low–mass main sequence star (see Section 5.6.1) to the residual spectrum, constraining the secondary to be at the same distance as the white dwarf. The

Table 5.4: The evolution of FWHM (in Å), equivalent width W (in Å), and line flux F (in 10^{-15}erg cm^{-2}s^{-1}) for the main Balmer and He I lines lines in the spectra of QZ Lib. Note that the uncertainty of the line flux accounts for the uncertainty of the relative flux in the line but does not include the errors introduced in our spectrophotometric flux calibration procedure (see Section 5.2.1).

	2004-03-15			2004-05-01		
Transition	FWHM	$-W$	F	FWHM	$-W$	F
H_α	28.6 ± 0.2	38.7 ± 0.8	35.3 ± 0.3	26.8 ± 0.2	157 ± 1.5	34.0 ± 0.3
H_β	26.2 ± 0.3	28.1 ± 0.4	24.9 ± 0.3	24.3 ± 0.3	73.5 ± 0.8	23.2 ± 0.3
H_γ	25.1 ± 0.3	21.7 ± 0.3	19.0 ± 0.3	23.6 ± 0.4	40.8 ± 0.9	16.4 ± 0.3
H_δ	24.5 ± 0.2	16.7 ± 0.3	15.4 ± 0.2	23.6 ± 0.4	28.1 ± 0.9	13.0 ± 0.5
He I λ6678	46 ± 3	3.4 ± 0.6	3.0 ± 0.2	39.0 ± 0.5	13.6 ± 0.5	2.9 ± 0.2
He I λ5875	35 ± 2	6.2 ± 0.8	6.2 ± 0.3	34.3 ± 0.6	23.3 ± 0.8	6.3 ± 0.4
He I λ4471	34 ± 3	5.1 ± 0.4	4.7 ± 0.2	31.5 ± 0.8	9.7 ± 0.5	4.3 ± 0.3

	2004-08-27			X–shooter average		
Transition	FWHM	$-W$	F	FWHM	$-W$	F
H_α	24.1 ± 0.1	214 ± 2.5	27.1 ± 0.3	21.4 ± 0.1	288 ± 7	12.8 ± 0.1
H_β	20.6 ± 0.2	69.1 ± 0.9	13.6 ± 0.2	17.5 ± 0.2	82 ± 3	5.6 ± 0.1
H_γ	18.8 ± 0.3	33.5 ± 0.7	8.1 ± 0.2	16.4 ± 0.5	43 ± 2	3.5 ± 0.1
H_δ	17.4 ± 0.4	21.7 ± 0.5	5.5 ± 0.2	15.6 ± 0.4	26 ± 2	2.3 ± 0.1
He I λ6678	33.6 ± 0.2	14 ± 0.9	1.9 ± 0.2	26.5 ± 0.4	13 ± 1	0.6 ± 0.1
He I λ5875	30.2 ± 0.2	23 ± 0.9	4.1 ± 0.3	25.5 ± 0.2	23 ± 2	1.3 ± 0.1
He I λ4471	26 ± 3.5	7 ± 1.5	1.7 ± 0.2	18.2 ± 0.5	4 ± 1	0.5 ± 0.1

Table 5.5: Best fit parameters for the isothermal and isobaric hydrogen slab in QZ Lib.

Hydrogen slab parameter	Value
Effective temperature (K)	$7\,100 \pm 300$
Pressure (dyn cm^{-2})	110 ± 40
Radial velocity (km s^{-1})	$1\,150 \pm 250$
Inclination (°)	30 ± 12
Geometrical height (cm)	$1.2(2) \times 10^7$

best–fit model is shown in the bottom panel of Figure 5.10 and returns a secondary star effective temperature of $T_{\rm eff} \simeq 1\,700$K.

5.7 Discussion

We used VLT/X–shooter optical and near–infrared spectroscopy to reconstruct the SED of QZ Lib, from $\lambda \simeq 3\,000$ Å down to $\lambda \simeq 23\,000$ Å. From a spectral fit to

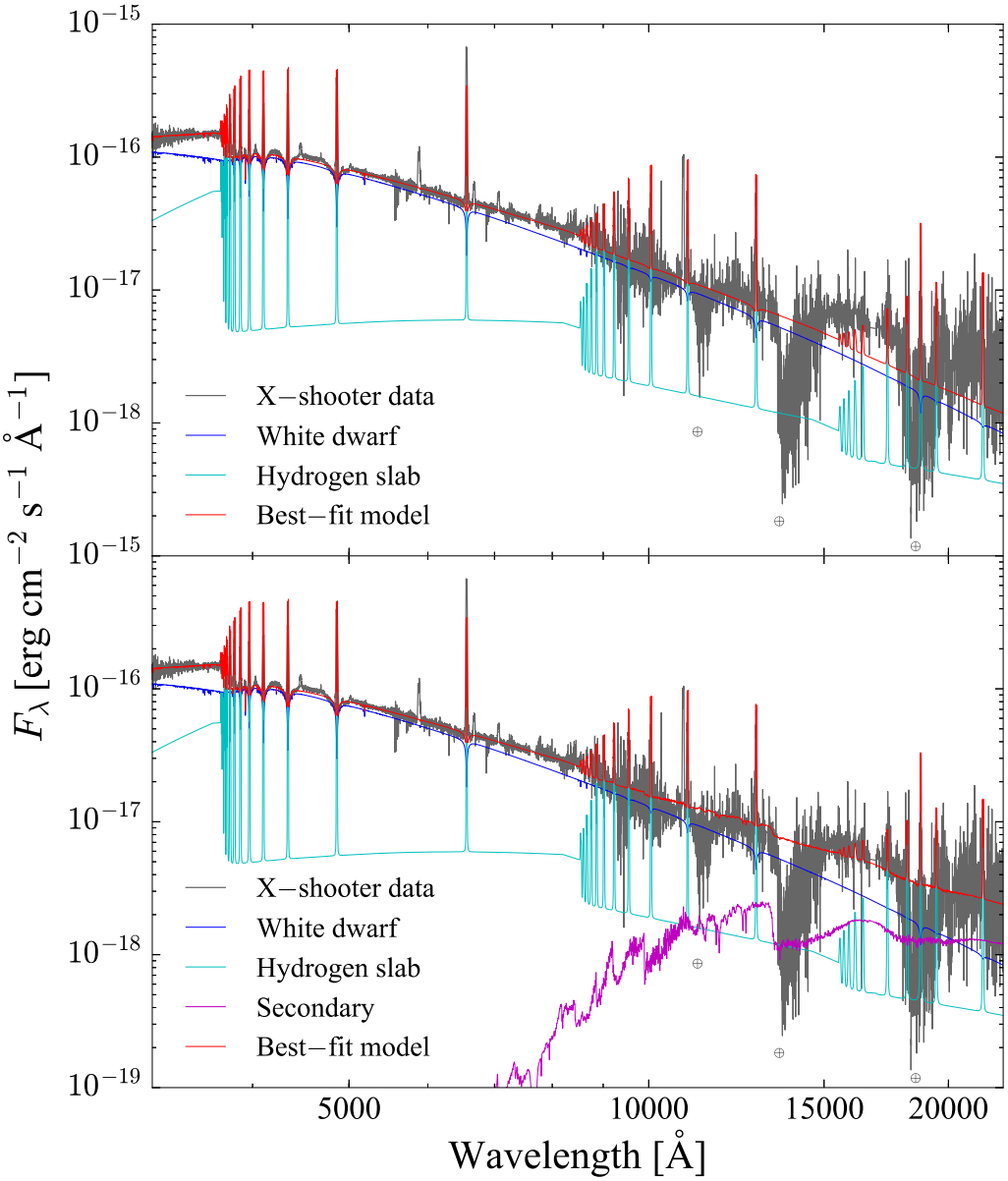

Figure 5.10: X–shooter average spectrum of QZ Lib (grey) along with the best–fit model (red) which is composed of a white dwarf (blue) and an isothermal and isobaric hydrogen slab (cyan) and a brown dwarf companion (purple, bottom). The Earth's symbols highlight the position of the strongest telluric absorption bands, which were not included in the fit.

Table 5.6: System parameters for QZ Lib.

System parameter	Value	Instrument
$P_{\rm orb}$ (min)	92.4 ± 0.3	EFOSC2
q	0.057 ± 0.005	EFOSC2
d (pc)	180 ± 80	EFOSC2
$T_{\rm eff}$ (K)	$10\,500 \pm 1\,500$	X–shooter
$T_{\rm sec}$ (K)	$\lesssim 1700$	X–shooter
$\gamma_{\rm WD}$ (km s^{-1})	-1.6 ± 1.5	EFOSC2
$K_{\rm WD}$ (km s^{-1})	37 ± 2	EFOSC2
$\log g$	8.35	fixed
$M_{\rm WD}$ (M$_\odot$)	0.8	fixed
$R_{\rm WD}$ (R$_\odot$)	0.01	fixed

the data, we have shown that the contribution from a white dwarf and an isothermal slab cannot adequately reproduce the flux in the red portion of the spectrum. Two additional emission sources can explain this infrared excess: the accretion disc and/or a brown dwarf secondary star.

The isothermal and isobaric hydrogen slab we included in the fit procedure is a good model to account for the emission lines that arise from the optically thin upper layers of the disc. However, if the central and colder regions of the disc are composed of an optically thick gas, they could contribute to the overall SED of the system in the form of an additional blackbody(–like) emission that is not accounted for by our model. At present, not much is known about the spectrum arising from the cool portion of the disc. In the past, this contribution has been modelled by dividing the disc into several annuli and then summing the emission of each annulus, approximated as a blackbody with an effective temperature set accordingly to the distance of the annulus from the white dwarf (Howell et al., 2006; Brinkworth et al., 2007; Howell et al., 2008). However, since this gas has a similar composition and effective temperature as the secondary, is very difficult to unambiguously identify the near–infrared flux as either the disc or donor emission. Given that the wavelength coverage of X–shooter is limited at the K–band, additional constraints on the SED at longer wavelengths are needed to distinguish between a stellar component or a disc contribution.

Although we cannot distinguish between the emission of the donor star and that of a possibly optically thick cool accretion disc, given the mass ratio of QZ Lib ($q = 0.057 \pm 0.006$), we can still conclude that its donor star must be a brown dwarf. In fact, considering a white dwarf mass lying in the range $0.6\,{\rm M}_\odot \lesssim M_{\rm WD} \lesssim 1.44\,{\rm M}_\odot$, the secondary star mass results $0.03\,{\rm M}_\odot \lesssim M_{\rm sec} \lesssim 0.08\,{\rm M}_\odot$, i.e. below the

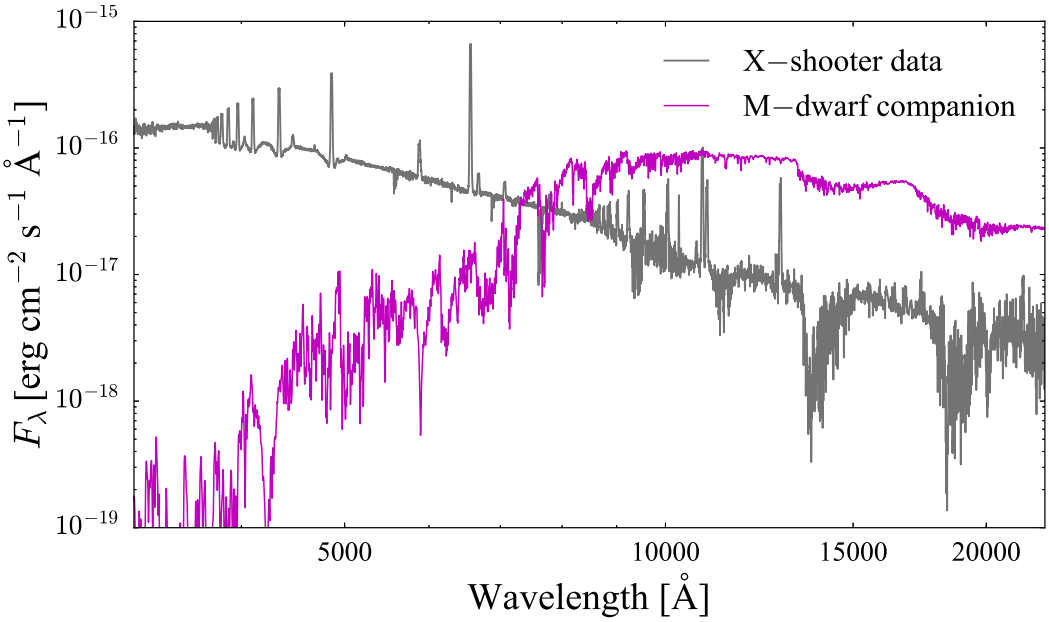

Figure 5.11: X–shooter spectrum of QZ Lib (grey) in comparison with the expected emission of a M6.5–dwarf companion (purple) as typical for a pre–bounce system with $P_{\rm orb} \simeq 90\,{\rm min}$ at a distance $d = 180\,{\rm pc}$.

hydrogen–burning limit and clearly in the brown dwarf regime. Furthermore the expected spectral type of the donor star in a pre–bounce CV at $P_{\rm orb} \simeq 90\,{\rm min}$ is a M6.5, corresponding to $M_{\rm sec} = 0.096\,{\rm M}_\odot$, $R_{\rm sec} = 0.144\,{\rm R}_\odot$ and $T_{\rm eff} = 2\,744\,{\rm K}$ (Knigge, 2006), would not be consistent with the observed SED. In fact, such a star at the distance of QZ Lib ($d \simeq 180\,{\rm pc}$) would clearly dominate the spectral appearance for $\lambda \gtrsim 7\,000\,{\rm Å}$ (Figure 5.11). Instead, our fit to the X–shooter data shows that the upper limit on the secondary effective temperature is $T_{\rm eff} \simeq 1\,700\,{\rm K}$, supporting the conclusion of a brown dwarf donor star (Figure 5.12, right panel).

As discussed before, the mass of the secondary star, i.e. the system mass ratio, is one of the strongest discriminants between pre and post–bounce systems (see e.g. figure 6 from Howell et al. 2001). Inspecting the location of QZ Lib in the $P_{\rm orb}-q$ distribution shown in the left panel of Figure 5.12 strongly suggests that it is in the regime of potential period bouncers, rather than on the pre–bounce evolutionary track. Owing to its low mass ratio QZ Lib has been previously suggested as a potential period bouncer by Patterson (2011) and, subsequently, also by the results of our *HST* survey, because of its cool white dwarf (Section 3.4.5). Our fit to the SED of QZ Lib provides additional strong support in favour of the period–bouncer nature of QZ Lib.

Alternatively, QZ Lib could be born with a brown dwarf donor star, therefore without following the standard model of CV evolution. In fact, these kind of binaries start mass transfer below the period minimum and then evolve towards

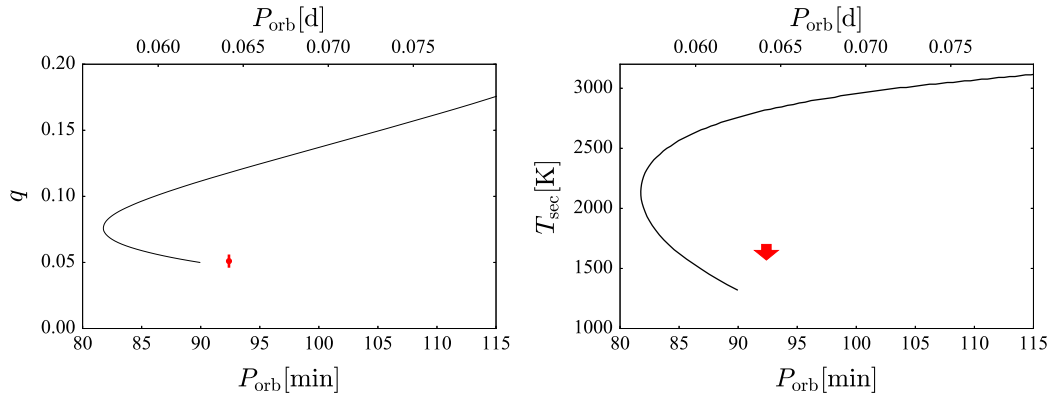

Figure 5.12: QZ Lib mass ratio (left) estimated using the $\epsilon - q$ relationship from Kato and Osaki (2013) and the upper limit on the effective temperature of its donor star (right) in comparison with the revised CV evolutionary track from Knigge et al. (2011, solid line, calculated assuming $M_{\rm WD} = 0.8\,{\rm M}_{\odot}$ for the left panel). These measurements clearly suggests a period bouncer system rather than a pre–bounce CV.

longer orbital periods, finally merging into the standard track of period bouncers (figure 1 from Kolb and Baraffe 1999). Even if this scenario cannot be ruled out, the population synthesis study from Politano (2004) has shown that CVs hosting brown dwarf donors with orbital periods above the period minimum are four times more likely to have followed the standard path of CV evolution (i.e. the donor has become substellar as a consequence of mass erosion during the CV evolution) than being born as a white dwarf plus brown dwarf binary, suggesting that QZ Lib is more likely a period bouncer CV.

5.8 Conclusions

We present photometric and spectroscopic time–resolved observations of the cataclysmic variable QZ Lib. From radial velocity measurements of the Hα emission line, we determine the orbital period $P_{\rm orb} = 0.06416(20)$ d that, combined with the superhump period ($P_{\rm SH} = 0.06557(14)$ d), yields the system mass ratio, $q = 0.057 \pm 0.006$. Assuming the mass of the white dwarf to be in the range $0.6\,{\rm M}_{\odot} \lesssim M_{\rm WD} \lesssim 1.44\,{\rm M}_{\odot}$, we found that the secondary mass is $0.03\,{\rm M}_{\odot} \lesssim M_{\rm sec} \lesssim 0.08\,{\rm M}_{\odot}$, and therefore the donor must be a brown dwarf.

From a spectral fit to the averaged X–shooter spectrum we measured the white dwarf effective temperature ($T_{\rm eff} = 10\,500 \pm 1\,500$ K). Modelling the data with a white dwarf and an isothermal and isobaric hydrogen slab does not adequately reproduce the observed flux in the reddest portion of the spectrum. Interpreting this weak infrared excess as the contribution from the donor star implies an upper

limit on its effective temperature, $T_{\rm sec} \lesssim 1\,700\,{\rm K}$, however, this excess could also originate from an optically thick accretion disc. The limited wavelength range of our observations does not allow to further investigate this possibility but, if the near–infrared excess arises from the disc, would imply the presence of an even colder secondary star, bringing our results into an even better agreement with the predicted evolutionary track of the period bouncer CVs.

Although we cannot exclude that QZ Lib is born with a brown dwarf donor, i.e. without following the standard evolutionary path of CVs, this scenario would be four times less likely than the detection of a period bouncer CV. We therefore argue that QZ Lib is a CV that has evolved through the period minimum. In fact, QZ Lib meets all the requirements for being a period bouncer: it has a brown dwarf companion, a low mass ratio and hosts the coolest white dwarf at the longest orbital period (see its position in Figure 3.24). This is the first CV for which all these requirements have been spectroscopically confirmed, ruling out a pre–bounce system still on its way to the period minimum and, instead, making QZ Lib the strongest period bouncer candidate identified so far.

The detection of period bouncer CVs is an important test for the theoretical prediction of the standard model of CV evolution. QZ Lib illustrates how some of these elusive systems could be hiding among the known CVs but have not been identified as such owing to the limited wavelength range in which they have been studied before and we illustrated how multi–wavelength observations, extending from the ultraviolet to the infrared, are one of the most powerful tool to unveil this major component of the present day Galactic CV population.

Chapter 6

CHiCaS: The Compact binary HIgh CAdence Survey

6.1 Introduction

As discussed in Section 1.6.3, the identification of period bouncers is challenging since they are expected to be intrinsically faint ($V \simeq 20.5$ mag, Section 3.4.5) while the current methods for CV identification are biased towards brighter, high mass accretion systems.

So far, several period bouncers candidates have been identified thanks to their low mass ratios ($q < 0.1$, Patterson 2011; Kato et al. 2015, 2016). However, the majority of these CVs are located near the period minimum and thus it is difficult to unambiguously establish whether they have already bounced back (see for example the case of SDSS1238 in Chapter 4). Alternatively, period bouncers can be identified either from the white dwarf effective temperature, since they are expected to host cold white dwarfs ($T_{\rm eff} \lesssim 11\,000$ K), as a consequence of the low mass accretion rate that characterises these systems (Figure 3.24, Pala et al. 2017), or from the detection (either photometric or spectroscopic) of the brown dwarf companion.

However, each of these methods suffers of major limitations: expensive ultraviolet observations are necessary for an accurate white dwarf temperature determination; in order to measure mass ratios, stage A superhumps are necessary but they are difficult to observe since they occur only during the first one or two days of the outburst. Finally, a spectroscopic detection of the secondary requires to reconstruct the SED of the system for which time consuming observations of individual systems are necessary. Therefore the lack of these systems in the observed CV population can be explained by limitations in the observational methods followed so far.

Another possibility is that our understanding of binary evolution is incomplete and the predicted period bouncers actually do no make up for the majority of the present day CV population. Critically uncertain areas in the theoretical modelling are (i) the evolution of stars undergoing mass loss, (ii) the common envelope phase during which the progenitor evolves up the giant branch and engulfs the secondary star, and (iii) the mechanisms of angular momentum loss. The number of identified period bouncers is still far from the fraction predicted by theory ($\simeq 40-70\%$, Kolb 1993; Knigge et al. 2011; Goliasch and Nelson 2015) and the lack of these highly evolved CVs undermines our confidence in the current models of compact binary evolution and formation, which are also used to describe the evolution of more complex systems, such as black hole binaries, X–ray transients, milli–second pulsars or SN Ia progenitors. Similarly, neutron star and black hole mergers are the sources of gravitational wave emission, and the recent detections of the first gravitational wave sources by the LIGO and Virgo experiments underlines the need for a proper understanding of binary formation and evolution. It appears thus urgent to carry out a stringent test on the present models of CV evolution and this Chapter presents a new observing program aimed to investigate this major discrepancy between theory and observations.

6.2 The search for period bouncers

Period bouncers have orbital periods in the range $80\,\mathrm{min} \lesssim P_{\mathrm{orb}} \lesssim 120\,\mathrm{min}$, and are characterised by low mass accretion rates ($\dot{M} \simeq 10^{-11}\,\mathrm{M_{\odot}\,yr^{-1}}$) which makes them undetectable through the usual methods used for identify CVs. In fact, their accretion discs and secondary stars are expected to be very faint, and the systems would hence resemble cool, faint and apparently single white dwarfs. However, CVs are tight binaries with orbital separations of the order of the solar radius, and $\simeq 15-20$ per cent of them will be seen under the right inclination that the Earth–sized white dwarfs will be eclipsed for a few minutes by their larger Jupiter–sized brown dwarf donors. This is very important because from the eclipse light curve analysis it is possible to determine the orbital period and the masses of both the white dwarf and the donor star (e.g. Littlefair et al. 2006), where the donor mass is critical to unambiguously distinguish between period bouncers from CVs that have not evolved through the period minimum yet (see Figure 1.14e).

Therefore, the ingredients to successfully identify this elusive major component of the CV population are deep observations, able to observe objects as faint as $V \simeq 20.5\,\mathrm{mag}$ (as expected for period bouncer CVs, Section 3.4.5), in combination with high–time resolution photometry, in order to reconstruct high cadence light curves and detect the eclipses of period bounce CVs lasting a few minutes. Fur-

thermore, CVs are relatively rare objects, characterised by a theoretically predicted space density of $\rho \simeq 2 \times 10^{-4} \mathrm{pc}^{-3}$ (de Kool, 1992). Therefore a large area of the sky needs to be surveyed to build a statistically significant sample, necessary to perform a stringent test of the predictions from population synthesis models. In order to unambiguously measure the orbital period of each system, the light curves should be obtained over, at least, three hours of consecutive observations. In this way, given that period bouncers have orbital periods in the range $80\,\mathrm{min} \lesssim P_{\mathrm{orb}} \lesssim 120\,\mathrm{min}$, the probability to detect at least one eclipse per system is maximised. Finally, multi–band photometry is required to select period bouncer candidates from their colours.

This observing strategy has been proven to be successful for shorter period binaries ($P_{\mathrm{orb}} \lesssim 70\,\mathrm{min}$) by two ongoing surveys: the RApid Temporal Survey (RATS, Ramsay and Hakala 2005) and the OmegaWhite survey (Macfarlane et al., 2015).

RATS is a survey aimed to identify new ultracompact binaries, specifically AM CVn stars, i.e. binary systems in which a white dwarf is accreting from a helium–rich degenerate companion. Using the Wide Field Camera (WFC) on the 2.5–meter Isaac Newton Telescope (INT), RATS has so far covered 31 square degrees at 30 s cadence, observing three million objects as faint as $g \simeq 23\,\mathrm{mag}$ (Barclay et al., 2011).

OmegaWhite is a survey with the same aim as RATS that uses OmegaCam at the 2.65–meter VLT Survey Telescope (VST) to search 400 square degrees of the sky at a median cadence of 2.7 min and a limiting magnitude $g \simeq 21.5\,\mathrm{mag}$. So far, OmegaWhite has observed 134 square degrees of the sky along the Galactic plane, for a total of 12.3 million stars (Toma et al., 2016).

Both surveys have led to the discovery of new AM CVns, CVs, pulsating stars and eclipsing binaries. However, they both observed each field for two hours, a strategy optimised for the detection of ultracompact binaries but not for period bouncer CVs. As explained above, longer observations are required to identify these highly evolved CVs and we here describe the Compact binary HIgh CAdence Survey (CHiCaS), which represents the first systematic attempt to unambiguously identify the elusive population of period bouncers.

6.3 The Compact binary HIgh CAdence Survey

CHiCaS is a high–cadence photometric survey carried out at the Javalambre Observatory using JAST/T80Cam (Section 2.3.3). The observations started on January 2017 and, by the end of 2018, CHiCaS will perform high–time resolution photometry at one minute cadence of 68 fields, corresponding to a total of 136 square degrees.

Reaching a limiting magnitude of $g \simeq 22$ mag in dark time and $g \simeq 21.5$ mag in gray time, the program will deliver lightcurve for $\simeq 2.5$ million objects. Moreover, using the Sloan *ugriz* and the Hα filters (Table 2.3), full colour information will be provided for every object in the survey footprint.

The fields have been identified within low galactic latitude ($|b| \simeq 15\,^{\circ}$) regions and, using the three-dimensional map of interstellar dust reddening based on Pan–STARRS 1 and 2MASS photometry (Green et al., 2015), low reddening ($E(B-V) < 0.05$) fields have been selected. Each field has been inspected by eye using DSS (Digitized Sky Survey) images to ensure that it contains a fair amount of objects and, at the same time, it is not too crowded and allows to perform accurate photometry.

The observing strategy consists in first acquiring one image in each of the following filters: the blue filter (*uJAVA*), all the Sloan filters (*gSDSS*, *rSDSS*, *iSDSS* and *zSDSS*) and the Hα filter (*J*0660), useful to identify Hα emission from the disc, one of the most prominent feature in a CV spectrum. From this multiband photometry, following the method from (Gentile Fusillo et al., 2015), we identify white dwarfs and CVs in our fields. Using the *gSDSS* filter, we then perform uninterrupted time–series photometry of each FoV for 3.6 hours, thus maximising the probability to identify at least one eclipse per period bouncer.

Given the theoretical CVs space density and assuming to detect systems out to $\simeq 350$ pc, we expect to find 0.48 CVs per square degree, that is a total of 67 CVs. Assuming that period bouncers make up for 70 per cent of the observed CVs and taking into account the probability that the system must be seen under the right inclination ($\simeq 16\%$) to detect eclipses, we expect to identify eight eclipsing period bouncers at the end of the program. Given the small number of systems we expect to detect, the significance of our results will require careful statistical considerations. Considering 95 per cent and 99 per cent confidence levels, the detection of, respectively, four and two eclipsing period bouncers would still be in agreement with the standard model of CV evolution. If, on the other hand, we will detect only one or none systems, our results will clearly indicate the failure of the current models used to describe CV evolution. As a final caveat, we have to remember that these numbers have been calculated assuming to detect a total of 67 CVs and, in order to carry out a statically significant test, these confidence levels need to be rescaled according to the total number of CVs we will identify in the CHiCaS footprint.

6.3.1 Scientific objectives

The main goal of this program is to carry out a critical test of binary evolution models by searching for the missing CV population of period bouncers. Moreover, at the same time, CHiCaS will deliver a large amount of data which will provide a valuable legacy of additional scientific results:

- Eclipsing systems are the gold standard to measure precise stellar masses and radii (Torres et al., 2010). Our survey will detect thousands of eclipsing binaries, including detached, semi-detached and contact systems. Of particular interest are double white dwarf binaries, which will provide the opportunity to investigate one of the possible channels leading to SN Ia explosions (Section 1.2).

- Asteroseismology is a powerful tool to study stellar interiors and determine physical parameters, including masses, temperatures, and magnetic fields. From our program we will obtain light curves of different kind of pulsators, including δ Scuti and GW Virginis stars. Furthermore, using the method from (Gentile Fusillo et al., 2016), we can also identify ZZ Ceti stars, investigating the fundamental properties (internal structure, core and envelope mass and magnetic field) of these pulsating white dwarfs.

- The period gap is one of the most prominent feature in the CV orbital period distribution. In this period range, CVs evolve as detached white dwarf plus main sequence star systems, hosting secondaries of spectral type M4–M6 (Zorotovic et al., 2016). Thanks to the multi–band images we acquire in our survey, we can easily identify these important objects from their colour (Rebassa-Mansergas et al., 2012). Their orbital periods will be determined from the ellipsoidal modulation in their light curves and, with only one follow-up spectrum, we can determine the spectral type of the secondary. In this way, we will identify the CVs that are presently crossing the period gap, carrying out another powerful test of CV evolution theory.

6.3.2 Observations

During the first ten months of the survey, multi–band and time–series photometry has been acquired for 33 and 14 fields, respectively. In this Section, we present the results of the observations of the field CHiCaS J065048+230614 (hereafter CHiCaS0650), for which both multiband and time–series photometry are available.

Multi–band photometry of CHiCaS0650 has been acquired on February 14, 2017, through thin clouds. Time–series photometry has been obtained on February 24, 2017. Seeing was about $3''$ and sky was again covered by thin clouds. The summary of the observations is reported in Table 6.1.

The basic data reduction is performed by CEFCA. This includes bias removal, flat fielding and the astrometric solution. Moreover, the sets of three exposures per filter are combined into one image for each filter with higher SNR (Figure 6.1) using SWarp [1]. The reduced data can be retrieved from their database.

[1] SWarp is a program that resamples and co-adds together FITS images (Bertin et al., 2002).

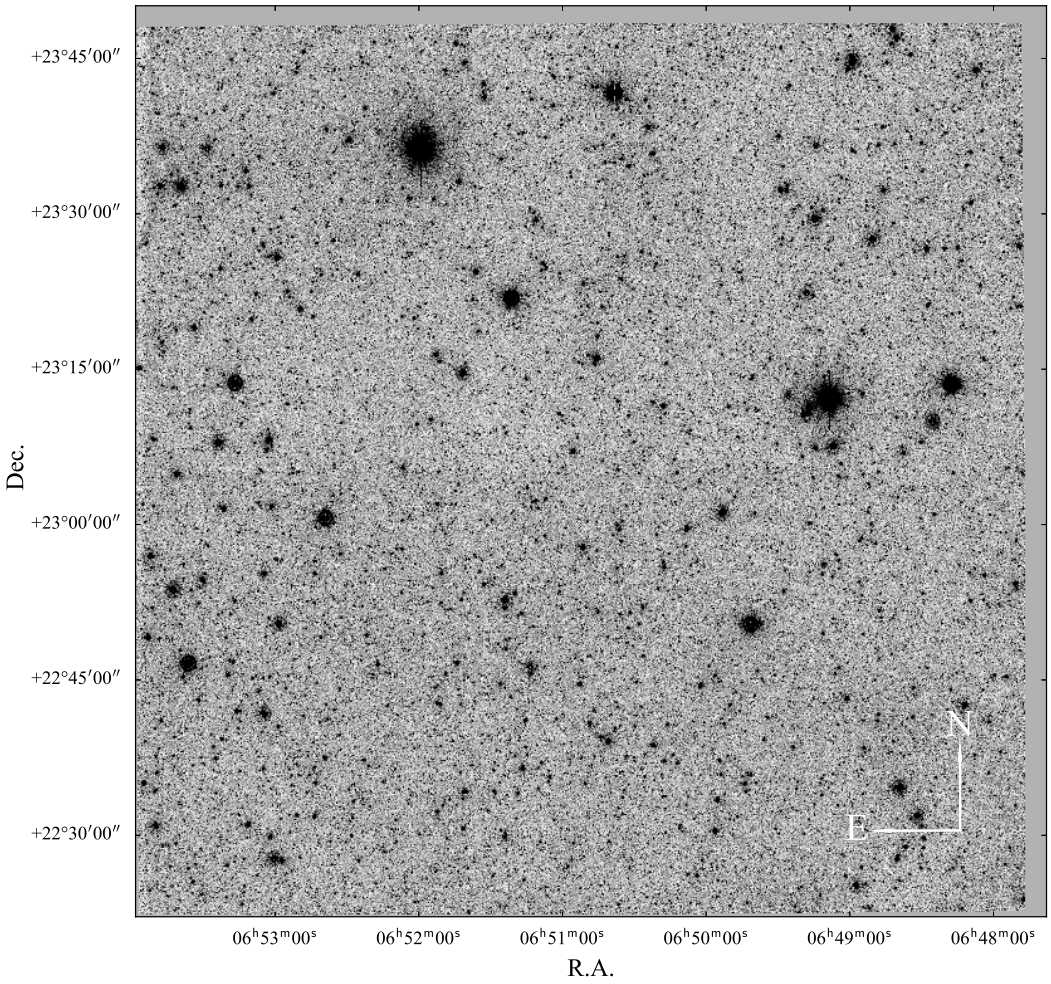

Figure 6.1: The *gSDSS*–band image of CHiCaSJ0650, obtained from the combination of three exposures of 60 s each. The field of view is $1.4° \times 1.4°$ wide and contains $\simeq 38\,000$ sources as faint as $g \simeq 21.5$ mag.

The photometry and lightcurve extraction was carried out following the subsequent procedure:

- a first run of SExtractor was performed on each image assuming a photometric aperture of five pixels in order to generate a preliminary catalogue containing the position and the FWHM of each source (see Section 2.4.2). In order to maximised the SNR, the median value of all the measured FWHMs was then multiplied by 1.5 and was used as input aperture for a second run of SExtractor. This returned a catalogue containing the positions and the instrumental magnitudes of all the identified sources in each image.

- The catalogue of each image generated in the previous step was then cross–matched with the APASS (Henden and Munari, 2014) catalogue, which provides photometry in the g, r and i filters. In the case of CHiCaS0650, 4160 ref-

Table 6.1: Summary of the observations of CHiCaS0650.

Date	Filter	$N_{\rm Exp}$	$t_{\rm Exp}$[s]
2017–02–14	*uJAVA*	3	300
2017–02–14	*gSDSS*	3	60
2017–02–14	*rSDSS*	3	57
2017–02–14	*iSDSS*	3	54
2017–02–14	*zSDSS*	3	363
2017–02–14	*J*0660	3	366
2017–02–24	*gSDSS*	180	60

erence stars were identified. For each one of them, the difference between the instrumental magnitude and the tabulated value was calculated. The median value was then added to the instrumental magnitude of all detected sources to perform the photometric calibration in the corresponding filter band.

- The previous steps returned the photometric calibration for both the multi–band and the time–series observations. The lightcurve extraction was then performed using the *gSDSS*–band image of CHiCaSJ0650 acquired on 2017–02–14 as a reference. Each detected source in this image was crossmatched with the catalogue of the time–series frames, thus providing the corresponding lightcurve.

6.3.3 Preliminary results

Colour–Colour Diagrams

Figure 6.2 shows the colour–colour diagrams for the $\simeq 38\,000$ sources we detected in CHiCaS0650. We here report the *instrumental* magnitudes since a photometric calibration has not yet been performed for the *uJAVA* and *J*0660 bands. Nonetheless, this does not affect the following analysis since it would only result in a shift of the y–axis values by a fixed amount, without changing the shape of the distribution.

White dwarf candidates can be selected thanks to their colours since they occupy the bluer region (top left corner) of the $(g - r,\ u - g)$ space. However, additional constraints are required in order to discriminate these candidates from other blue objects that populate the same colour region, such as quasars. Since white dwarfs are nearby objects, they are characterised by high proper motions that can be used to distinguish them from these contaminants.

Gentile Fusillo et al. (2015) have developed a method that, by combining multi–band photometry and proper motions, provides the probability for an object being a white dwarf ($P_{\rm WD}$). Therefore, we retrieved the proper motion for

Table 6.2: White dwarf candidates from CHiCaS0650.

α	δ	g (mag)	$P_{\rm WD}$ (%)
06:47:48.17	23:14:08.36	18.73	88.1
06:47:53.13	22:57:57.83	19.37	87.3
06:48:33.62	23:25:43.66	20.20	89.8
06:48:46.22	23:03:03.62	17.45	95.9
06:49:28.66	23:38:36.47	15.78	87.5
06:49:32.81	23:35:50.83	17.65	90.0*
06:49:49.51	23:27:42.29	20.09	84.5
06:50:09.61	23:23:50.94	20.33	94.6*
06:50:21.42	23:45:09.28	19.88	93.1
06:50:25.20	23:10:51.06	19.04	99.3
06:50:41.30	23:09:54.10	18.58	99.9
06:50:44.73	23:00:19.64	20.31	83.4
06:51:22.27	22:26:09.05	16.39	74.4
06:51:45.10	23:36:48.57	19.76	93.1
06:52:03.05	22:38:52.09	20.36	93.9
06:52:04.66	23:43:55.11	19.73	97.6
06:52:23.38	23:00:27.62	20.21	77.1
06:53:28.51	23:13:29.79	20.20	97.5

Notes. The systems highlighted with a star are the two CV candidates.

the sources in CHiCaS0650 from the PPMXL catalogue (Roeser et al., 2010) and, following the method of Gentile Fusillo et al. (2015), we identified 18 stars with a probability of being a white dwarf $P_{\rm WD} > 70\%$. These candidates are listed in Table 6.2. In the $(g-r,\ u-g)$ plane (top panel of Figure 6.2), the majority of the objects sit on the main sequence track while the white dwarf candidates (blue) occupy the bluer region. Two of them (triangles) are redder than the others, as suggested by their location on the right side of the $(r-i,\ r-H\alpha)$ plane, indicating the presence of an infrared excess. These systems are CVs candidates in which the excess could arise from a late–type companion. Alternatively, a white dwarf with a debris disc could also explain the observed colour excess (e.g. Girven et al. 2011). Since these two systems do no show eclipses (see below) that would confirm the presence of a companion, follow–up spectroscopy is required in order to establish the origin of the infrared excess.

Figure 6.3 shows the location of the white dwarf (blue dots) and the CV (blue triangles) candidates in the colour–magnitude diagram, for which *calibrated* magnitudes are reported. The diagram also shows that the limiting magnitude we could achieve on the night of the observation is $g \simeq 21.5$ mag.

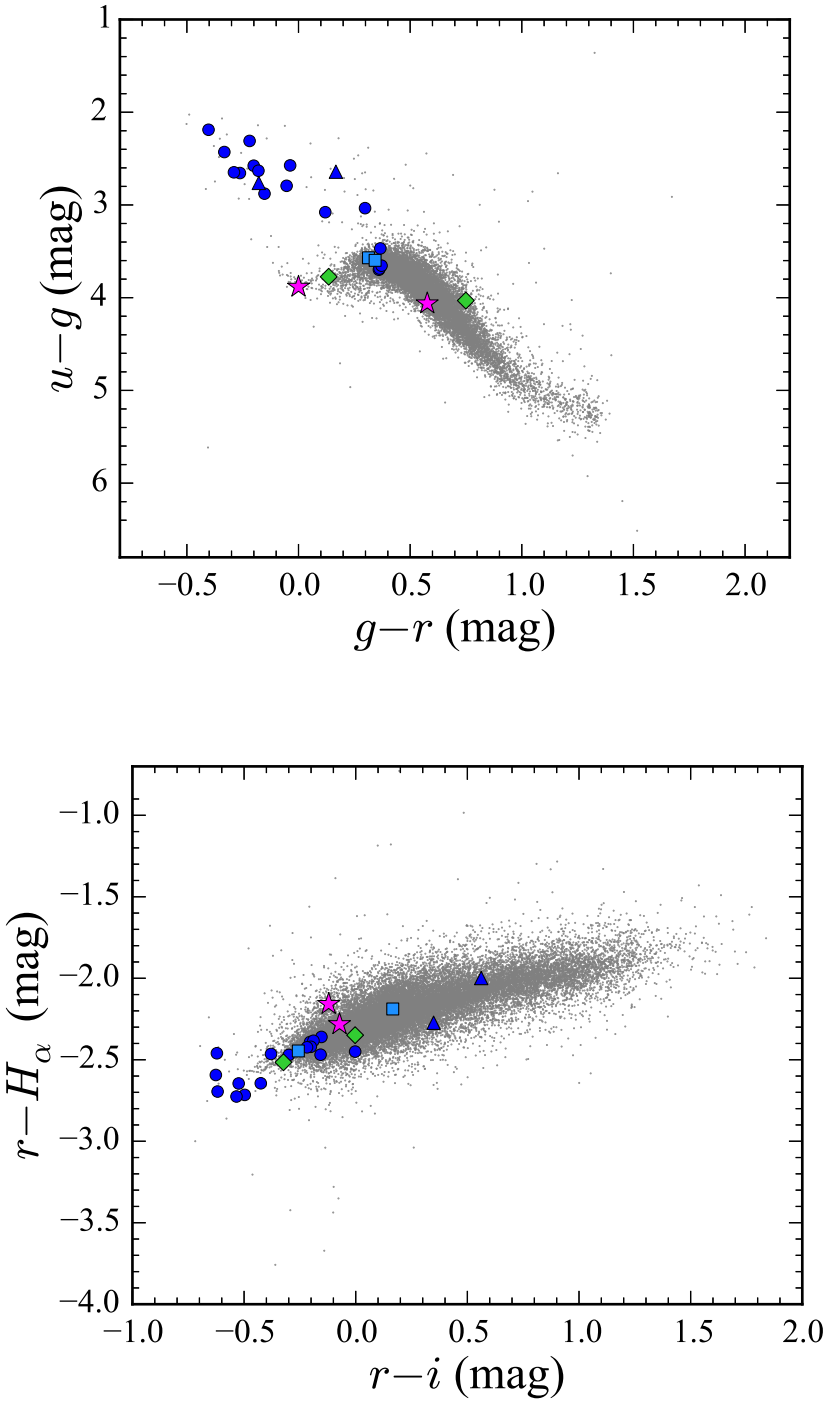

Figure 6.2: Colour–colour diagrams for CHiCaS0650, *instrumental* magnitudes are reported. The blue circles are the white dwarf candidates while the blue triangles are the two CV candidates. The stars, the squares and the diamonds are, respectively, the contact and eclipsing binaries and the pulsating stars whose lightcurves are shown in Figure 6.5.

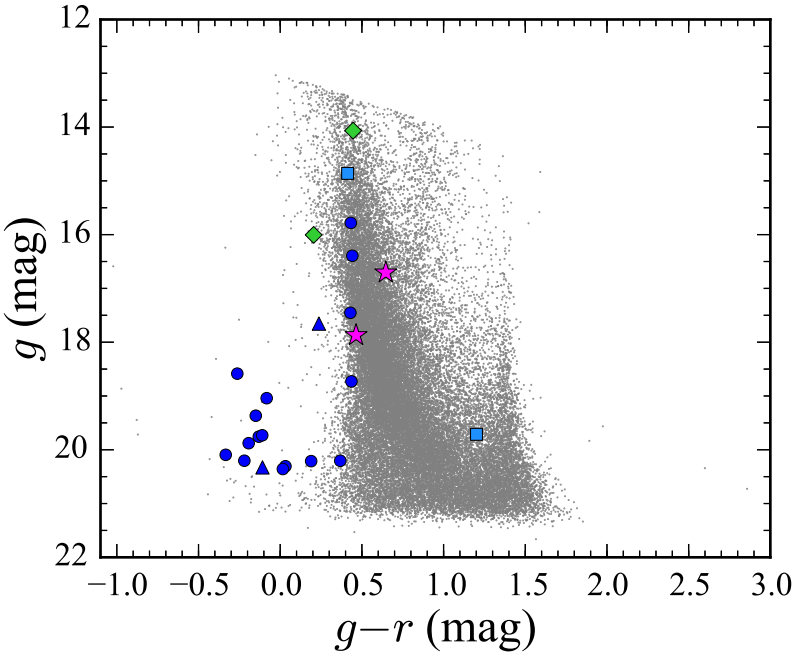

Figure 6.3: Colour–magnitude diagram for CHiCaS, *calibrated* magnitudes are reported. The blue circles are the white dwarf candidates while the blue triangles are the two CV candidates. The stars, the squares and the diamonds are, respectively, the contact and eclipsing binaries and the pulsating stars whose lightcurves are shown in Figure 6.5.

Time Series

We show sample light curves of the objects with a probability of being a white dwarf $P_{\rm WD} > 70\%$ in Figure 6.4 (top CV candidates, bottom white dwarf candidates). These objects are not listed either in Simbad or in the Montreal White Dwarf Database (Dufour et al., 2017) thus making this the first identification of these systems.

Moreover, by delivering light curves for all the objects in the field of view, our program provides a valuable legacy of ancillary data: we detected several contact binaries (Figure 6.5, top), eclipsing systems (Figure 6.5, middle) and pulsating stars (Figure 6.5, bottom). Of particular relevance is the light curve of the eclipsing system shown in the middle left panel: its detection illustrates that our observations will be able to identify period bouncer eclipses, which should have similar magnitudes and depths. Finally, the analysis of these eclipses, pulsations and ellipsoidal modulations yields important additional scientific results, providing a large sample of stars for which effective temperatures and masses can be accurately determined.

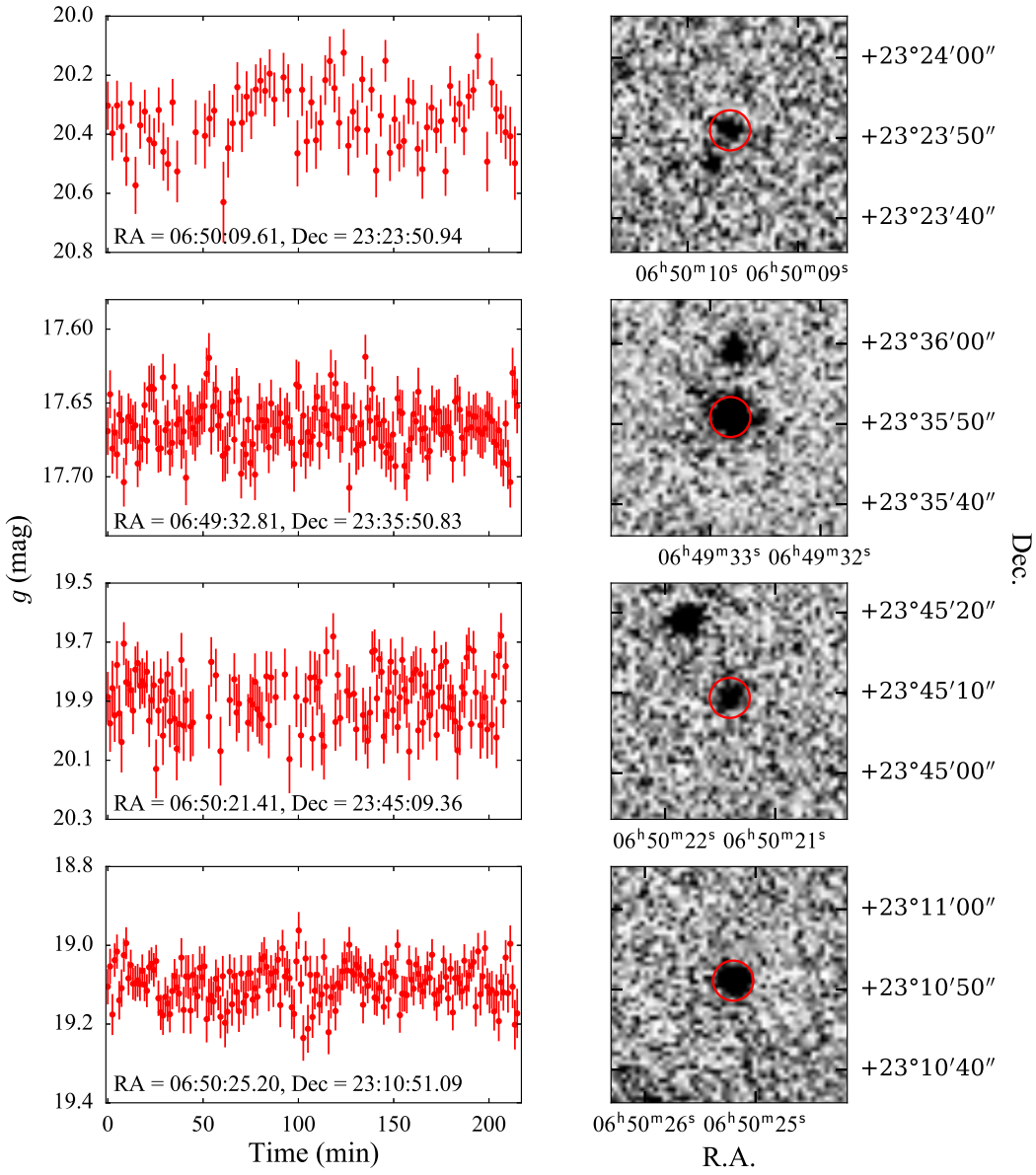

Figure 6.4: On the left, the lightcurves of the two CV candidates (first and second panels from the top) and sample lightcurves for two white dwarf candidates (third and fourth panels from the top) from CHiCaS0650 are plotted. On the right, for each star, a $30'' \times 30''$ cut–out from the *gSDSS*–band image of CHiCaS0650 from 2017–02–14 is shown. All the targets (red circles) are well resolved and are not blended with background sources.

6.4 Summary and future work

CHiCaS is the the first systematic attempt to unambiguously identify the population of period bouncers. This survey will provide a complete and unbiased view into short term variability: by observing 136 square degrees of the sky at one minute cadence,

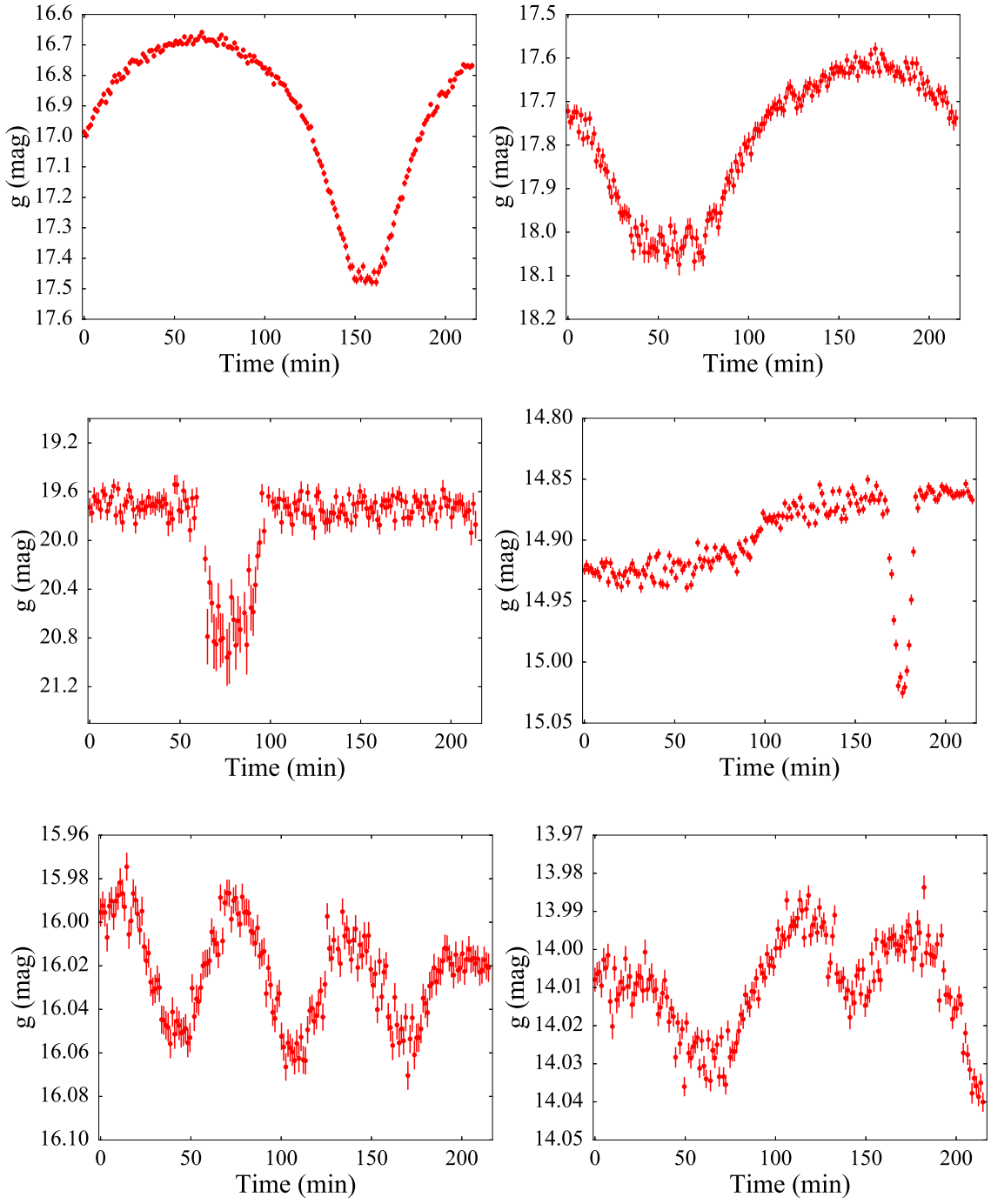

Figure 6.5: Sample lightcurves for six stars from CHiCaS0650 showing ellipsoidal modulations (top), eclipses (middle) and pulsations (bottom).

it will deliver lightcurves and full colour information for $\simeq 2.5$ million stars as faint as $g \simeq 21.5$ mag.

From the analysis of the photometry for one of the 68 fields in the CHiCaS

footprint, we have extracted the lightcurves for $\simeq$ 38 000 stars. The first observations of this program have shown that high–cadence time–series photometry with JAST/T80Cam allows the identification of faint CVs and white dwarfs, binary systems (either detached, semi/detached or in contact) and pulsating stars. Specifically, we have identified 16 new white dwarf candidates and two new CV candidates. Although no eclipse has been identified in the light curves of the two CV candidates, the two stars show an infrared excess which could imply the presence of either an companion or a debris disc. Follow–up observations are necessary to establish the origin of this colour excess.

Period bouncers are expected to be intrinsically faint and our results have proved our capability to detect systems with similar magnitudes and similar eclipse depths (Figure 6.5, middle left). If period bouncers do represent a major component of the present day Galactic CV population, thanks to this photometric survey we will be able to identify them thus carrying out a critical test on the current models of CV evolution.

At present, the photometric calibration of the $gJAVA$, $rJAVA$ and $iJAVA$ bands has been carried out using APASS (Henden and Munari, 2014). Calibration of the $uJAVA$ and $zJAVA$ bands requires SDSS photometry and several of our fields overlap with the SDSS footprint. Once multi–band photometry of these fields is acquired, we will be able to accurately calibrate all the bands. From this accurate calibration, using the method of Gentile Fusillo et al. (2016), we will be able to identify ZZ Ceti stars and to investigate the fundamental properties (internal structure, core and envelope mass and magnetic field) of these pulsating WDs.

Finally, one of the most prominent feature in the CV orbital period distribution is the lack of systems in the period gap, where CVs evolve as detached white dwarf plus main sequence star binaries, hosting secondaries of spectral type M4–M6. Once also the u–band is calibrated, we will be able to identify these systems from their colours (Rebassa-Mansergas et al., 2012). Their orbital periods will be determined from the ellipsoidal modulation in their light curves and, with only one follow–up spectrum, we can determine the spectral type of the secondary. In this way, we will identify the CVs that are presently crossing the period gap, carrying out another stringent test on CV evolution.

Chapter 7

Concluding summary and future work

7.1 Summary

In the last decades, the developments in observational technologies have highlighted major discrepancies between the current model of CV evolution and the observations, thus undermining our confidence in the model of the formation and evolution of all kind of compact binaries, such as X–ray transients, milli–second pulsars, double degenerate binaries and, maybe most importantly, SN Ia progenitors.

The aim of the work presented in this thesis has been to carry out a stringent test of the current models of CV evolution by enlarging the sample of well characterised systems and removing the current observational biases that limit our understanding of the physics of binary evolution in mass exchanging systems.

One of the best tracers of CV evolution is the mass accretion rate that can be inferred from the white dwarf effective temperature, which is set by the compressional heating of the accreted material. Prior to this work, the sample of systems with an accurate effective temperature measurement was limited to 43 CVs, most of them located at short orbital periods. The large *HST* observing program described in Chapter 3 has enlarged this census to a total of 76 CV white dwarfs.

By empirically determining the mass transfer rates as a function of orbital period, we tested the model for the present day CV population. We found that long–period systems ($P_{\rm orb} > 3\,{\rm hr}$) have, on average, mean mass–transfer rates about one order of magnitude higher than those of the systems at $P_{\rm orb} < 2\,{\rm hr}$. At a first glance, this is in accordance with the predictions of AML mechanisms driving their evolution. However, inspecting this qualitative agreement between observations and theoretical predictions in more detail, many outstanding discrepancies are found:

1. At orbital periods $P_{\rm orb} \gtrsim 3\,{\rm hr}$, the observed temperatures present a large scatter, with nova like CVs being hotter and dwarf novae being cooler than

predicted by the theory. Although it is clear that the evolution of CV in this period range is not fully understood yet, the interpretation of these results is not straightforward since we are limited by the small number of available effective temperatures. In fact, the sampling is very uneven: out of the 76 CVs with a white dwarf $T_{\rm eff}$ measurement, only 12 are at $P_{\rm orb} \gtrsim 3\,{\rm hr}$. Among them, only three lie in the range $3\,{\rm hr} < P_{\rm orb} < 4\,{\rm hr}$, eight systems are concentrated in the period range $4\,{\rm hr} < P_{\rm orb} < 5\,{\rm hr}$ and only one measurement is currently available for $P_{\rm orb} \gtrsim 5\,{\rm hr}$.

2. Below the period gap, the measured mass accretion rates imply the presence of additional AML mechanisms beyond pure GWR. Residual magnetic braking and/or CAML could mitigate the disagreement between observations and models, although will be challenging to distinguish between these possibilities. In fact, the proposed CAML descends from an empirical recipe and it has been suggested to arise from nova explosion, but the current knowledge of these eruptions is too limited to allow definitive conclusions. To test the possibility of residual magnetic braking, an intensive study of the donor stars in CVs below the period gap is required. However, in this period range, the secondary stars are intrinsically faint, making their detection and observation difficult.

3. One of the most striking discrepancies between the standard model of CV evolution and the observations is the dearth of period bouncer systems. While observational biases could play a major role in this missing population, it is also possible that our understanding of binary evolution is incomplete and the period bouncers are intrinsically less numerous. Critically uncertain areas in the theoretical modelling are (1) the evolution of stars undergoing mass loss, (2) the common envelope phase during which the progenitor evolves up the giant branch and engulfs the secondary star, and (3) the mechanisms of angular momentum loss, which are also the key ingredients to understand the exact pathways leading to SNe Ia.

Constraining the white dwarf masses to a few per cent is very important in order to understand if CVs could be SNe Ia progenitors. The number of CV white dwarfs with an accurate mass determination is so far limited to $\simeq 50$. The X–shooter program presented in Chapter 3 has added four new systems to this sample and our results have shown that phase–resolved spectroscopic observations allow to measure CV white dwarf masses with an accuracy of $\simeq 5\,$per cent. However, this method is limited by the fact that spectroscopic signatures of both the white and secondary need to be identified in the SED and this is not always possible owing to the contamination from the accretion flow. An alternative method to measure

CV white dwarf masses requires the combination of ultraviolet spectroscopy and the distance to the system. In its next data releases, the *Gaia* mission will provide accurate parallaxes for all the CVs for which ultraviolet spectroscopy is available and thus will allow to quadruple the number of CV white dwarfs with an accurate mass measurements.

Furthermore, this X–shooter observing program has delivered the SED for 23 CV white dwarfs and we have studied in details two of them: SDSS J123813.73–033933.0 (SDSS1238, Chapter 4) and QZ Lib (Chapter 5).

SDSS1238 is a remarkable CVs, showing quasi–periodic brightenings and a double–humped modulation at half the orbital period. We have revealed the connection between these phenomena and the heating of a fraction of the white dwarf. We conclude that the origin of the variability of SDSS1238 are spiral density waves most likely combined with thermal instabilities in the accretion disc, that modulate the accretion onto the white dwarf. If this is the case, the long outburst recurrence time of SDSS1238 could be explained by the disc being periodically drained of material during the brightenings. However, we cannot rule out the possibility that the brightenings arise from low amplitude non–radial pulsations of the white dwarf.

In the case of QZ Lib, the study of the SED has provided important constraints on the temperature of its donor star. This result, combined with the low mass ratio of the system and the low temperature of the white dwarf (which is the coolest systems at the longest orbital period below the period gap), strongly suggests that QZ Lib is a period bouncer. This result illustrates that some of the elusive period bouncers are probably hiding among the known CVs, and that multi–wavelength observations are a powerful tool to identify them as such.

The most commonly used techniques to identify period bouncers (the spectroscopic identification of a brown dwarf companion, a low mass ratio and a cool white dwarf), all suffer of some limitations due to either the necessity of expensive space–based or large aperture ground–based telescopes, or the detection of the stage A superhumps during the first phases of an outburst. In Chapter 6 we have presented CHiCaS, the Compact binary HIgh CAdence Survey, the first systematic attempt to unambiguously identify this major component of the CV population which is not subject to the aforementioned restrictions. By performing three hours of uninterrupted time series photometry at one minute cadence over 136 square degrees of the sky, CHiCaS will unambiguously identify, via detection of their eclipses, the predicted large population of period bouncers. Moreover, the program will deliver the lightcurves of $\simeq$ 2.5 million objects, providing a complete and unbiased view into the short term variability of eclipsing binaries, pulsating stars and CVs in the period gap.

7.2 Future work

The results of this works have shown that we are still far from a complete understanding of CV evolution and additional efforts are required to fill the gap between theory and observations.

We will continue with a detailed analysis of the individual systems in our *HST* sample, measuring rotation rates and abundances. This enlarged sample of well–characterised CV white dwarfs will provide robust observational constraints on the response of white dwarfs to the accretion of mass, angular momentum and energy.

Thanks to the wide wavelength coverage of X–shooter extending into the near–infrared, we can also fully characterise the secondary star when its signature is detected in the SED of the system. This allows us to investigate the response of the secondary stars to the mass loss process at different orbital periods, which is another powerful tool to further constrain the evolution of CVs.

As mentioned before, in April 2018, *Gaia* will provide accurate parallaxes for all the target of our large *HST* program. By accurately measuring their masses, we will carry out a stringent test of the mass erosion versus mass growth hypotheses of CV white dwarfs.

Finally, the CHiCaS fields overlapping with the SDSS footprint will be observed by the end of 2017, thus allowing the photometric calibration of all filter bands. The combination of full colour information and high–time resolution photometry will finally provide a definitive answer to the question on whether period bouncers exist or not, solving an outstanding problem of the current model of CV evolution.

Bibliography

Abbott B.P. et al., 2016a. *ApJ*, 818:L22.

Abbott B.P. et al., 2016b. *Physical Review Letters*, 116(24):241103.

Abbott B.P. et al., 2017. *Physical Review Letters*, 118(22):221101.

Ak T. et al., 2005. *PASA*, 22:105–110.

Allard F., Homeier D., and Freytag B., 2012. *Philosophical Transactions of the Royal Society of London Series A*, 370:2765–2777.

Althaus L.G. et al., 2010. *A&A Rev.*, 18:471–566.

Andronov N., Pinsonneault M., and Sills A., 2003. *ApJ*, 582:358–368.

Araujo-Betancor S. et al., 2003. *ApJ*, 583:437–445.

Araujo-Betancor S. et al., 2005a. *ApJ*, 622:589–601.

Araujo-Betancor S. et al., 2005b. *A&A*, 430:629–642.

Armitage P.J., 2011. *ARA&A*, 49:195–236.

Arras P., Townsley D.M., and Bildsten L., 2006. *ApJ*, 643:L119–L122.

Augusteijn T. and Wisotzki L., 1997. *A&A*, 324:L57–L60.

Augusteijn T. et al., 1996. *A&A*, 311:889–900.

Aungwerojwit A. et al., 2006. *A&A*, 455:659–672.

Aviles A. et al., 2010. *ApJ*, 711:389–398.

Baraffe I. et al., 1997. *A&A*, 327:1054–1069.

Barclay T. et al., 2011. *MNRAS*, 413:2696–2708.

Barwig H. and Schoembs R., 1983. *A&A*, 124:287–293.

Bell K.J. et al., 2015. *ApJ*, 809:14.

Bell K.J. et al., 2016. *ApJ*, 829:82.

Bell K.J. et al., 2017. In P.E. Tremblay, B. Gaensicke, and T. Marsh, editors, *20th European White Dwarf Workshop*, volume 509 of *Astronomical Society of the Pacific Conference Series*, 303.

Bergeron P., Wesemael F., and Fontaine G., 1991. *ApJ*, 367:253–269.

Bergeron P. et al., 2011. *ApJ*, 737:28.

Bertin E. and Arnouts S., 1996. *A&AS*, 117:393–404.

Bertin E. et al., 2002. In D.A. Bohlender, D. Durand, and T.H. Handley, editors, *Astronomical Data Analysis Software and Systems XI*, volume 281 of *Astronomical Society of the Pacific Conference Series*, 228.

Borucki W.J. et al., 2010. In *American Astronomical Society Meeting Abstracts #215*, volume 42 of *Bulletin of the American Astronomical Society*, 215.

Branch D. and Tammann G.A., 1992. *ARA&A*, 30:359–389.

Brinkworth C.S. et al., 2007. *ApJ*, 659:1541–1562.

Bullock E. et al., 2011. *AJ*, 141:84.

Cardelli J.A., Clayton G.C., and Mathis J.S., 1989. *ApJ*, 345:245–256.

Cenarro A.J. et al., 2010. In *Modeling, Systems Engineering, and Project Management for Astronomy IV*, volume 7738 of *Proc. SPIE*, 77380V.

Chabrier G. and Baraffe I., 1997. *A&A*, 327:1039–1053.

Chandrasekhar S., 1931. *ApJ*, 74:81.

Charbonneau P. and MacGregor K.B., 1997. *ApJ*, 486:502–520.

Chen A. et al., 2001. *MNRAS*, 325:89–110.

Chochol D. et al., 2012. *Contributions of the Astronomical Observatory Skalnate Pleso*, 42:39–79.

Chote P. and Sullivan D.J., 2016. *MNRAS*, 458:1393–1401.

Damineli A., 1996. *ApJ*, 460:L49.

De Donder E. and Vanbeveren D., 2004. *New Astronomy Reviews*, 48:861–975.

de Kool M., 1992. *A&A*, 261:188–202.

Delfosse X. et al., 1998. *A&A*, 331:581–595.

Dhillon V.S., 1996. In A. Evans and J.H. Wood, editors, *IAU Colloq. 158: Cataclysmic Variables and Related Objects*, volume 208 of *Astrophysics and Space Science Library*, 3.

Dillon M. et al., 2008. *MNRAS*, 386:1568–1578.

Diplas A. and Savage B.D., 1994. *ApJ*, 427:274–287.

Dufour P. et al., 2007. *Nature*, 450:522–524.

Dufour P. et al., 2017. In P.E. Tremblay, B. Gaensicke, and T. Marsh, editors, *20th European White Dwarf Workshop*, volume 509 of *Astronomical Society of the Pacific Conference Series*, 3.

Eggleton P.P., 1983. *ApJ*, 268:368.

Eldridge J.J., Izzard R.G., and Tout C.A., 2008. *MNRAS*, 384:1109–1118.

Epelstain N. et al., 2007. *MNRAS*, 374:1449–1456.

Eracleous M. et al., 1994. *ApJ*, 433:313–331.

Farihi J. et al., 2010. *MNRAS*, 404:2123–2135.

Feline W.J. et al., 2004. *MNRAS*, 355:1–10.

Feline W.J. et al., 2005. *MNRAS*, 364:1158–1167.

Ferrario L., de Martino D., and Gänsicke B.T., 2015. *Space Sci. Rev.*, 191:111–169.

Flannery B.P., 1975. *MNRAS*, 170:325–331.

Fontaine G. and Wesemael F., 1987. In A.G.D. Philip, D.S. Hayes, and J.W. Liebert, editors, *IAU Colloq. 95: Second Conference on Faint Blue Stars*, 319–326.

Foreman-Mackey D. et al., 2013. emcee: The MCMC Hammer. Astrophysics Source Code Library.

Frank J., King A., and Raine D.J., 2002. *Accretion Power in Astrophysics: Third Edition*.

Freudling W. et al., 2013. *A&A*, 559:A96.

Fuhrmann K. et al., 2017. *ApJ*, 836:139.

Gänsicke B.T. and Beuermann K., 1996. *A&A*, 309:L47–L50.

Gänsicke B.T., Beuermann K., and de Martino D., 1995. *A&A*, 303:127–136.

Gänsicke B.T., Beuermann K., and Thomas H.C., 1997. *MNRAS*, 289:388–392.

Gänsicke B.T. and Koester D., 1999. *A&A*, 346:151–157.

Gänsicke B.T. et al., 1999. *A&A*, 347:178–184.

Gänsicke B.T. et al., 2003. *ApJ*, 594:443–448.

Gänsicke B.T. et al., 2005. *ApJ*, 629:451–460.

Gänsicke B.T. et al., 2006. *ApJ*, 639:1039–1052.

Gänsicke B.T. et al., 2009. *MNRAS*, 397:2170–2188.

Gänsicke B.T. et al., 2012. *MNRAS*, 424:333–347.

Gehrz R.D. et al., 1998. *PASP*, 110:3–26.

Gentile Fusillo N.P., Gänsicke B.T., and Greiss S., 2015. *MNRAS*, 448:2260–2274.

Gentile Fusillo N.P., Hermes J.J., and Gänsicke B.T., 2016. *MNRAS*, 455:2295–2307.

Gentile Fusillo N.P. et al., 2017. *MNRAS*, 468:971–980.

Giammichele N., Bergeron P., and Dufour P., 2012. *ApJS*, 199:29.

Giampapa M.S. and Liebert J., 1986. *ApJ*, 305:784–794.

Gianninas A., Bergeron P., and Ruiz M.T., 2011. *ApJ*, 743:138.

Girven J. et al., 2011. *MNRAS*, 417:1210–1235.

Godon P. et al., 2004a. *ApJ*, 612:429–436.

Godon P. et al., 2004b. *ApJ*, 602:336–341.

Godon P. et al., 2016. *ApJ*, 833:146.

Goliasch J. and Nelson L., 2015. *ApJ*, 809:80.

Green G.M. et al., 2015. *ApJ*, 810:25.

Green J.C. et al., 2012. *ApJ*, 744:60.

Greenstein J.L. and Trimble V.L., 1967. *ApJ*, 149:283.

Groot P.J., 2001. *ApJ*, 551:L89–L92.

Guerrero J., García-Berro E., and Isern J., 2004. *A&A*, 413:257–272.

Hamada T. and Salpeter E.E., 1961. *ApJ*, 134:683.

Hameury J.M. et al., 1998. *MNRAS*, 298:1048–1060.

Han Z. et al., 1995. *MNRAS*, 277:1443–1462.

Hassall B.J.M. et al., 1983. *MNRAS*, 203:865–885.

Hawley J.F. and Balbus S.A., 1998. In S. Howell, E. Kuulkers, and C. Woodward, editors, *Wild Stars in the Old West*, volume 137 of *Astronomical Society of the Pacific Conference Series*, 273.

Hellier C., 2001. *Cataclysmic Variable Stars*.

Henden A. and Munari U., 2014. *Contributions of the Astronomical Observatory Skalnate Pleso*, 43:518–522.

Hermes J.J. et al., 2015. *ApJ*, 810:L5.

Hillman Y. et al., 2016. *ApJ*, 819:168.

Hoard D.W. et al., 2004. *ApJ*, 604:346–356.

Hodgkin S.T., Jameson R.F., and Steele I.A., 1995. *MNRAS*, 274:869–883.

Holberg J.B. and Bergeron P., 2006. *AJ*, 132:1221–1233.

Horne K., 1986. *PASP*, 98:609–617.

Horne K. and Marsh T.R., 1986. *MNRAS*, 218:761–773.

Horne K. et al., 1994. *ApJ*, 426:294–307.

Howell S.B., Nelson L.A., and Rappaport S., 2001. *The Astrophysical Journal*, 550:897–918.

Howell S.B. et al., 2006. *ApJ*, 646:L65–L68.

Howell S.B. et al., 2008. *ApJ*, 685:418-427.

Huang S.S., 1966. *Annales d'Astrophysique*, 29:331.

Hubeny I., 1988. *Computer Physics Communications*, 52:103–132.

Hubeny I. and Lanz T., 1995. *ApJ*, 439:875–904.

Huber D. et al., 2016. *ApJS*, 224:2.

Iben Jr. I., 1991. *ApJS*, 76:55–114.

Iben Jr. I. and Tutukov A.V., 1984. *ApJS*, 54:335–372.

Imada A. et al., 2006. *PASJ*, 58:383–388.

Imada A. et al., 2007. In Y.W. Kang, H.W. Lee, K.C. Leung, and K.S. Cheng, editors, *The Seventh Pacific Rim Conference on Stellar Astrophysics*, volume 362 of *Astronomical Society of the Pacific Conference Series*, 212.

Ishioka R., Sekiguchi K., and Maehara H., 2007. *PASJ*, 59:929–.

Isogai M. et al., 2015. *PASJ*, 67:7.

Ivanova N. and Taam R.E., 2004. *ApJ*, 601:1058–1066.

Jeans J.H., 1902. *Philosophical Transactions of the Royal Society of London Series A*, 199:1–53.

Joergens V., Spruit H.C., and Rutten R.G.M., 2000. *A&A*, 356:L33–L36.

Jura M., 2003. *ApJ*, 584:L91–L94.

Kalirai J.S. et al., 2008. *ApJ*, 676:594-609.

Kalomeni B. et al., 2016. *ApJ*, 833:83.

Karttunen H. et al., editors, 2007. *Fundamental Astronomy*.

Kasle D.B. and Morgan J.S., 1991. In O.H. Siegmund and R.E. Rothschild, editors, *EUV, X-Ray, and Gamma-Ray Instrumentation for Astronomy II*, volume 1549 of *Proc. SPIE*, 52–58.

Kato T., 2004. *vsnet-campaign-dn*, 4126,7,8.

Kato T. and Osaki Y., 2013. *PASJ*, 65:115.

Kato T. et al., 2009. *PASJ*, 61:S395–S616.

Kato T. et al., 2015. *PASJ*, 67:105.

Kato T. et al., 2016. *PASJ*, 68:65.

Kausch W. et al., 2015. *A&A*, 576:A78.

Kepler S.O. et al., 2007. *MNRAS*, 375:1315–1324.

King A.R., 1988. *QJRAS*, 29:1–25.

King A.R. and Kolb U., 1995. *ApJ*, 439:330–336.

King A.R., Wynn G.A., and Regev O., 1991. *MNRAS*, 251:30P–32P.

Kitchin C.R., 2013. *Astrophysical Techniques*.

Kiyota S., 2004. *vsnet-campaign-dn*, 4123,4.

Kleinman S.J. et al., 2013. *ApJS*, 204:5.

Knigge C., 2006. *MNRAS*, 373:484–502.

Knigge C., Baraffe I., and Patterson J., 2011. *ApJS*, 194:28.

Knigge C. et al., 2000. *ApJ*, 539:L49–L53.

Koester D., 2009. *A&A*, 498:517–525.

Koester D., 2010. *Mem. Soc. Astron. Italiana*, 81:921–931.

Koester D. and Knist S., 2006. *A&A*, 454:951–956.

Koester D., Schulz H., and Weidemann V., 1979. *A&A*, 76:262–275.

Koester D. and Wolff B., 2000. *A&A*, 357:587–596.

Koester D. et al., 1985. *A&A*, 142:L5–L8.

Kolb U., 1993. *A&A*, 271:149.

Kolb U. and Baraffe I., 1999. *MNRAS*, 309:1034–1042.

Kolb U. and Stehle R., 1996. *MNRAS*, 282:1454–1460.

Kononov D.A. et al., 2015. *Astronomy Reports*, 59:191–198.

Kopal Z., editor, 1978. *Dynamics of close binary systems*, volume 68 of *Astrophysics and Space Science Library*.

Kowalski P.M. and Saumon D., 2006. *ApJ*, 651:L137–L140.

Kraft R.P., 1967. *ApJ*, 150:551.

Lallement R. et al., 2014. *A&A*, 561:A91.

Leonard P.J.T., 1989. *AJ*, 98:217–226.

Liebert J., Bergeron P., and Holberg J.B., 2005. *ApJS*, 156:47–68.

Lin D.N.C. and Papaloizou J., 1979. *MNRAS*, 186:799–812.

Linsky J.L. et al., 1995. *ApJ*, 455:670.

Littlefair S.P. et al., 2006. *Science*, 314:1578.

Littlefair S.P. et al., 2008. *MNRAS*, 388:1582–1594.

Livio M. and Pringle J.E., 1994. *ApJ*, 427:956–960.

Long K.S., Blair W.P., and Raymond J.C., 1995. *ApJ*, 454:L39.

Long K.S., Brammer G., and Froning C.S., 2006. *ApJ*, 648:541–558.

Long K.S. et al., 1993. *ApJ*, 405:327–336.

Long K.S. et al., 2003. *ApJ*, 591:1172–1183.

Long K.S. et al., 2004. *ApJ*, 602:948–959.

Long K.S. et al., 2009. *ApJ*, 697:1512–1528.

Lorén-Aguilar P., Isern J., and García-Berro E., 2009. *A&A*, 500:1193–1205.

Lubow S.H. and Shu F.H., 1975. *ApJ*, 198:383–405.

Lund M.N. et al., 2015. *ApJ*, 806:30.

Macfarlane S.A. et al., 2015. *MNRAS*, 454:507–530.

MacGregor K.B. and Charbonneau P., 1997. *ApJ*, 486:484–501.

Malkov O. and Zinnecker H., 2001. *MNRAS*, 321:149–154.

Massa D. et al., 2014. Updated Absolute Flux Calibration of the COS FUV Modes. Technical report.

Matthews O.M. et al., 2006. *MNRAS*, 372:1593–1601.

Maza J. and Gonzalez L.E., 1983. *IAU Circ.*, 3854.

McAllister M.J. et al., 2017. *MNRAS*, 467:1024–1032.

Mennickent R.E. and Diaz M., 1996. *A&A*, 309:147–154.

Mennickent R.E. and Diaz M.P., 2002. *MNRAS*, 336:767–773.

Mennickent R.E. and Tappert C., 2001. *A&A*, 372:563–565.

Mennickent R.E. et al., 2001. *A&A*, 376:448–459.

Mestel L., 1968. *MNRAS*, 138:359.

Meyer F. and Meyer-Hofmeister E., 1984. *A&A*, 132:143–150.

Meyer F. and Meyer-Hofmeister E., 1994. *A&A*, 288:175–182.

Mukai K., 2017. *PASP*, 129(6):062001.

Nelan E.P. and Wegner G., 1985. *ApJ*, 289:L31–L33.

Nelemans G. et al., 2016. *ApJ*, 817:69.

Neustroev V.V. et al., 2017. *MNRAS*, 467:597–618.

Nomoto K., 1982. *ApJ*, 253:798–810.

Oizumi S. et al., 2007. *PASJ*, 59:643–651.

Osaki Y., 1974. *PASJ*, 26:429–436.

Osaki Y., 1989. *PASJ*, 41:1005–1033.

Osaki Y., 1996. *PASP*, 108:39–60.

Osaki Y. and Kato T., 2013. *PASJ*, 65:95.

Osaki Y. and Meyer F., 2002. *A&A*, 383:574–579.

Paczyński B., 1967. *Acta Astronomica*, 17:287.

Paczynski B., 1976. In P. Eggleton, S. Mitton, and J. Whelan, editors, *Structure and Evolution of Close Binary Systems*, volume 73 of *IAU Symposium*, 75.

Paczynski B. and Sienkiewicz R., 1983. *The Astrophysical Journal*, 268:825–831.

Pala A.F. et al., 2017. *MNRAS*, 466:2855–2878.

Paquette C. et al., 1986. *ApJS*, 61:197–217.

Parker E.N., 1955. *ApJ*, 122:293.

Parsons S.G. et al., 2012. *MNRAS*, 419:304–313.

Patterson J., 1984. *ApJS*, 54:443–493.

Patterson J., 1998. *PASP*, 110:1132–1147.

Patterson J., 2011. *MNRAS*, 411:2695–2716.

Patterson J., Thorstensen J.R., and Kemp J., 2005a. *PASP*, 117:427–444.

Patterson J. et al., 1996. *PASP*, 108:748.

Patterson J. et al., 2000. *PASP*, 112:1567–1583.

Patterson J. et al., 2005b. *PASP*, 117:1204–1222.

Pavlenko E., 2009. In *Journal of Physics Conference Series*, volume 172 of *Journal of Physics Conference Series*, 012071.

Pavlenko E.P. et al., 2014. *PASJ*, 66:113.

Paxton B. et al., 2015. *ApJS*, 220:15.

Pearson K.J., 2006. *MNRAS*, 371:235–244.

Pelletier C. et al., 1986. *ApJ*, 307:242–252.

Perlmutter S. et al., 1999. *ApJ*, 517:565–586.

Piro A.L., Arras P., and Bildsten L., 2005. *ApJ*, 628:401–410.

Pojmanski G., 1997. *Acta Astronomica*, 47:467–481.

Politano M., 2004. *ApJ*, 604:817–826.

Pretorius M.L. and Knigge C., 2012. *MNRAS*, 419:1442–1454.

Pretorius M.L. et al., 2004. *MNRAS*, 352:1056–1060.

Prialnik D. and Kovetz A., 1995. *ApJ*, 445:789–810.

Price A. et al., 2004. *PASP*, 116:1117–1122.

Raddi R. et al., 2015. *MNRAS*, 450:2083–2093.

Rafikov R.R., 2016. *ApJ*, 831:122.

Raghavan D. et al., 2010. *ApJS*, 190:1–42.

Ramsay G. and Hakala P., 2005. *MNRAS*, 360:314–321.

Rappaport S., Verbunt F., and Joss P.C., 1983. *ApJ*, 275:713–731.

Rebassa-Mansergas A., Schreiber M.R., and Gänsicke B.T., 2013. *MNRAS*, 429:3570–3577.

Rebassa-Mansergas A. et al., 2012. *MNRAS*, 419:806–816.

Rebassa-Mansergas A. et al., 2014. *ApJ*, 790:28.

Reiners A. and Basri G., 2008. *ApJ*, 684:1390-1403.

Riess A.G. et al., 1998. *AJ*, 116:1009–1038.

Ritter H., 1976. *MNRAS*, 175:279–295.

Ritter H., 1987. *Mem. Soc. Astron. Italiana*, 58:133–138.

Ritter H. and Kolb U., 2003. *A&A*, 404:301–303.

Rodríguez-Gil P. et al., 2004. *A&A*, 424:647–655.

Rodríguez-Gil P. et al., 2009. *A&A*, 496:805–812.

Rodríguez-Gil P. et al., 2012. *MNRAS*, 422:2332–2340.

Rodríguez-Gil P. et al., 2015. *MNRAS*, 452:146–157.

Roeser S., Demleitner M., and Schilbach E., 2010. *AJ*, 139:2440–2447.

Rogoziecki P. and Schwarzenberg-Czerny A., 2001. *MNRAS*, 323:850–858.

Sana H. et al., 2012. *Science*, 337:444.

Sarna M.J., Antipova J., and Ergma E., 1999. In S.E. Solheim and E.G. Meistas, editors, *11th European Workshop on White Dwarfs*, volume 169 of *Astronomical Society of the Pacific Conference Series*, 400.

Savoury C.D.J. et al., 2011. *MNRAS*, 415:2025–2041.

Schatzman E., 1962. *Annales d'Astrophysique*, 25:18.

Schenker K., Kolb U., and Ritter H., 1998. *MNRAS*, 297:633–647.

Schmidtobreick L. et al., 2004. *Inf. Bull. Variable Stars*, 5508:1.

Schreiber M.R., Hameury J.M., and Lasota J.P., 2003. *A&A*, 410:239–252.

Schreiber M.R., Hameury J.M., and Lasota J.P., 2004. *A&A*, 427:621–635.

Schreiber M.R., Zorotovic M., and Wijnen T.P.G., 2016. *MNRAS*, 455:L16–L20.

Schreiber M.R. et al., 2010. *A&A*, 513:L7.

Schwarzenberg-Czerny A., 1996. *ApJ*, 460:L107.

Shu F.H., 1982. *The Physical Universe*. University Science Books.

Siess L., 2007. *A&A*, 476:893–909.

Sion E.M., 1995. *ApJ*, 438:876–886.

Sion E.M., 1999. *PASP*, 111:532–555.

Sion E.M. et al., 1994. *ApJ*, 430:L53–L56.

Sion E.M. et al., 1995. *ApJ*, 445:L31–L34.

Sion E.M. et al., 1998. *ApJ*, 496:449–453.

Sion E.M. et al., 2001. *ApJ*, 555:834–838.

Sion E.M. et al., 2008. *ApJ*, 681:543–553.

Slevinsky R.J. et al., 1999. *PASP*, 111:1292–1297.

Smette A. et al., 2015. *A&A*, 576:A77.

Southworth J. et al., 2008. *MNRAS*, 391:591–606.

Southworth J. et al., 2009. *A&A*, 507:929–937.

Spruit H.C., 1987. *A&A*, 184:173–184.

Spruit H.C., 1998. *ArXiv Astrophysics e-prints*.

Spruit H.C. and Ritter H., 1983. *A&A*, 124:267–272.

Steeghs D., Harlaftis E.T., and Horne K., 1997. *MNRAS*, 290:L28–L32.

Steeghs D. et al., 2001. *ApJ*, 562:L145–L148.

Steeghs D. et al., 2003. *MNRAS*, 339:810–816.

Stetson P.B., 1992. In D.M. Worrall, C. Biemesderfer, and J. Barnes, editors, *Astronomical Data Analysis Software and Systems I*, volume 25 of *Astronomical Society of the Pacific Conference Series*, 297.

Stockman H.S. et al., 1994. *ApJ*, 430:323–331.

Szkody P., 1985. *AJ*, 90:1837–1851.

Szkody P. and Mateo M., 1986. *AJ*, 92:483–489.

Szkody P. et al., 2002a. *AJ*, 123:430–442.

Szkody P. et al., 2002b. *ApJ*, 575:L79–L82.

Szkody P. et al., 2002c. In B.T. Gänsicke, K. Beuermann, and K. Reinsch, editors, *The Physics of Cataclysmic Variables and Related Objects*, volume 261 of *Astronomical Society of the Pacific Conference Series*, 21.

Szkody P. et al., 2003. *AJ*, 126:1499–1514.

Szkody P. et al., 2004. *AJ*, 128:1882–1893.

Szkody P. et al., 2005. *AJ*, 129:2386–2399.

Szkody P. et al., 2006. *AJ*, 131:973–983.

Szkody P. et al., 2007. *AJ*, 134:185–194.

Szkody P. et al., 2009. *AJ*, 137:4011–4019.

Szkody P. et al., 2010. *ApJ*, 710:64–77.

Szkody P. et al., 2011. *AJ*, 142:181.

Szkody P. et al., 2012. *ApJ*, 753:158.

Szkody P. et al., 2016. *ArXiv e-prints*.

Szkody P. et al., 2017. *AJ*, 153:123.

Tappert C. et al., 2003. *A&A*, 408:651–661.

Templeton M.R., 2007. *AAVSO Alert Notice*, 349.

Templeton M.R. et al., 2006. *PASP*, 118:236–245.

The LIGO Scientific Collaboration and The Virgo Collaboration, 2017. *ArXiv e-prints*.

The LIGO Scientific Collaboration et al., 2017. *ArXiv e-prints*.

Thorstensen J.R., 2003. *AJ*, 126:3017–3029.

Thorstensen J.R. and Fenton W.H., 2003. *PASP*, 115:37–42.

Thorstensen J.R. and Taylor C.J., 1997. *PASP*, 109:1359–1363.

Thorstensen J.R. and Taylor C.J., 2001. *MNRAS*, 326:1235–1242.

Thorstensen J.R. et al., 1996. *PASP*, 108:73.

Thorstensen J.R. et al., 2002a. *PASP*, 114:1117–1123.

Thorstensen J.R. et al., 2002b. *PASP*, 114:1108–1116.

Thorstensen J.R. et al., 2009. *PASP*, 121:465–477.

Timothy J.G. and Bybee R., 1977. In *Electron Devices Meeting, 1977 International*, 465–468. IEEE.

Tody D., 1986. In D.L. Crawford, editor, *Instrumentation in astronomy VI*, volume 627 of *Proc. SPIE*, 733.

Tody D., 1993. In R.J. Hanisch, R.J.V. Brissenden, and J. Barnes, editors, *Astronomical Data Analysis Software and Systems II*, volume 52 of *Astronomical Society of the Pacific Conference Series*, 173.

Toloza O. et al., 2016. *ArXiv e-prints*.

Toma R. et al., 2016. *MNRAS*, 463:1099–1116.

Torres G., Andersen J., and Giménez A., 2010. *A&A Rev.*, 18:67–126.

Townsley D.M. and Bildsten L., 2003. *The Astrophysical Journal*, 596:L227–L230.

Townsley D.M. and Bildsten L., 2004. *ApJ*, 600:390–403.

Townsley D.M. and Gänsicke B.T., 2009. *The Astrophysical Journal*, 693:1007–1021.

Tremblay P.E., Bergeron P., and Gianninas A., 2011. *ApJ*, 730:128.

Tremblay P.E. et al., 2013. *A&A*, 559:A104.

Tutukov A. and Yungelson L., 1979. In P.S. Conti and C.W.H. De Loore, editors, *Mass Loss and Evolution of O-Type Stars*, volume 83 of *IAU Symposium*, 401–406.

Tylenda R., 1981. *Acta Astronomica*, 31:127.

Uemura M. et al., 2010. *PASJ*, 62:613–620.

Unda-Sanzana E. et al., 2008. *MNRAS*, 388:889–897.

Van Grootel V. et al., 2015. *A&A*, 575:A125.

van Spaandonk L. et al., 2010. *ApJ*, 715:L109–L112.

Vanderburg A. et al., 2015. *Nature*, 526:546–549.

Verbunt F. and Zwaan C., 1981. *A&A*, 100:L7–L9.

Vernet J. et al., 2011. *A&A*, 536:A105.

Warner B., 1973. *MNRAS*, 162:189–196.

Warner B., 1995. *Cambridge Astrophysics Series*, 28.

Webbink R.F., 1976. *ApJ*, 209:829–845.

Webbink R.F., 1984. *ApJ*, 277:355–360.

Webbink R.F., 1985. *Stellar evolution and binaries*, 39.

Webbink R.F. and Wickramasinghe D.T., 2002. *MNRAS*, 335:1–9.

Whelan J. and Iben Jr. I., 1973. *ApJ*, 186:1007–1014.

Whitehurst R., 1988. *MNRAS*, 232:35–51.

Wijnen T.P.G., Zorotovic M., and Schreiber M.R., 2015. *A&A*, 577:A143.

Williams R.E., 1980. *ApJ*, 235:939–944.

Woodgate B.E. et al., 1998. *PASP*, 110:1183–1204.

Woudt P.A. and Warner B., 2002. *Ap&SS*, 282:433–438.

York D.G. et al., 2000. *AJ*, 120:1579–1587.

Zharikov S.V. et al., 2006. *A&A*, 449:645–653.

Zharikov S.V. et al., 2008. *A&A*, 486:505–509.

Zorotovic M., Schreiber M.R., and Gänsicke B.T., 2011. *A&A*, 536:A42.

Zorotovic M. et al., 2010. *A&A*, 520:A86.

Zorotovic M. et al., 2016. *MNRAS*, 457:3867–3877.